Alternative Estimators for Weak Gravitational Lensing

by

Sanaz Vafaei

B.Sc. Physics, Shahid Beheshti University, 2004

M.Sc. Astronomy, The University of British Columbia, 2006

A THESIS SUBMITTED IN PARTIAL FULFILLMENT
OF THE REQUIREMENTS FOR THE DEGREE OF

Doctor of Philosophy

in

THE FACULTY OF GRADUATE STUDIES

(Physics)

The University Of British Columbia

(Vancouver)

April 2012

© Sanaz Vafaei, 2012

Abstract

Weak gravitational lensing provides a means to measure the total mass in the Universe. The incoming light from distant galaxies is disturbed by the inhomogeneity of the dark matter distribution along the line of sight. The correlations of shape in an observed galaxy population can be used to probe the total mass density fluctuations in the Universe. Studies of correlations between galaxy shapes have been the basis of weak lensing research. In this thesis we investigate various non-conventional weak lensing statistics that are complementary to the traditional two-point shear correlation functions. The goal is to constrain the matter density $\Omega_{\rm m}$ and normalization of matter power spectrum σ_8 parameters. These higher order statistics have long been advocated as a powerful tool to break measured degeneracies between cosmological parameters. Using ray-tracing simulations, which incorporate important survey features such as a realistic depth-dependent redshift distribution, we find that joint two- and three-point correlation function analysis is a much stronger probe of cosmology than the two-point analysis alone.

We apply the higher order statistics technique to the 160 deg^2 of the Canada-France-Hawaii-Telescope Legacy Survey (CFHTLS) and show preliminary results from the joint two- and three-point likelihood analysis. We reveal the possibilities that lie in the projected mass probability distribution function to discriminate models with different values of the matter density parameter. In the process we develop a hybrid data set based on the simulations and the CFHTLenS data for systematics testing and covariance matrix estimations. Our error analysis includes all non-Gaussian terms, finding that the coupling between cosmic variance and shot noise is a non-negligible contribution.

Preface

The work on testing of the numerical simulations presented in chapter 5, is a submitted article, titled as “Gravitational Lensing Simulations I : Covariance Matrices and Halo Catalogues”, with Sanaz Vafaei as a co-author (Harnois-Deraps et al. [2012]). Sanaz Vafaei performed the weak lensing tests on the simulations. This work has been carried out in collaboration with Dr. Ludovic van Waerbeke and Joachim Harnois-Deraps.

The work presented in chapter 6 is published under the title “Breaking the Degeneracy: Optimal Use of Three-point Weak Lensing Statistics”, with Sanaz Vafaei as the primary author (Vafaei et al. [2010]). Co-authors are Dr. Tingting Lu, Dr. Ludovic van Waerbeke, Dr. Elisabetta Semboloni, Dr. Catherine Heymans, and Dr. Uei-Li Pen.

Numerical Simulations developed in collaboration with Dr. Tingting Lu, and explained in chapter 6 were used in the publication of Semboloni et al. [2011b] for covariance matrix calculations. Sanaz Vafaei is a co-author of this work for providing the numerical simulations.

The Canada-France-Hawaii-Telescope Lensing Survey (CFHTLenS) data was used in the analysis presented in chapter 7. This work has been carried out in collaboration with Dr. Ludovic van Waerbeke, Dr. Elisabetta Semboloni and the CFHTLenS collaboration. The results will be included in the publication in preparation with Sanaz Vafaei as the first author.

The work presented in chapter 8 has been carried out in collaboration with Dr. Ludovic van Waerbeke and Dr. Patrick Valageas and Dr. Dipak Munshi. The publication of this work is in preparation with Sanaz Vafaei as the first author.

Finally, the clone catalogues produced by Sanaz Vafaei, described in chapter

9 will be used in numerous scientific publications of the CFHTLenS collaboration for covariance matrix estimation and systematics tests.

Table of Contents

List of Tables

List of Figures

Glossary

2-3PCF	2- or 3-Point Correlation Function
BAO	Baryon Acoustic Oscillation
BPZ	Bayesian Photometric Redshifts
CADC	Canadian Astronomy Data Centre
CAMB	Code for Anisotropies in the Microwave Background
CCD	Charged Coupled Device
CDM	Cold Dark Matter model
CFHT	Canada France Hawaii Telescope
CFHTLenS	Canada France Hawaii Lensing Survey (Systematics Team)
CFHTLS	Canada France Hawaii Telescope Legacy Survey
CMB	Cosmic Microwave Background
COSMOS	COSMic evOlution Survey
CTIO	Cerro Tololo Inter-american Observatory
DEC	Declination
DES	Dark Energy Survey
FT	Fourier Transform

JDEM	Joint Dark Energy Mission
FRW	FRW-Universe (Friedmann-Robertson-Walker)
HST	Hubble Space Telescope
KSB	Kaiser, Squires and Broadhurst method
KIDS	Kilo Degree Survey
LSS	Large Scale Structure
LSST	Large Synoptic Survey Telescope
Pan-STARRS	The Panoramic Survey Telescope And Rapid Response System
PDF	Probability Distribution Function
PS	Power Spectrum
PSF	Point Spread Function
rms	root mean square
RA	Right Ascension
SDSS	Sloan Digital Sky Survey
VIMOS	Visible imaging Multi-Object Spectograph
VLT	Very Large Telescope
VVDS	VVDSVIMOS VLT Deep Survey
WMAP7	Seven-year Wilkinson Microwave Anisotropy Probe

Acknowledgments

As a friend once said, “No one finishes a PhD alone.” This thesis would not have been possible without the help and inspiration from many people.

First and foremost, I would like to thank my supervisor Dr. Ludovic van Waerbeke for his brilliant ideas, guidance, endless support and encouragement over the course of my studies.

I would like to sincerely thank Dr. Douglas Scott and Dr. Jasper Wall, for their detailed feedback on this manuscript and my work. They provided me with a tremendous amount of support and opportunities to learn.

I am so grateful to my university examiners, Dr. Gary Hinshaw and Dr. Purang Abolmaesumi, for their invaluable time and their interest in my work.

I wish to thank my external examiner, Dr. Gary Bernstein, for the thorough and constructive comments on this thesis.

I am thankful to the rest of my committee members: Dr. Vesna Sossi and Dr. Joerg Rottler.

I am particularly thankful to Dr. Elisabetta Semboloni who mentored me and whose expertise really improved the quality of my research.

I wish to thank all past and present members of the UBC weak lensing team: Jonathan Benjamin, Jessica Ford, Dr. Hendrik Hildebrandt, Dr. Martha Milkeraitis and Dr. David Woods.

I would also like to thank all the members of the CFHTLenS collaboration for their hard work to improve the quality of the data which part of this thesis is based on.

I gained a lot from discussions with my friend and collaborator Joachim Harnois-Deraps over the years.

I am very thankful to my friend Dr. Claudia Mignone who kindly edited parts of this manuscript.

My special thanks goes to Dr. Thomas Erben and Dr. Martin Kilbinger for helpful discussions.

It was an absolute pleasure working with Dr. Patrick Valageas and Dr. Dipak Munshi.

I also benefited from visiting other institutes throughout my studies. I would like to thank Dr. Peter Schneider, Dr. Henk Hoekstra and Dr. Elisabetta Semboloni for hosting my visits.

This work was partly supported by University Graduate Fellowship (UGF). All N-body simulations were performed on the Canada Foundation for Innovation funded CITA Sunnyvale and SciNet clusters. The analysis of the simulations was performed on WestGrid computing resources, which are funded in part by the Canada Foundation for Innovation, Alberta Innovation and Science, BC Advanced Education, and the participating research institutions.

I would also like to thank Ovidiu Toader for his immediate help in my daily computer related issues. I would like to thank Swarn Rai, Bridget Hamilton and Oliva Dela Cruz-Cordero for their help and encouragement over the course of my studies. Thanks to all past and present office mates of room 310 for their friendship.

I would like to express my appreciation to my friends, Bruno Mundim, Rodrigo Pereira, Dominic Marchand, Genevieve Brisson, Claudia Mignone, Elisabetta Semboloni, Shannon Greeley and Anna-Lena Riegel for the many colorful moments we shared.

Last but not least I would like to thank my family. I can not express enough gratitude to my parents, Golnaz and Nosratollah Vafaei, and my dear sister, Avisa, for their unconditional love and encouragement. I thank Mr. Lucci from whom I learned so much.

Finally, words alone cannot express the thanks I owe to my partner Anup, for his endless energy, smile, love and support every single step of the way.

To my dearest grandparents,
Maman Mehri & *Baba Doktor*, *Maman Beh* & *Baba Haji*.

Chapter 1

Introduction

Cosmology is the branch of astronomy concerned with the study of the Universe as a whole, of its content, origin, evolution and fate. Astronomical observations can probe luminous objects such as stars and galaxies, and have done so extensively over the past decades. This has unleashed many unexpected and unexplained phenomena. Galaxies seem to rotate faster than predicted by the gravitational effects exerted by luminous matter only. Another classic example is the accelerated expansion of the Universe discovered by observations of supernovae type Ia. Cosmologists have attributed these effects to the so-called dark matter and dark energy. These cosmic components, whose nature is still unknown, are currently the basis of many cosmological studies. According to the standard model of cosmology supported by observations (Komatsu et al. [2011]), dark matter and dark energy are largely dominant and only a small fraction of the Universe consists of baryonic matter.

One way to study the dark matter is to observe large portions of the sky, compiling extensive surveys of galaxies to map the distribution of light across the Universe. With the aid of theoretical models, it is possible to infer the properties of the matter density field underlying the distribution of galaxies, which contains dark matter as well. This method relies on assumptions that link the amount of luminous matter (galaxies) to dark matter. Another popular tool for studying the dark matter distribution is known as gravitational lensing. Just like an optical lens, which deflects the incoming light from a source to an observer, gravitational lenses deflect

the light emitted by distant galaxies as it passes by them, due to their large masses. The phenomenon of light deflection in the vicinity of strong gravitational fields was predicted by Einstein's general theory of relativity and subsequently observed, first during a solar eclipse, then in the case of bright quasars and later in a number of other astrophysical contexts. Any massive object that lies between the source and the observer can act as a gravitational lens. Examples of these objects include, stars, galaxies, and clusters of galaxies. In addition, the whole matter distribution in the Universe, known as the large-scale structure (LSS) is also responsible for lensing effects. The lensing scenario caused by the large-scale structure is referred to as the cosmic shear.

In the weak lensing regime, the light coming from a distant galaxy, which is characterised by a certain shape, will pass through the large-scale structure of the Universe on its journey to the observer, thus being continuously deflected by massive objects along the way. As a result, the observer sees the galaxy with a distorted shape (shear), which could be a more elongated or compressed with respect to the original shape. Figure 1.1 shows the schematics of distortions affecting the source galaxies (on the left) and resulting in the observed galaxies (on the right) due to the presence of a gravitational lens in between the sources and the observer. One can see that the resulting image perceived by the observer is not identical to the original source galaxy due to the many deflections along the way.

The weak lensing reconstruction technique aims at studying these distorted images and finding a link back to the structure of the gravitational lens that caused the distortion, which generally consists of both luminous and dark (hence invisible) matter. This method is a very powerful probe of the dark matter distribution in the Universe, since it is independent of the nature and dynamical state of the matter in the lens, and only depends on its mass. Evidently, it is impossible to tell by how much the shape of the original galaxy is distorted, since we do not have access to its intrinsic shape. However, this can be overcome by employing a sufficiently large sample of galaxies, as statistical properties of the distortions can lead to an estimate of the matter distribution causing the distortions.

In practice, lensers study the correlation between any pair of galaxies separated by a certain angular separation on the sky. In the (reasonable) assumption that the original orientations of the source galaxies are completely random, the light from

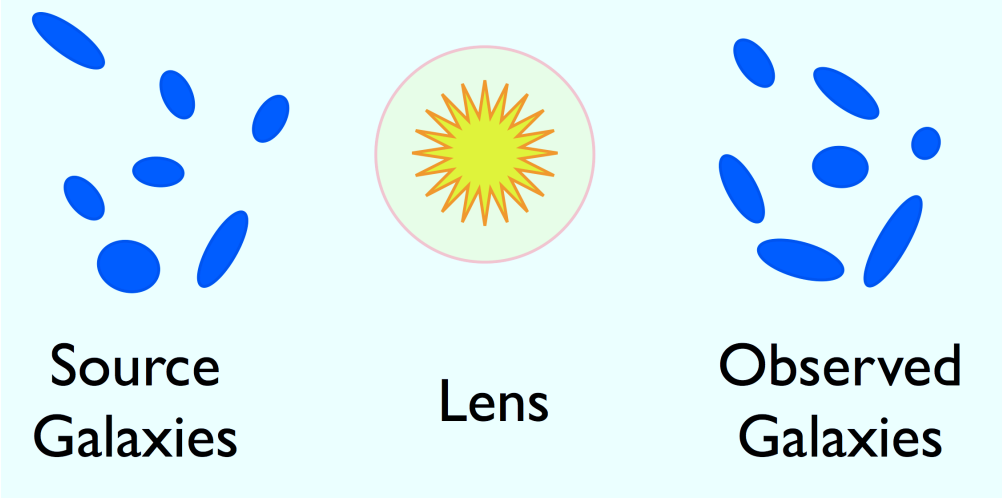

Figure 1.1: A given distribution of source galaxies (left) becomes distorted (right) due to their light passing through a gravitational lens (centre) on the way to the observer.

two galaxies passing though the same gravitational lens will result in a correlation in their observed distorted shapes, since the deflection is exerted by the same intervening massive body. The correlation between every pair of observed galaxies as a function of their separation is measured in terms of the so-called two-point correlation function. Combined with the knowledge of the redshift distribution of the source galaxies (i.e. knowledge of their distances from us), the two-point correlation function can be related to the properties of the matter density along the observer's line of sight. We refer to statistics involving the two-point correlation function as two-point statistics throughout this thesis.

In cosmology, the properties of the Universe are expressed in terms of a number of cosmological parameters. When studying the dark matter distribution in the Universe, we are usually interested in parameters that express the amount of matter, relative to other cosmic components and the level of its "clumpiness" on different scales in the Universe. With the aid of weak lensing two-point correlation functions we can estimate these parameters. This is the fundamental idea behind cosmological parameter estimation. Like any other probe of cosmology that is sensitive to these parameters, however, the two-point statistics provide a degenerate estimate

of the matter density and its clumpiness, as the two parameters are related to each other. The left panel of figure 1.2 shows the schematics of this degeneracy which implies that the combination of the two parameters accepted by this analysis is not unique. Ideally we wish to obtain the tightest possible constraints on the parameters (i.e. to estimate both of them with the highest precision). Is it possible to break this degeneracy by combining separate observational clues whose dependence on the parameters are different from each other, as shown in the right panel of figure 1.2. This is interesting because the weak lensing constraints on the "clumpiness" parameter can be combined with those from cosmic microwave background studies in order to break the degeneracy between this parameter and other parameters, such as neutrino mass. Also tighter contraints on the matter density in the Universe, can be used to rule out some of the dark matter candidates. Dark energy is believed to be the reason behind the accelerated expansion of the Universe. With the aid redshift information of the galaxies, one can study the evolution of matter density, which is directly related to the dark energy component of the Universe.

The goal of this thesis is to explore methods, beyond the two-point correlation function, that provide improved (i.e. tighter) constraints on the desired cosmological parameters when combined with the two- point statistics. For this purpose we explore two main avenues in the field of weak gravitational lensing: higher order statistics; and Probability Distribution Function (PDF) statistics. Other probes of cosmology, such as galaxy surveys have already implemented higher order statistics in their analysis. Below we list the various angles this thesis sets to explore:

3-point statistics of simulations: Instead of looking at pairs of galaxies, we focus on the correlation function between groups of three galaxies. We refer to calculations involving three-point correlation functions, hereafter as "three-point statistics". Figure 1.3 shows the schematics of correlating shapes of three galaxies rather than two. With the aid of numerical simulations, we show that there is a great improvement on the cosmological parameter estimations when the three-point statistics are included in the analysis.

2+3-point statistics analysis of CFHTLenS data: In the next stage, we apply the three-point statistics to study the state of the art weak lensing data set of the Canada-France-Hawaii Telescope Lensing Survey. This work presents the first cosmological constraints ever obtained from the combination of two- and three-

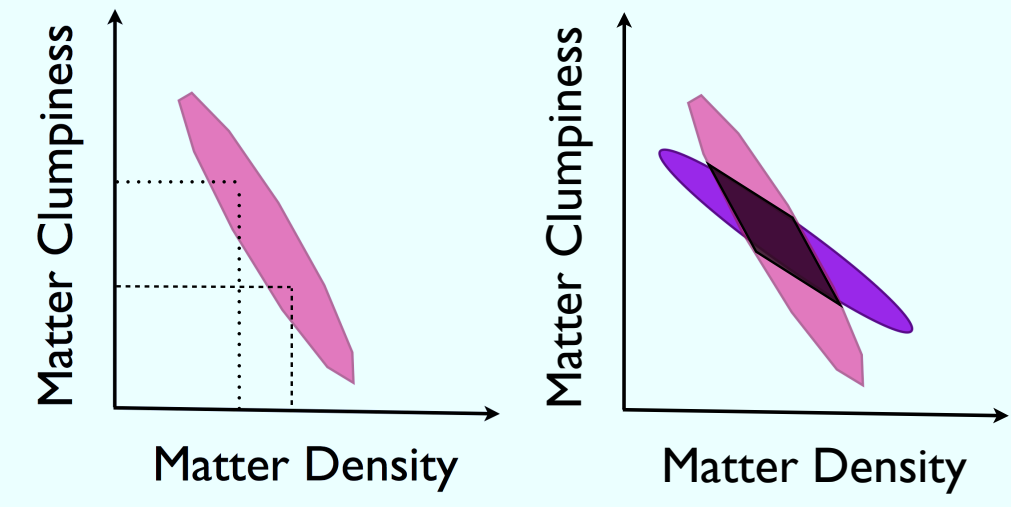

Figure 1.2: (Left) The schematics of constraints in the parameter space. The banana shaped contour shows that there is a degeneracy between the two parameters of interest; the matter density and its clumpiness. (Right) The allowed region in parameter space shrinks when different probes of cosmology are combined together, resulting in the smaller grey area (i.e. tighter constraints on the parameters).

point statistics applied to ground-based observations.

Numerical simulation testing: As part of testing the methods, we take advantage of a large set of numerical simulations. As part of this work, we tested the accuracy and sanity of these simulations carefully and extensively. The resulting data set is in agreement with all the weak lensing theoretical predictions and proves to be extremely useful in many areas of weak lensing studies.

Statistics of 2D matter distribution: The shapes of galaxies become distorted due to the presence of matter along the path between them and the observer. It is in principle possible to reconstruct the 2D projected matter distribution along the way by means of the observed distortions. We explore the probability distribution function of the simulated 2D matter distribution to infer the cosmological parameters underlying such distribution. This method is developed as complementary to the two- and three-point statistics.

Statistics of emptiest regions on the sky: The 2D projected matter distribu-

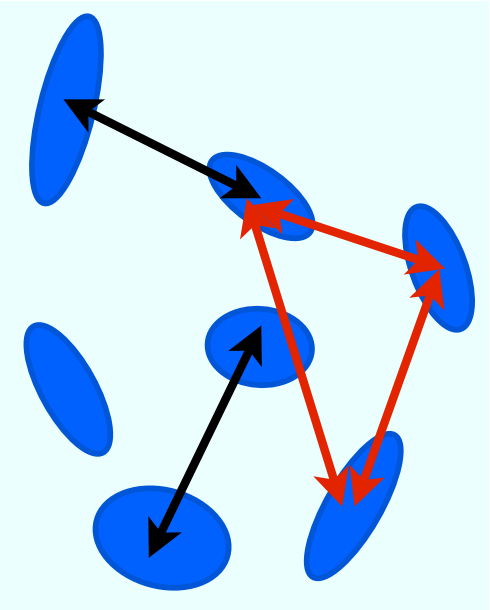

Figure 1.3: The configuration for two-point (black) and three-point (red) correlation functions.

tion is highly clustered and has portions that are emptier than others. We conduct a study of such areas and build a technique to infer the cosmological matter parameters from the least dense regions.

Clone of CFHTLenS production: As part of the development of the simulations, we combine them with the data to produce simulated weak lensing catalogues that can be used both for method testing and also for assessing systematics effects present in the data. These replicas of the data are referred to as "Clone". We use these clones for the analysis of all statistical studies throughout this thesis.

The structure of the thesis is illustrated in the flowchart in figure 1.4. The blue boxes refer to the background information. This includes chapters 2, 3 and 4. In chapter 2 we review the relevant cosmological framework. The expert reader might skip this chapter. In chapter 3 we review the theory of gravitational lensing. Chapter 4 reviews a number of statistics to study gravitational lensing that have been proposed in the literature and that are used in ongoing studies. We also apply these statistics to carefully test the numerical simulations we discuss in chapter 5.

Chapter 6 is the publication of the work on the 2+3-point statistical analysis of numerical simulations as a path-finder to chapter 7, where the findings are applied to the data. Original work is shown in orange boxes, where green boxes show the simulation and data that are used for all the studies. In chapter 8 we explore other means to improve constraints on the cosmological parameters that involve studying the full probability distribution function of the 2D projected matter along the line of sight. Also in chapter 9 we combine the simulations and the data to generate a clone of the data set for likelihood analysis of the 2+3-point statistics. Finally, in chapter 10, we summarize the results and discuss the future avenues of the work.

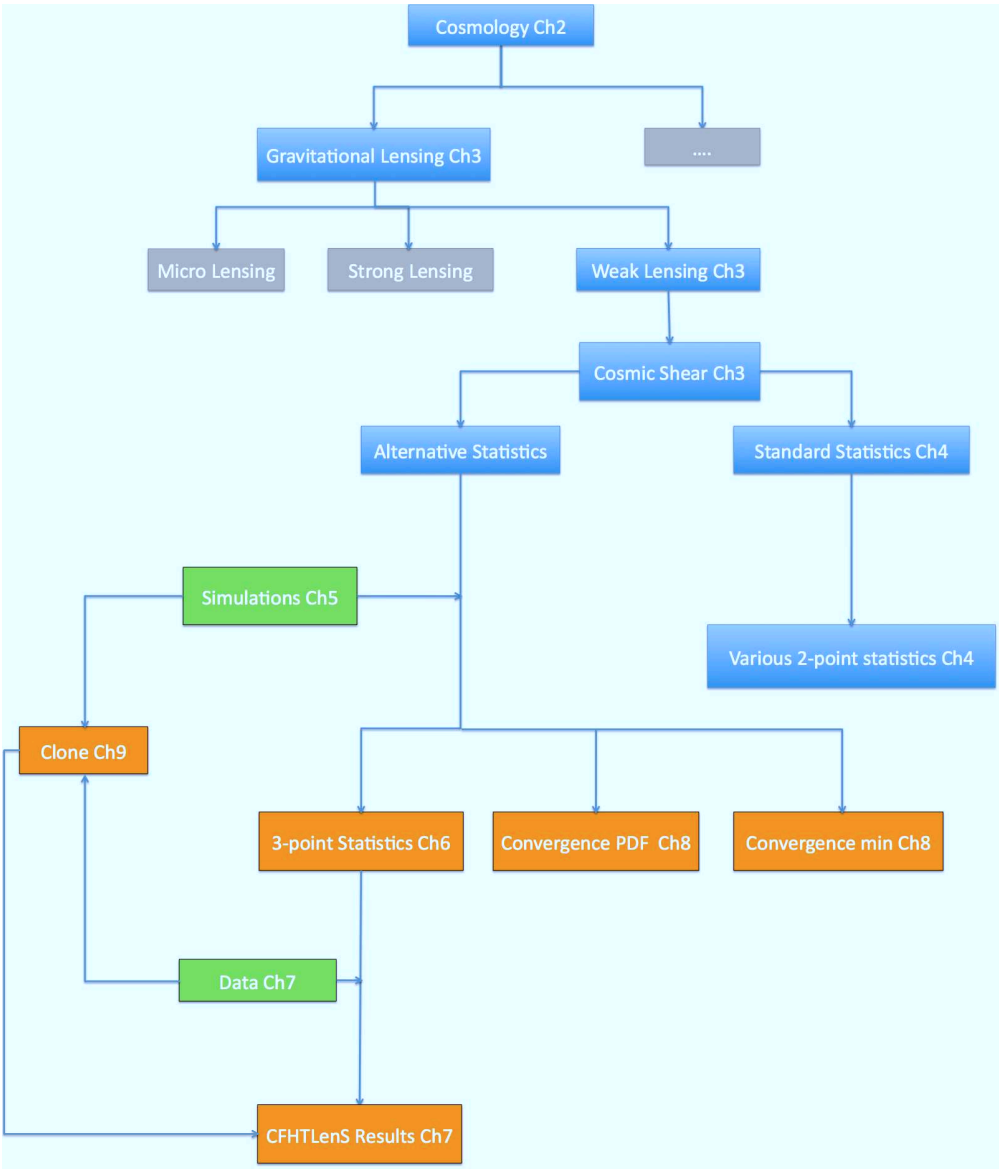

Figure 1.4: The overall structure of this thesis. Blue boxes represent the review chapters. Green boxes show the original work developed for this thesis, including analysis, and orange boxes are the descriptions of the simulation and data used in this work. The grey boxes represent other branches of cosmology and gravitational lensing which are not directly related to this work.

Chapter 2

Cosmology

Cosmology is the science of the physical Universe and its properties as a whole. In this thesis, we aim to study the matter distribution of the Universe through weak gravitational lensing analysis. The theory of weak lensing is based on fundamental theories of cosmology. This chapter explains the modern framework of cosmology, known as the standard model.

The standard model aims to explain the overall shape and structure of the Universe and describe its time evolution. In the following sections, we explain the general concepts of the standard model for the homogeneous Universe. We will discuss the extension of the model to the inhomogeneous Universe, which captures non-linear structure formations. The results discussed will be used later in this thesis as we explain the observations and the theoretical predictions of weak gravitational lensing due to effects of such large-scale matter inhomogeneities.

As part of this chapter we also review the definition of cosmological parameters and the matter power spectrum which will appear throughout this thesis. Weak gravitational lensing studies aim to estimate the matter power spectrum through the observation of galaxy shapes.

More detailed explanation of topics of this chapter can be found in many cosmology textbooks and reviews (e.g. Peebles [1980], Peebles [1993], Peacock [1999] and Dodelson [2003]). The purpose of this chapter is to provide the reader with an outline of the basic concepts of cosmology, and to introduce useful definitions which will be used later. The cosmology expert reader may skip this chapter

entirely.

2.1 The Standard Model of Cosmology

Gravitational lensing studies the distortions of galaxy shapes due to light deflections caused by the gravitational field of the matter distribution in the Universe. The simplest assumption to make, about how the matter in the Universe is distributed, is that the matter in the universe is homogeneous and isotropic at very large scales. This is called the Cosmological Principle. There are several sources of evidence that support this theory. For example, the cosmic microwave background (CMB) radiation, the remnant heat from the Big Bang, has a temperature which is highly uniform over the entire sky. This fact strongly supports the notion that the gas which emitted this radiation long ago was very uniformly distributed.

According to the theory of General Relativity [Einstein, 1916], matter distribution directly influences four-dimensional space time. A metric which describes the four dimensional distance between two events in a homogeneous and isotropic space-time was suggested by Robertson [1935] and Walker [1936], nowadays known as the Robertson-Walker metric:

$$\mathrm{d}s^2 = c^2\mathrm{d}t^2 - a^2(t)\left[\mathrm{d}\chi^2 + f_K^2(\chi)(\mathrm{d}\theta^2 + \sin^2\theta\mathrm{d}\varphi^2)\right]. \tag{2.1}$$

Here χ is the radial comoving coordinate (see equation 2.3 for the definition), and θ and φ the angular coordinates. $f_K(\chi)$ is the comoving angular diameter distance, which is a function of the space curvature K:

$$f_K(\chi) = \begin{cases} K^{-\frac{1}{2}}\sin(K^{\frac{1}{2}}\chi), & \text{for } (K>0),\ \text{Sphere;} \\ \chi, & \text{for } (K=0)\ \text{Flat;} \\ (-K)^{-\frac{1}{2}}\sinh((-K)^{\frac{1}{2}}\chi), & \text{for } (K<0),\ \text{Hyperboloid.} \end{cases} \tag{2.2}$$

Angular diameter distance $f_K(\chi)$ ties the comoving transverse separation to the angular size. In equation 2.1, $a(t)$ is the scale factor, which describes the global expansion or contraction of the Universe. In an expanding Universe the scale factor increases with time. So if a photon was emitted at time t_e with wavelength λ_e, it

will be observed at a later time t_0 by a comoving observer at wavelength λ_0 which will be longer than the emitted wavelength. The comoving distance χ between the emitting source and the observer is constant (Comoving distances stretch with expansion.) Also light travels on a "null" geodesic (for radial light rays $\mathrm{d}\theta^2 = 0$ and $\mathrm{d}\varphi^2 = 0$, so $\mathrm{d}s^2 = 0$), so the metric becomes $c\mathrm{d}t = -a\mathrm{d}\chi$. Thus

$$\chi = \int_{t_e}^{t_0} \frac{c\mathrm{d}t}{a} = \text{constant}, \tag{2.3}$$

hence

$$\frac{\mathrm{d}t_0}{\mathrm{d}t_\mathrm{e}} = \frac{\lambda_0}{\lambda_\mathrm{e}} = \frac{a(t_0)}{a(t_\mathrm{e})} \equiv 1 + z, \tag{2.4}$$

where $a(t_0) \equiv 1$. So redshift z is defined as the relative change in wavelength due to expansion (contraction) of the Universe (see [Van Waerbeke and Mellier, 2003] for a review on deflections of light bundles as they pass through the large-scale structure of the Universe.).

Einstein developed a mathematical relation between the metric of space-time and the energy and pressure at that point, known as the "field" equations [Einstein, 1916]. Using Robertson-Walker metric (equation 2.1) in combination with Einstein's field equations, one obtains two relations between the scale factor $a(t)$, curvature K and angular diameter distance $f_K(\chi)$ and the energy density $\rho(t)$ and pressure $p(t)$ content of the Universe for a perfect homogeneous and isotropic fluid as

$$\left(\frac{\dot{a}}{a}\right)^2 = \frac{8\pi G}{3}\rho - \frac{3Kc^2}{a^2} + \frac{\Lambda}{3}; \tag{2.5}$$

$$\ddot{a} = -\frac{4\pi G}{3}\left(\frac{3p}{c^2} + \rho\right) + \frac{\Lambda}{3}a. \tag{2.6}$$

Here the dots represent time derivatives and Λ is known as the cosmological constant, representing the vacuum energy component in the Universe. Equations 2.5 and 2.6 are known as the Friedmann equations and can be combined into the continuity equation:

$$\frac{\mathrm{d}}{\mathrm{d}t}(\rho a^3 c^2) = -p\frac{\mathrm{d}a^3}{\mathrm{d}t}. \tag{2.7}$$

The above equation 2.7 is an expression of the conservation of energy, in the sense

Matter	$w = 0$	$p = 0$	$\rho_{\rm m} \propto a^{-3}$	$a \propto t^{2/3}$
Radiation	$w = 1/3$	$p = \rho_{\rm r} c^2/3$	$\rho \propto a^{-4}$	$a \propto t^{1/2}$
Vacuum	$w = -1$	$p = -\rho_\Lambda c^2$	$\rho = \text{const}$	$a \propto \exp\left(\sqrt{\frac{8\pi G}{3}\rho}t\right)$

Table 2.1: Equation of state, functional behaviour of the density and scale factor for different cosmological ingredients.

that the energy change in a fixed comoving volume is compensated by the pressure times the volume change. This equation can be interpreted as the cosmological version of the first law of thermodynamics, resembling the adiabatic equation.

When combined with the equation of state ($p = w\rho c^2$), equation 2.7 indicates how the density of each energy component of the Universe evolves with time. Note that w here is the equation of state parameter. The Friedmann equations (2.5 and 2.6) can be solved for components with different choices of constant values of w. For constant w we have $\rho \propto a^{-3(1+w)}$. Table 2.1 shows the equation of state and density contribution of various components that contribute to the total energy budget of the Universe. Since the density of different components has different scale factor dependence, they each dominate the total energy of the Universe over the other components at different cosmological epochs.

Note that the pressure-less matter density $\rho_{\rm m} = \rho_{\rm b} + \rho_{\rm CDM}$ consists of contributions from baryonic matter $\rho_{\rm b}$ and cold dark matter $\rho_{\rm CDM}$. Also $\rho_{\rm r}$ is the radiation contribution from CMB photons and relativistic cosmic background neutrinos with $w = 1/3$. Another kind of species is the cosmological constant with the assigned energy density of ρ_Λ and $w = -1$, which acts as an repulsive force.

We can parameterize the expansion of the Universe by introducing the Hubble parameter such that $H \equiv \dot{a}/a$, which denotes the relative expansion rate. The Hubble constant is the present value of the Hubble parameter, written as $H_0 = 100h$ km s^{-1} Mpc^{-1}, where the observational uncertainty is hidden in h. The most recent value of h as measured by WMAP7 results [1] Komatsu et al. [2011] is 0.710 $\pm$ 0.025. The critical density $\rho_{\rm crit}$ is the total ($\rho_{\rm m} + \rho_{\rm r} + \rho_\Lambda$) energy density of the

[1] http://lambda.gsfc.nasa.gov/product/map/current/params/

Universe today (at $t = t_0$), which is required for flat curvature ($K = 0$):

$$\rho_{\rm crit} = \rho_{\rm c,0} \equiv \frac{3c^2 H_0^2}{8\pi G} = (9.2 \pm 1.8) \times 10^{-27} \text{kg m}^{-3}. \tag{2.8}$$

The relative density of each of the components can be written as fractions of the critical density such that $\Omega_{\rm x} = \rho_{\rm x}/\rho_{\rm c,0}$. $\Omega_{\rm x}$ is the density parameter. So the Friedmann equation 2.5 can be written in terms of the density parameters as

$$\left(\frac{H(t)}{H_0}\right)^2 = \frac{\Omega_{\rm r}}{a^4} + \frac{\Omega_{\rm m}}{a^3} + \frac{1 - \Omega_{\rm m} - \Omega_\Lambda - \Omega_{\rm r}}{a^2} + \Omega_\Lambda, \tag{2.9}$$

and for curvature K:

$$K = \left(\frac{H_0}{c}\right)^2 (\Omega_{\rm m} + \Omega_{\rm r} + \Omega_\Lambda - 1). \tag{2.10}$$

Note that $\Omega_{\rm r}$ can be neglected, since it has a small contribution to the total energy budget of the Universe today. So for a flat curvature Universe, the condition ($\Omega_{\rm m} + \Omega_\Lambda = 1$) applies.

One of the main focuses of cosmological observations over the past decade has been to measure the cosmological density parameters to the highest precision possible. Different probes have measured most of the parameters within reasonably small errors and have shown the concordance of the ΛCDM model.

One of the main goals of this thesis also is to use weak gravitational lensing observables to constrain a subset of cosmological parameters, including the matter density parameter $\Omega_{\rm m}$. Future chapters will explain the procedure further.

2.2 Cosmological Distances

The comoving distance χ as shown in equation 2.3, is the fundamental distance measure in cosmology. This distance remains constant between two comoving observers. For a radial photon on the null geodesic $c{\rm d}t = -a{\rm d}\chi$ one gets ${\rm d}\chi = -c{\rm d}a/(Ha^2)$ [2]. The comoving distance as a function of the density parameters can

[2]Note that the minus sign comes from the fact that the distance is measured backwards in time, from the observer to the source, whereas the cosmic time increases towards the observer.

then be written as

$$D_{\rm com}(z_1,z_2) \equiv \chi(z_1,z_2) = \frac{c}{H_0}\int_{a(z_2)}^{a(z_1)} {\rm d}a \left[a\Omega_{\rm m} + a^2(1-\Omega_{\rm m}-\Omega_\Lambda) + a^4\Omega_\Lambda\right]. \tag{2.11}$$

When $z \to \infty$, χ_h is called the horizon and marks the largest comoving distance such that the source and observer are in causal contact. The horizon size increases with time, so that structures that are larger than the horizon at a given time will enter the horizon at later times.

The transverse comoving separation, used to estimate the comoving volumes is then

$$D_{\rm trans} = f_K(\chi)\theta, \tag{2.12}$$

where θ is the angular size and $f_K(\chi)$ is the comoving angular diameter distance as shown in equation 2.2.

Another measure of cosmological distance is the angular diameter distance $D_{\rm ang} = \delta L/\delta\vartheta$, which relates the physical size of an object δL at redshift z_2 to its apparent angular size on the sky $\delta\vartheta$ as seen by observer at redshift z_1:

$$D_{\rm ang}(z_1,z_2) = a(z_2)\, f_K(\chi(z_1,z_2)). \tag{2.13}$$

The angular diameter distance is very important in gravitational lensing (see section 3.2 for the lens equation). For the ΛCDM cosmology, the maximum $D_{\rm ang}$ occurs at $z \approx 1.5$ and then decreases again at higher redshifts.

2.3 Large Scale Structure

As explained in previous parts the Universe is homogeneous and isotropic at large scales, so the Friedmann-Robertson-Walker (FRW) cosmology (see sections 2.1) is sufficient to describe the overall dynamics of the Universe. On smaller scales however, the Universe is highly clustered (scales below few hundred Mpc.) These clumps of matter (today's galaxies and cluster and filaments etc.) originated from very small density perturbations due to gravitational instabilities in the nearly uniform matter distribution of the early Universe. In this section we will describe the basics of structure formation and evolution in the Universe.

2.3.1 Linear Perturbation Theory

The density contrast δ is defined as

$$\delta(\boldsymbol{x},a) \equiv \frac{\rho(\boldsymbol{x},a)-\bar{\rho}}{\bar{\rho}(a)}, \tag{2.14}$$

where $\bar{\rho}$ is the average density for the FRW-Universe (Friedmann-Robertson-Walker Universe, homogeneous and isotropic) at a given scale factor a, and $\boldsymbol{x}$ is the comoving spatial position. In the regime of weak gravitational potential, and for small adiabatic perturbations, $\delta \ll 1$, one can use linear Newtonian perturbation theory to describe the structure evolution. The relation between the gravitational potential and its corresponding density contrast is given by the Poisson equation,

$$\nabla^2\phi = \frac{3H_0^2\Omega_{\mathrm{m}}}{2a}\delta, \tag{2.15}$$

where the differentiation is with respect to the comoving coordinates. A general form of the solution δ can be written as $\delta(\boldsymbol{x},a) = \delta_+(a)\triangle_+(\boldsymbol{x}) + \delta_-(a)\triangle_-(\boldsymbol{x})$. The decaying mode $\delta_-(a)$ is a fast vanishing function, so it can be neglected for late times.The growing mode $\delta_+(a)$ has the form

$$\delta_+(a) = \frac{5\Omega_{\mathrm{m}}}{2a}\frac{\mathrm{d}a}{\mathrm{d}\tau}\int_0^a \mathrm{d}a' \left[1+\Omega_{\mathrm{m}}\left(\frac{1}{a'}-1\right)+\Omega_\Lambda\left(a'^2-1\right)\right]^{-\frac{3}{2}}, \tag{2.16}$$

where τ is the dimensionless time variable $\tau = H_0 t$. This equation is normalized such that for the Einstein-de-Sitter Universe $\delta_+(a) = a$ for $a > a_{\mathrm{eq}}$. The value of $a_{\mathrm{eq}} \approx 3.2^{-5}\Omega_{\mathrm{m}}^{-1}h^{-2}$, and represents the scale factor at the time the transition between radiation domination to matter domination occurred. Before a_{eq} the growing mode δ_+ scales as a^2. The growth factor is then defined as

$$D_+(a) = \frac{\delta_+(a)}{\delta_+(a=1)}, \tag{2.17}$$

where $\delta_+(a=1)$ is the linear density contrast extrapolated to the present epoch.

When only baryonic matter is considered, based on observations of CMB fluctuations at the time of recombination ($z \approx 1000$), the baryon density perturbations

were on the order of 10^{-5}. They could have only grown by a factor of $1/a \approx 10^3$ afterwards, leading to perturbations of the order 10^{-2} today. Observations show perturbations of much larger amplitude than that, implying that baryon-only matter cannot explain the current structures. This is one of the strongest arguments for the existence of some non-baryonic, weakly interacting matter in the Universe, now called Dark Matter.

2.3.2 Growth Suppression

For density perturbations, there exists a critical scale called the Jeans length. This is the minimum length at which a self-gravitating instability overcomes the opposing pressure gradient. On lengths smaller than the Jean's length, the opposing pressure stops the density perturbations from growing. Before matter-radiation equality, the Jean's length was of the size of the horizon, hence no structure smaller than the horizon could grow. A perturbation with a comoving wavelength $\lambda > d_{\rm h}$, however could grow, and at some later point in time, when the horizon gets larger, enter the horizon at scale factor $a_{\rm enter}$. If the entrance occurs before matter-radiation equality, the perturbation gets suppressed compared to the same scale perturbation that enters the horizon after equality by a factor $(a_{\rm enter}/a_{\rm eq})^2$. The size of the horizon at the time of matter-radiation equality defines a characteristic length scale for large scale structure, $d_{\rm h}(a_{\rm eq} = 12(\Omega_{\rm m}h^2)^{-1}$ Mpc . In the matter domination era however, this scale decreases to zero, and so structures of all sizes start to grow. In order to compare perturbations of all scales, one must consider the Fourier counterparts of the density contrast, $\delta_{\boldsymbol{k}}$, where $\boldsymbol{k}$ is the comoving wave-vector. The transfer function is then defined [Eisenstein and Hu, 1998] as

$$T_k = \frac{\delta_k(a=1)}{\delta_k(a_i)} \frac{\delta_{k=0}(a_i)}{\delta_{k=0}(a=1)}, \tag{2.18}$$

where $k = 0$ represents an arbitrarily large scale. The scale factor a_i of the initial density fluctuations $\delta_k(a_i)$ has to be chosen such that at this time no scales of interest have entered the horizon, so that T_k is independent of a_i. The fitting formula

given in [Bardeen et al., 1986] is

$$T_k = \frac{\ln(1+2.34q)}{2.34q}\left[1+3.89q+(16.1q)^2+(5.46q)^3+(6.71q)^4\right]^{-\frac{1}{4}} \quad (2.19)$$

where $q \equiv k/(\Gamma h)\mathrm{Mpc}^{-1}$ and Γ is called the shape parameter, originally set to $\Omega_\mathrm{m}h$. In 1994 ([Peacock and Dodds, 1994]) showed that the fitting formula 2.19 is also valid for a small baryon contribution to the overall matter if the shape parameter Γ is set to

$$\Gamma = \Omega_\mathrm{m}h\ \exp(-2\Omega_\mathrm{b}). \quad (2.20)$$

So an increase in baryon density shifts the transfer function to smaller scales without changing its shape. This approach of including the baryonic matter contribution is only an approximation, since the acoustic oscillations in the baryon-photon plasma before decoupling have not been taken into account.

2.3.3 Matter Power Spectrum and σ_8

The matter density contrast δ is described as a random field, so it can only be studied via its statistical properties. A random field can be fully described by its moments. In the case of Gaussian random field the first two moments are sufficient to completely describe the field. We assume such Gaussian random fields to represent the initial inhomogeneities in the early Universe. As long as the perturbations grow linearly they remain Gaussian. Most cosmological studies and experiments focus on examining the power spectrum of the matter, which is the Fourier transform of the second order moments. The power spectrum of the density fluctuations P_δ is defined as

$$\langle\hat{\delta}(\boldsymbol{k},a)\hat{\delta}(\boldsymbol{k'},a)^*\rangle = (2\pi)^3\delta_\mathrm{D}(\boldsymbol{k}-\boldsymbol{k'})P_\delta(k,a), \quad (2.21)$$

where δ_D is the Dirac delta function and the angle brackets represent ensemble averages. For a given scale factor, a, the power spectrum depends only on the modulus of the wave-vector k. We will show later that cosmic shear data can directly provide a projected version of the power spectrum of density fluctuations. The power spectrum $P_\delta(k,a)$ for some later time can be calculated from the initial

one as

$$P_\delta(k,a) = \frac{D_+^2(a) T_k^2 P_\mathrm{i}(k)}{D_+^2(a)}. \tag{2.22}$$

For the initial power spectrum $P_\mathrm{i}(k) \equiv P(k, a_\mathrm{i})$, one can assume a simple and scale-free power law $P_\mathrm{i}(k) \propto k^n$, with the spectral index n. The origin of the initial density fluctuations is assumed to be quantum fluctuations at the Planck scale, which are then inflated to macroscopic fluctuations. The normalization of the power spectrum is fixed by the parameter σ_8, which is defined as the variance of the density fluctuations in spheres of radius 8 h^{-1} Mpc. Observationally, for the variance of galaxy counts, one gets $\sigma_8 \approx 1$, hence the choice of radius size. However, the measurements of σ_8 with different methods do not agree completely. Below are few examples of such methods:

- Normalization by cosmic microwave background anisotropies, e.g. Banday et al. [1997]. The fluctuations in the temperature of the microwave background can be translated into the amplitude of the power spectrum. These measurements are done on large angular scales, so such a method is valid for large physical scales (small k) only. The other contamination arises from the fact that CMB fluctuations measure the amplitude of both scalar and tensor perturbation modes, where the density fluctuations resulting in growth only originates from scalar modes. σ_8 is partially degenerate with τ (the re-ionization optical depth) and Ω_m.

- Normalization by the local variance of the galaxy counts (e.g. Bardeen et al. [1986], Davis and Peebles [1983], White et al. [1987] and Kaiser [1984]). This method is based on the idea that galaxies are unbiased tracers of the underlying dark matter fluctuations. However, there are uncertainties on how galaxies trace dark matter and so values different than unity are expected for σ_8. So if we can measure the local variance of galaxy counts within a fixed volume, as well as setting an expression for the bias, we can fix the normalization of the density power spectrum. This fixed volume has been conventionally chosen to be a sphere with radius of $8h^{-1}$Mpc, since the galaxy number r.m.s. was shown to be 1. on such a scale.

- Normalization by the local abundance of galaxy clusters (e.g. White et al. [1993]). Assuming that galaxy clusters form as a result of dark matter density perturbations, we can use the spatial cluster number density to determine the amplitude of the power spectrum. The point of this method is that the cluster normalization can only determine the amplitude of the power spectrum at scales of order of 10 h^{-1}Mpc, which is the typical dark matter fluctuation scale for galaxy clusters to collapse. When dealing with gravitational lensing by large scale structure, the scale sensitivity is around $k_0^{-1} \sim 12(\Omega_0 h^2)$Mpc, which makes the galaxy cluster normalization method favourable. The main problem with this method however, arises from the mass calibration, which uses the X-ray mass-temperature relation, which is poorly known.

In summary, σ_8 represents the variance of the density fluctuations and can be thought of as an indicator for the level of clumpiness in the matter distribution in the Universe. Along with the matter density parameter $\Omega_{\rm m}$, σ_8 is the other cosmological parameter that this thesis aims to provide constraints on, using cosmic shear measurements. Cosmic shear, like many other cosmological probes, is degenerate for some cosmological parameter combinations. The idea in this thesis is to explore how the non-conventional cosmic shear statistics help break the degeneracies within the cosmic shear capabilities and also in combination with other cosmological probes. Better estimation of σ_8 and Ω_m allows for the alleviation of the residual parameter degeneracies Komatsu et al. [2009]. A noticeable example is the mass of neutrino obtained by CMB measurements, which is degenerate with σ_8 parameter (Tereno et al. [2009]; Dunkley et al. [2009]). Independent constraints on σ_8 parameter by cosmic shear measurements can constrain the neutrino mass indirectly.

2.3.4 Matter Bi-spectrum

In the highly non-linear regime via gravitational collapse, non-Gaussian features in the matter field arise. To inspect the deviations from Gaussianity, the inclusion of higher order statistics is inevitable. The Fourier transform of the third order moment is referred to as the bispectrum. Even if the initial conditions are Gaussian,

the non-linear dynamics leads to development of non-Gaussianities in the density field. The density contrast was defined previously in equation 2.14, where ρ is the matter density, with $\rho \geq 0$. Since the average density contrast $\langle\delta\rangle = 0$ and $\delta \geq -1$, this implies that in the highly non-linear regime, $\langle\delta^2\rangle$, the probability distribution of the density contrast δ, will be far from Gaussian. Weak gravitational lensing effects arise from the total matter distribution, so the higher order lensing statistics can be used to probe the non-Gaussianity. The three-point correlation function is the lowest-order statistic that can be used to detect non-Gaussianity. The Fourier space counterpart of it is called the bispectrum and is defined as

$$\langle\hat{\delta}(\boldsymbol{k}_1)\hat{\delta}(\boldsymbol{k}_2)\hat{\delta}(\boldsymbol{k}_3)\rangle = (2\pi)^3\delta_{\rm D}(\boldsymbol{k}_1+\boldsymbol{k}_2+\boldsymbol{k}_3)B_\delta(k_1,k_2,k_3), \tag{2.23}$$

where $\delta_{\rm D}$ is the Dirac delta function. Isotropy implies that $B(k_1,k_2,k_3)$ is solely a function of the wavenumbers $\boldsymbol{k_1}$, $\boldsymbol{k_2}$ and $\boldsymbol{k_3}$.

2.3.5 Non-linear Evolution

By simple observations, one can see various small-scale structures that are formed at later cosmic times, such as galaxies and clusters of galaxies. To describe these phenomena linear perturbation theory is no longer sufficient, and non-linear approaches are needed. Non-linear perturbations are seeds for forming structures such as galaxies and clusters. In order to include such effects in the theoretical predictions, large numerical simulations are performed. Each simulation realization starts with a Gaussian random field, which then evolves with the initial power spectrum over time. The resulting dark matter structures, appearing at later times in the simulation, are then used to find a fitting formula for the non-linear power spectrum. Two popular choices of such fitting formulae are currently widely used in cosmological studies: Peacock and Dodds [Peacock and Dodds, 1996] and Halofit [Smith et al., 2003].

Figure 2.1 shows the linear and non linear matter power spectrum calculated with the `smith2.c` code developed by Martin Kilbinger, based on `halofit.f` of Smith et al. [2003]. We used the following cosmological parameters: $\Omega_{\rm m} = 0.279$, $\Omega_\Lambda = 0.721$, $\sigma_8 = 0.817$, $\Gamma = 0.25$ and $n = 0.96$. The redshift distribution

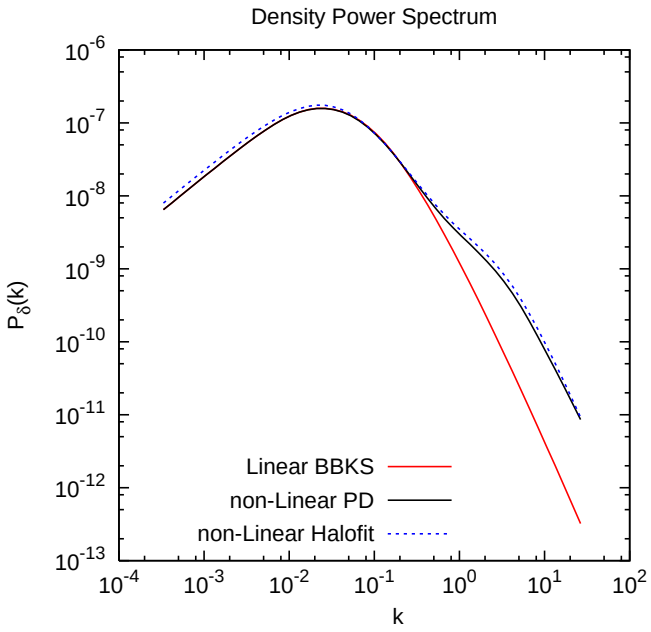

Figure 2.1: Matter power spectrum P_δ.

is based on Brainerd et al. [1996]:

$$p(z)\mathrm{d}z = \frac{\beta}{z_0\Gamma(3/\beta)}\left(\frac{z}{z_0}\right)^2 \exp-\left(\frac{z}{z_0}\right)^\beta \mathrm{d}z, \tag{2.24}$$

with the free parameters β and z_0, which were chosen to be 1.5 and 1.0, respectively. Γ denotes the Eulerian gamma function (different from the power spectrum shape parameter). One can see that the two nonlinear formulae are relatively similar. However, the linear power spectrum fails to represent the non linear effects of the power spectrum and hence it is very important to include the non-linear corrections.

The aim of this chapter was to provide the reader with a basic foundation in cosmology, as will be needed to follow the future chapters, when theoretical predictions are used against numerical simulations and as means of producing likelihood estimations for the cosmological parameters.

Chapter 3

Gravitational Lensing and Cosmic Shear

In this chapter we explain the basics of gravitational lensing in general and the weak lensing branch of it in particular. We discuss the theory of lensing along with the lens equations and the lensing shear and convergence, which will be extensively used in the later chapters. We introduce the shear γ and convergence κ and show their relationship. Later when producing simulations we will follow the process explained in this chapter to construct the convergence and shear maps. We also show the link between the convergence and matter power spectra, which is the main building block of relating lensing measurements with cosmological parameters. Throughout this chapter, the bold symbols represent vectors, while the non-bold symbols represent scalars.

3.1 The Deflection Angle $\hat{\alpha}$ and Thin Lens Approximation

In 1915, Einstein predicted a shift in the position of stars near the Sun due to the deflection of light caused by the Sun's gravitational field, and in 1920, measurements during a solar eclipse confirmed the predictions. Soon afterwards, it was realized that for certain lens configurations, large enough deflections can occur and produce multiple images of background sources. Consequently in 1979, the first

double image of the lensed quasar 0957+561 was discovered. Since then gravitational lensing has become a major research area in the astronomical field.

Deflection angle is the most basic parameter in gravitational lensing, which quantifies the light deflection due to a tidal field ϕ of a certain matter distribution. In a simple case of a point mass, the Schwarzchild radius is $R_s = 2GM/c^2$. The path of a light ray coming from a distant source, passing the point mass at a distance $\xi \gg R_s$ will be bent due to the gravitational potential of the point mass. The distance ξ has to be much smaller than the distance between the source, lens and observer. The path of the light can then be approximated by piecewise straight lines. The deflection angle is much smaller than unity and can be written as

$$\hat{\alpha} = \frac{4GM}{c^2 \xi}. \tag{3.1}$$

In the case of an extended distribution of point masses m_i, assuming that the impact parameter is much larger than the Schwarzchild radius, one can write the deflection angle as the sum of individual deflections. Consider a coordinate system where r_3 is along the direction between the lens and the observer, and (r_1, r_2) represents the plane perpendicular to this direction. So the deflection angle at position $\boldsymbol{\xi}$ is

$$\begin{aligned} \hat{\boldsymbol{\alpha}}(\boldsymbol{\xi}) &= \frac{4G}{c^2} \Sigma_i m_i(\boldsymbol{\xi}', r_3) \frac{\boldsymbol{\xi} - \boldsymbol{\xi}'}{|\boldsymbol{\xi} - \boldsymbol{\xi}'|^2} \\ &= \frac{4G}{c^2} \int \mathrm{d}^2\xi' \int \mathrm{d}r_3 \rho(\boldsymbol{\xi}', r_3) \frac{\boldsymbol{\xi} - \boldsymbol{\xi}'}{|\boldsymbol{\xi} - \boldsymbol{\xi}'|^2}. \end{aligned}$$

Here ρ represents the continuous mass distribution. Note that $\boldsymbol{\xi}$ is now a two-dimensional quantity. By defining the surface mass density $\Sigma(\boldsymbol{\xi}) = \int \mathrm{d}r_3 \rho(\boldsymbol{\xi}', r_3)$, the deflection angle can be written as

$$\hat{\boldsymbol{\alpha}}(\boldsymbol{\xi}) = \frac{4G}{c^2} \int \mathrm{d}^2\xi' \Sigma(\boldsymbol{\xi}') \frac{\boldsymbol{\xi} - \boldsymbol{\xi}'}{|\boldsymbol{\xi} - \boldsymbol{\xi}'|^2}. \tag{3.2}$$

The above expression is valid as long as the extension of the lens along the path of light is significantly smaller than the distance between source, lens and observer.

This condition is called the thin lens approximation, and it is well satisfied for lensing by galaxies and clusters, but fails in the case of the cosmic shear, which is lensing caused by the whole span of large-scale structure along the line of sight.

3.2 The Lens Equation

The lens equation relates the position of the images and the source by the geometrical configuration of the lensing system, as shown in figure 3.1. Let $D_{\rm d}$ be the distance between the lens (deflector) and observer, $D_{\rm s}$ the distance between the source and observer, and $D_{\rm ds}$ the distance between the lens and source. The lens and source planes are perpendicular to the line of sight, connecting the observer to the lens. The source is located at distance $\boldsymbol{\eta}$ from this optical axis and the impact parameter is $\boldsymbol{\xi}$. One can establish the following relation with the aid of the similar triangles theorem

$$\boldsymbol{\eta} = \frac{D_{\rm s}}{D_{\rm d}}\boldsymbol{\xi} - D_{\rm ds}\hat{\boldsymbol{\alpha}}(\boldsymbol{\xi}). \tag{3.3}$$

Converting distances to angles via $\boldsymbol{\eta} = D_{\rm s}\boldsymbol{\beta}$ and $\boldsymbol{\xi} = D_{\rm d}\boldsymbol{\theta}$, and defining the reduced deflection angle $\boldsymbol{\alpha}(\boldsymbol{\theta}) \equiv D_{\rm ds}/D_{\rm s} \cdot \hat{\boldsymbol{\alpha}}(D_{\rm d}\boldsymbol{\theta})$ results in the simple form of the lens equation:

$$\boldsymbol{\beta} = \boldsymbol{\theta} - \boldsymbol{\alpha}(\boldsymbol{\theta}). \tag{3.4}$$

So the lens equation relates the source position, $\boldsymbol{\beta}$, to the observed position(s) $\boldsymbol{\theta}$. The deflection angle $\boldsymbol{\alpha}$ depends on the mass distribution of the deflector.

3.3 Convergence and Shear

In this section we explain the definitions for the lensing convergence and shear, as these terms will be extensively used throughout this thesis.

The critical surface mass density is defined as:

$$\Sigma_{\rm cr} \equiv \frac{c^2}{4\pi G}\frac{D_{\rm s}}{D_{\rm d}D_{\rm ds}}. \tag{3.5}$$

One can then define the dimensionless surface mass density $\kappa \equiv \sum(D_{\rm d})/\sum_{\rm cr}$, also called convergence. The value of κ distinguishes between different lensing regimes. A lens system with $\kappa \geq 1$ is called a "strong" lens and $\kappa \ll 1$ represents a "weak"

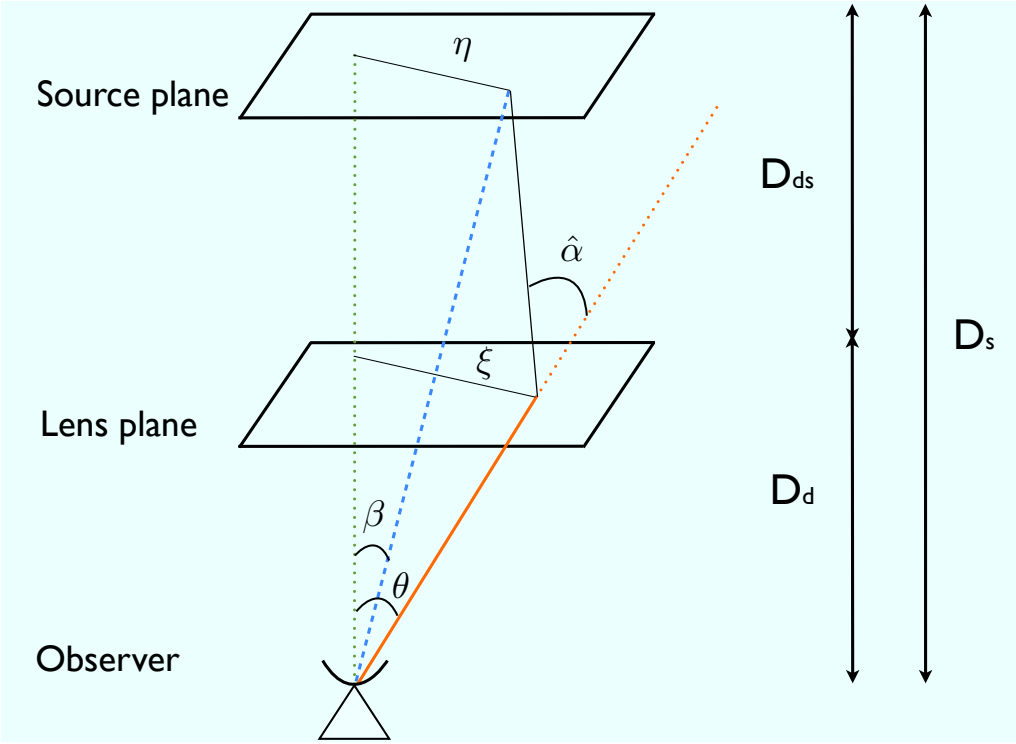

Figure 3.1: The basic lensing configuration for a source, located at distance D_s and a mass concentration at distance D_d. The optical axis connects the observer and the center of the mass concentration and extends to the source plane. The source plane is perpendicular to the optical axis at the source distance. The cross section of optical axis with the planes are chosen to be the origins of the coordinate systems on the planes. $\hat{\alpha}$ denotes the deflection angle, $\boldsymbol{\beta}$ is the angular position of the source in absence of the deflector plane and $\boldsymbol{\theta}$ is the angle by which, the source is observed. All the angles are two-dimensional vectors, drawn here as projected angles for simplicity.

lensing system. Using the definition of critical surface mass density in equation 3.5, one can rewrite equation 3.2 as

$$\boldsymbol{\alpha}(\boldsymbol{\theta}) = \frac{1}{\pi}\int \mathrm{d}^2\theta' \kappa(\boldsymbol{\theta'})\frac{\boldsymbol{\theta}-\boldsymbol{\theta'}}{|\boldsymbol{\theta}-\boldsymbol{\theta'}|^2}. \tag{3.6}$$

The deflection angle is the gradient of the so-called deflection potential, $\boldsymbol{\alpha} = \nabla\psi$, which is:

$$\boldsymbol{\psi}(\boldsymbol{\theta}) = \frac{1}{\pi}\int \mathrm{d}^2\theta' \kappa(\boldsymbol{\theta'})\ln|\boldsymbol{\theta}-\boldsymbol{\theta'}|. \tag{3.7}$$

This potential satisfies the 2-D Poisson equation

$$\nabla^2\psi = 2\kappa. \tag{3.8}$$

For the lens equation 3.4, the Jacobian of the mapping can be written as

$$\frac{\partial\beta_i}{\partial\theta_j} \equiv A_{ij} = \delta_{ij} - \frac{\partial^2\psi}{\partial\theta_i\partial\theta_j}. \tag{3.9}$$

The Jacobian maps the intrinsic position to the observed position. The shear is then defined as

$$\gamma_1 \equiv \frac{1}{2}(\partial_1\partial_1\psi - \partial_2\partial_2\psi),\ \gamma_2 \equiv \partial_1\partial_2\psi. \tag{3.10}$$

For convergence κ one can write

$$\kappa \equiv \frac{1}{2}(\partial_1\partial_1\psi + \partial_2\partial_2\psi). \tag{3.11}$$

The Jacobian matrix, parameterized with convergence and shear, can be written as

$$A = \frac{\partial\beta_i}{\partial\theta_i} = \begin{pmatrix} 1-\kappa-\gamma_1 & \gamma_2 \\ \gamma_2 & 1-\kappa+\gamma_1 \end{pmatrix}. \tag{3.12}$$

As seen in equations 3.10 and 3.11, shear γ and convergence κ are interrelated through the gravitational potential. In order to obtain the direct relation between shear and convergence one rewrites these equations in Fourier space:

$$\hat{\kappa}(\boldsymbol{\ell}) = -\frac{1}{2}(\ell_1^2+\ell_1^2)\hat{\psi}(\boldsymbol{\ell}); \tag{3.13}$$

$$\hat{\gamma}_1(\boldsymbol{\ell}) = -\frac{1}{2}(\ell_1^2 - \ell_1^2)\hat{\psi}(\boldsymbol{\ell}); \tag{3.14}$$

$$\hat{\gamma}_2(\boldsymbol{\ell}) = -\ell_1^2\ell_2^2\hat{\psi}(\boldsymbol{\ell}). \tag{3.15}$$

Here ℓ is the two dimensional wave vector, conjugate to $\boldsymbol{\theta}$. The linear relation between the transformed components $\hat{\kappa}$, $\hat{\gamma}_1$ and $\hat{\gamma}_2$ can be written as

$$\begin{pmatrix} \hat{\gamma}_1 \\ \hat{\gamma}_2 \end{pmatrix} = \ell^{-2} \begin{pmatrix} {\ell_1}^2 - {\ell_2}^2 \\ 2\ell_1\ell_2 \end{pmatrix} \hat{\kappa}, \tag{3.16}$$

$$\hat{\kappa} = \ell^{-2}[(\ell_1^2 - \ell_2^2), (2\ell_1\ell_2)] \begin{pmatrix} \hat{\gamma}_1 \\ \hat{\gamma}_2 \end{pmatrix}. \tag{3.17}$$

We take advantage of equations 3.16 and 3.17 later in this thesis when converting simulated convergence maps into shear maps. Also this is the basis of mass reconstruction using lensing. We can quantitatively reconstruct the surface mass distribution of a cluster lens using the method of Kaiser and Squires [1993], which is based on the procedure above. Figure 3.2a shows a sample of the simulated δ-maps that are used in other parts of this thesis. A whole series of such δ-maps from the source redshift to the observer are used to generate κ-maps by integration over the source-lens geometry (See figure 3.2b). These maps are then turned into shear maps by using the formalism above. The resulting shear maps for the particular κ-maps shown are presented in figure 3.3a and 3.3b.

In analogy to equation 2.21 the power spectra of the convergence and shear are:

$$\langle \hat{\kappa}(\boldsymbol{s})\hat{\kappa}^*(\boldsymbol{s'})\rangle = (2\pi)^2\delta_{\mathrm{D}}(\boldsymbol{s}-\boldsymbol{s'})P_\kappa(s), \tag{3.18}$$

$$\langle \hat{\gamma}(\boldsymbol{s})\hat{\gamma}^*(\boldsymbol{s'})\rangle = (2\pi)^2\delta_{\mathrm{D}}(\boldsymbol{s}-\boldsymbol{s'})P_\gamma(s), \tag{3.19}$$

and from equations 3.13, 3.14 and 3.15 we obtain that $P_\kappa = P_\gamma$.

Based on Liouville's theorem [1], the surface brightness is conserved by gravitational lensing, so the observed intensity I at a position $\boldsymbol{\theta}$ is related to the intensity

[1] Liouville's theorem states that, an object at redshift z with radiation surface brightness i_{e}, as measured by an observer at rest, has observed surface brightness $i_{\mathrm{o}} = i_{\mathrm{e}}(1+z)^{-4}$.

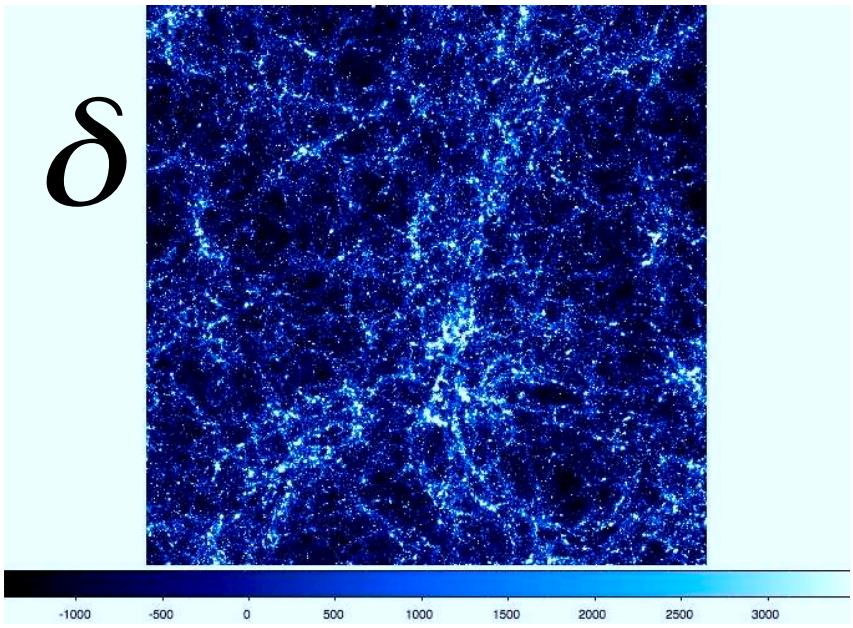

(a)

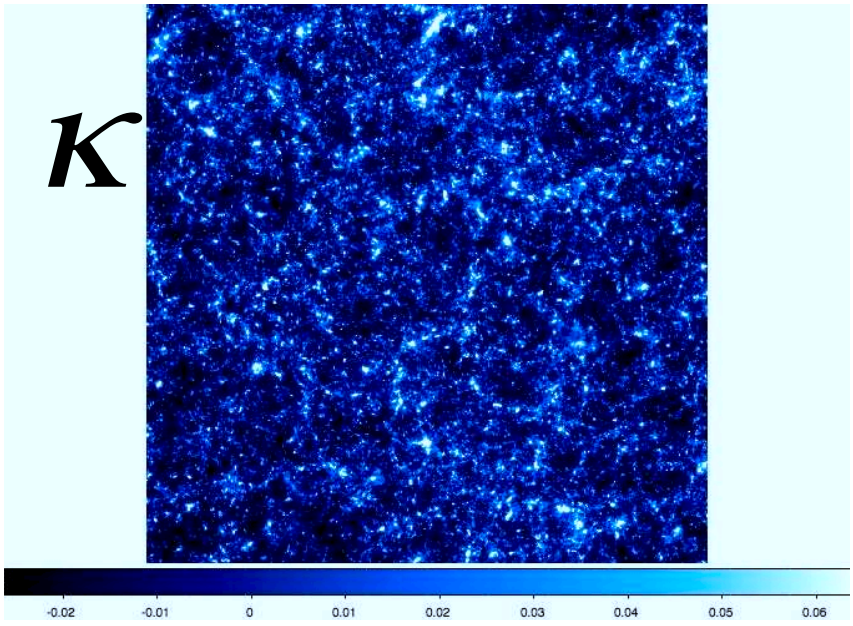

(b)

Figure 3.2: (a) The simulated δ-map. (b) The simulated κ-map at redshift z=1.0. The maps span 3.5° on each side.

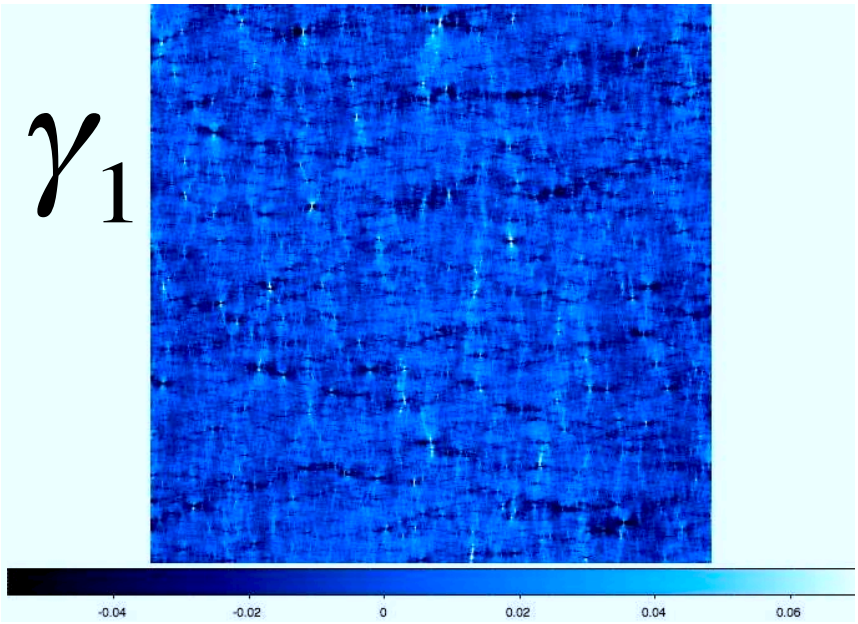

(a)

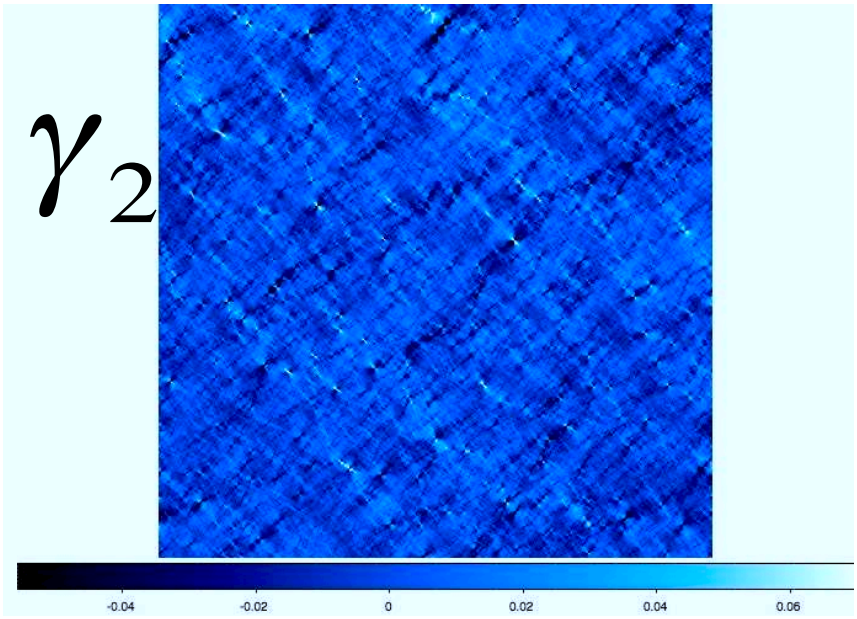

(b)

Figure 3.3: (a) The simulated γ_1 and (b) γ_2-maps at z=1.0. The maps span 3.5° on each side.

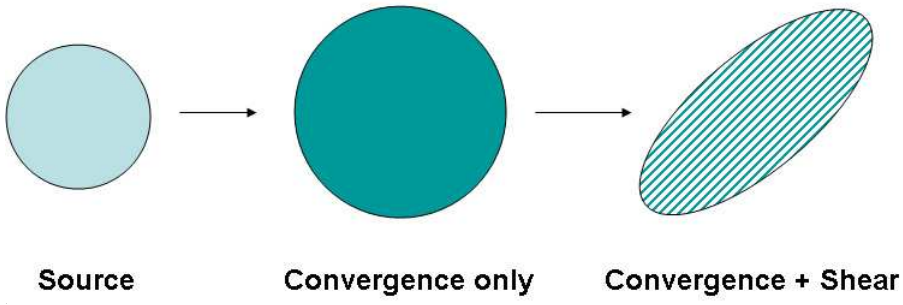

Figure 3.4: The effect of shear and magnification on the image of a circular object. Convergence causes magnification and shear stretches the object into an elliptical shape (shear).

in the source plane I^s as: $I(\boldsymbol{\theta}) = I^s(\boldsymbol{\beta}(\boldsymbol{\theta}))$. Assuming that the angular extent of the source is smaller than the scale on which the lens properties change, one can linearize this relation in the vicinity of the image position $\boldsymbol{\theta_0}$ to

$$I(\boldsymbol{\theta}) = I^s(\boldsymbol{\beta}(\boldsymbol{\theta_0}) + A(\boldsymbol{\theta_0})(\boldsymbol{\theta} - \boldsymbol{\theta_0})), \tag{3.20}$$

which maps a circular source to an elliptical image. The convergence is the diagonal part of the Jacobian, so it isotropically magnifies the image, whereas the shear γ is the trace-free part and distorts the image. Figure 3.4 shows schematically the effects of shear and magnification on a circular source.

3.4 Weak Gravitational Lensing Measurements

The regime in which $\kappa \ll 1$ and $|\gamma| \ll 1$ is referred to as the weak lensing regime. There, the level of distortion of the distant source galaxies is much smaller than the typical intrinsic ellipticities of those galaxies. This is why it is impossible to tell whether an individual source is affected by it or not. By observing a large number of galaxies, however, one can statistically detect the weak shear. In practice, in order to measure the shape of galaxies, most of which are faint and small, we rely on the brightness distribution of the image on the Charged Coupled Device (CCD).

First the centre of the isolated brightness distribution is located by:

$$\bar{\boldsymbol{\theta}} \equiv \frac{\int \mathrm{d}^2\theta q_{\mathrm{I}}[I(\boldsymbol{\theta})]\boldsymbol{\theta}}{\int \mathrm{d}^2\theta q_{\mathrm{I}}[I(\boldsymbol{\theta})]}, \tag{3.21}$$

where q_I is a weight function. Next the second-moment tensor of the brightness distribution is calculated as

$$Q_{ij} \equiv \frac{\int \mathrm{d}^2\theta q_{\mathrm{I}}[I(\boldsymbol{\theta})](\theta_i - \bar{\theta_i})(\theta_j - \bar{\theta_j})}{\int \mathrm{d}^2\theta q_{\mathrm{I}}[I(\boldsymbol{\theta})]}, i, j = 1, 2. \tag{3.22}$$

The complex ellipticity ε is then defined as:

$$\varepsilon \equiv \frac{Q_{11} - Q_{22} + 2iQ_{12}}{Q_{11} + Q_{22} + 2(Q_{11}Q_{22} - Q_{12}^2)^{\frac{1}{2}}}. \tag{3.23}$$

The intrinsic ellipticity of the source ε^{s} is the related to the observed ellipticity ε^{o} as:

$$\varepsilon^{\mathrm{s}} = \begin{cases} \frac{\varepsilon^{\mathrm{o}} - g}{1 - g^* \varepsilon^{\mathrm{o}}} & \text{for } |g| \leq 1; \\ \frac{1 - \varepsilon^{\mathrm{o}*} g}{\varepsilon^{\mathrm{o}*} - g^*} & \text{for } |g| > 1. \end{cases} \tag{3.24}$$

Here g is the reduced shear, defined as

$$g \equiv \frac{\gamma}{1 - \kappa}. \tag{3.25}$$

For the case of weak lensing where $\kappa \ll 1$ and $|\gamma| \ll 1$, then $g \approx \gamma$, so we have

$$\varepsilon^{\mathrm{o}} \approx \varepsilon^{\mathrm{s}} + \gamma, \tag{3.26}$$

which states that the observed ellipticity is the sum of the intrinsic ellipticity and the distortions caused by gravitational lensing. This makes no assumption on value of ε^{o}. The upper limit of ε^{o} is equal to unity by construction. One can simply assume that the intrinsic orientation of source galaxies is random, due to statistical isotropy of the large scale structure. Then the expectation value of the intrinsic ellipticity $\langle \varepsilon^{\mathrm{s}} \rangle = 0$ for a large enough sample. Therefore, the observed ellipticity can be taken as a very noisy, but unbiased estimator of the shear

$$\langle \varepsilon^o \rangle = \gamma. \tag{3.27}$$

This is the idea behind the data processing which produced the data set used in our analysis in future chapters.

3.5 Cosmic Shear

Cosmic shear is the weak gravitational lensing of high-redshift galaxies due to the matter distribution inhomogenities of the large-scale structure in the Universe. Cosmic shear was first detected by Van Waerbeke et al. [2000], Kaiser et al. [2000], Wittman et al. [2000] and Bacon et al. [2000] in 2000. The light bundles passing through the large-scale structure of the Universe get distorted, and as a result the shape and size of the observed galaxies are altered. Therefore, the statistics of such distortions can be directly linked back to the statistical properties of the large-scale structure (Gunn [1967], Blandford et al. [1991], Miralda-Escude [1991] and Kaiser [1992]). Cosmic shear involves the investigation of the correlation between the distorted shapes of the galaxies and the underlying cosmological properties responsible for the amount of distortion. The main challenge here is that these distortions are very weak and hence difficult to measure. Also, unlike the ordinary weak lensing discussed before, the light deflection does not occur in a single lens plane any longer, but throughout the full 3-D matter distribution. This implies that a modified prescription of weak lensing optics is needed. In other words, the difference between cosmic shear and general weak lensing is that the thin lens approximation is no longer valid, since the light emitted by background sources gets continuously distorted by the matter distribution along the line of sight. One then has to calculate the detailed path of the distorted light. Here we skip the detailed derivation of light bundle propagation through the 3-D matter distribution. The reader is referred to Bartelmann and Schneider [2001] for more details. The conclusion there is that, although the thin lens approximation is no longer valid in case of cosmic shear, one can still consider a stack of multiple lens planes to reconstruct the large-scale structure lensing effect. So for sources at a single redshift z_s in the lowest-order approximation, the 3-D matter distribution can be considered as an effective surface mass density $\kappa_{\rm eff}$ as ordinary weak lensing. This $\kappa_{\rm eff}$ can be obtained by line

of sight integration of the density contrast δ, weighted by geometrical factors entering the lens equation. In order to calculate the effective surface mass density, we need to relate κ to the fractional density contrast δ. Recall equation 2.15 and the 3-D Poisson equation 3.8, to obtain the effective convergence as

$$\kappa(\boldsymbol{\theta},\chi) = \frac{3H_0^2\Omega_{\rm m}}{2c^2}\int_0^{\chi} {\rm d}\chi' \frac{f_K(\chi')f_K(\chi-\chi')}{f_K(\chi)}\frac{\delta(f_K(\chi')\boldsymbol{\theta},\chi')}{a(\chi')}. \tag{3.28}$$

As can be seen above, the convergence κ is proportional to matter density parameter $\Omega_{\rm m}$ since lensing is sensitive to $\Delta\rho \propto \delta\Omega_{\rm m}$, not just the density contrast itself. From now on we drop the phrase "effective" from the naming for simplicity. Note that for cosmic shear analysis we always mean the effective convergence due to the full large-scale structure along the line of sight. When the source galaxies follow a redshift distribution with $p_z(z){\rm d}z = p_\chi(\chi){\rm d}\chi$, the effective surface mass density becomes

$$\kappa(\boldsymbol{\theta}) = \int {\rm d}\chi p_\chi(\chi)\kappa(\boldsymbol{\theta},\chi) = \frac{3H_0^2\Omega_{\rm m}}{2c^2}\int_\chi^{\chi_h} {\rm d}\chi g(\chi) f_K(\chi)\frac{\delta(f_K(\chi)\boldsymbol{\theta},\chi)}{a(\chi)}, \tag{3.29}$$

with

$$g(\chi) = \int_\chi^{\chi_h} {\rm d}\chi' p_\chi(\chi')\frac{f_K(\chi'-\chi)}{f_K(\chi')}, \tag{3.30}$$

which is the source redshift weighted lens efficiency factor $\frac{D_{\rm ds}}{D_{\rm s}}$ for a density fluctuation at distance χ. χ_h is the comoving horizon distance, obtained when $a \to 0$.

3.6 Link Between Matter and Convergence Power Spectra

It is very important to find the relationship between matter and convergence power spectra. Weak lensing observations provide an estimate of the convergence power spectrum. In order to provide cosmological interpretation from the weak lensing signal, the relationship between the convergence power spectrum and the underlying matter power spectrum must be established. This is the main building block of all lensing predictions, and the basis of the lensing measurement interpretations. By observing the shapes of the galaxies, one can use the lensing observables to

estimate the lensing statistics through various methods. The lensing statistics are related to the convergence power spectrum, which in turn can be linked to the matter power spectrum and its cosmological dependences. It is assumed that the density field δ is a random field realization. Cosmologists are trying to find the properties of this random field, not a specific realization of it. The second order statistical properties of the density field can be described in terms of the power spectrum. Limber's equation (Limber [1953]) is the basis of relating the properties of the random field to its power spectrum. For the δ (homogeneous and isotropic) 3D random field, one can write the 2D projections as

$$g_i(\boldsymbol{\theta}) = \int \mathrm{d}\chi q_i(\chi)\delta(f_K(\chi)\boldsymbol{\theta},\chi), \tag{3.31}$$

which are also homogenous and isotropic random fields. The q_is are the weight functions. The correlation function is then

$$C_{12} = \langle g_1(\boldsymbol{\varphi}_1)g_2(\boldsymbol{\varphi}_2)\rangle \equiv C_{12}(|\boldsymbol{\varphi}_1 - \boldsymbol{\varphi}_2|), \tag{3.32}$$

which only depends on the modulus of the separation ($\boldsymbol{\varphi}$) between the two points. Considering the Fourier transform of C_{12}, one can obtain P_{12}, which is the convergence power spectrum and depends linearly on $P_\delta(k)$ (Kaiser [1992] and Kaiser [1998]). We have

$$P_{12}(\ell) = \int \mathrm{d}\chi \frac{q_1(\chi)q_2(\chi)}{f_K^2(\chi)} P_\delta\left(\frac{\ell}{f_K(\chi)}, \chi\right), \tag{3.33}$$

when the large scale structure in δ are much smaller than the effective range $\Delta\chi$ of the projection. Here ℓ is the Fourier transform of the variable θ, and is related to θ by $s = 2\pi/\theta = 2.16\times10^4\ (\theta/\mathrm{arcmin})^{-1}$. The 2D power-spectrum at angular scale $1/\ell$ can be found from the 3D power at length scale $f_K(\chi)(1/\ell)$, integrated over χ. Comparing equation 3.28 and 3.33, we see that $\kappa(\boldsymbol{\theta})$ is a projection of δ with the weights $q_1(\chi) = q_2(\chi) = (3/2)(H_0/c)^2\Omega_\mathrm{m} g(\chi) f_K(\chi)/a(\chi)$. So we obtain

$$P_\kappa(\ell) = \frac{9H_0^4\Omega_\mathrm{m}^2}{4c^2}\int_0^{\chi_h} \mathrm{d}\chi \frac{g^2(\chi)}{a^2(\chi)} P_\delta\left(\frac{\ell}{f_K(\chi)}, \chi\right). \tag{3.34}$$

The advantage here is that by use of weak lensing observables, we can measure P_κ, which can be used to constrain the 3D power spectrum P_δ. In the next chapter we explain how the various cosmic shear statistics are related to the convergence power spectrum P_κ.

In section 2.3.5 we showed the matter power spectrum for the linear and non-linear regimes. Here, using equation 3.34, we show the convergence power spectrum for the same cosmological parameters in figure 3.5. One can see that the nonlinear effects kick in at $\ell = 100$ and larger. These scales correspond to angular sizes on the sky of the size of 100 arcminutes and below. The exact turn off point depends on the redshift distribution and cosmological model. On the other hand, the weak lensing sensitivity peaks at about 10 arcminutes on the sky, which corresponds to structure size, of around 1 h Mpc^{-1}, since that is the scale of galaxy clusters. This scale however, falls in the non-linear regime of the power spectrum. This means that the scales probed by weak lensing are within the non-linear part of the power spectrum. We can obtain constraints on these parameters by comparing the lensing signal with the non-linear predictions. The non-linear scales correspond to galaxy clusters and measurements of their abundance yields a robust measure of the power near this scale for a given matter density $\Omega_{\rm m}$. The point to emphasize here is that one needs to apply the nonlinear corrections to the convergence and matter power spectrum before correct interpretation of lensing measurements can be made.

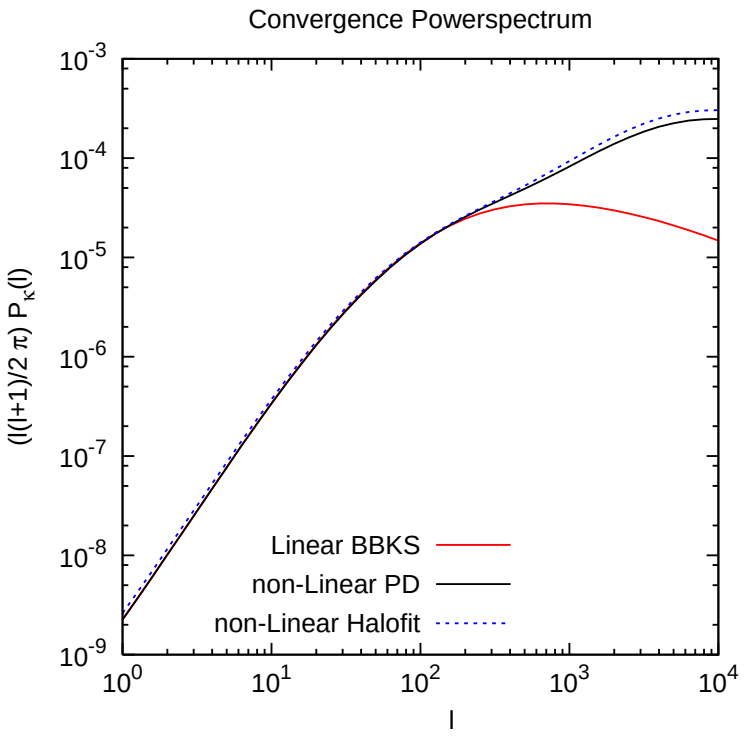

Figure 3.5: The linear and nonlinear convergence power spectrum P_κ.

Chapter 4

Cosmic Shear Statistics

In chapter 3 the connection between cosmology and cosmic shear was discussed. Cosmic shear is a direct measure of the projected matter power spectrum which depends itself on the cosmological model. Shear in the weak lensing regime can only be measured statistically, by averaging over a large number of galaxies. In this chapter we explain the various statistics of cosmic shear, which have been established, studied and widely used over the past few years. We then discuss the standard estimators of the shear statistics that are used to measure the shear from observed galaxy ellipticities. For more details on the topic of weak lensing statistics, see Schneider et al. [2002a]. We start with the two-point statistics and then move on to higher moments. The inhomogeneities that cause the shear are isotropic (no preferred direction). This results in cosmic shear acting as an isotropic random field, with all the first moments equal to zero. The focus of this thesis is to explore the cosmic shear estimators beyond the standard two-point statistics into the three-points and other alternative methods, such as using the full shape of the probability distribution function. Three-point statistics can be used to measure the non-Gaussianity of the large-scale structure. Also by considering alternative non-conventional cosmic shear estimators one can in principle break the existing degeneracies between cosmological parameters when only two-point statistics are considered. Here we first set the foundation using the two-point statistics and then extend the discussion to higher orders.

As explained earlier, shear is a two-component quantity (equation 3.10). We

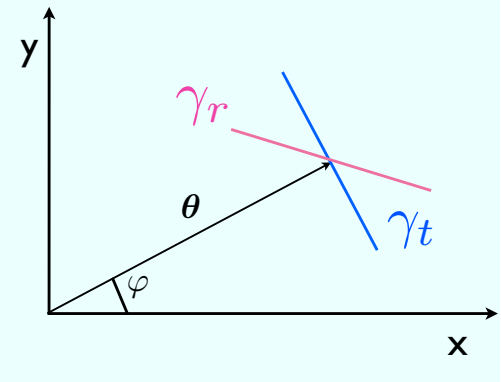

Figure 4.1: The γ_t-γ_r orientation with respect to each other.

can then construct four two-point correlation functions with different combinations of the shear components. The coordinate system used to decompose the shear elements is chosen to be the direction of the vector θ connecting the pair of galaxies. One defines the tangential and cross-components of the shear with respect to that direction

$$\gamma_t = -\Re(\gamma e^{-2i\varphi}) = -\gamma_1 \cos 2\varphi - \gamma_2 \sin 2\varphi; \tag{4.1}$$

$$\gamma_r = -\Im(\gamma e^{-2i\varphi}) = \gamma_1 \sin 2\varphi - \gamma_2 \cos 2\varphi. \tag{4.2}$$

Here φ is the polar angle of the connecting vector θ. Figure 4.1 shows the tangential and cross-components of the shear. Note that the two components have 45° angle separation. Also figure 4.2 shows the range of both ellipticity components and how they relate to the orientation of an ellipse.

4.1 Two-point Correlation Function

The two-point shear correlation functions ξ_+ and ξ_- are defined as

$$\xi_\pm(\theta) \equiv \xi_{tt} \pm \xi_{rr}, \tag{4.3}$$

where

$$\xi_{tt} = \langle \gamma_t(\vartheta)\gamma_t(\vartheta+\theta)\rangle, \tag{4.4}$$

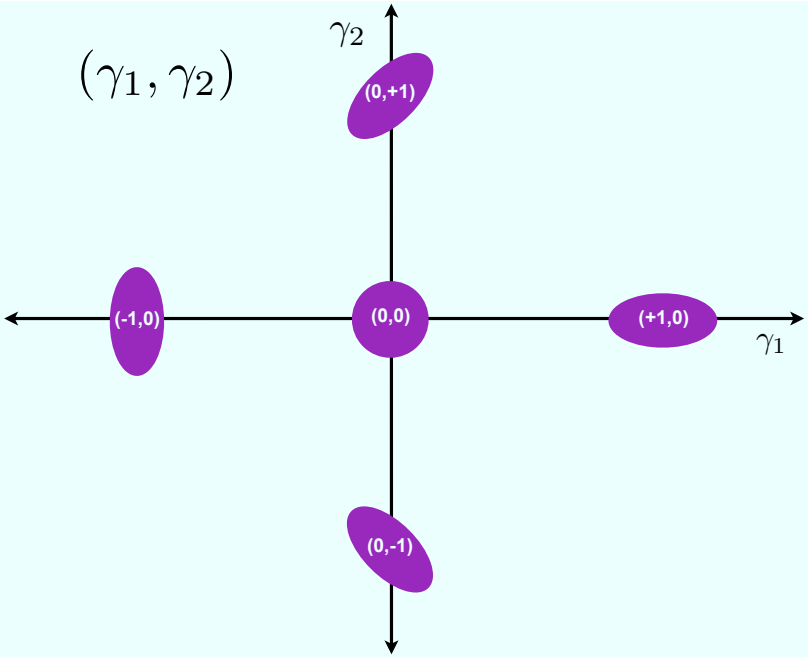

Figure 4.2: The ellipse orientation for a range of shear component γ_1 and γ_2 values.

and

$$\xi_{rr} = \langle \gamma_r(\vartheta)\gamma_r(\vartheta+\theta)\rangle. \tag{4.5}$$

Since the shear caused by the large scale structure is a homogeneous and isotropic random field, equations 4.3 only depends on the size of the connecting vector θ. The other two correlation functions that contain mixed terms of γ_t and γ_r vanish due to parity symmetry. In parallel one can write the correlation function for convergence κ as the following:

$$\xi_{\kappa\kappa} = \langle \kappa(\vartheta)\kappa(\vartheta+\theta)\rangle. \tag{4.6}$$

The Fourier transform of the convergence two-point correlation function is defined as the convergence power spectrum P_κ, since the convergence field can be considered as a homogeneous and isotropic random field. Using equation 3.14 one can

write equation 4.3 in Fourier space as in Kaiser [1992] and find

$$\xi_{(+,\kappa)}(\theta) = \frac{1}{2\pi}\int_0^\infty \mathrm{d}s s P_\kappa(s) J_0(s\theta), \tag{4.7}$$

$$\xi_{-}(\theta) = \frac{1}{2\pi}\int_0^\infty \mathrm{d}s s P_\kappa(s) J_4(s\theta), \tag{4.8}$$

where J_ν is the Bessel function of the first kind of order ν. The above equations indicate how the two-point correlation functions are related to the convergence κ power spectrum and hence the cosmology. Later in chapter 5 we take advantage of these relations and test the sanity of the simulations against theoretical predictions based on the input cosmology of the simulations.

4.2 Top-hat Variance

In addition to the two-point correlation function, one can consider two-point estimators inside of an aperture. One choice of the aperture window is of the shape of a "top-hat" within which the shear dispersion can be calculated Kaiser [1992]. The mean shear inside an aperture of radius θ can be written as

$$\overline{\gamma}(\theta) = \frac{1}{\pi\theta^2}\int_{\text{aperture}} \mathrm{d}^2\vartheta\,\gamma(\vartheta). \tag{4.9}$$

The dispersion of the square of the absolute mean shear is then

$$\langle|\overline{\gamma}|^2(\theta)\rangle = \frac{1}{2\pi}\int_0^\infty \mathrm{d}s s P_\kappa(s)\left(\frac{2J_1(s\theta)}{s\theta}\right)^2, \tag{4.10}$$

which shows the connection to cosmology through P_κ. Note that $I_{\mathrm{TH}}(s\theta) = \left(\frac{2J_1(s\theta)}{(s\theta)}\right)$ and $I^2_{\mathrm{TH}}(s\theta)$ is the top-hat filter function (Blandford et al. [1991]). Equation 4.10 is used to make theoretical predictions.

In practice the top-hat variance is calculated through integrations of the two-point correlation functions ξ_+ and ξ_-, where $\xi_\pm$ are in turn measured by correlating the shear values of pairs of galaxies in the data set, as shown in equation 4.4 and 4.5. In order to estimate the top-hat variance $\langle|\overline{\gamma}|^2(\theta)\rangle$ from the 2-point correlation

functions, the following integration has to be calculated

$$\begin{aligned}\langle|\overline{\gamma}|^2(\theta)\rangle &= \int_0^\theta \frac{\mathrm{d}\vartheta}{\theta^2}\xi_+(\vartheta)S_+(\frac{\vartheta}{\theta});\\ &= \int_0^\theta \frac{\mathrm{d}\vartheta}{\theta^2}\xi_-(\vartheta)S_-(\frac{\vartheta}{\theta}).\end{aligned} \tag{4.11}$$

Here S_+ and S_- are well defined functions given in Schneider et al. [2002b]. The blue line in figure 4.3 shows the filter response function of the top-hat filter in comparison to other filters, which we will discuss in the following section.

4.3 Aperture Mass Variance

Another aperture based statistic is the dispersion of so called aperture mass [Schneider et al., 1998]. The aperture mass is defined as

$$M_{\mathrm{ap}}(\theta) = \int_{\mathrm{aperture}} \mathrm{d}^2\vartheta U(\vartheta)\kappa(\vartheta), \tag{4.12}$$

where κ is the convergence and $U(\vartheta)$ is the compensated filter, i.e. $\int_0^\theta \mathrm{d}\vartheta\,\vartheta U(\vartheta) = 0$. The choice of $U(\vartheta)$ is arbitrary as long as the function chosen is compensated. One can also express M_{ap} in terms of the tangential shear:

$$M_{\mathrm{ap}}(\theta) = \int_{\mathrm{aperture}} \mathrm{d}^2\vartheta Q(\vartheta)\gamma_t(\vartheta), \tag{4.13}$$

with the condition that $Q(\vartheta) = \frac{2}{\vartheta^2}\int_0^\vartheta \mathrm{d}\rho\rho U(\rho) - U(\vartheta)$. Note that the tangential shear component at each point is taken with respect to the centre of the aperture. The dispersion of M_{ap} can be calculated as follows:

$$\begin{aligned}\langle M_{\mathrm{ap}}^2(\theta)\rangle &= \int \mathrm{d}^2\theta' U(\theta')\int \mathrm{d}^2\theta U(\theta)\langle\kappa(\theta')\kappa(\theta)\rangle\\ &= \int \mathrm{d}^2\theta' U(\theta')\int \mathrm{d}^2\theta U(\theta)\int \frac{\mathrm{d}^2 s}{(2\pi)^2}\mathrm{e}^{\mathrm{i}\mathbf{s}\cdot(\theta'-\vartheta)}P_\kappa(s)\\ &= 2\pi\int_0^\infty \mathrm{d}s s P_\kappa(s)\left(\int_0^\theta \mathrm{d}\vartheta\,\vartheta U(\vartheta)\mathrm{J}_0(s\vartheta)\right)^2.\end{aligned} \tag{4.14}$$

The form of the compensated filter U is general as long as it satisfies the con-

dition above. However, several popular choices have widely been used in weak lensing studies. One of these is the functional form used by Schneider et al. [1998]:

$$U_\theta(\vartheta) = \frac{9}{\pi\theta^2}\left(1-\frac{\vartheta}{\theta^2}\right)\left(\frac{1}{3}-\frac{\vartheta^2}{\theta^2}\right). \tag{4.15}$$

This has corresponding $Q(\vartheta)$:

$$Q_\theta(\vartheta) = \frac{6}{\pi\theta^2}\left(\frac{\vartheta}{\theta^2}\right)\left(1-\frac{\vartheta^2}{\theta^2}\right). \tag{4.16}$$

The dispersion of $M_{\rm ap}$ then simplifies to

$$\langle M_{\rm ap}^2(\theta)\rangle = \frac{1}{2\pi}\int_0^\infty {\rm d}s s P_\kappa(s)\left(\frac{24J_4(s\theta)}{(s\theta)^2}\right)^2. \tag{4.17}$$

Note here that $I_\ell(s\theta) = 24J_4(s\theta)/(s\theta)^2$ and $I_\ell^2(s\theta)$ is the aperture mass filter function. The green line in figure 4.3 shows the filter response function of the aperture mass filter used here.

Another choice of aperture function form was suggested by van Waerbeke [1998] and later Crittenden et al. [2002], which hereafter will be referred to as the compensated Gaussian filter (not to be confused with the aperture mass filter we explained above). For this choice of filter form, $U(\vartheta)$ is

$$U_\theta(\vartheta) = \frac{\vartheta^2}{2\pi\theta^2}\left(1-\frac{\vartheta^2}{4\pi\theta^2}\right)\exp\left(-\frac{\vartheta^2}{2\theta^2}\right), \tag{4.18}$$

with the corresponding shear filter $Q(\vartheta)$ as

$$Q_\theta(\vartheta) = \frac{\vartheta^2}{4\pi\theta^2}\exp\left(-\frac{\vartheta^2}{2\theta^2}\right). \tag{4.19}$$

This choice leads to $I_\ell(s\theta) = \frac{(s\theta)^2}{2}\exp\left(-\frac{(s\theta)^2}{2}\right)$. The filter response of the compensated Gaussian filter is shown in cyan (light blue) in figure 4.3 The disadvantage of the compensated filter is its broad support, although they have a strong fall off for $\vartheta \gg \theta$. The advantage, however, is the convenience of analytic properties of this filter, which is the reason we compute the higher order statistics on the data

using the compensated Gaussian filter in the future chapter 7.

In practice one can estimate $\langle M_{\rm ap}^2 \rangle$ from the shear correlation in the data. The relationship between the two-point shear correlation functions and the aperture statistic is as follows:

$$\langle M_{\rm ap}^2 \rangle(\theta) = \int_0^{2\theta} \frac{{\rm d}\vartheta\,\vartheta}{\theta^2} \xi_{\pm}(\vartheta) T_{\pm}\left(\frac{\vartheta}{\theta}\right), \tag{4.20}$$

where $T_{\pm}$ are simple well defined functions which depend on the choice of the compensated filter function. For the standard aperture mass filter the form of $T_{\pm}$ can be found in Schneider et al. [2002b], whereas for the compensated Gaussian filter the functional form is shown in Jarvis et al. [2003]. In summary all two-point statistics can be estimated from the two-point shear correlation function. This is very useful, because each of the two-point statistics are related to the convergence power spectrum which, in turn is related to the matter power spectrum and hence cosmological parameters of the Universe.

Like all the other two-point statistics discussed above, the aperture mass variance is also a linear function of the convergence power spectrum. Each of the two-point statistics is a unique filtered version of the convergence power spectrum. The filter functions for each case are plotted in figure 4.3.

4.4 E- and B-modes of the Shear

The relations between shear, convergence and gravitational potential leads to the following (Kaiser [1995] and Schneider et al. [2002a]):

$$\nabla\kappa = \begin{pmatrix} \partial_1\gamma_1 + \partial_2\gamma_2 \\ \partial_2\gamma_1 - \partial_1\gamma_2 \end{pmatrix} \equiv \mathbf{u}. \tag{4.21}$$

The vector $\mathbf{u}$ can be considered as the potential of κ. However the noise and the systematic measurement errors from the data, introduce a curl (non-gradient) component to $\mathbf{u}$ which is referred to as the "B-mode". Also the intrinsic alignment of source galaxies [Brown et al., 2002], source clustering of galaxies and higher order lensing (lens-lens coupling) can cause non-gradient terms [Schneider et al., 2002a]. In analogy to the electromagnetic field and in order to separate the gradient

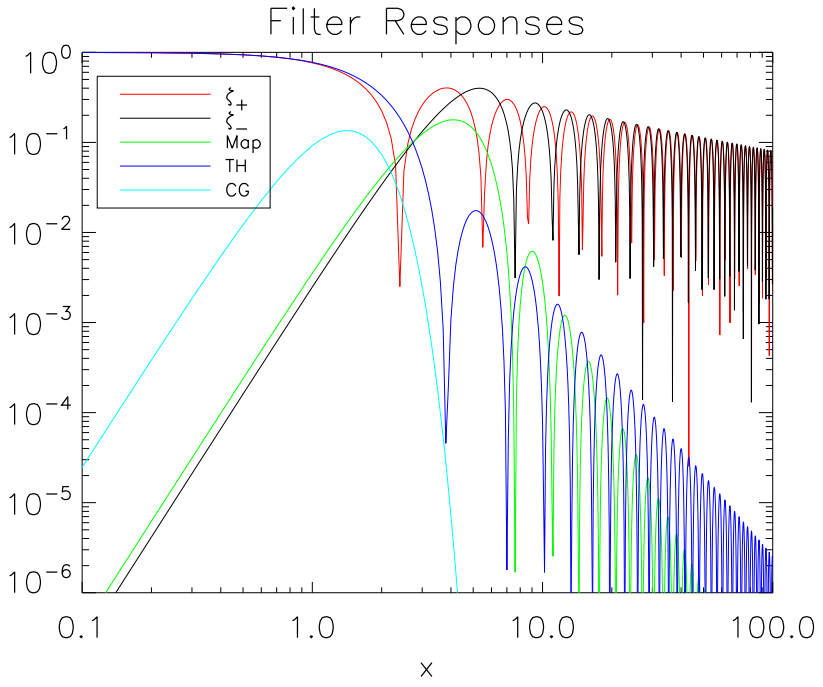

Figure 4.3: The filter response for various functions involved in the lensing statistics. The red line shows $J_0(x)$ for ξ_+, the black line $J_4(x)$ for ξ_-, the green line $(\frac{24J_4(x)}{x^2})^2$ for regular aperture map M_{ap}, the dark blue line $(\frac{2J_1(x)}{x})^2$ for top-hat, and finally the cyan (light blue) line shows $(\frac{x^2}{2}\exp(-\frac{x^2}{2}))^2$ for the compensated Gaussian filter, which is a form of aperture filter.

and curl parts of $\mathbf{u}$, new quantities κ^E and κ^B are defined such that:

$$\nabla^2\kappa^E = \nabla\cdot\mathbf{u}; \tag{4.22}$$

$$\nabla^2\kappa^B = \nabla\times\mathbf{u} \equiv \partial_1 u_2 - \partial_2 u_1. \tag{4.23}$$

Also the E- and B-mode potentials are defined by the Poisson equation

$$\nabla^2\psi^{E,B} = 2\kappa^{E,B}, \tag{4.24}$$

where the E- and B-modes can be combined into complex quantities for simplicity of calculations:

$$\psi \equiv \psi^{\mathrm{E}} + i\psi^{\mathrm{B}}; \tag{4.25}$$

$$\kappa \equiv \kappa^{\mathrm{E}} + i\kappa^{\mathrm{B}}. \tag{4.26}$$

So the complex shear $\gamma = \frac{1}{2}(\partial_{11} - \partial_{22})\psi + i\partial_{12}\psi$, with respect to the new potential can be written as

$$\gamma_1 + i\gamma_2 = \frac{1}{2}(\partial_{11}\psi^{\mathrm{E}} - \partial_{22}\psi^{\mathrm{E}}) - \partial_{12}\psi^{\mathrm{B}} + i[\partial_{12}\psi^{\mathrm{E}} + \frac{1}{2}(\partial_{11}\psi^{\mathrm{B}} - \partial_{22}\psi^{\mathrm{B}})]. \tag{4.27}$$

The convergence power spectrum can also be decomposed into E- and B-modes, $P_\kappa = P_\kappa^{\mathrm{E}} + P_\kappa^{\mathrm{B}}$, such that the following relationships hold:

$$\langle \hat{\kappa}(\mathbf{s})\hat{\kappa}^*(\mathbf{s}')\rangle = \langle \hat{\gamma}(\mathbf{s})\hat{\gamma}^*(\mathbf{s}')\rangle = (2\pi)^2\delta_D(\mathbf{s}-\mathbf{s}')(P_\kappa^{\mathrm{E}}(s) - P_\kappa^{\mathrm{B}}(s)), \tag{4.28}$$

where P_κ^{E} and P_κ^{B} are the spectral power densities of κ^{E} and κ^{B} from equation 4.26. Then, in analogy to equation 4.3, we obtain the correlation functions

$$\xi_+ = \frac{1}{2\pi}\int_0^\infty \mathrm{d}s s J_0(\theta s)(P_\kappa^{\mathrm{E}}(s) + P_\kappa^{\mathrm{B}}(s)), \tag{4.29}$$

$$\xi_- = \frac{1}{2\pi}\int_0^\infty \mathrm{d}s s J_4(\theta s)(P_\kappa^{\mathrm{E}}(s) - P_\kappa^{\mathrm{B}}(s)), \tag{4.30}$$

which can be inverted to give

$$P_\kappa^{\mathrm{E,B}} = \pi\int_0^\infty \mathrm{d}\theta\theta(\xi_+(\theta)J_0(s\theta) \pm \xi_-(\theta)J_4(s\theta)). \tag{4.31}$$

Also following Schneider et al. [2002b], one can define

$$\xi_{\mathrm{EE}} = \frac{1}{2\pi}\int_0^\infty \mathrm{d}s s P_\kappa^{\mathrm{E}}(s)J_0(\theta s). \tag{4.32}$$

These authors showed that in the absence of B-modes, $\xi_{\mathrm{EE}} = \xi_+$. In chapter 5 we test the simulations by calculating the quantity ξ_{EE} and comparing to the predic-

tions from ξ_+, which is an indicator of simulations being free of B-modes.

In practice we use the aperture mass statistics to study E- and B-modes of the shear separately. Another form of the aperture mass statistics, in analogy to equation 4.33, can be written for the cross-component of shear γ_r:

$$M_\perp(\theta) = \int_{\text{aperture}} \mathrm{d}^2\vartheta Q(\vartheta)\gamma_r(\vartheta), \tag{4.33}$$

where θ is the radius of the aperture. We can then write the dispersion equations in terms of E- and B-mode power spectra as

$$\langle M^2_{\text{ap},\perp}(\theta)\rangle = \frac{1}{2\pi}\int_0^\infty \mathrm{d}s s P_\kappa^{E,B}(s)\left(\frac{24\mathrm{J}_4(s\theta)}{(s\theta)^2}\right)^2. \tag{4.34}$$

This implies that the measurement of these two aperture dispersions leads directly to estimation of E- and B-mode contributions to the overall power spectrum. In absence of B-modes, $\langle M^2_\perp\rangle$ is expected to vanish. In practice we arrive at the measurement of $\langle M^2_{\text{ap},\perp}(\theta)\rangle$ through the correlation functions, so the aperture dispersion can be expressed as

$$\langle M^2_{\text{ap},\perp}(\theta)\rangle = \frac{1}{2\theta^2}\int_0^{2\pi}\mathrm{d}\theta'\theta'\left[\xi_+(\theta')T_+\left(\frac{\theta'}{\theta}\right) \pm \xi_-(\theta')T_-\left(\frac{\theta'}{\theta}\right)\right]. \tag{4.35}$$

Although the true source of the B-mode contributions is not completely known, it is believed to have several possible explanations. Regardless of its nature, B-mode measurement is an important part of weak lensing analysis. The aim of all data reduction and shape measurement pipelines is to reduce the residual systematics in the data as much as possible, to eliminate their contribution to the B-mode measurements. Although in most cases there are still left over B-modes in the data, it is useful as a guideline to either remove the points with higher B-modes from the analysis, or to consider increasing the error estimated on the E-modes to better accommodate the existence of B-modes in the data (Van Waerbeke et al. [2002]). Figure 4.4 shows the orientation of shear for E- and B-modes. The top row shows the E-modes when the centre consists of a mass distribution (left) or void (right), while the bottom row pictures the curl orientations of the B-mode.

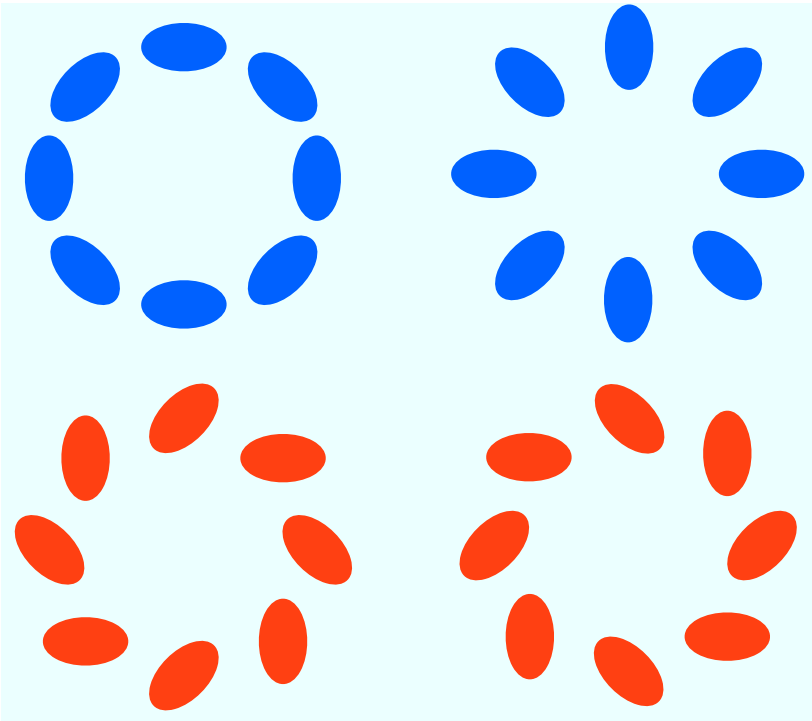

Figure 4.4: The schematics of E- and B-modes. Top row shows the E-mode in the presence of a massive centre (left) or a void (right). The bottom row shows the orientation of the B-modes.

4.5 Windowed Second and Third Moments

Another means of estimating the two- and three-point statistics of top-hat and compensated filters is to apply the filter function to the reconstructed convergence map directly. Shear components γ_1 and γ_2 are related to the convergence κ by equation 3.17. There is a large area of weak lensing research which involves perfecting the methods of mass reconstruction, given that the shear from data is noisy and potentially mixed with systematics, and also that there are gaps in the positions due to masking effects. However, assuming one obtains a mass reconstructed convergence map, one can apply the corresponding filter $U(\vartheta)$ to the maps directly and measure the variance and third moment of the convergence within the filter aperture. In this process the convergence map is convolved with the shape of the filter

function. The calculation speed can be improved if the convolution routine is substituted by multiplications of the Fourier counterparts of both the convergence map and the filter function. We employ this approach in the following section of the thesis: (1) in chapter 5 for computing the windowed two- and three-point statistics to test the sanity of the simulations against the theoretical predictions; (2) in chapter 6 for computation of the covariance matrices as well as all the statistics; (3) in chapter 7 for calculations of covariance matrices from the simulations; and (4) in chapter 8 to measure the PDF statistics and the related covariance matrices. We will later explain each of the cases extensively, however, the goal of this chapter is to introduce the various lensing statistics and their relation to the matter power spectrum.

4.6 Theoretical Predictions

Throughout this thesis we repeatedly compare the measurements of the simulations and data, to the theoretical prediction. This section briefly explains how these prediction are generated. The forward process proceeds as follows. A certain choice of cosmological parameters lead to a certain value of energy density ρ, as seen in section 2.1. Then density ρ is related to the density contrast δ as in equation 2.14. The solution to the Poisson equation 2.15, involves a growing mode δ_+ and a decaying mode δ_-, as shown in equation 2.16, which depend on the cosmological parameters. We compute the growth factor D_+ (see equation 2.17) from δ_+. The transfer function T_k is then calculated through 2.18 via the fitting formula of equation 2.19 [Bardeen et al., 1986], known as the BBKS formula. The BBKS formula does not take into account the effects of baryonic matter, so an alternative option is to use the Eisenstein & Hu formula [Eisenstein and Hu, 1998]. Regardless of the choice, by obtaining the desired transfer function and growth factor, one can calculate the matter power spectrum P_δ as in equation 2.22. To include the effects of non-linear structure formation at lower redshift, one has to apply corrections to the P_δ. The two common options are P& D (Peacock and Dodds [1996]) or Halofit (Smith et al. [2003]) approach, which we discussed previously. Regardless of the choice, we arrive at the matter power spectrum P_δ, which is related to the convergence power spectrum P_κ via Limber's equation 3.34. We showed earlier in this

chapter how the convergence power spectrum is related to each of the weak lensing shear statistics. This is the basis of all the theoretical predictions used in this thesis. For chapter 5 we include the transfer function calculations of the `camb` software (Seljak and Zaldarriaga [1996], Lewis et al. [2000]) rather than fitting formulae for greater accuracy.

Chapter 5

Numerical Simulations

Gravity is a non-linear process, hence the predictions from linear theory of large scale structures are only valid on the largest scales, or the earliest times, where most of the matter fluid was still in the linear regime. In the context of the detection of weak lensing, however, photon trajectories are probing a broad dynamical range, and are mostly sensitive to galactic scale structures, where the matter fields are highly non-linear. Although higher order perturbation theory can be used to describe the underlying densities, the accuracy of the calculations are limited by the complex dynamics. We thus need to rely on N-body simulations in order to generate non-linear densities, and to extract from them non-linear weak-lensing maps via a ray-tracing algorithm. Two sets of simulations were used in this thesis:

- Set I: This set was developed in collaboration with Tingting Lu (UofT) who ran the N-body simulations. As part of this thesis we extensively tested the quality of these simulations. These simulated maps were used in the publication Vafaei et al. [2010] on optimal survey design for higher-order lensing statistics, which covers work presented here in chapter 6. In order to avoid repetition, the details of this set are left to be explained in the next chapter as part of the published article. This set was also used in Semboloni et al. [2011b] to calculate the covariance matrices for the first ever space-based cosmological parameter constraint using three-point correlation functions.

- Set II: Following the work with set I, we further realized the great need of having a simultaneously large and accurate set of simulations available for weak lensing studies. Stable covariance matrices have to be computed over many samples. Also the accuracy of the simulations affects the likelihood analysis directly. The production of a large set of simulations can be computationally expensive and time consuming. The simulations were run by our collaborator Joachim Harnois-Deraps on clusters at Canadian Institute of Theoretical Astrophysics (CITA). We tested every step of the process and certain adjustments to the simulation box size and geometry were applied. Various interpolation schemes, κ-γ conversion methods, etc., were also tested. Given that the simulations were built for the weak lensing studies, we tested their sanity with various lensing two-point statistics, explained in section 4.1, chapter 4 and compared with theoretical predictions described in section 4.6.

The final set proved to be a great accomplishment for the CFHTLenS collaboration, as it will be used for covariance matrix calculations of various scientific projects within the collaboration. These simulations are also used for systematics testing. We generated the clone of the CFHTLenS, (simulated data set resembling the data in all aspects except shear) based on this set, which will be explained in more detail in chapter 9.

In this chapter, we explain the details of simulation generation and show the results of accuracy testing of the set against theoretical predictions. The cosmological parameters used in this set were based in WMAP7 (Komatsu et al. [2011]) results, as listed in table 5.1.1.

5.1 Numerical Method

Dark matter particle numerical simulations are widely used in weak lensing studies. They can be used to test the fundamental assumptions adopted in making analytical predictions, or to examine the systematics effects, all to work out an optimal analysis strategy. They can also be used in covariance matrix calculations where no analytical model exists, such as higher order statistics that probe the complicated non-linear effects. In that case a large number of realizations are required, with an

accuracy that extends below the arcminute scale. In this section, we describe some of the considerations one must keep in mind when performing such calculations.

In an ideal world, one would simulate the complete past light cone that connects the observer to the light sources, for a given opening angle and pixel resolution. Unfortunately, for sources that extend to redshift of a few, this cannot be simulated all at once, since the far end of the cosmological volume is at an earlier time than the near end. This is, however, the only way one can model the largest radial modes of a survey. Luckily, these radial modes contribute very little to the weak lensing signal [Limber, 1953]. The coherence scales of the largest structures which contribute to the signal rarely extend over more than a few times the size of large clusters, so simulation box sizes of the order of a few hundreds of h^{-1}Mpc generally suffice to model the relevant structures. These simulated boxes can then be stacked so as to create a pencil-shaped volume, or a line-of-sight (LOS), inside of which photons are propagated.

One can use a different simulation for each redshift box, as done by White and Hu [2000], but this is CPU-consuming, since a single LOS involves running between 10 and 40 N-body simulations. For covariance matrix measurements, we need hundreds of these high precision LOS, hence we opted for the common work around, which consists in treating different redshift density dumps of a single simulation as different sub-volumes of the same past light cone. Because the large-scale structures evolve across redshift slices, there exists a systematic correlation between the lenses. This correlation, however, can be minimized by randomly rotating the boxes and shifting the origin. This procedure allows us to reduce the number of simulations required for our measurements by at least an order of magnitude.

The next stage consists in calculating the photon geodesics in the large-scale structures, and to compute the cumulative deformation acquired along each trajectory. The most accurate calculations are performed by computing these geodesics in three dimensions, along their trajectory, starting from the observer's camera and progressing towards higher redshifts [Vale and White, 2003]. Such ray-tracing methods provide one of the most reliable estimates of the cumulative shear, convergence and deflection angle measured at each pixel of the observer's camera, but needs to be calculated at run time, or one is required to store the full density

contrasts in memory. Cosmological codes which perform ray-tracing calculations at run time [Kiessling et al., 2011] typically run much slower, and analyses that use the full three-dimensional densities (Vale and White [2003] and Hilbert et al. [2009]) have a large memory footprint, two limiting factors for the task at hand here.

However, it was shown by Vale and White [2003] that differences in lensing maps obtained from the mid-plane "tiling" technique is less than 0.1%, with indistinguishable effects on the two- and three-point functions. This tiling approach consist in collapsing the cosmological sub-volumes into their mid-planes, creating two dimensional slabs (or tiles) and calculating the geodesics on these thin lenses. Typically, all tiles have the same comoving dimension, and the past light cone is interpolated onto a set of pixels, whose sizes correspond to the angular resolution of the simulated telescope. In the weak lensing regime, these trajectories are close to straight lines, so that Born's approximation is very accurate (Schneider et al. [1998]; Vale and White [2003]). Here we opt for a line-of-sight integration along the unperturbed photon paths.

5.1.1 N-Body Simulations

The N-body simulations are produced by `cubep3m`, an improved version of `PMFAST` (Merz et al. [2005]) that is both `mpi` and `openmp` parallel, memory local and also allows for particle-particle (pp) interaction at the sub-grid level. 1024^3 particles are placed on a 2048^3 grid and their initial grid displacements and velocities are calculated from the Zel'dovich approximation (Zel'Dovich [1970]; Shandarin and Zel'dovich [1989]) with a transfer function obtained from `CAMB` (Seljak and Zaldarriaga [1996]). The following cosmological parameters are used as simulation input, and in theoretical predictions : $\Omega_\Lambda = 0.721$, $\Omega_m = 0.279$, $\Omega_b = 0.046$, $n_s = 0.96$, $\sigma_8 = 0.817$ and $h = 0.701$.

This work is meant to outperform the dynamical range of previous weak lensing simulations: we need sub-arcminute precision and a field of view of a few degrees per side. We designed our LOS such that each pixel has an opening angle of 0.21 arcmin on each side, with Npix = 1024^2 pixels in total, for a total opening angle of 3.58° per side.

In order to reduce the wasted cosmological volume that falls outside the past light cone, we produced two sets of simulations, following the strategy of White and Hu [2000], which used 6 box sizes to z = 1. It would be computationally too expensive to run that many distinct volumes, but we find that two sizes offer a good trade off. High redshift ($z > 1.0$) volumes are produced from simulations with a comoving side of L = 231.1 h^{-1}Mpc, while the low redshift ones are L = 147.0 h^{-1}Mpc per side. These volumes are chosen such that the boundaries of the past light cone intersect with the edges of the smaller box exactly at z = 1 (in the given cosmology). The cone then enters the larger volume, and meets its boundary at z = 2.0 (see figure 5.1). Some of the outer ray bundles eventually leave the simulated volume at larger redshifts larger than 2.0, in which case we enforce the periodicity of the simulations. This situation applies only to the last four lenses, hence the total amount of repeated structures is very small. This is even further suppressed by the lensing kernel, which favors redshifts closer to z = 1, 1.5, and by the fact such high redshifts have fewer galaxies to start with.

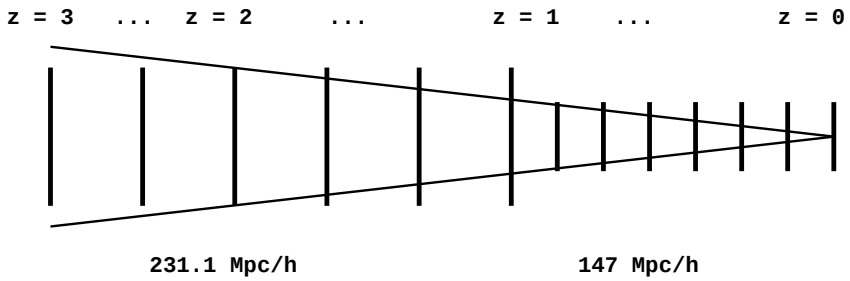

Figure 5.1: Geometry of the lines-of-sight. The global simulated volume consists of two adjacent rectangular prisms, collapsed as a series of thin lenses. As explained in the text, high redshift lenses have higher comoving volume, but the same number of grid cells, or pixels; this is meant to reduce the volume that falls outside of the past light cone. The observer sits at $z = 0$, from where we shoot the rays; $z = 1$ is the junction between the small (lower-z) and large (higher-z) simulation boxes; the past light cone escapes the simulated volume beyond $z = 2$, and we exploit the periodicity of the boundary condition to populate the edges of the most remote lenses and halo catalogues; we store lenses and halos up to $z = 3$.

With these choices of cosmological parameters and simulation volumes, the particle's mass in the large box (L = 231.1 h^{-1}Mpc) and small box (L = 147.0 h^{-1}Mpc) are 1.2759 $\times$ 10^9 and 3.2837 $\times$ 10^8 $M_\odot$, respectively.

The initial redshifts are selected such as to optimize both the run time and the accuracy of the N-body code. These are chosen to be z_i = 40.0 and 200.0 for the large and small box respectively. The reason for choosing different starting redshifts resides in the fact that the smaller box is probing smaller scales, hence it needs to start earlier, when the linear regime is valid. Each simulation is then evolved with `cubep3m`. At each of the lens redshifts tabulated in 5.1.1, the dark matter particles are placed onto an N^3 grid = 2048^3 grid. That grid is then collapsed in three different ways along each of the 3 Cartesian axes, producing triplets of slabs. These lens redshifts, z_ℓ, are found by slicing into cubes our simulated volume, starting and ending at z = 0.0 and z = 3.0, respectively, and solving for the redshift at the centre of the comoving box.

5.2 Discrete Convergence Equation

As mentioned previously, we approximate that the photon trajectories as straight lines, such that the integral of 3.28 can be performed pixel by pixel. We convert the integral over χ into a discrete sum at the lens locations $\chi(z_\ell)$. The infinitesimal element dχ becomes d$L/n_{\rm grid}$, where $n_{\rm grid}$ = 2048 and L = 147.0 or 231.1 h^{-1}Mpc, depending on the redshift of the lens. Under the single source plane approximation, we can thus write the convergence field κ as (Munshi et al. [2008])

$$\kappa(\boldsymbol{x}) = \frac{3H_0^2\Omega_{\rm m}}{2c^2}\sum_{z_\ell}^{z_{\rm s}} \delta_{\rm 2D}(\boldsymbol{x})(1+z_\ell)\chi(z_\ell)\left(1-\frac{\chi(z_\ell)}{\chi(z_{\rm s})}\right)d\chi, \tag{5.1}$$

where $\delta_{\rm 2D}(x)$ is the 2-D density contrast field. The shear components can be conveniently computed from κ, following the procedure of Kaiser and Squires [1993] which was explained in section 3.3. We emphasize that the Fourier transforms are non-local operations and must therefore be calculated on the full, periodic, simulated slab, before the interpolation onto the lenses. For this operation, we work under a flat sky approximation, which allows us to perform the Fourier transforms in the traditional plane wave basis. We then zoom into the cross-section of the light

Slice	z_ℓ	z_s	χ_l	χ_s
1	0.025	0.0494	73.5000	147.0
2	0.075	0.9999	220.5000	294.0
3	0.126	0.1515	367.5000	441.0
4	0.178	0.2045	514.5000	588.0
5	0.232	0.2589	661.5000	735.0
6	0.287	0.3149	808.5000	882.0
7	0.344	0.3727	955.5000	1029.0
8	0.402	0.4324	1102.5000	1176.0
9	0.463	0.4942	1249.5000	1323.0
10	0.526	0.5583	1396.5000	1470.0
11	0.591	0.6249	1543.5000	1617.0
12	0.659	0.6941	1690.5000	1764.0
13	0.730	0.7664	1837.5000	1911.0
14	0.804	0.8418	1984.5000	2058.0
15	0.881	0.9206	2131.5000	2205.0
16	0.961	1.0033	2278.5000	2352.0
17	1.071	1.1416	2467.5506	2583.1
18	1.215	1.2915	2698.6519	2814.2
19	1.371	0.4545	2929.7531	3045.3
20	1.542	1.6326	3160.8543	3276.4
21	1.728	1.8280	3391.9556	3507.5
22	1.933	2.0433	3623.0569	3738.6
23	2.159	2.2817	3854.1580	3969.7
24	2.411	2.5467	4085.2593	4200.8
25	2.691	2.8429	4316.3605	4431.9
26	3.004	3.1757	4547.4618	4663.0

Table 5.1: Redshifts of the lenses z_ℓ. The projections for $z > 1.0$ are produced with L=231.1 h^{-1}Mpc simulations, while those for lower z are obtained from L = 147.0 h^{-1}Mpc$/h$, as described in the text. The table lists the corresponding source redshift and the comoving distances for every lens and source plane for each simulation box.

cone and the simulation slab and interpolate the region to a 1024^2 grid.

5.3 Test I: Power Spectra

In this section, we quantify the accuracy of the weak lensing simulations. We first measure the matter density power spectrum of the simulated three dimensional density fields, i.e. before the collapse and pixel interpolation, and compare to the non-linear theoretical predictions of CAMB (Seljak and Zaldarriaga [1996], Lewis et al. [2000]). We then estimate the convergence power spectrum of the simulated lines of sight, compare to non-linear predictions, and extract the effective resolution of the simulated fields.

5.3.1 Matter Power Spectrum $\mathbf{P}_\delta$

The power spectrum of matter density $P(k)$ is a fast and informative test of the quality of the simulations. It probes the growth of structures at all scales available within the simulations, and comparison with reliable theoretical models informs us of the accuracy and the resolution limit. For a given over-density field $\delta(\boldsymbol{x})$, the power spectrum can be calculated from its Fourier transform $(\boldsymbol{k})$ as described previously by equation 2.21.

In our simulations, the grid is discrete, so are the Fourier modes, and the volume average turns into an angle average. We extract the power spectrum for our 185 simulations at two redshifts, $z = 0.961$ and $z = 0.025$, and present the results in figure 5.2. The error bars are the 1σ deviations from the mean. We observe from this figure that the simulations seem to model well the structures at least down to $k = 20.0\ h$/Mpc, which corresponds to a comoving length of about 315 h^{-1}kpc.

In the linear theory of structure formation, different Fourier modes of the matter density grow independently, such that the error bars on the power spectrum are well described by Gaussian statistics. For non-linear scales, however, the phases of different Fourier modes start to couple together (Meiksin and White [1999], Coles and Chiang [2000] and Chiang et al. [2002]), hence the two-point function no longer contains all the information about the fields. Higher order statistics, i.e. bispectrum and trispectrum, are then needed in order to improve the calculations, but simulations do provide the most accurate estimates, provided convergence is

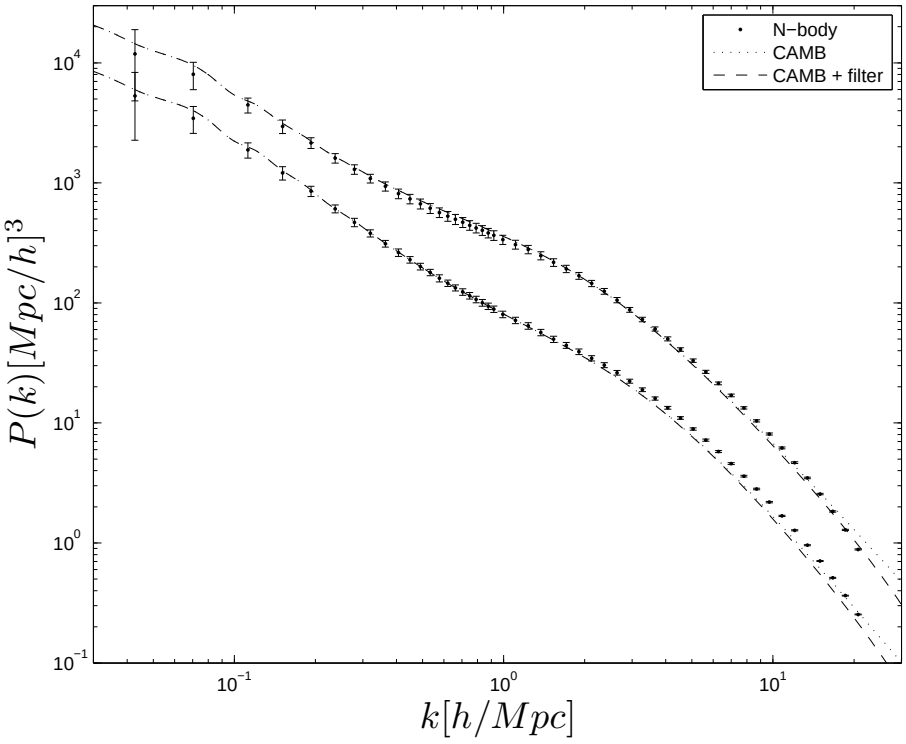

Figure 5.2: Power spectrum of 185 N-Body simulations, at redshifts of 0.961 (bottom curve) and 0.025 (top curve). The solid and dashed lines are the non-linear predictions, with and without the Gaussian filter. The error bars shown here are the standard deviation over our sampling. We observe a slight overestimate of power in the simulations for scales smaller than k = 3.0 h/Mpc.

achieved.

The power spectrum covariance matrix is defined as

$$C(k,k') = \langle P(k)\bar{P}(k)\rangle\langle P(k')\bar{P}(k')\rangle, \tag{5.2}$$

where $\bar{P}(k)$ refers to the best estimate of the mean and k,k' are the wave-vectors. The amount of correlation between different scales is better visualized with the cross-correlation coefficient matrix, which is obtained from $C(k,k')$ via

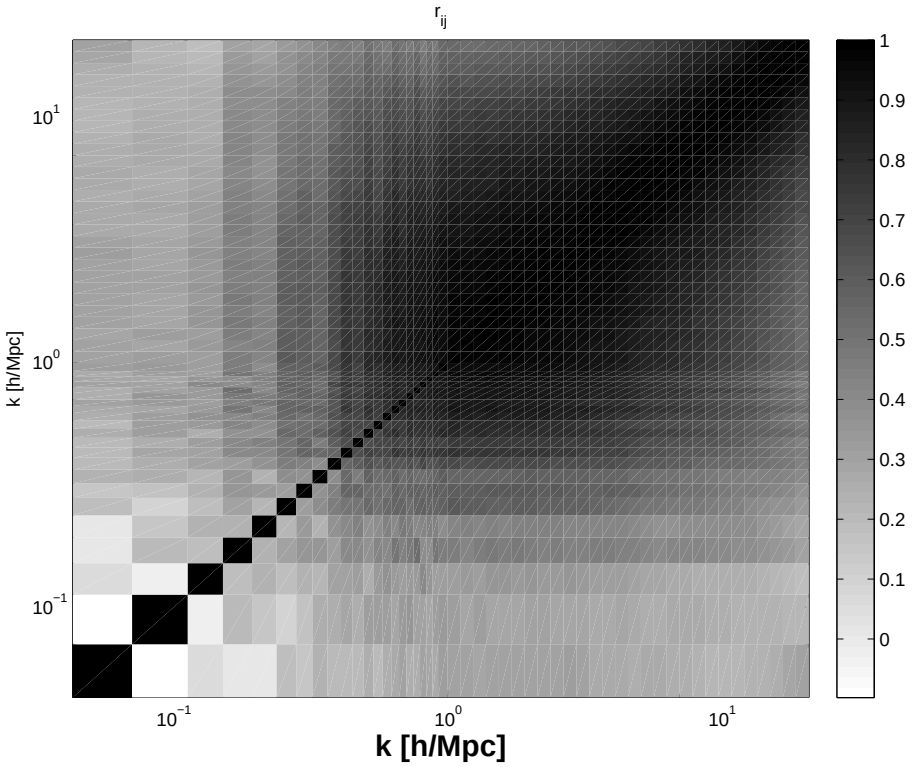

Figure 5.3: The correlation coefficient matrix of the density power spectrum, measured from of 185 N-Body simulations, at redshift of 0.961. Modes at $k \sim 0.5\ h/\mathrm{Mpc}$, corresponding to $\theta \sim 18'$, are more than 40% correlated.

$$\rho(k,k') = \frac{C(k,k')}{\sqrt{C(k,k)C(k',k')}}, \tag{5.3}$$

and is shown for $z = 0.961$ in figure 5.3. We see that it is almost diagonal at larger scales (lower k), while measurements become correlated as we progress towards smaller scales (higher k). This effect occurs at even larger scales for smaller redshifts, since the fields had more time to grow non-linear structures. At $k \approx 0.5$ h/Mpc, for instance, the Fourier modes are intrinsically more that 40% correlated. This corresponds to an angle of $\theta \approx 18$' on the sky, and $\ell \approx 1200$.

5.3.2 Convergence Power Spectrum $\mathbf{P}_\kappa$

In order to quantify the resolution of our lensing maps, we measure the angular power spectrum of the κ field, and compare the results with the non-linear predictions from `CAMB` (Seljak and Zaldarriaga [1996]; Lewis et al. [2000]). The power spectrum of the convergence field $\kappa(\theta)$ is defined as

$$\langle \kappa(\boldsymbol{\ell_1})\kappa(\boldsymbol{\ell_2})\rangle = (2\pi)^2\delta_D(\boldsymbol{\ell_1}+\boldsymbol{\ell_2})P_\kappa(\ell_1), \tag{5.4}$$

where $\boldsymbol{\ell}$ is the Fourier component corresponding to the real space vector $\boldsymbol{\theta}$ and again, the angle brackets refer to angle averages. The convergence power spectrum, estimated from our simulations, is shown in figure 5.4, where the error bars are the 1σ standard deviation. A note to the reader that $P_\kappa(\ell)$ and $C_\kappa(\ell)$ have been used interchangeably to represent the convergence power spectrum P_κ. It is presented in the dimensionless form, i.e. $\ell(\ell+1)/(2\pi)C_\kappa(\ell)$, which has the advantage of showing clearly which angles are probing the linear regime (dimensionless power much less than unity) and which ones probe non-linear structures. We observe that modes with $\ell < 1000$ have power less than 0.1, which is a good indicator that linear theory still holds, and that these multipoles are reasonably well described by Gaussian statistics.

When compared to the non-linear theoretical model, we find good agreement in the linear regime, while the theoretical predictions slightly underestimate the power for $\ell > 1000$, consistent with the observations of Hilbert et al. [2009]. The strong drop at $\ell \sim 30,000$ is caused by limitations in the resolution, which corresponds to an angle of about $0.7'$.

As mentioned earlier, the smallest angles of weak lensing observations are probing the non-linear regime of the underlying density field, and it is known that the statistics describing the uncertainty in the weak lensing power spectrum are non-Gaussian (Doré et al. [2009]). Although most of the departures from Gaussianity are currently lost in the observation noise, future lensing surveys are expected to bring this noise down, such that non-Gaussian statistics will play an increasingly important role. The non-linear dynamics effectively correlate the error bars on small scales, an effect that can be visualized from the cross-correlation coefficient matrix of the angular power spectrum, shown in figure 5.5. As expected, we

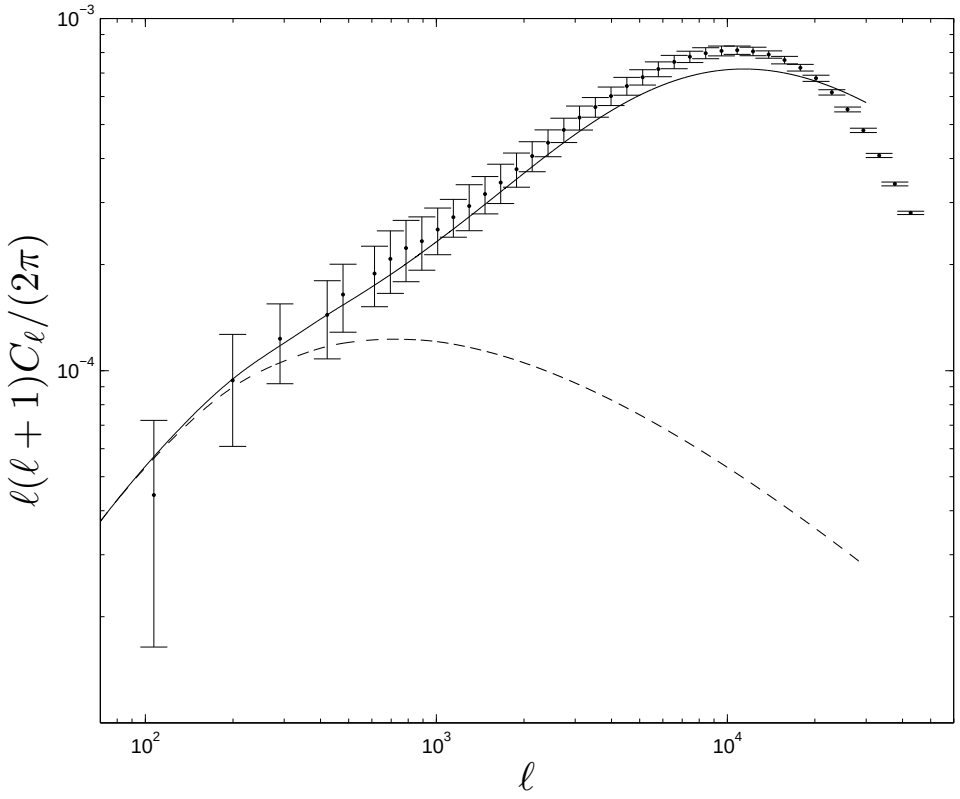

Figure 5.4: Convergence power spectrum, measured from 185 N-Body simulations, where the source plane is a Dirac delta function placed at $z = 3$. The solid line is the non-linear prediction (based on `CAMB` [Lewis et al., 2000] with `halofit` modifications from [Smith et al., 2003]), and the error bars are the 1σ standard deviation over our sampling. We observe a slight over-estimate of power in the simulations for $\ell > 1000$ compared to non-linear predictions (solid line), which is also visible in the smallest scales of the three dimensional dark matter power spectrum (i.e. figure 5.2). The linear predictions are represented by the dashed line.

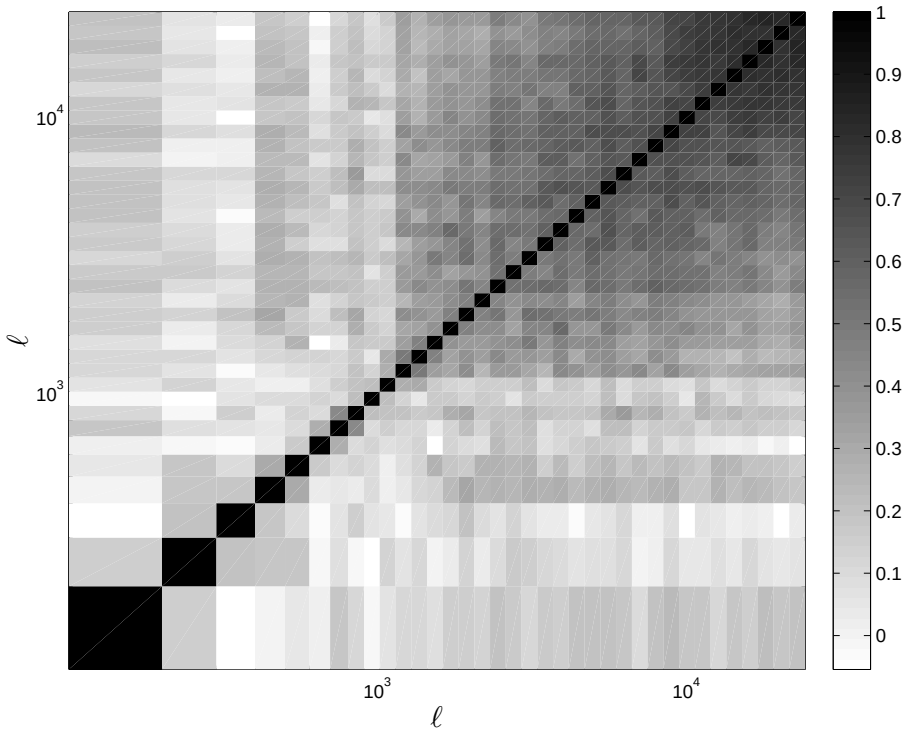

Figure 5.5: The correlation coefficient matrix of the convergence power spectrum, measured from 185 LOS. As for most calculations in this chapter, the source plane is placed at a redshift of $z = 3.004$.

observe that all the multipoles with $\ell > 1000$ are more than 40% correlated, while lower multipoles, probing mostly larger scales, are much less correlated.

5.4 Test II: Two-point Functions

The two-point functions of the lensing field provide a wealth of information about many cosmological parameters, and precise measurements of the lensing power spectrum. Different statistical estimators and filtering techniques are sensitive to different scales, systematics and secondary effects, and generally correlate scales in a unique way [Vafaei et al., 2010]. Hence the optimal approach for measurements involving cosmic shear and convergence really depends on the observation and the

parameters investigated.

To mimic the shear and convergence detection from a galaxy survey, we Poisson sample each of the maps with $100,000$ random points and construct mock catalogues. The object positions are assigned randomly within the area of 12.84 deg^2 from which the shear and convergence values are extracted.

In this section we show a series of plots for nine selected redshift slices, ranging from low to medium to high redshifts. Each plot contains results from some particular lensing statistic compared to theoretical predictions, as explained in section 4.6. We follow these plots with the correlation coefficient matrix for two of the redshift choices to indicate the level of correlation between the scales for that particular statistic. The shear and convergence statistics are listed in order of appearance below:

- **Shear Two-point Correlation Function**: The shear two-point correlation function (see section 4.1) is a strong indicator of cosmic shear signal. In the absence of lensing the two-point shear correlation function averages to zero, hence a positive signal indicates a detection of cosmic shear. Here we compute the tangential and rotated shear correlation functions on the noise-free simulations (equations 4.4 and 4.5). Figure 5.6 shows ξ_{tt}, and figure 5.8 shows the ξ_{rr} measurement in comparison to the theoretical predictions for 9 selected redshift slices. The error bars represent the 1σ deviation between 185 lines of sight for a single 12.84 deg^2 map. The agreement between the simulations and the theoretical predictions is well within the error bars, which allows us to conclude that the signal is well resolved, at least down to one arcmin. We next show, in figure 5.7, the cross-correlation coefficient matrices related to the ξ_{tt} measurements, for source redshifts of 3.0 (top) and 1.0 (bottom). These show that the error bars are at least 50% correlated for the highest redshift, and up to 80% for lower redshift sources. Figure 5.9 shows the ξ_{rr} counterpart, which also shows strong correlation.

- **The Shear E/B Decomposition**: We previously defined the E/B decomposition in section 4.4. These statistics are widely believed to be the most robust check of systematics [Crittenden et al., 2002]. For our simulations, we checked that the ξ_{BB} is consistent with zero, while the ξ_{EE} measurements

are shown in figure 5.10. Again, we observe a good agreement with the theoretical predictions. These error bars are also correlated by at least 50%, and even stronger for bins closer to the diagonal, as seen in figure 5.11 for z=1.0 and z=3.0.

- **Convergence Two-point Correlation Function**: Following the procedure of the shear fields, we calculate the two-point $\kappa - \kappa$ correlation function and power-spectrum from the convergence mock catalogues. Equation 4.6 shows the definition of the two-point convergence correlation function $\xi_{\kappa\kappa}$. In figure 5.12, we present the measured two-point convergence correlation function along with the theoretical prediction, as a function of separation angle θ. The agreement extends well below the arcminute scale, at all redshifts. The cross-correlation coefficient matrices corresponding to these measurements are presented in figure 5.13.

- **Window Integrated Shear Correlation Function (Top-hat)**: Section 4.2 explained the link between the integration of correlation functions with certain filters to the matter power spectrum. One advantage of the top-hat filter is that it probes scales as large as the field of view. We compare our measurements from the simulations with non-linear predictions in figure 5.14, as a function of the opening angle of the top-hat filter. We find good agreement at all redshifts, although lower redshifts exhibit a small bias. The cross-correlation matrices are presented in figure 5.15 and show that there is a strong correlation between most measurements.

- **Window Integrated Shear Correlation Function (Aperture)**: In section 4.3 we discussed the aperture mass filter statistics in details. Here we show the results of computing the aperture mass variance through correlation functions on the simulated mock catalogues that originated from our numerical simulations. We present in figure 5.16 our measurements of $\langle M_{\rm ap}^2 \rangle$ from the simulations, as a function of smoothing scale θ. Here the choice of aperture filter [Schneider et al., 1998] is taken as the compensated filter and not the compensated Gaussian. We observe that for redshifts larger than one, the agreement extends down to an arcminute, whereas lower redshifts suffer

from a lack of variance at angles of a few arcminutes. This is caused by limitations in the resolution due to strong zooming from the simulation grid onto the pixel map. This effect is also expected from the top-hat variance, but appears at much smaller angles. We recall that an aperture mass is constructed with a compensated filter, which has a strong damping tail, hence for an opening angle θ, it is really sensitive to smaller scales $\sim \theta/5$. The cross-correlation coefficient matrices are presented in figure 5.17.

- **Window Statistics on Convergence Maps (Top-hat and Aperture Mass)**: Aside from the mock galaxy catalogues, we test the accuracy of the simulations on the maps directly. We smooth the κ-maps with filters identical to those used before (top-hat and aperture) and calculate the variance and third moment of the convergence field on the smoothed maps. Section 4.5 explains this process in more detail. We present the second moments of κ in figures 5.18 and 5.20, comparing with the predictions, for the aperture and top-hat filters, respectively. The third moment for aperture and top-hat filters follow in figures 5.22 and 5.24. Also the correlation coefficient matrices for two selected redshift slices for the second moment top-hat and aperture are shown in figures 5.19 and 5.21, while figure 5.23 and 5.25 demonstrate the correlation coefficient matrices for the third moment case.

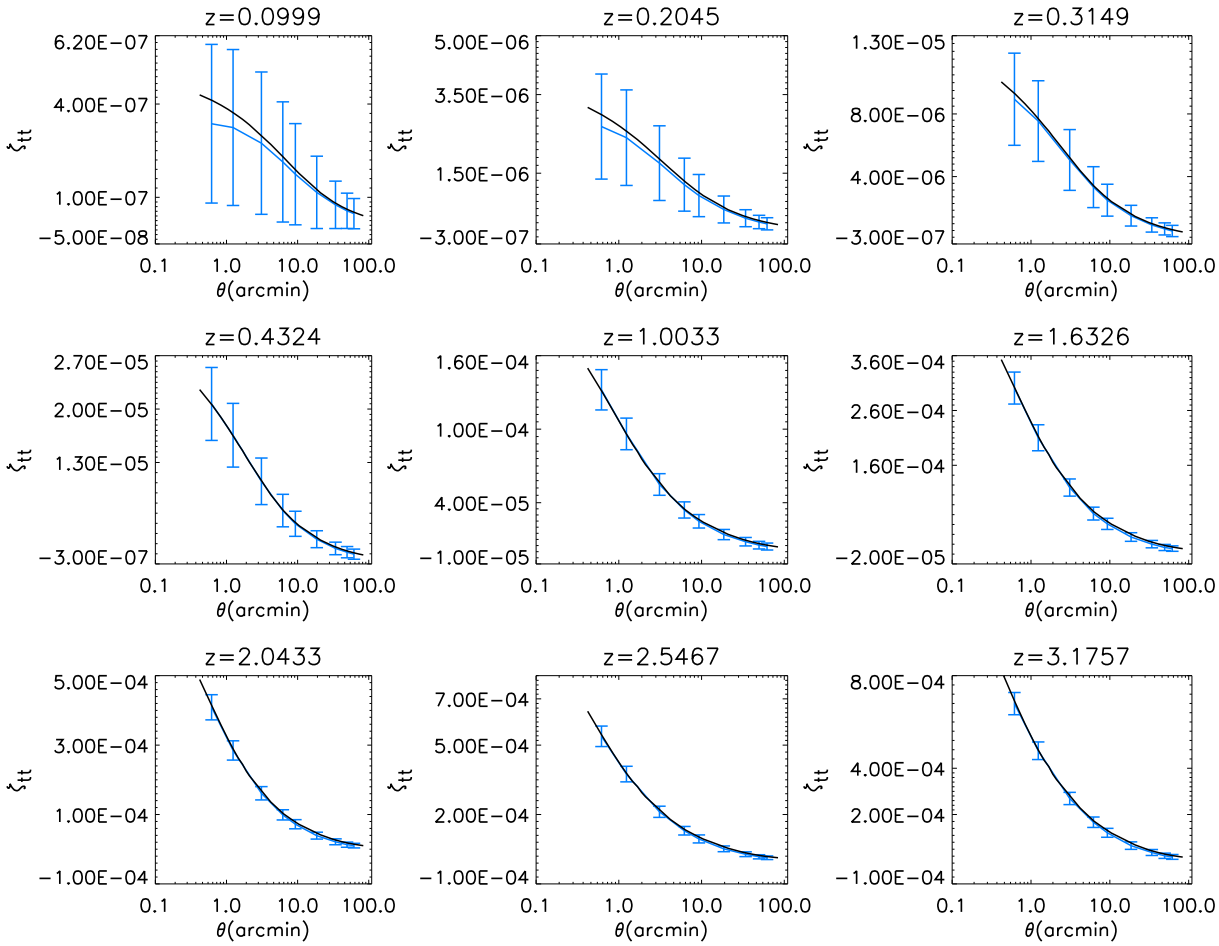

Figure 5.6: The blue line shows the measurement of the shear correlation function ξ_{tt} component from 185 simulated lines of sight. The error bars represent the variance between the lines of sight for a single 12.84 deg^2 map. The black line shows the theoretical prediction for the input cosmology of the simulations.

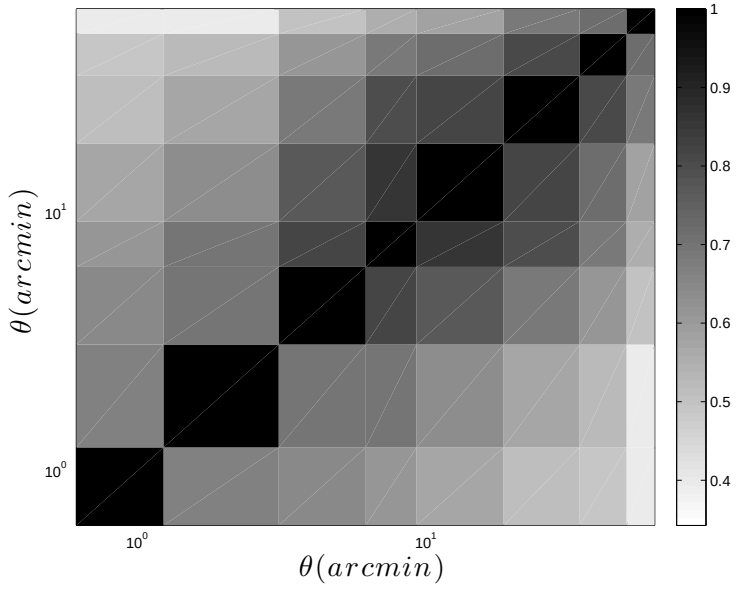

(a)

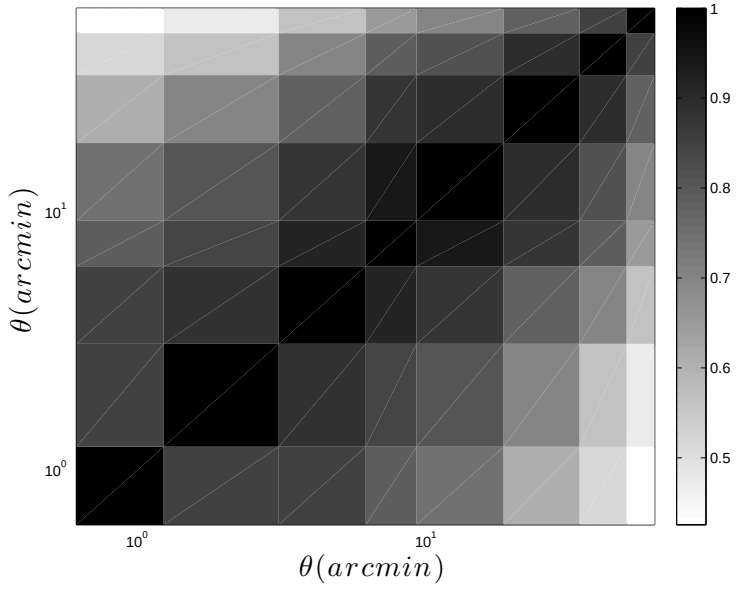

(b)

Figure 5.7: Cross-correlation coefficient matrix of the ξ_{tt} two-point function, with the source plane at $z \sim 3.0$ (top) and $z \sim 1.0$ (bottom).

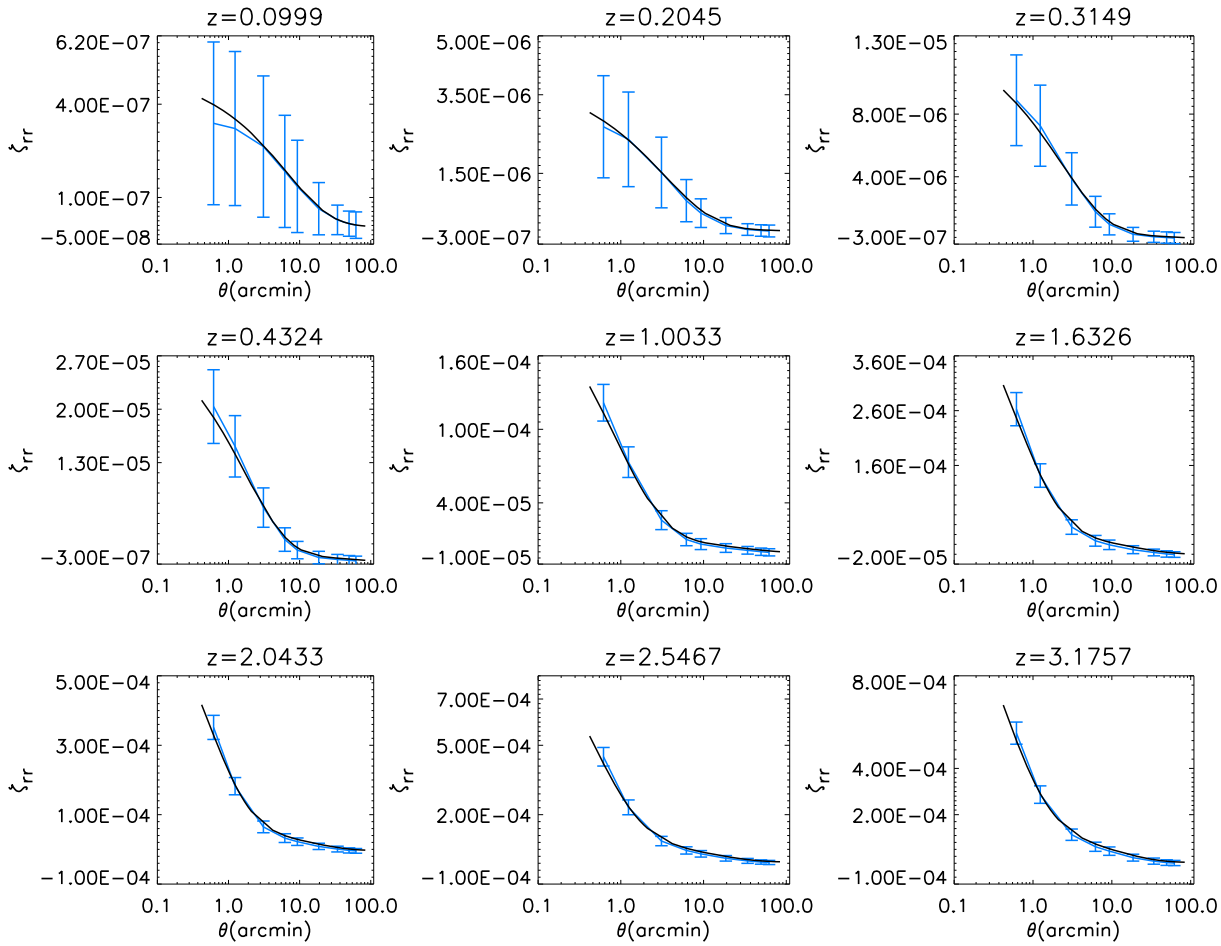

Figure 5.8: The shear correlation function ξ_{rr} component.

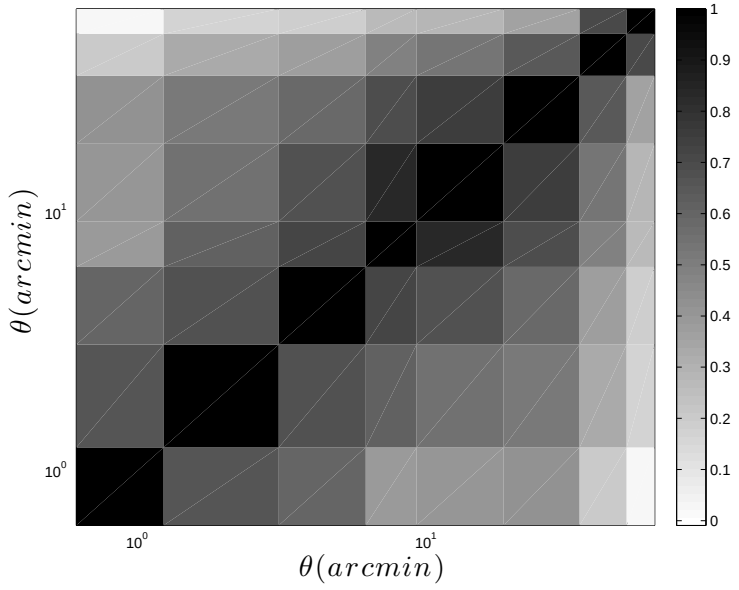

(a)

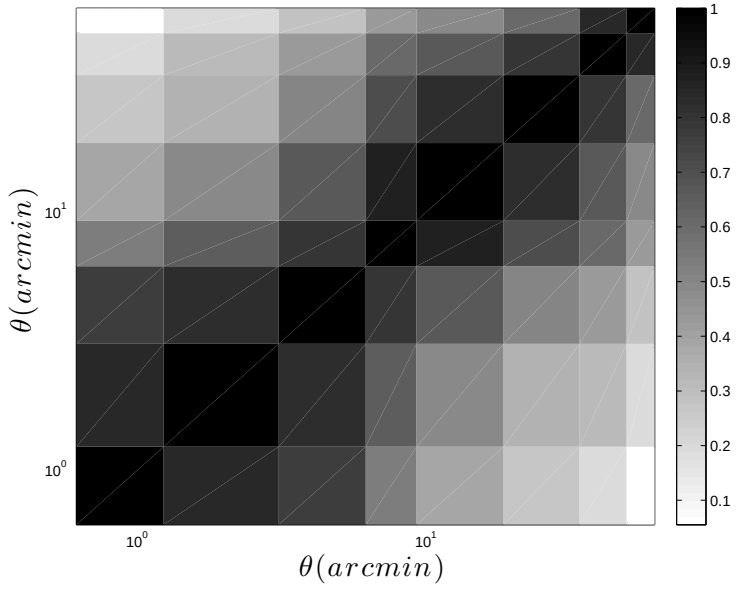

(b)

Figure 5.9: Cross-correlation coefficient matrix of the $\xi_{\rm rr}$ two-point function, with the source plane at $z \sim 3.0$ (top) and $z \sim 1.0$ (bottom).

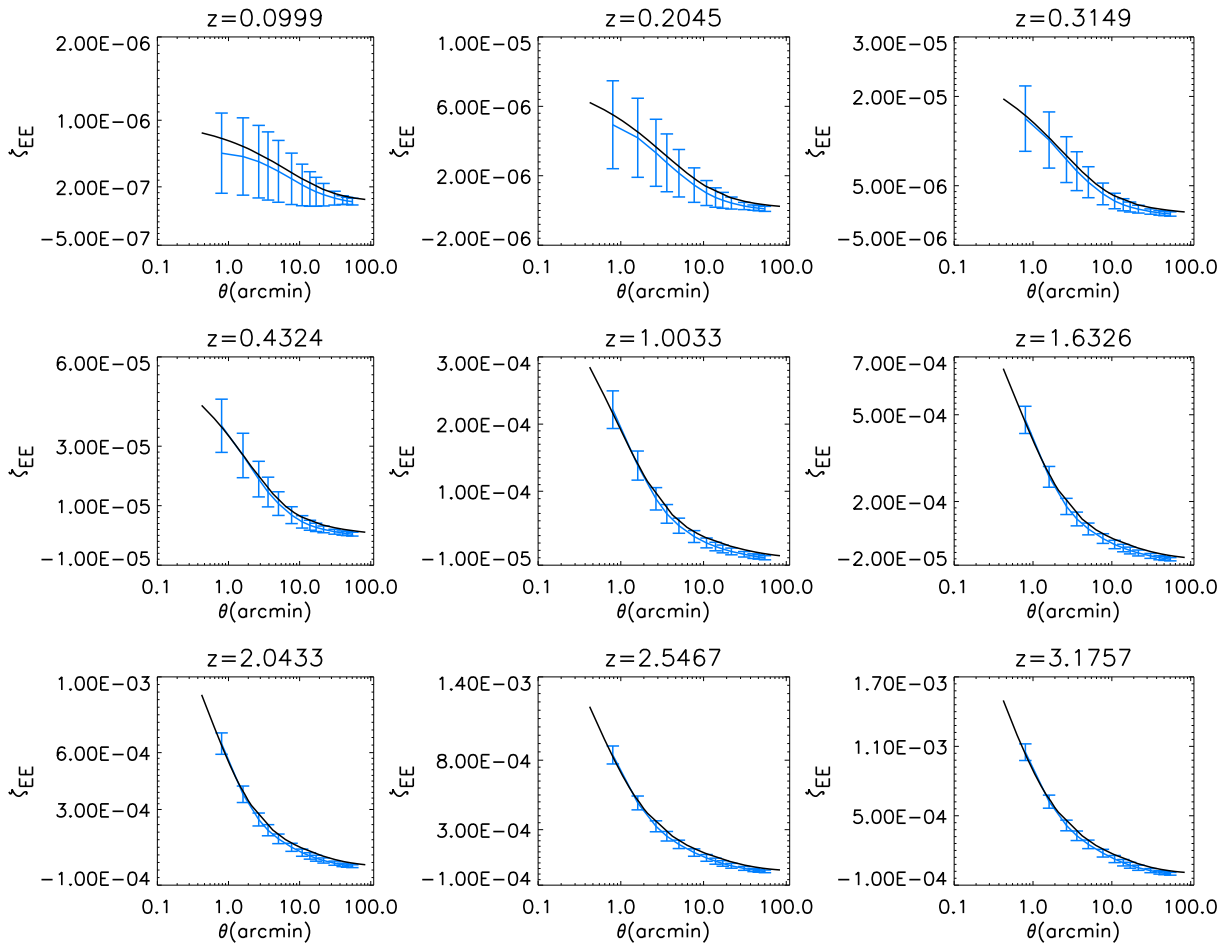

Figure 5.10: The ξ_{EE} measured from shear maps. Error bars are 1σ deviation from 185 lines of sight for a single 12.84 deg^2 map.

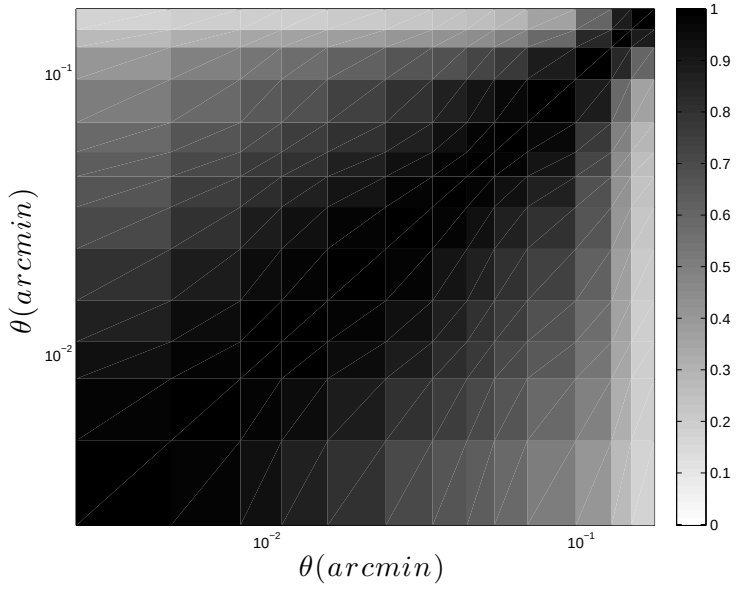

(a)

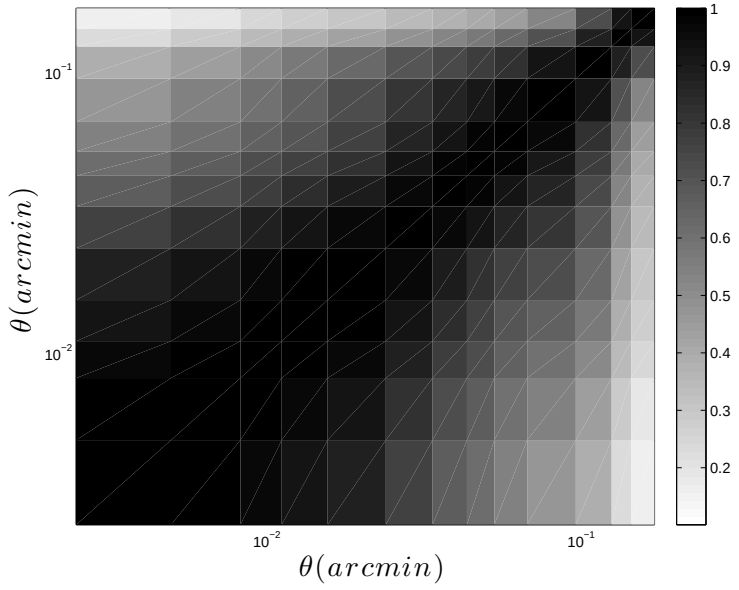

(b)

Figure 5.11: The cross-correlation coefficient matrix of the ξ_{EE} two-point function, with the source plane at $z \sim 3.0$ (top) and $z \sim 1.0$ (bottom).

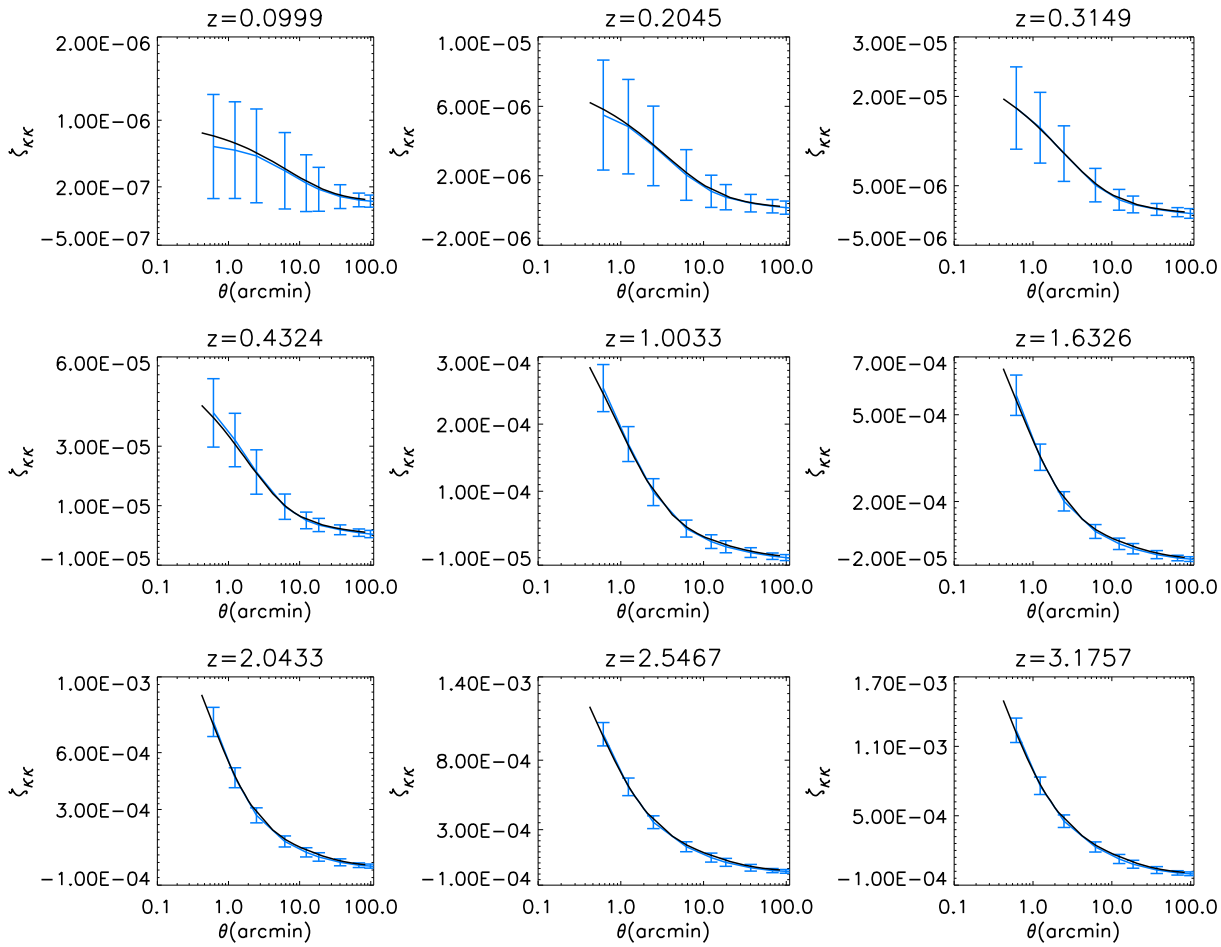

Figure 5.12: The convergence correlation function $\xi_{\kappa\kappa}$. The error bars are the 1σ standard deviation in the sampling of our 185 realizations for a single 12.84 deg^2 map.

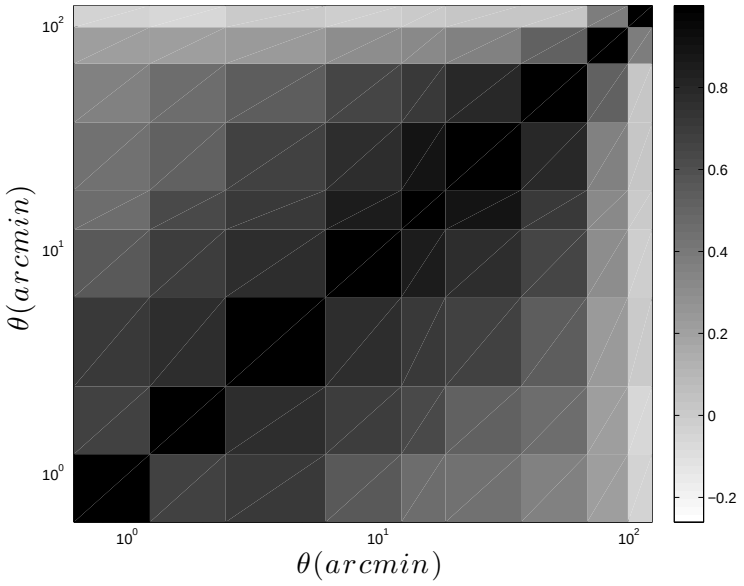

(a)

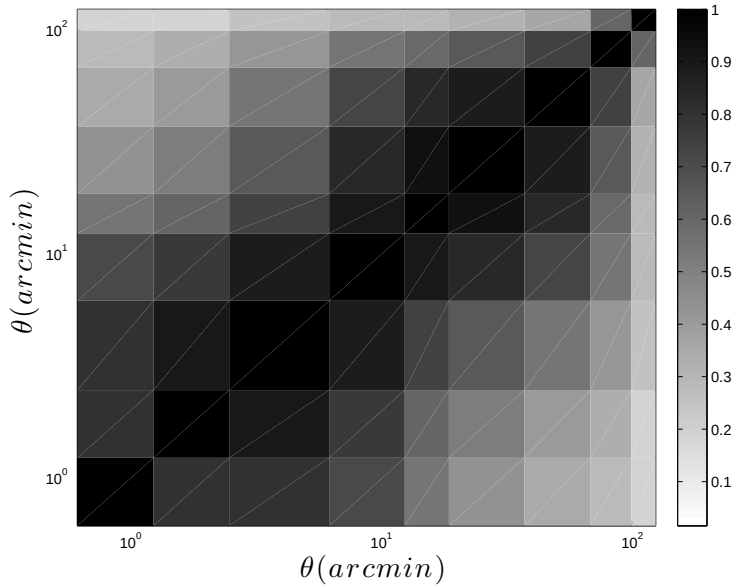

(b)

Figure 5.13: The cross-correlation coefficient matrix of the convergence two-point function $\xi_{\kappa\kappa}$, with the source plane at $z \sim 3.0$ (top) and $z \sim 1.0$ (bottom).

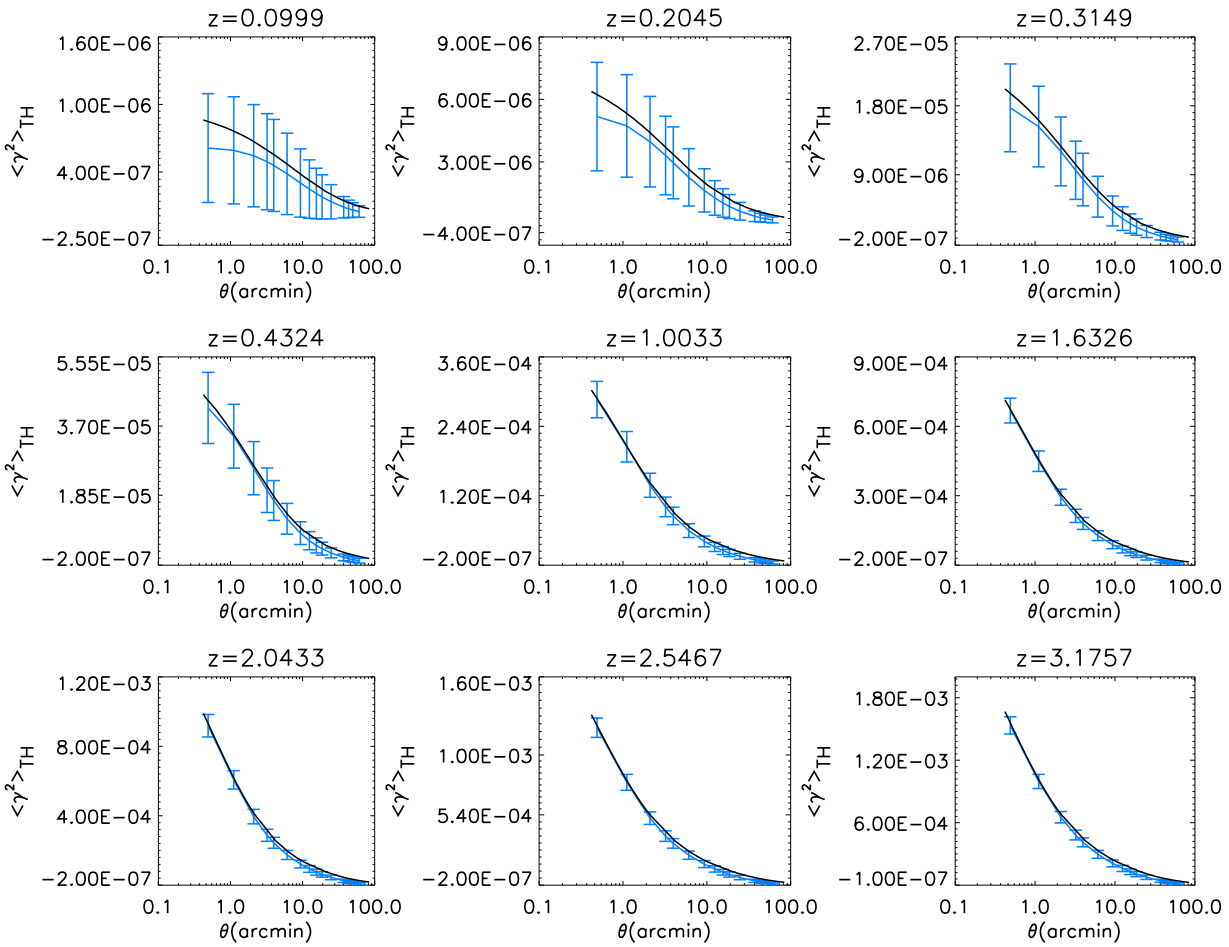

Figure 5.14: top-hat variance, $\langle|\overline{\gamma}|^2\rangle$ measured from shear mock catalogues through the integrated correlation function. The calculations are done based on integrating the correlation function with top-hat related functions.

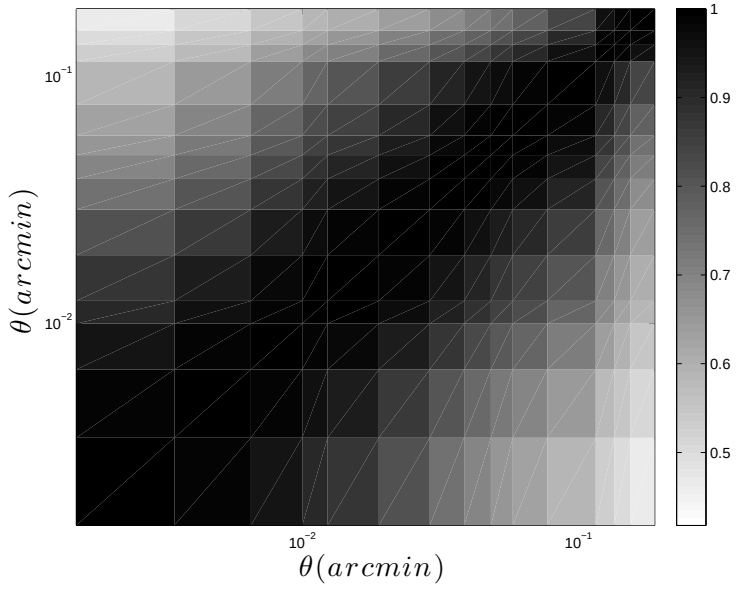

(a)

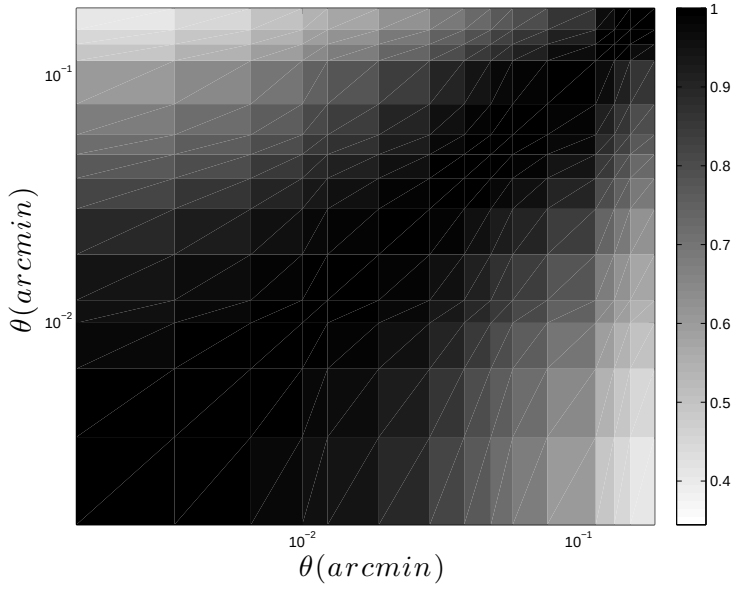

(b)

Figure 5.15: The cross-correlation coefficient matrix of the top-hat variance, with the source plane at $z \sim 3.0$ (top) and $z \sim 1.0$ (bottom).

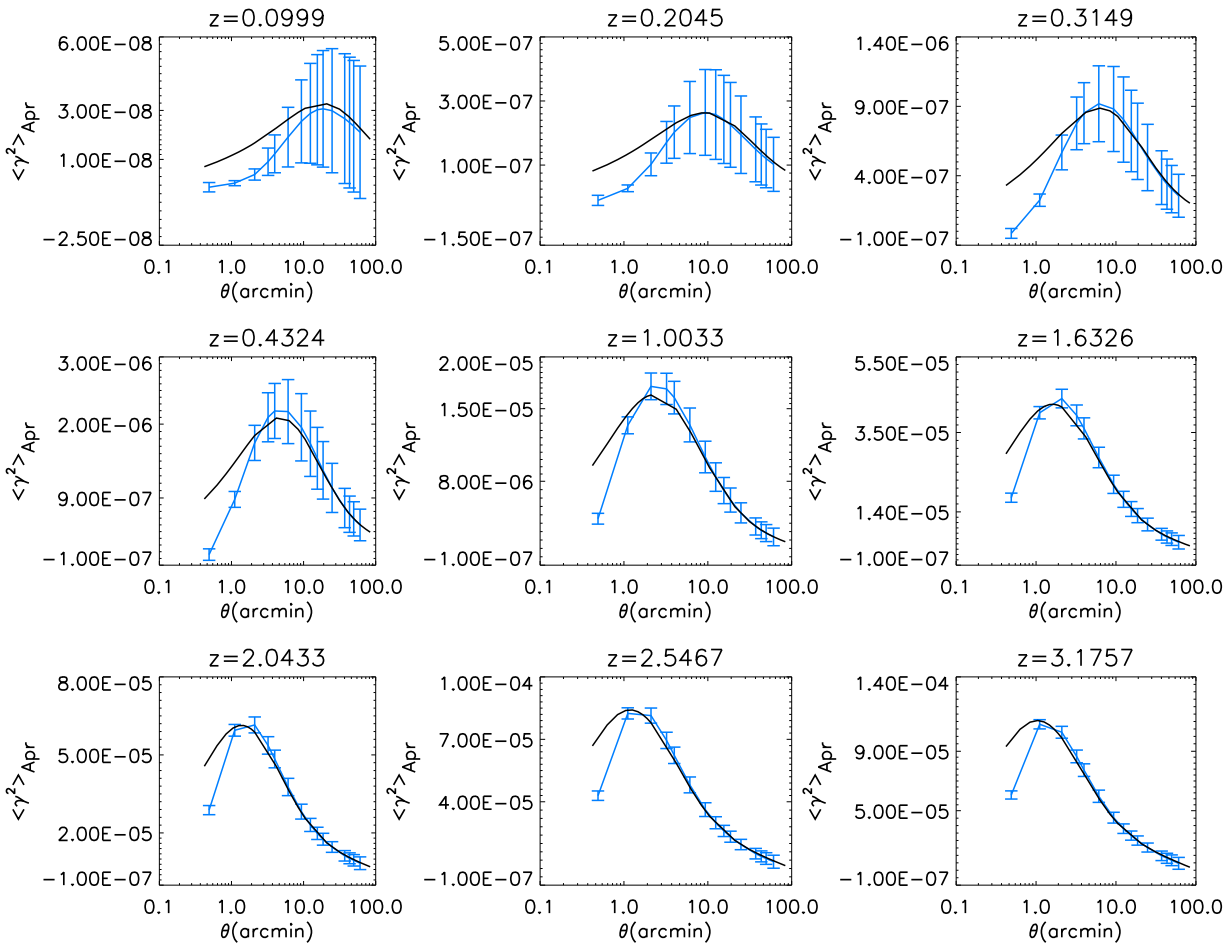

Figure 5.16: The integrated correlation function $\langle M_{\rm ap}^2 \rangle$ measured from shear catalogues. The choice of filter is that of Schneider et al. [1998].

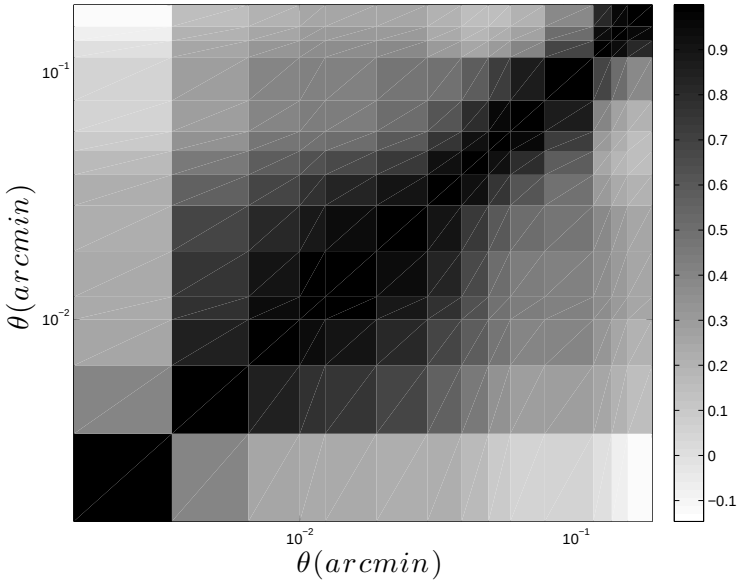

(a)

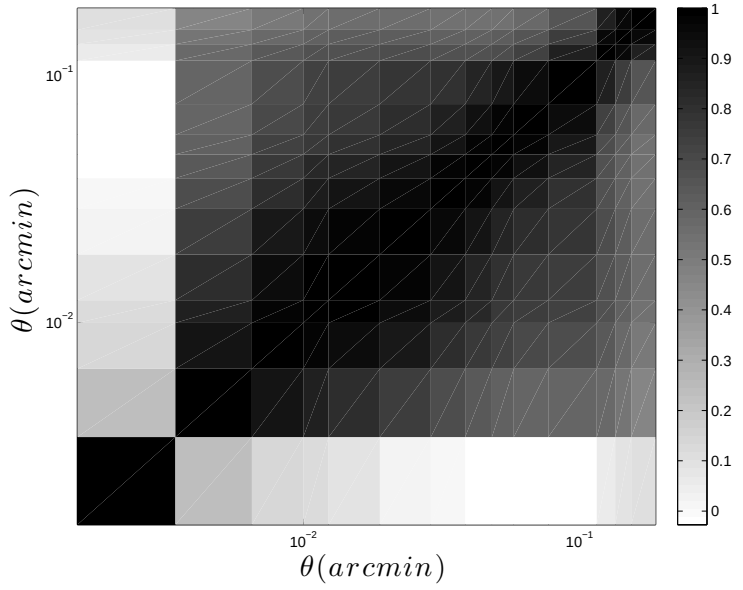

(b)

Figure 5.17: Cross-correlation coefficient matrix of the aperture mass variance, with the source plane at $z \sim 3.0$ (top) and $z \sim 1.0$ (bottom).

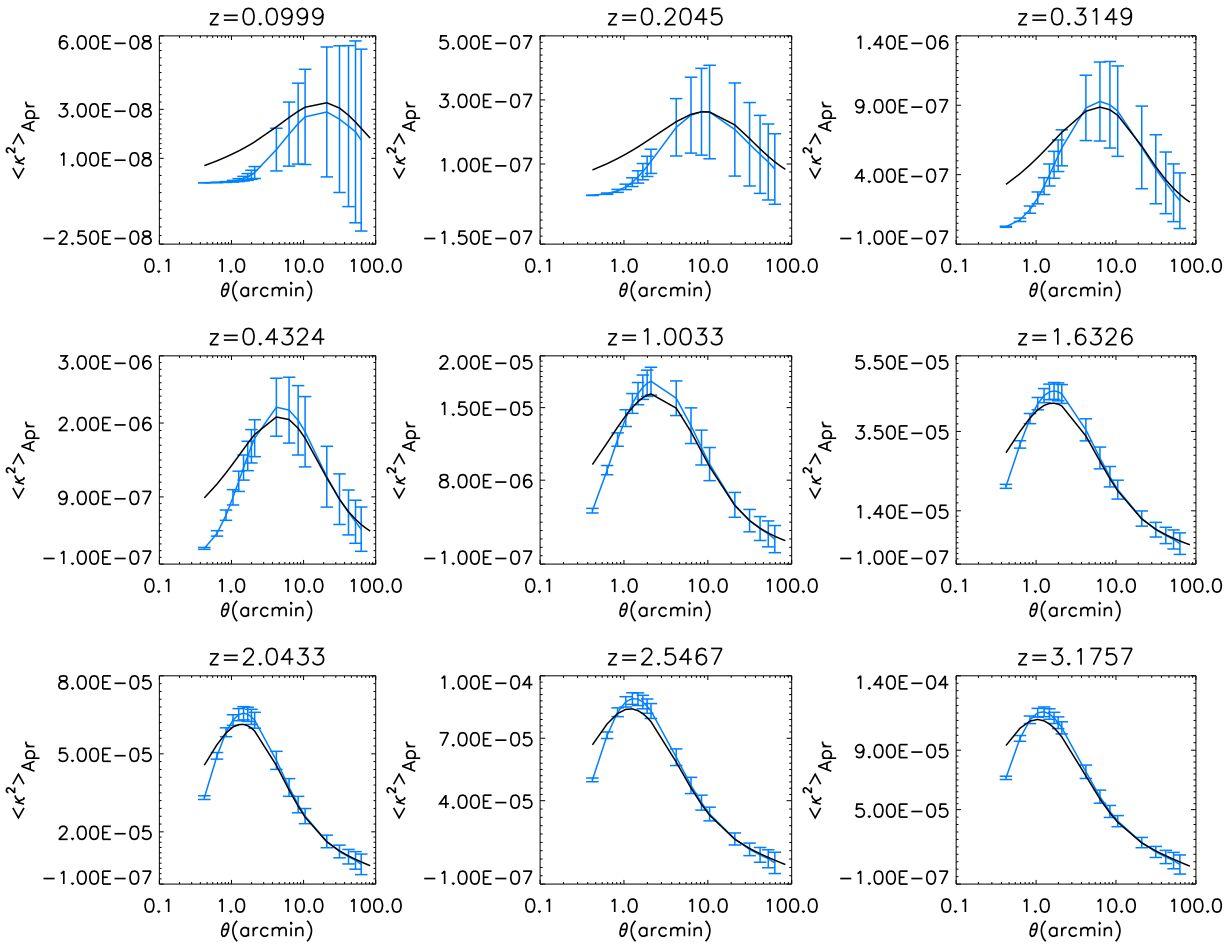

Figure 5.18: The $\langle\kappa^2\rangle$ estimate for convergence κ-maps smoothed with aperture mass filter.

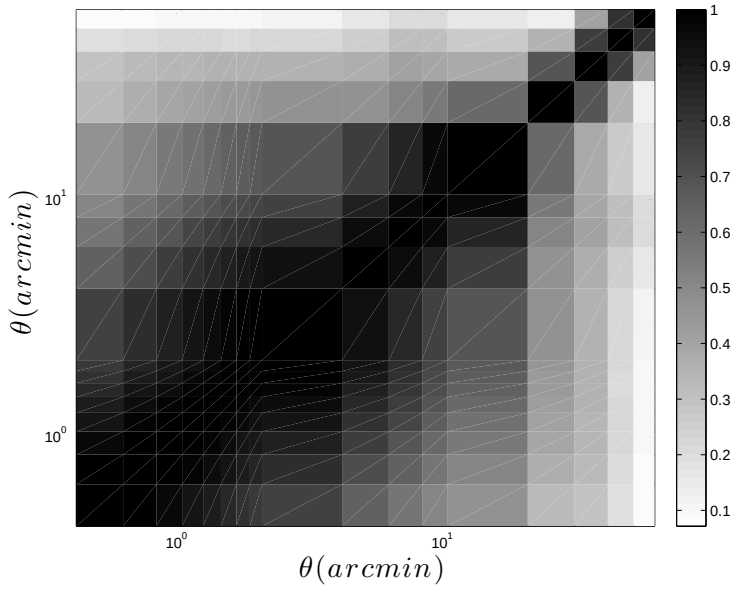

(a)

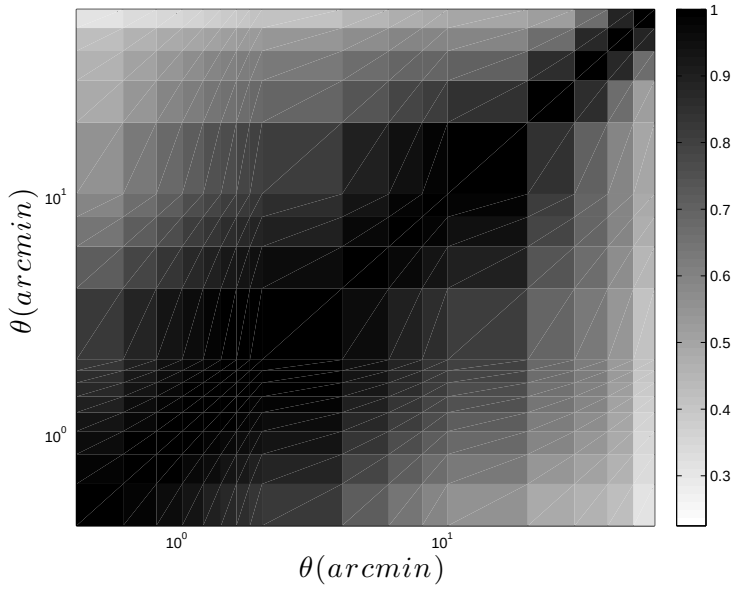

(b)

Figure 5.19: The cross-correlation coefficient matrix of the second moment of convergence maps smoothed with the aperture filter, with the source plane at $z \sim 3.0$ (top) and $z \sim 1.0$ (bottom).

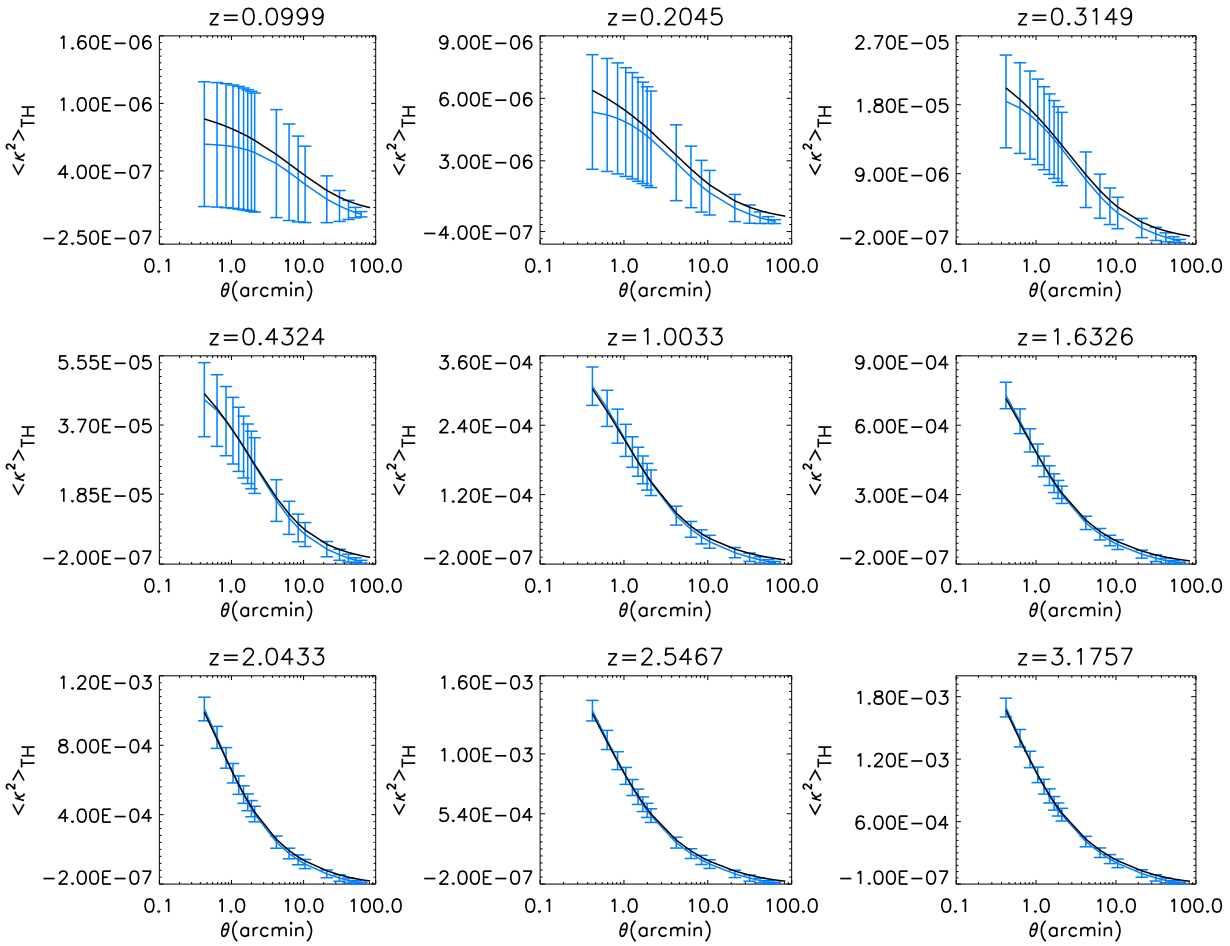

Figure 5.20: The $\langle \kappa^2 \rangle$ estimate for convergence κ-maps smoothed with a top-hat filter.

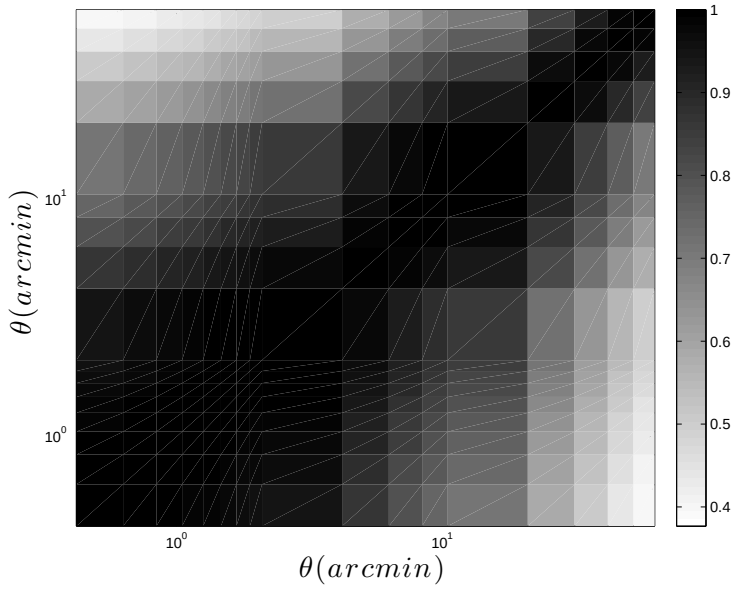

(a)

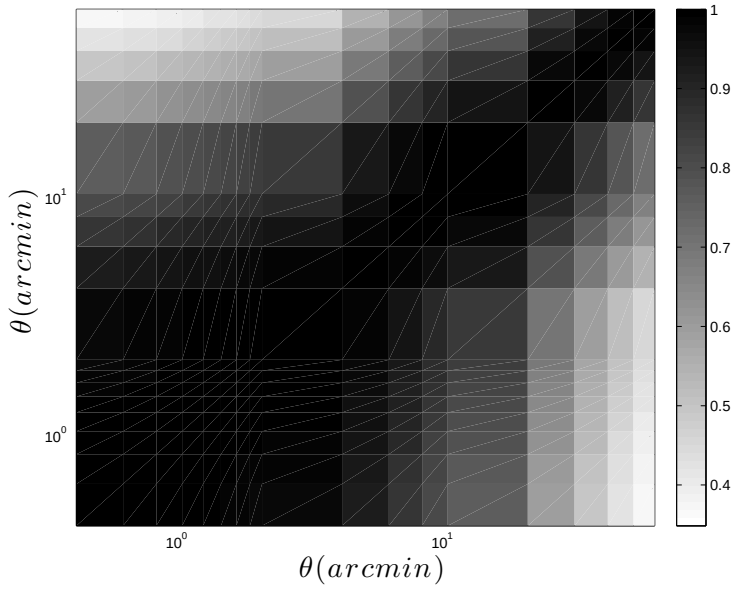

(b)

Figure 5.21: The cross-correlation coefficient matrix of the second moment of convergence maps smoothed with a top-hat filter, with the source plane at $z \sim 3.0$ (top) and $z \sim 1.0$ (bottom).

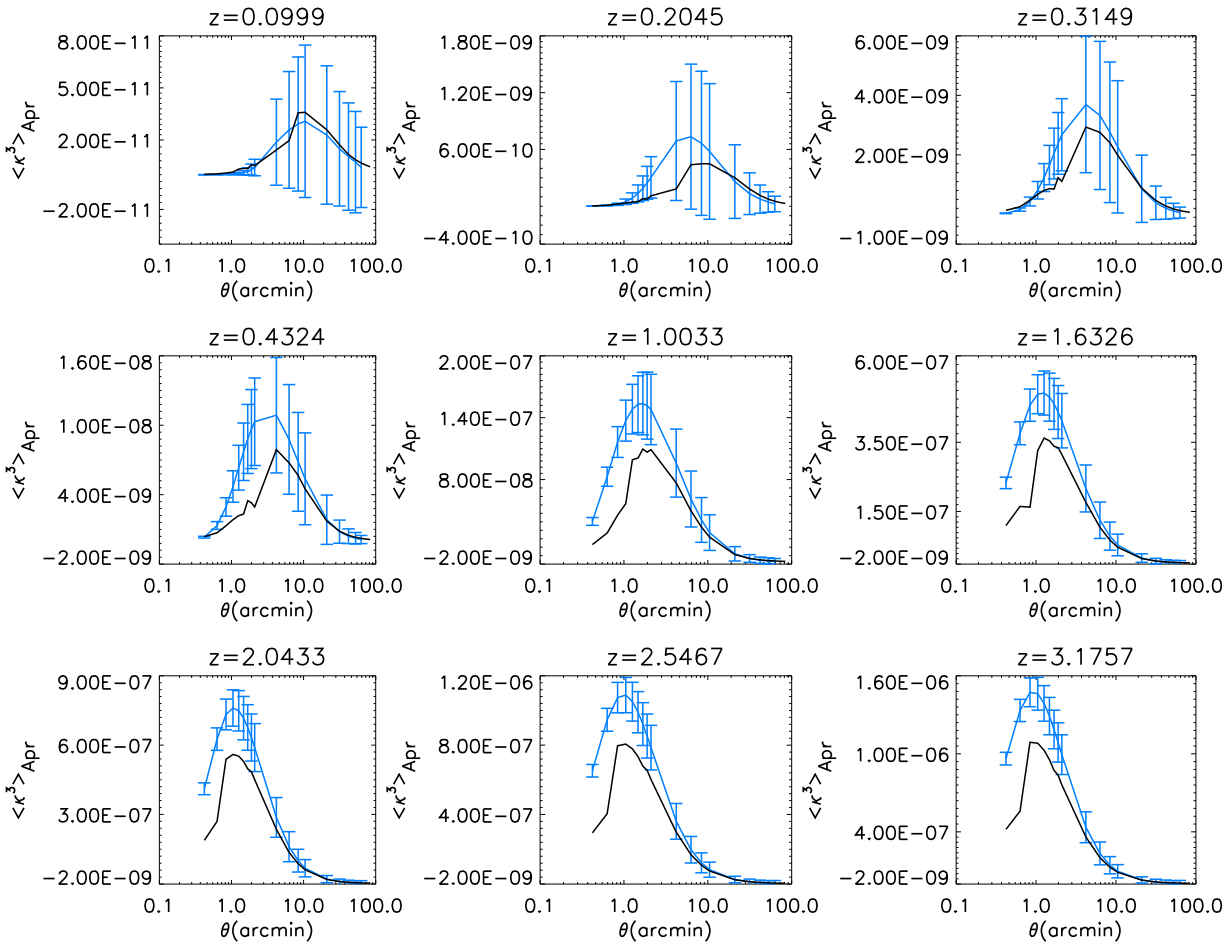

Figure 5.22: The $\langle\kappa^3\rangle$ estimate for convergence κ-maps smoothed with the aperture mass filter.

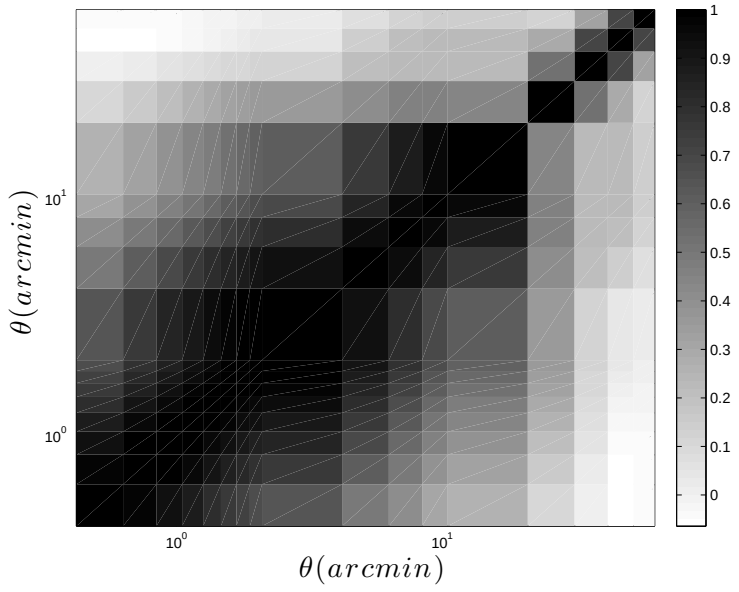

(a)

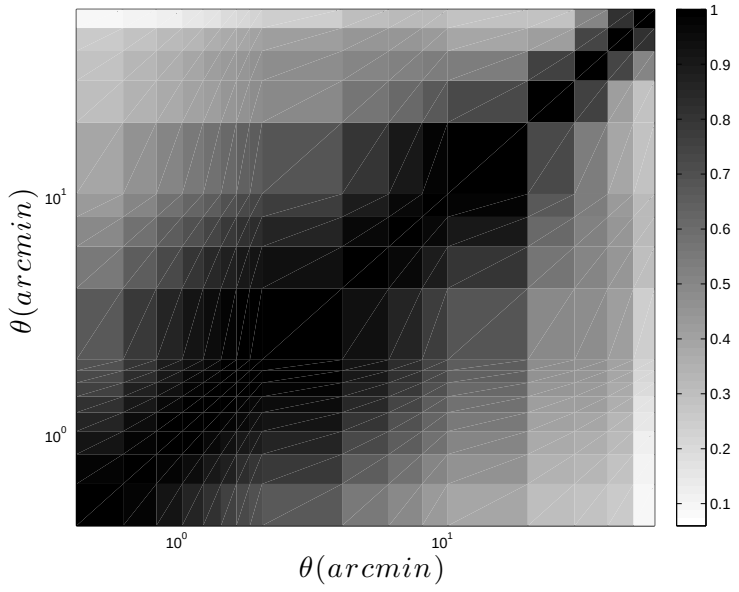

(b)

Figure 5.23: The cross-correlation coefficient matrix of the third moment of convergence maps smoothed with the aperture filter, with the source plane at $z \sim 3.0$ (top) and $z \sim 1.0$ (bottom).

5.5 Conclusion

We have generated a set of 185 high-resolution N-body simulations from which we constructed past light cones with a ray-tracing algorithm. The weak lensing signal that is extracted is well resolved from a few degrees down to below an arcminute. We have measured non-Gaussian error bars on a variety of weak lensing estimators, including 2-point correlation and mass aperture functions. These error bars are essential for a correct estimate of cosmological parameters, which so far has relied on assumptions that are less accurate. With the next generation of lensing surveys, non-Gaussian error bars are expected to deviate significantly from Gaussian prescriptions, therefore techniques such as those presented here will be required. For each estimator, we find excellent agreement between the mean of our measurements and non-linear predictions, which testifies to the quality of the simulations. We have also measured and presented the correlation coefficient matrices for these weak lensing estimators, and showed that the error bars between different angular measurements are at least 50% correlated, with regions up to 90% correlated, as the two angles get similar in size.

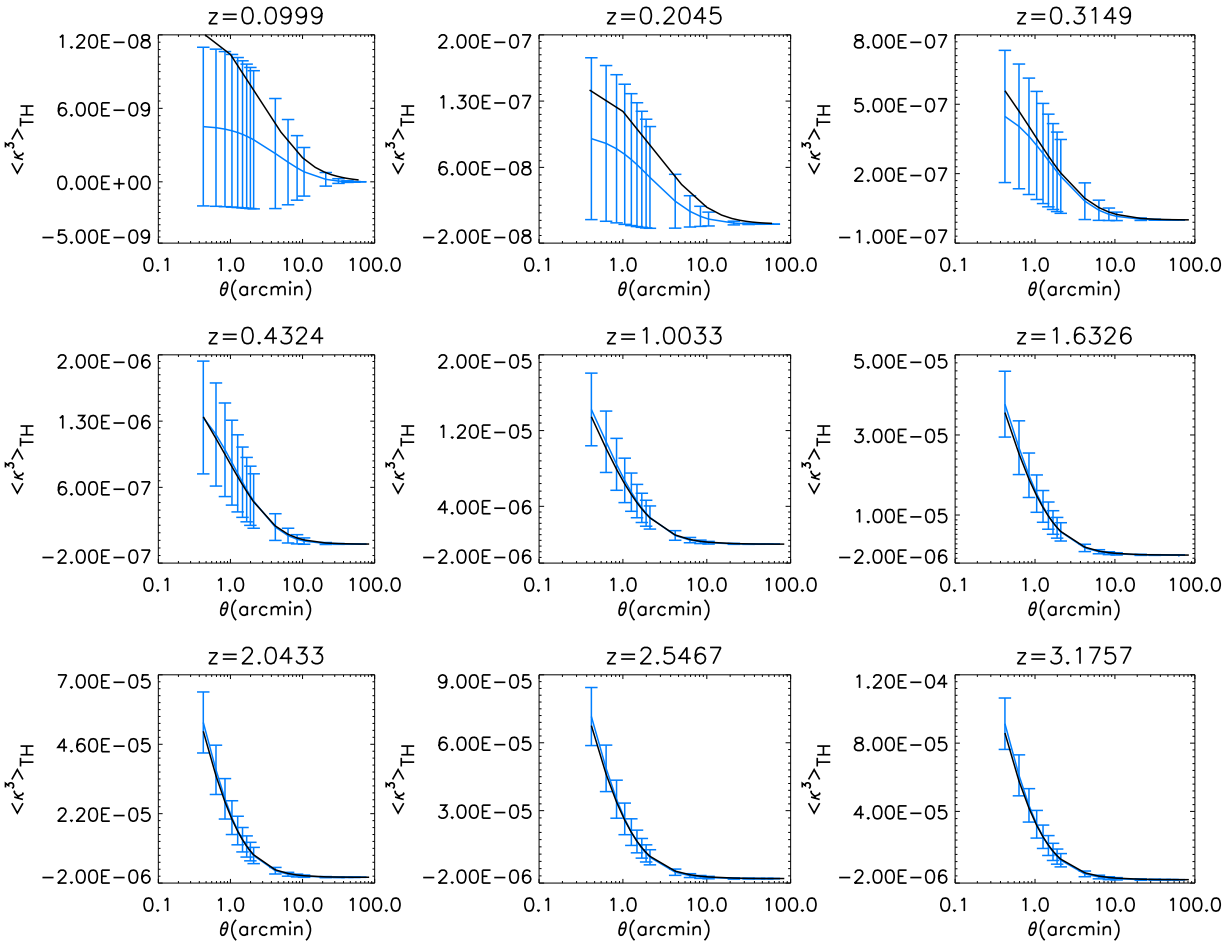

Figure 5.24: The $\langle\kappa^3\rangle$ estimate for convergence κ- maps smoothed with a top-hat filter.

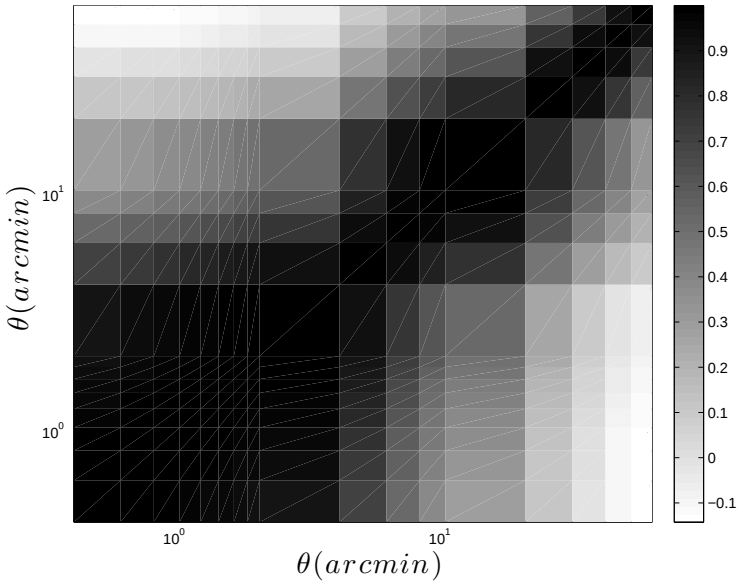

(a)

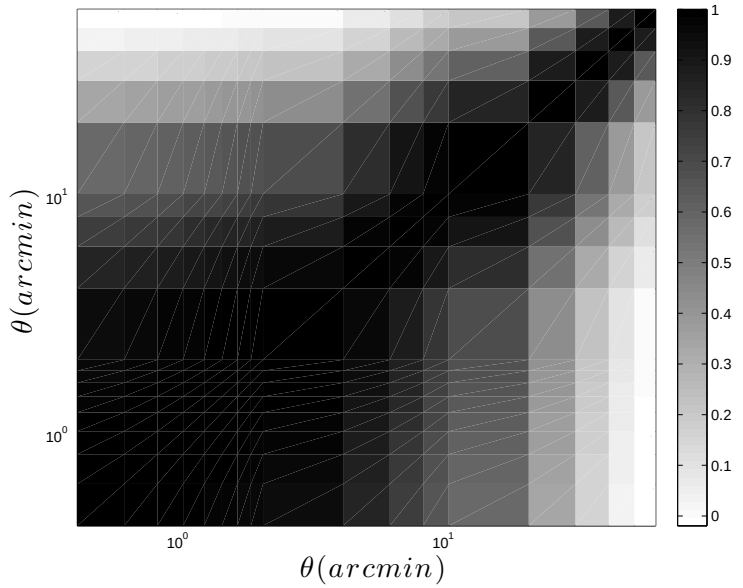

(b)

Figure 5.25: The cross-correlation coefficient matrix of the third moment of convergence maps smoothed with top-hat filter, with the source plane at $z \sim 3.0$ (top) and $z \sim 1.0$ (bottom).

Chapter 6

Optimal Survey Design for Weak Lensing Three-point Statistics

6.1 Motivation

Weak gravitational lensing by large scale structure is a unique tool to probe the matter distribution of the Universe regardless of its dynamical state. When combined with redshift information weak lensing can be used as a probe for dark energy evolution as the expansion of the Universe affects the mass clustering at different redshifts. Dark energy constraints from weak lensing rely on accurate measurements of the dark matter power spectrum amplitude. The two-point cosmic shear statistics offer a powerful technique to measure the matter normalization parameter σ_8 and the mass density parameter $\Omega_{\rm m}$ combined (see for example the earlier results from CFHTLS by Benjamin et al. [2007] and Fu et al. [2008] and also from COSMOS survey by Schrabback et al. [2010]). One of the important goals for better determination of the cosmological parameters is to improve the individual measurement of σ_8 and $\Omega_{\rm m}$. Better estimation of σ_8 and $\Omega_{\rm m}$ allows for alleviation of the residual parameter degeneracies [Komatsu et al., 2009]. A noticeable example is the neutrino mass [Tereno et al., 2009].

Bernardeau et al. [1997] and van Waerbeke et al. [1999] advocated for three-point shear statistics as a powerful estimator to break the degeneracy between σ_8 and $\Omega_{\rm m}$. In particular, a certain ratio of two- and three-point statistics, called

"skewness", was shown to be independent of σ_8.

At the time our work in this chapter was carried out, there have only been three detections of the three-point shear statistics reported from the VIRMOS survey (Bernardeau et al. [2003] and Pen et al. [2003]) and from the CTIO survey [Jarvis et al., 2005]. Unfortunately, for these surveys, the signal-to-noise ratio remains low and there were no reliable forecasts of three-point statistics which took into account realistic galaxy number counts and shape noise as well as non-Gaussian contributions in the cosmic variance. Therefore, the interpretation of the measurement was not well-established. In Van Waerbeke et al. [2001b] the authors concluded that the three-point statistics of the lensing signal is greatly enhanced at small angular scales because of the non-linear gravitational clustering, but they did not provide an estimate of the signal-to-noise ratio for different survey depths. In van Waerbeke et al. [1999] it was shown that the skewness of the convergence can be measured from mass maps reconstructed from the shear measured on individual galaxies. However, a realistic population of source galaxies was not considered, and the simulations were limited to second order perturbation theory. Kilbinger and Schneider [2005] showed that one can learn additional information by combining the two- and three-point statistics, but again neither a realistic source galaxy distribution nor different survey strategies were considered. Takada and Jain [2004] also showed that combining the power spectrum and bispectrum tomography information enhances the accuracy of cosmological parameter estimations.

In this chapter we investigate the optimal use of three-point statistics in a weak lensing analysis of large scale structure, considering several new aspects that have been neglected in previous works:

- A realistic noise contribution using ray-tracing simulations calibrated on existing surveys is included.
- Realistic forecasting for the two- and three-point statistics for different survey strategies is provided.
- For a fixed observing time, wide-shallow and narrow-deep strategies are considered. The impact of the survey's depth on both the galaxy number density and the source redshift distribution is quantified. Surveys with different

characteristics are affected differently by cosmic variance, with wider surveys probing a much larger number of modes than narrow surveys. Here we carefully investigate this aspect by comparing the performance of various simulated surveys which use a realistic source distribution.

- The source distribution has been derived using galaxy counting as a function of redshift, as measured in real data for a fixed limiting magnitude.
- The full likelihood analysis with covariance matrices are computed from a large set of ray-tracing simulations. It is therefore an extension of previous works which used Fisher matrices to gauge the performance of weak lensing surveys (e.g. Amara and Réfrégier [2007]).
- Following Zhang et al. [2003] a comparison of different smoothing filters is included.
- A range of most optimal smoothing scales are found by investigating the various contributions of noise and signal to the full covariance matrix.
- The best survey strategy for detecting the skewness of the convergence S_3 as a means of breaking the degeneracy between Ω_m and σ_8 is studied. The idea first emerged in Bernardeau et al. [1997] and van Waerbeke et al. [1999], but its feasibility never quantified.
- The efficiency of combining the two- and three-point statistics is quantified.
- Two- and three-point statistics forecasts for the completed CFHTLS survey and the KiDS survey are calculated.

This chapter is organised as follows. In section 6.2, we summarize the background theory of the two- and three-point statistics of the convergence field, where notations and definitions are also introduced. The details of the method are described in section 6.3. Optimal survey strategies are shown in section 6.4, and section 6.5 shows the predictions of two- and three-point measurements of the simulated complete CFHTLS-Wide survey area and depth. The upcoming Kilo Degree Survey geometry is also discussed here as an example of the accuracy achievable

on the measurement of the two- and three-point statistics in the near future. Finally, in section 6.6, the conclusions of this study are stated.

6.2 Theory Background

Following Miralda-Escude [1991] and Kaiser [1992] we can write the convergence κ at a given sky position θ as

$$\kappa(\theta) = \frac{3}{2}\frac{H_0^2}{c^2}\Omega_{\rm m}\int_0^\infty \omega(z)\delta(\chi,\theta){\rm d}\chi, \tag{6.1}$$

where χ is the angular comoving distance, $\Omega_{\rm m}$ is the mass density parameter at the present day, δ is the matter density contrast and $\omega(z)$ for a given redshift z is given by

$$\omega(z) = (1+z)\chi(z)\int_z^\infty n(z_{\rm s})\left[1-\frac{\chi(z)}{\chi(z_{\rm s})}\right]{\rm d}z_{\rm s}. \tag{6.2}$$

Here $\omega(z)$ depends on the cosmological parameters and the galaxy source distribution function $n(z_{\rm s})$. The convergence maps are obtained from ray-tracing simulations, as described in Section 6.3.1.

Note that this analysis employs the convergence field κ, which is proportional to the projected mass density. The convergence can be obtained from the shear data $\gamma=(\gamma_1,\gamma_2)$ either by appropriate weighting with an aperture filter, or from mass reconstruction with e.g. a top-hat or Gaussian filter. Therefore, the conclusions of this study apply to the convergence and the shear without distinction. We are interested in the measurement of $\langle\kappa^2\rangle$, $\langle\kappa^3\rangle$ and the skewness $S_3(\kappa)$ defined as

$$S_3 = \frac{\langle\kappa^3\rangle}{\langle\kappa^2\rangle^2}. \tag{6.3}$$

Skewness is essentially a measure of the clustering of the mass distribution, as defined in Bernardeau et al. [1997]. According to perturbation theory, S_3 provides a measurement of $\Omega_{\rm m}$ independent of the normalization of power spectrum σ_8. For this reason, the skewness of the convergence appears as a very attractive probe of cosmology and a useful technique to break degeneracies among other cosmological

parameters.

6.3 Analysis Method

6.3.1 Ray-tracing Simulations

This analysis is based on a set of simulated κ-maps (referred to as Set I in chapter 5). The set consists of 60 lines of sight, each containing 40 redshift slices from $z = 0.020$ to $z = 3.131$. These are generated from 22 independent N-body simulations by randomization. As a result, the different lines of sight are not totally independent on large scales. However they can still be considered approximately independent on scales smaller than 1°.

The Multiple Lens-Plane ray-tracing approximation method was used to generate the lensing convergence map: the dark matter distribution in the Universe is approximated by a series of mass sheets. The N-body simulations are on a grid of 1728^3 points with 856^3 particles, and the box size is 120 h^{-1}Mpc. The mass density in the simulation box is projected to the mid-plane at a series of characteristic redshifts. The output redshifts are picked so that the consecutive time slices can represent the continuous evolution of the large scale structure. The three orthogonal axes of the box are *x*, *y*, and *z*. For every output redshift, we make three projection sheets, parallel to the *xy*, *yz* and *xz* planes. We choose one projection sheet out of the three of one N-body simulation in a random order, as well as randomly shifting the sheet transverse to the projection direction. This technique is employed to avoid creating periodicity in the projection. Rays are shot through these mass sheets. We calculate κ on every sheet and project them along lines of sight after the random shift and rotation.

The maps are on 1024×1024 grid with spacing of 0.21 arcmin. Thus the total area is about 12.84 deg^2 for each line of sight. We use the cosmological paramaters values based on WMAP3 results [Spergel et al., 2007] : $\Lambda_{\rm CDM}$ with $\Omega_{\rm m} = 0.24$, $\Omega_\Lambda = 0.76$ and $\sigma_8 = 0.74$. Figure 6.1 shows a schematic of the different redshift slices which were combined for each line of sight.

The N-body simulations are generated by the `CUBEPM` code, which is the successor of `PMFAST` [Merz et al., 2005]. `CUBEPM` is MPI parallelized particle-mesh

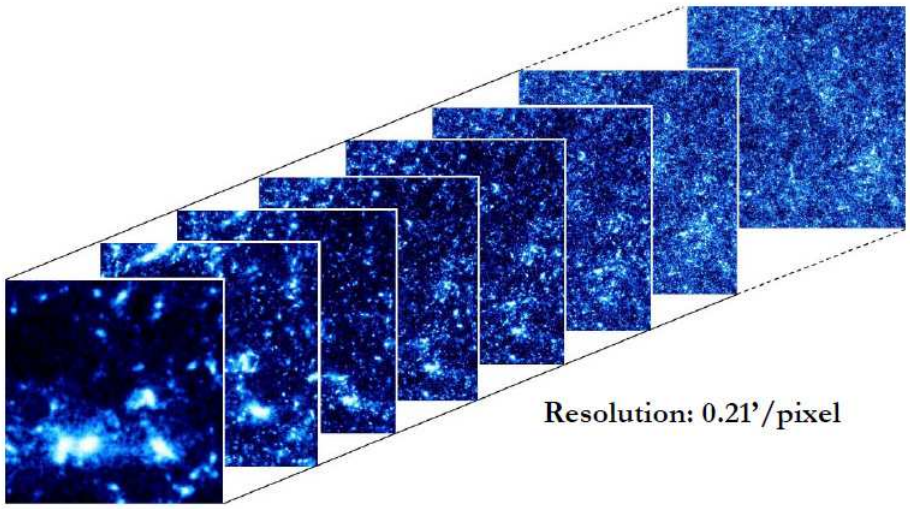

Figure 6.1: A schematic of the simulated convergence maps at different redshift slices.The maps are on a 1024^2 grid with 0.21 arcmin per pixel. The redshift ranges from z=0.020 to z=3.131.

(PM) code, and has particle-particle force implement at sub-grid scales. It is further parallelized by shared-memory `OpenMP` on each node. The simulation volume (which is also called simulation box) is cubically decomposed into n^3 sub-volumes, and the calculation of each sub-volume is performed on one node of the cluster. The total number of nodes used in simulation is n^3 with $n = 3$ here. The code can be run on up to 1000 nodes. The simulations are run on the Sunnyvale cluster of CITA.

For each of the redshift slices the average $\langle\kappa^2\rangle$, $\langle\kappa^3\rangle$ and S_3 are measured and the signal is compared with a theoretical model. The two-point cosmological predictions are based on the Peacock and Dodds [Peacock and Dodds, 1996] non-linear fit, whereas the three-point shear statistics predictions use the bispectrum non-linear fit derived in Scoccimarro [1998] and implemented for lensing studies in Van Waerbeke et al. [2001b]. The excellent agreement between the measured and the predicted signal can be seen in figure 6.2, where the results for low, intermediate and high redshift slices are shown. The agreement in all cases is within 1-σ error-

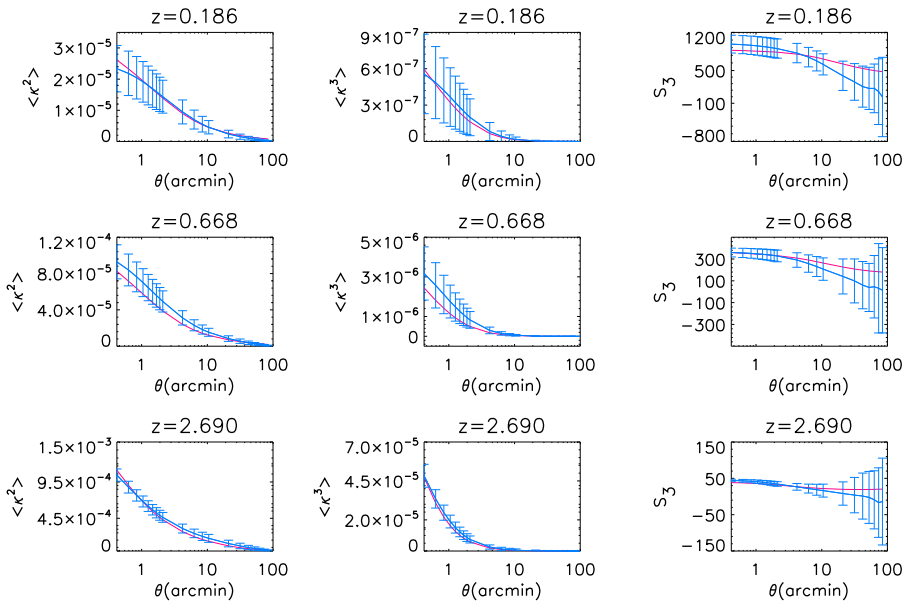

Figure 6.2: Agreement between the measurements and the theoretical predictions for three individual redshift slices. The low redshift slice is at z=0.186, the medium slice at 0.668 and the high redshift slice is at 2.690. The blue lines show the measurements on the simulated 12.84 deg^2 data, and the pink lines show the theoretical prediction for the same cosmological model at the same redshift. The measurements in each panel are made from data smoothed with a top-hat filter. The error bars represent the cosmic variance over 60 lines of sight.

bar.

6.3.2 Galaxy Number Density and Redshift Distribution

In this paper we compare different survey strategies with varying source redshift distribution that is dependent on the survey depth. We calibrate the redshift distribution from existing optical surveys with photometric redshift information and populate the ray-tracing slices accordingly. The focus here is on ground based surveys, but the result can be straightforwardly extended to space data with an appropriate scaling of the shot noise (which directly depends on the galaxy shape

$m_{\rm lim}$	α	β	z_0	$z_{\rm med}$
22.5	0.76	6.85	1.05	0.68
23.0	0.71	5.30	1.14	0.72
23.5	0.81	3.15	1.19	0.80
24.0	0.80	2.72	1.26	0.84
24.5	0.96	1.70	1.07	0.91
25.0	0.85	1.90	1.26	0.96
25.5	1.46	1.30	0.75	1.02
26.0	1.71	1.27	0.68	1.04

Table 6.1: The best fit values of α, β and z_0 corresponding to equation (6.4) for several *i*-band limiting magnitudes. These parameters were used to generate theoretical models for Section 6.4 to determine the best survey strategy. The last column contains the median redshift $z_{\rm med}$ for each magnitude cut.

noise and number density).

The galaxy number density and redshift distribution as a function of limiting magnitude are estimated from the CFHTLS-Deep survey catalogue in the *i*-band Ilbert et al. [2006]. To model the galaxy redshift distribution $n(z)$ for surveys of different magnitude limit $m_{\rm lim}$, the method described in Heymans et al. [2006b] and van Waerbeke et al. [2006] was employed, modeling $n(z, m_{\rm lim})$ as

$$n(z, m_{\rm lim}) = \frac{\beta}{z_0 \Gamma\left(\frac{1+\alpha}{\beta}\right)} \left(\frac{z}{z_0(m_{\rm lim})}\right)^{\alpha} \exp\left[-\left(\frac{z}{z_0(m_{\rm lim})}\right)^{\beta}\right]. \qquad (6.4)$$

The best parametric fit to equation (6.4) for limiting magnitude $i = 24.5$ corresponds to α=0.96, β=1.70 and z_0=1.07. Figure 6.3 shows the histogram of the normalized galaxy redshift distribution from the CFHTLS-Deep survey catalogue [Ilbert et al., 2006] at $m_{\rm lim} = 24.5$ and the best fit $n(z)$ from equation (6.4). Table 6.1 summarizes the values of α, β, z_0 and the median redshift $z_{\rm med}$ for the other magnitude cuts used in this paper. Equation (6.4) yields a realistic source redshift distribution for a given survey's depth [van Waerbeke et al., 2006]. Thus, the theoretical predictions built based on the appropriate form of equation (6.4) match the κ-maps weighted by the galaxy number density derived from the CFHTLS-deep catalogues.

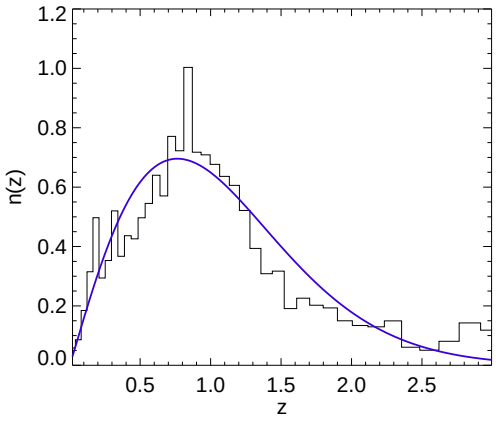

Figure 6.3: Fit to the normalized galaxy number density from the CFHTLS-Deep survey catalogue Ilbert et al. [2006]. The black line shows the histogram of the galaxy number density and the dark blue line is the fitted curve. The limiting magnitude $m_{\rm lim}$ =24.5 with the fitting formula given by equation (6.4). Here α, β and z_0 are 0.96, 1.70 and 1.07, respectively.

6.3.3 Statistical Noise

The source of shot-noise in weak lensing studies depends on the intrinsic ellipticity characterized by the r.m.s.σ_ε and by the number density of galaxies $n_{\rm g}$. It was shown in van Waerbeke [2000] that the noise in a smoothed convergence map can simply be derived from the intrinsic ellipticity noise and the galaxy number density. In particular, it was shown that the noise in a pixelated smoothed κ map is simply given by a smoothed uncorrelated Gaussian noise with r.m.s.σ_ε. If $n_{\rm g}$ denotes the number density of galaxies and $W(\theta)$ the 2-dimensional smoothing function, then the correlation function of the convergence noise is

$$\langle \kappa_n(\theta)\kappa_n(\theta')\rangle = \frac{\sigma_\varepsilon^2}{2}\frac{1}{\Theta^2 n_{\rm g}}\int d\ell e^{i\ell\cdot(\theta-\theta')}\left|\tilde{W}(\ell)\right|^2, \tag{6.5}$$

where $\kappa_n(\theta)$ is the convergence noise map and $\tilde{W}(\ell)$ is the Fourier transform of the smoothing window $W(\theta)$. Θ is the pixel size, so $\Theta^2 n_{\rm g}$ is the average number of galaxies per pixel. Note that the simulated κ-maps are pixelized by construction

and then smoothed with smoothing filters.

The galaxy ellipticity r.m.s. measured on CFHTLS-deep data is $\sigma_\varepsilon^2 = (\sigma_{\varepsilon_1}^2 + \sigma_{\varepsilon_2}^2) = 0.44$. For the purpose of this paper we will assume that σ_ε is constant as a function of redshift and galaxy type. The convergence noise variance per pixel (before smoothing with W) is therefore given by

$$\sigma_\kappa^2 = \frac{\sigma_\varepsilon^2}{2} \frac{1}{\Theta^2 n_\mathrm{g}}. \tag{6.6}$$

Note that the noise model considered here implicitly assumes source galaxies are distributed randomly in each redshift slice. By construction, this choice ignores any potential effect caused by source clustering, which is known to be a source of contamination for three-point statistics (Bernardeau [1998] and Forero-Romero et al. [2007]).

6.3.4 Smoothing Filters

Convergence statistics can be measured from smoothed κ-maps (which can be obtained from smoothed shear maps from the data). Various statistics can be built by using different smoothing filters. Following the widely accepted choice the top-hat, and two types of compensated (the total area under the filter window is equal to zero) filters were considered. The two compensated filters used were the ones introduced in Schneider et al. [1998] (hereby referred to as the aperture filter) and in van Waerbeke [1998] (which is hereby referred to as the compensated Gaussian (cG)). They are defined as in equations 4.15 and 4.18 respectively.

Figure 6.4 shows the excellent agreement between the ray-tracing simulation and the predictions for different smoothing filters. The measurements are based on a realistic redshift distribution corresponding to a ground based survey with limiting magnitude $m_\mathrm{lim} = 24.5$ with n_g=22 galaxies per arcmin^2. The error bars reflect the statistical noise and cosmic variance for a 12.84 deg^2 survey. From equations 4.15 and 4.18, the smoothing scale for the two filters are related as $\theta_\mathrm{cG} = \theta_\mathrm{ap}/2\sqrt{2}$, therefore the maximum smoothing scale chosen for the compensated Gaussian filter is 25 arcminutes, compared to 84 arcminutes for the top-hat and aperture filters.

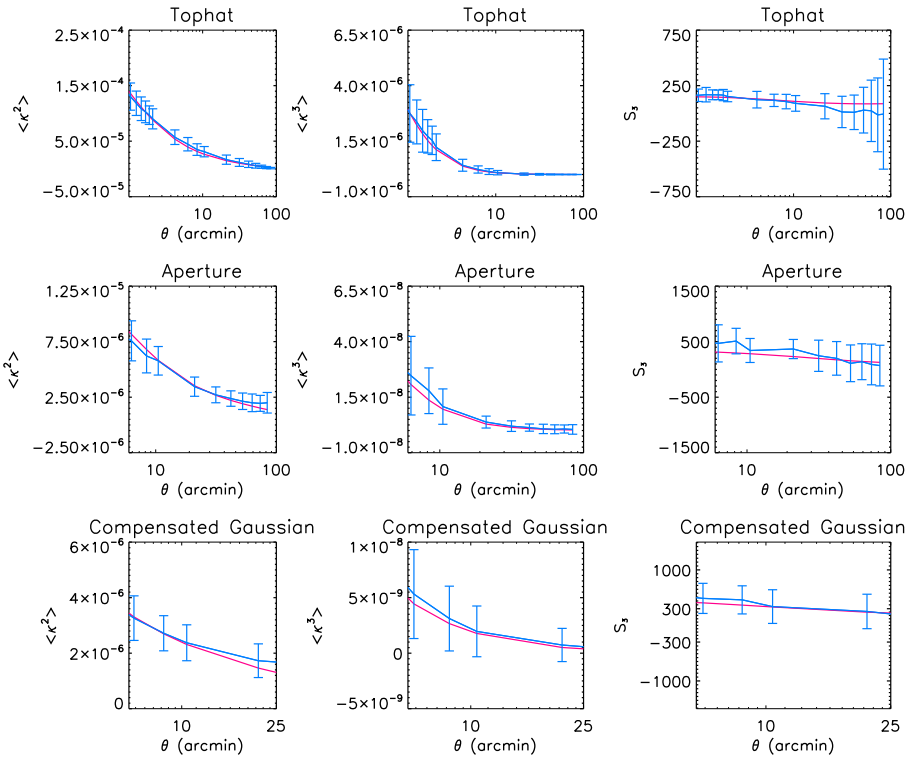

Figure 6.4: The agreement between the measurements and the theoretical predictions based on the fitted galaxy population. The blue lines show the measurements on the simulated 12.84 deg^2 data, and the pink lines show the theoretical prediction for the same cosmological model and the full redshift distribution. The measurements in each panel are performed on smoothed data, with top-hat, aperture mass and compensated Gaussian filters in order. The errorbars include both cosmic variance and statistical noise resulting from n_g= 22 galaxies per arcmin^2.

6.3.5 Estimate of the Covariance Matrix

Cosmological parameter forecasting requires the estimate of the covariance matrix. Semi analytical methods are available in the literature (Schneider et al. [2002a] and Joachimi et al. [2008]), but rely on the assumption of Gaussian statistics. An extension to the non-linear angular scales has been recently developed (Semboloni et al. [2007], Eifler et al. [2008] and Pielorz et al. [2010]), however the three-point statistics and source redshift distribution and shape noise of realistic surveys were not considered. In this work the full covariance matrix **C** was estimated directly from the ray-tracing simulation as in Semboloni et al. [2007] and Eifler et al. [2008], by taking into account the realistic characteristics of lensing surveys described in the previous sections. For each survey strategy, the total covariance matrix was calculated as follows. For each noise-free κ line of sight, the redshift slices were combined and weighted according to equation 6.1 with the corresponding redshift distribution and galaxy number density. A noise map was then added following the method described in Section 6.3.3. Finally, the two- and three-point statistics were measured over 20 smoothing scales. The covariance matrix of the statistic x measured at two smoothing scales θ_i and θ_j is defined as

$$\mathbf{C}(\theta_i,\theta_j) \equiv \langle (x(\theta_i)-\mu(\theta_i))(x(\theta_j)-\mu(\theta_j))\rangle, \tag{6.7}$$

where x is here either $\langle\kappa^2\rangle$, $\langle\kappa^3\rangle$ or S_3 and μ is the average calculated from the entire simulation set.

It was shown by Hartlap et al. [2007] that the inverse of the covariance matrix estimated from a finite number of ray-tracing simulations is biased. The authors derived a simple formula to correct for this effect which relates the number of scales p used in the two- (or three-) point statistics and the number n of lines-of-sight. The covariance matrix simply has to be replaced by $\alpha^*\mathbf{C}$, where α^* when the mean is determined from the data, is given by

$$\alpha^* = \frac{(n-1)}{(n-1)-p-1}. \tag{6.8}$$

Hartlap et al. [2007] showed that this correction is applicable only when $n-2$ exceeds the number of scales p, otherwise the covariance matrix **C** is not invert-

ible. In this paper $n = 60$ simulations were used, and the statistics were measured over $p = 20$ angular scales for the top-hat and aperture filters and $p = 14$ for the compensated Gaussian filter. The values of α^* for these filters were then 1.55 and 1.28, respectively. For joint likelihood calculations the joint covariance matrices were rescaled by $\alpha^* = 3.28$ for top-hat and aperture filters and $\alpha^* = 1.97$ for the compensated Gaussian filter.

Because of the limited area covered by the simulations it is not possible to compute the covariance matrices for very large surveys. Fortunately, the angular scales where the non-linear effects are important (typically less than half a degree for the two- and three- point statistics) are much smaller than the 12.84 deg^2 field-of-view of a simulation field. Those are also the scales where the lensing signal is best measured. Therefore the covariance matrices can be computed in the non-linear regime from the different realizations, and simply rescaled according to the survey size for surveys exceeding the simulation box. The measurements for a larger survey is simply obtained from dividing the measurements from the 12.84 deg^2 case, by the ratio of the survey areas. This is an excellent approximation for angular scales much smaller than the simulation box, which was the case in our study since the largest scale used to measure the statistics was 84 arcminutes, which is much smaller than the dimension of $3.5^\circ \times 3.5^\circ$ of the simulation box. In order to verify that the rescaling is a valid approach, the following procedure was performed. A selection of six elements of the covariance matrix $\mathbf{C_{ij}}$ were chosen. For each case, the element of the covariance matrix was computed on the full 12.84 deg^2 (A) simulation and smaller fraction of it (A_0). The term $\frac{A}{A_0}$ shows the ratio of the original simulation size to sub-sections of it. Each $\mathbf{C_{ij}}$ element is then computed on various sub-sections of the simulation field. The dependence of covariance matrix elements on the survey area is found to be nearly linear. Figure 6.5 illustrates the scaling applied to some elements of the two- and three-point statistic covariance matrices. The dotted lines show linear fit ($y = mx + b$) to the covariance matrix elements measurements as a function of survey area. As it can be seen the behaviour of the covariance measurements follows the linear function. This is the basis of the rescaling of the covariance matrix to the larger survey areas as needed in this work.

In order to verify that the covariance matrix computed using ray-tracing simu-

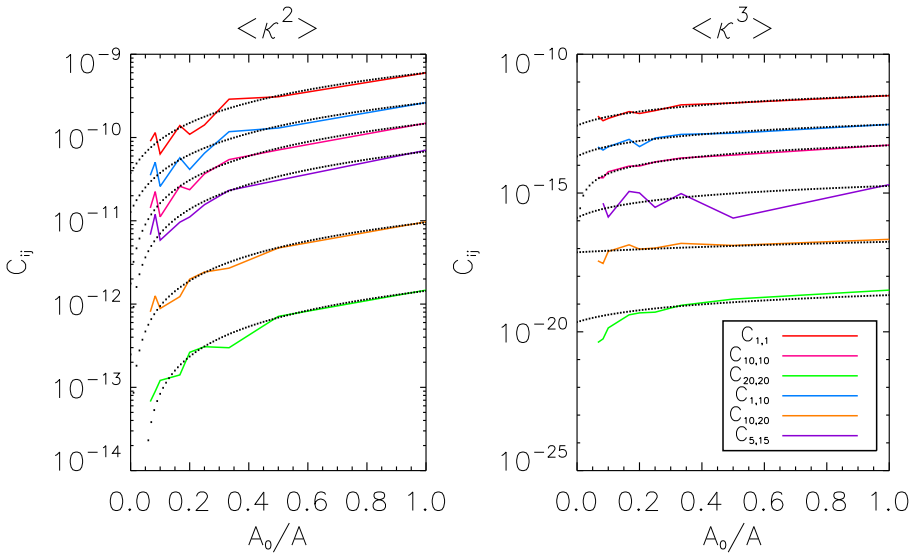

Figure 6.5: The $\mathbf{C_{ij}}$ elements of the covariance matrix as a function of the ratio of the original κ-map simulation area (12.84 deg^2) over the survey area. The solid colored lines are the $\mathbf{C_{ij}}$ elements from the simulated maps and the black dotted lines are the straight line fit to each of them. The left figure shows the $\mathbf{C_{ij}}$ of $\langle\kappa^2\rangle$ and the right one is the same for $\langle\kappa^3\rangle$. Here the covariance matrix contains only the cosmic variance contribution. The scales are as follows: i=1 is 0.42'; i=5 is 1.26'; i=10 is 4.20'; i=15 is 31.5' and i=20 is 84.0'. This shows that the change in the covariance matrix of the cosmic variance is inversely proportional to the survey area. Hence this result was used to rescale the covariance matrices in the likelihood calculation to the desired survey area.

lations converges to the one computed in the Gaussian approximation for large angular scales, the following procedure was performed: Gaussian realizations of the field κ were generated and then the covariance matrix was calculated in the same way as the ray-tracing simulations. Efstathiou et al. [1985] and Salmon [1996] described a simple way to generate cosmological Gaussian fields by convolving white-noise with a filter whose transfer function is given by the square root of the power spectrum. The power spectrum was directly computed from the sample of ray-tracing simulations, so that the resulting Gaussian fields have the same cosmol-

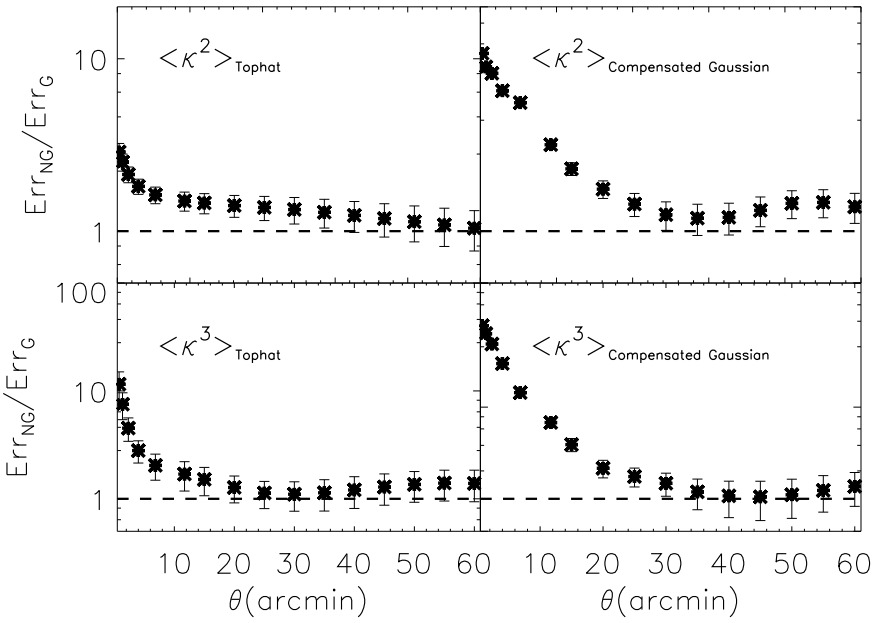

Figure 6.6: The ratio of non-Gaussian to Gaussian error estimated for convergence κ two- and three-point statistics. On large scales the non-Gaussian errors estimated from the ray-tracing simulations converge to the Gaussian limit. The results for the top-hat and compensated Gaussian filters are shown in the left and right columns, respectively.

ogy. Using this method, 60 lines of sight were generated and the covariance matrix of the Gaussian fields was computed as described by equation (6.8). Figure 6.6 shows the ratio of the non-Gaussian to Gaussian errors (i.e. the square root of the diagonal elements of the covariance matrix) for the two- and three-point statistics of the top-hat and compensated Gaussian filters. It can be seen that for large scales the ratio converges to unity as expected. At small scales this ratio is larger than the unity due to the non-linear evolution of matter fluctuations. Moreover, for a given angular scale, the ratio between non-Gaussian and Gaussian errors is larger when one uses the compensated Gaussian filter than when the top-hat filter is used. The reason lies in the fact that for a given characteristic scale, the compensated

Gaussian filter peaks at smaller scales than the top-hat filter. The ratio between non-Gaussian and Gaussian covariance depends on the average redshift of the survey and for this test a distribution characterized by an average redshift $z \sim 1.4$ was used. The ratio would have been much higher if a much shallower survey was chosen.

6.4 Survey Design and Observing Strategy

6.4.1 Optimal Smoothing Scale

The covariance matrix contains three terms (Schneider et al. [2002a]) :

$$\mathbf{C} = \mathbf{C}_{\rm ss} + \mathbf{C}_{\rm ns} + \mathbf{C}_{\rm nn} \tag{6.9}$$

where $\mathbf{C}_{\rm ss}$ is the pure signal (i.e. noise free) cosmic variance, $\mathbf{C}_{\rm nn}$ is the pure noise covariance and $\mathbf{C}_{\rm ns}$ is the cross-correlation term. The goal in this section is to determine at which angular scale the measurement of the two- and three-point shear statistics has a better signal-to-noise ratio. For this purpose the covariance matrix was separated into the three terms introduced above and their amplitudes for different filters were explored. Practically $\mathbf{C}_{\rm ss}$ can be calculated from the noise-free ray-tracing realizations, since it only contains the cosmic variance between different simulations. The term $\mathbf{C}_{\rm nn}$ can be calculated from noise-only maps, generated by weighted Gaussian noise realizatios. This term contains statistical noise only. Among the three parts of the covariance matrix: $\mathbf{C}_{\rm ss}$, $\mathbf{C}_{\rm nn}$, and $\mathbf{C}_{\rm ns}$, the mixed term $\mathbf{C}_{\rm ns}$ is the most computationally expensive to calculate. The reason is that the noise contribution to the covariance matrix converges more slowly than the cosmic variance contribution, and in practice, it is necessary to estimate the noise from more than 60 noise realizations. For the two-point statistics there are analytical formulae in Schneider et al. [2002a], but there is currently no equivalent for the three-point statistic and the skewness of the convergence. In order to inspect the three different terms, the covariance matrix was calculated as follows. For each noise realization, a $\mathbf{C}$ was calculated, which was relatively noisy because it was obtained from one noise pattern. Then the average of $\mathbf{C}$ was taken over ten noise realizations. The covariance matrix thus obtained was specialized for a given noise statistical prop-

erty, and the whole calculation was repeated each time the observing conditions affecting the noise were changed. $\mathbf{C}_{\rm nn}$ was calculated separately over ten thousand realizations. The average $\mathbf{C}_{\rm ss}$ and $\mathbf{C}_{\rm nn}$ were used to determine the cross term $\mathbf{C}_{\rm ns}$. Because of the averaging process one obtains a covariance matrix which has a relatively small noise making $\mathbf{C}$ invertible. To illustrate the contribution of each of these parts the diagonal elements of the $\mathbf{C}_{\rm ss}$, $\mathbf{C}_{\rm nn}$, $\mathbf{C}_{\rm ns}$ and $\mathbf{C}$ were extracted as the noise term for each smoothing scale.

Figure 6.7 shows the relative contribution of different terms in the covariance matrix. The noise-to-signal ratio for the individual components of the covariance matrix are shown. The blue (long dashed) line is the signal-signal which is the result of cosmic variance only. The noise-noise term is shown with the black (short dashed) line. The mixed term was derived from $\mathbf{C} - \mathbf{C}_{\rm ss} - \mathbf{C}_{\rm nn}$ and is shown in red (dash-dotted) line and the green (solid) line shows the total noise over signal ratio. As expected the finding was that small scales were dominated by statistical noise and the large scales by cosmic variance, where the signal is low. Interestingly, the mixed noise term is non-negligible for the two- and three-point statistics, so the future high precision surveys will have to take it into account. The mixed noise term is strongly dominant for the skewness.

In agreement with Zhang et al. [2003] a range of optimal angular scales (between one arcminute and half a degree) was found for which the total noise affecting the two-point shear statistics is minimal. This is also the case for the three-point statistics.

6.4.2 Wide and Shallow Versus Deep and Narrow

Many of the future lensing surveys will have a limited observing time and a full sky coverage will not be possible. The question will arise whether a deep and narrow survey performs better than a large and shallow survey. Therefore, it is important to quantify what is the optimal balance between survey size and depth, given a fixed observing time. It is expected that very shallow surveys would provide a poor weak lensing measurement due to the small lensing efficiency for nearby sources, and deep-narrow surveys will be limited by cosmic variance. The trade-off between those radically different survey designs must include a proper estimate

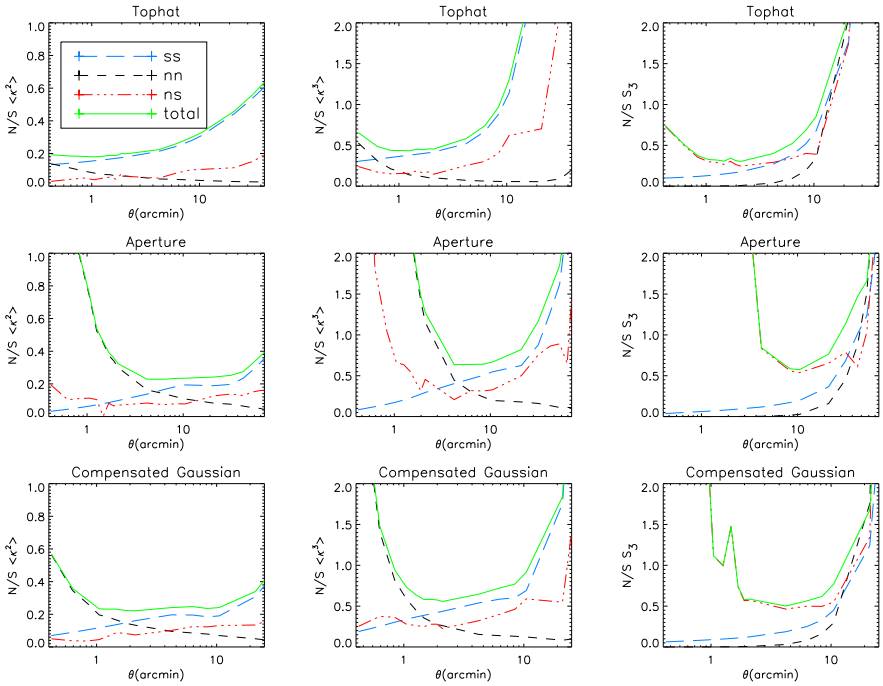

Figure 6.7: The noise-to-signal ratio for the cosmic variance only in blue (long dashed) line, statistical noise only in black (short dashed) line, the mixed term in red (dash-dotted) line and the total noise in green (solid). The $\langle\kappa^2\rangle$, $\langle\kappa^3\rangle$ and S_3 measurements were calculated for a simulated 12.84 deg^2 data smoothed with top-hat, aperture and compensated Gaussian filter (from top to bottom).

of the amplitude of the lensing signal and shot noise as function of survey depth.

The relation between limiting magnitude and survey area for a fixed observing time was derived from the algorithm developed in Bernstein [2001]. The galaxy number density was obtained by selecting galaxies whose signal-to-noise detection level was larger than 7 and which are also well resolved for weak lensing studies following the criteria given in Section 6.3.2. Table 6.2 shows the survey area and limiting magnitude for each case investigated here.

The likelihood of a model given the data can be written as

$$\mathscr{L} = \exp\left[-\frac{1}{2}(d-m)^T * \mathbf{C}^{-1} * (d-m)\right], \tag{6.10}$$

Area(deg^2)	1400	1150	900	514	257	115	45	20
$m_{\rm lim}$	22.5	23.0	23.5	24.0	24.5	25.0	25.5	26.0
$n_{\rm g}/arcmin^2$	2	5	9	14	22	28	37	45
GF	1.8	4.0	5.0	2.5	2.4	1.5	1.3	–*

Table 6.2: The area and *i*-band limiting magnitude and the corresponding galaxy number density of different surveys with the same observing time. The gain factor GF is the ratio between the $\Omega_{\rm m}$ 1σ width of the two-point statistics contours over that of the two- and three-point statistics joint contour. (*) Due to the truncated likelihood 1σ contours the GF is not calculated for the deepest survey.

where *d* is the measurement on the simulations (data) and *m* is the theoretical model for the same measured statistics. The theoretical model is the predictions for two- or three-point statistics, with varying $\Omega_{\rm m}$ and σ_8 parameters. All the other cosmological parameters are kept constant to those values of the simulations. Also the dependence of the covariance matrix on the choice of cosmological parameters is ignored here, due to limitations of the simulation set used here. $\mathbf{C}^{-1}$ is the inverse covariance matrix over all lines of sight. As described in the previous section the covariance matrix was computed directly by using the simulations and its inverse had been re-calibrated using equation (6.8). The likelihood contours were performed in the $\Omega_{\rm m}-\sigma_8$ parameter space. $\Omega_{\rm m}$ was varied between 0.1 and 1.0, with 0.05 intervals, and σ_8 values were between 0.50 and 1.50, with 0.05 intervals.

Figure 6.8 shows the pink (dark grey) contours for $\langle\kappa^2\rangle$ and cyan (light grey) for $\langle\kappa^3\rangle$ likelihood for top-hat filter. The filled contours show the joint $\langle\kappa^2\rangle-\langle\kappa^3\rangle$ likelihood. The $\langle\kappa^2\rangle$ and $\langle\kappa^3\rangle$ contours become more degenerate for deep and narrow surveys, whereas for wide and shallower surveys it appears clearly that the $\langle\kappa^2\rangle$ and $\langle\kappa^3\rangle$ likelihood contours have a different orientation in the $\Omega_{\rm m}-\sigma_8$ plane, which explains why the joint analysis works better for wide and shallow surveys. One can see indeed that the individual two- and three-point statistics contours for the wide and shallow surveys become large again due to a larger noise, but the joint analysis remains competitive. This could be attributed to the larger sensitivity of the three-point statistics to non-linear effects for shallow surveys as a consequence

of the projection of mass along the line-of-sight (i.e. identical angular scale probes more non-linear scales for shallow rather than deep surveys). For the joint two- and three-point statistics analysis, the medium depth surveys ($m_{\rm lim}$ =23.5 or 24.0) appear optimal. It is clear that for a fixed observing time, our results favor the medium shallow-wide surveys. The gain factor GF is defined as the ratio of the 1σ error width of the $\langle\kappa^2\rangle$ contours over that of joint $\langle\kappa^2\rangle - \langle\kappa^3\rangle$ measurements which quantifies the improvement when the joint statistics is considered. This value is calculated from the likelihood contours which include the full noise terms and correlation between vaious smoothing scales are reflected in the contour size. It is also common to quote the figure of merit, in order to judge the optimal survey design. The figure of merit is defined as the inverse of the area spanned by the 1-σ likelihood contour. So tighter constraints result in smaller contour area and hence, larger figure of merit. The relationship between the figure of merit (FoM) and gain factor (GF) used in this work, can be considered as: $FoM \propto GF^{-2}$. The values of the GF corresponding to the likelihood contours of figure 6.8 are shown in table 6.2.

Unfortunately, the skewness of the convergence, defined in equation (6.3), does not appear to yield as powerful constraints as the combined two- and three-point statistics. Figure 6.9 shows the error contours using S_3 for three choices of limiting magnitude and survey area. The observing time here was fixed, like for the previous analysis. As expected, the dependence on σ_8 is very weak, but one can see that the width of the contours along the $\Omega_{\rm m}$ axis is much larger than the $\Omega_{\rm m}$ constraints one gets from the joint analysis shown in Figure 6.8. Following the same trend as joint $\langle\kappa^2\rangle - \langle\kappa^3\rangle$ likelihood results shown in figure 6.8, the medium depth surveys lead to the most optimal skewness measurement. The constraints for the shallower surveys (i.e.$m_{\rm lim}$ =22.5 and 23.0) are not shown here. Those surveys give poor cosmological constraints, as the mixed $\mathbf{C_{ns}}$ term of the covariance at the scales of interest becomes large. Overall, the skewness does not appear to be as attractive a statistic to break the σ_8-$\Omega_{\rm m}$ degeneracy as previously advocated (Bernardeau et al. [1997] and van Waerbeke et al. [1999]). Measuring the skewness on the current and near future lensing surveys will be very challenging, and it is clear that a large fraction of the sky is needed in order to bring the noise contributions to a low enough level for precision cosmology.

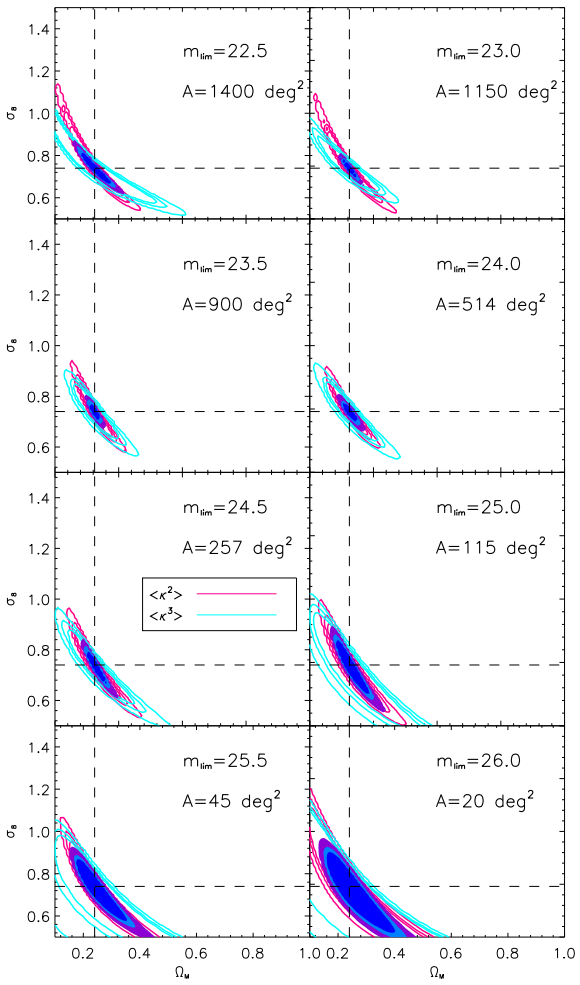

Figure 6.8: The likelihood analysis for various survey depths and areas with fixed observing time for $\langle\kappa^2\rangle$, $\langle\kappa^3\rangle$ smoothed with the top-hat filter. The observing time is equal for all cases, while the survey area and depth vary. Table 6.2 shows the values for $m_{\rm lim}$ with the corresponding survey areas. The pink (dark grey) contours indicates the 1σ, 2σ and 3σ errors for the $\langle\kappa^2\rangle$ statistics and the cyan (light grey) contours are the same for the $\langle\kappa^3\rangle$. The covariance matrix contains both the cosmic variance and the statistical noise. Here the joint likelihood shown in filled contours is calculated by taking into the account the $\langle\kappa^2\rangle - \langle\kappa^3\rangle$ correlations at different scales.

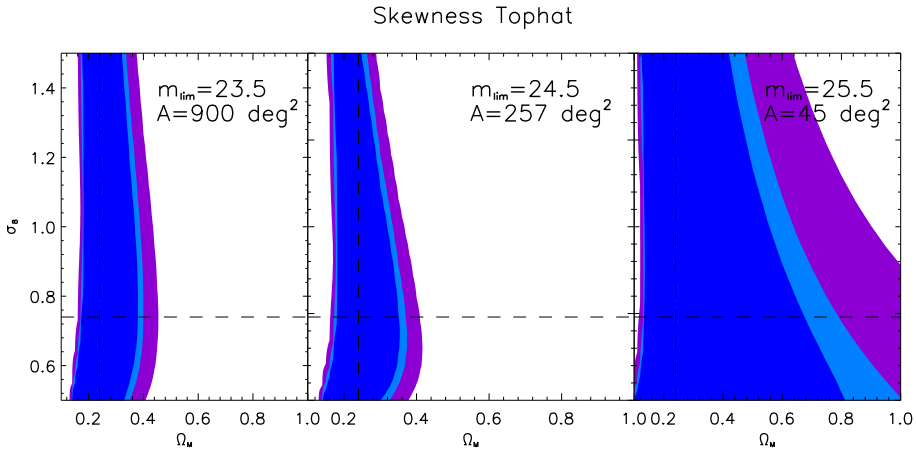

Figure 6.9: The likelihood analysis for various survey depths and areas with fixed observing time for skewness S_3 smoothed with the top-hat filter. The observing time is equal for all cases, while the survey area and depth vary. Table 6.2 shows the values for $m_{\rm lim}$ with the corresponding survey areas. The covariance matrix contains both the cosmic variance and the statistical noise. The skewness measurements are optimal for shallower surveys.

The reason why the skewness is hard to measure lies in the fact that the variation of the skewness amplitude for different $\Omega_{\rm m}$ models is largely absorbed by the cosmic variance of this estimator. This is not the case for the two- and three-point statistics taken separately. Figure 6.10 shows the comparison between various predicted cosmological models and the measurements from the simulations. $\langle\kappa^2\rangle$, $\langle\kappa^3\rangle$ and S_3 were measured for survey area of 12.84 deg^2 of limiting magnitude of 24.5 over the 60 lines of sight. The blue line shows the measured data points; the errorbars contain both cosmic variance and statistical noise. The pink (solid) line is the fiducial model ($\Omega_{\rm m}$=0.24, Ω_Λ=0.76 and σ_8=0.74). The black (dotted), green (dashed) and red (dash-dotted) lines are models with the same $\sigma_8 = 0.75$ and values of $\Omega_m = 0.20, 0.40$ and 0.80 respectively, while the purple (dash-dot-dotted) line corresponds to a model with $\Omega_m = 0.30$ but $\sigma_8 = 0.50$. The plot shows that the measurement of $\langle\kappa^2\rangle$ and $\langle\kappa^3\rangle$ are much more sensitive to the $\Omega_{\rm m}$, σ_8 param-

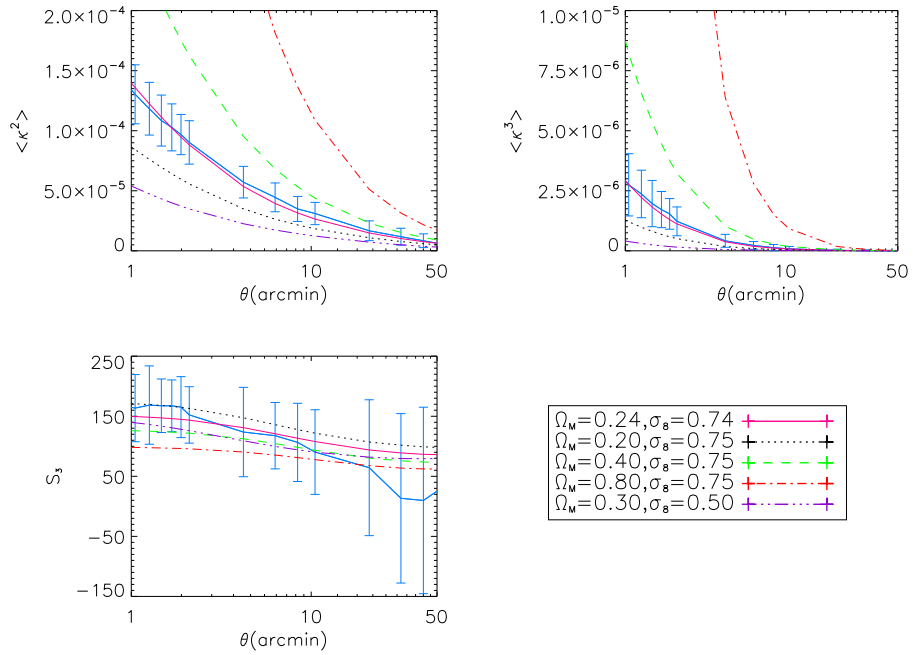

Figure 6.10: The comparison between the measured values of $\langle\kappa^2\rangle$, $\langle\kappa^3\rangle$ and S_3 and different cosmological models over a survey area of 12.84 deg^2. The blue line shows the measured data points, and the pink (solid) line is the fiducial model. The black (dotted), green (dashed) and red (dash-dotted) lines are models with the same $\sigma_8 = 0.75$ and values of $\Omega_\mathrm{m} = 0.20, 0.40$ and 0.80, respectively, while the purple (dash-dot-dotted) line corresponds to a model with $\Omega_\mathrm{m} = 0.30$ but $\sigma_8 = 0.50$. The plots show that the measurement of $\langle\kappa^2\rangle$ and $\langle\kappa^3\rangle$ are much more sensitive to the Ω_m, σ_8 parameters than the skewness S_3. This is why we cannot currently constrain the $\Omega_\mathrm{m} - \sigma_8$ plane with skewness measurements.

eters than the skewness S_3, therefore their ability to separate various cosmological models is stronger.

6.5 Canada-France-Hawaii Legacy Survey Three-point Statistics Predictions

The Canada-France-Hawaii Telescope Legacy Survey covers 170 deg^2 in four seperate patches [Fu et al., 2008]. Measurements of the two-point cosmic shear statistics have been published using the first year (Hoekstra et al. [2006], Semboloni et al. [2006] and Benjamin et al. [2007]) and third year data release [Fu et al., 2008] in addition to studies of galactic scale dark matter halos [Parker et al., 2007]. At the time our work on this project was carried out, the full CFHTLS data had not yet been released. The goal of this work was to predict the expected improvement for cosmological parameter constraints, using a combination of two- and three-point lensing statistics on the completed CFHTLS-wide survey. For this purpose, a mock CFHTLS-wide survey type of 170 deg^2 was generated using a limiting magnitude of $m_{\rm lim} = 24.5$ (i-band) with $n_{\rm g}$=22 galaxies per arcmin^2, $z_{\rm med}$=0.91 and σ_ε=0.44 and the potential contamination by residual systematics was ignored.

Figure 6.11 shows the $\Omega_{\rm m}$ and σ_8 error contours from a joint measurement of $\langle\kappa^2\rangle$ and $\langle\kappa^3\rangle$ for the three filters used in this study. It is clear that the top-hat filter leads to a more significant degeneracy breaking between $\Omega_{\rm m}$ and σ_8, which can be understood by the fact that this filter preserves modes with wavelengths larger than the smoothing size, while the aperture filters are not sensitive to large scale variations. The joint two- and three-point analysis of the completed CFHTLS-Wide will constrain $\Omega_{\rm m}$ and σ_8 to 17% and 10%, respectively. This corresponds to a gain factor (GF) of ~ 2.5 (for $\Omega_{\rm m}$) and ~ 2.1 (for σ_8) improvement on the two-point analysis alone when the top-hat filter is used. It is interesting to compare figure 6.11 to a generalized χ^2 approach which can serve to quantify the performance of the different filters. The generalized χ^2 is defined as

$$\frac{S}{N} = \sqrt{d^T * \mathbf{C}^{-1} * d}, \tag{6.11}$$

where $\mathbf{C}$ is the covariance matrix of the statistics under consideration. This approach takes the correlation between scales, as well as noise levels of each fileter into account. The results for a 12.84 deg^2 survey and limiting magnitude $m_{\rm lim} = 24.5$ are shown in table 6.3, and they indicate that for two-point statistics the different filters are equivalent. The top-hat filter outperforms the aperture filters for

the three-point statistics. It is a direct illustration that top-hat preserves small and large scale modes, and it is therefore more sensitive to non-linear effects. This invalidates the fact that the compensated Gaussian filter is the most efficient measure of the skewness of the convergence [Zhang et al., 2003]. The reason lies in the fact that for a fair comparison the maximum smoothing scale for compensated Gaussian filter may not exceed a third of top-hat and aperture smoothing radii. This can be seen by looking at the equations which define the shape of the filters (see Section 6.3.4).

S/N	$\langle\kappa^2\rangle$	$\langle\kappa^3\rangle$	S_3
Top-hat	6.19	2.68	5.45
Aperture	6.05	1.61	2.17
compensated Gaussian	6.93	1.88	3.24

Table 6.3: The generalized χ^2 results for top-hat, aperture and compensated Gaussian filters. The full covariance matrix is that of the 12.84 deg^2 maps. The data d is from the κ-maps smoothed with top-hat, aperture and compensated Gaussian filters. The correlation between the scales are contained in the signal-to-noise ratio. For example, although the measurements with top-hat filter result in a larger signal, they are highly correlated, unlike the aperture filter measurements, which have lower signal with less correlation between the measurement scales.

The joint $\langle\kappa^2\rangle - \langle\kappa^3\rangle$ likelihood analysis with top-hat, aperture and compensated Gaussian filters proved to be promising, whereas the skewness which is in principle a very interesting statistic inferred very weak cosmological constraints even for the current largest weak lensing survey at 170 deg^2. Figure 6.12 shows skewness likelihood contours obtained using both top-hat and compensated Gaussian filter for CFHTLS-like survey confirming what stated above about the poor efficiency of the skewness.

One of the forthcoming weak lensing surveys is the KIlo Degree Survey (KIDS area of 1500 deg^2 at $m_{\rm lim}$=23.5). We performed for the KIDS survey the same analysis as for the CFHTLS-Wide to forecast the accuracy of the likelihood constraints using two- and three-point shear statistics. Moreover, for comparison the calculations were repeated for a survey with the same observing time needed for the KiDS survey but different total area and depth. The results establish which survey design

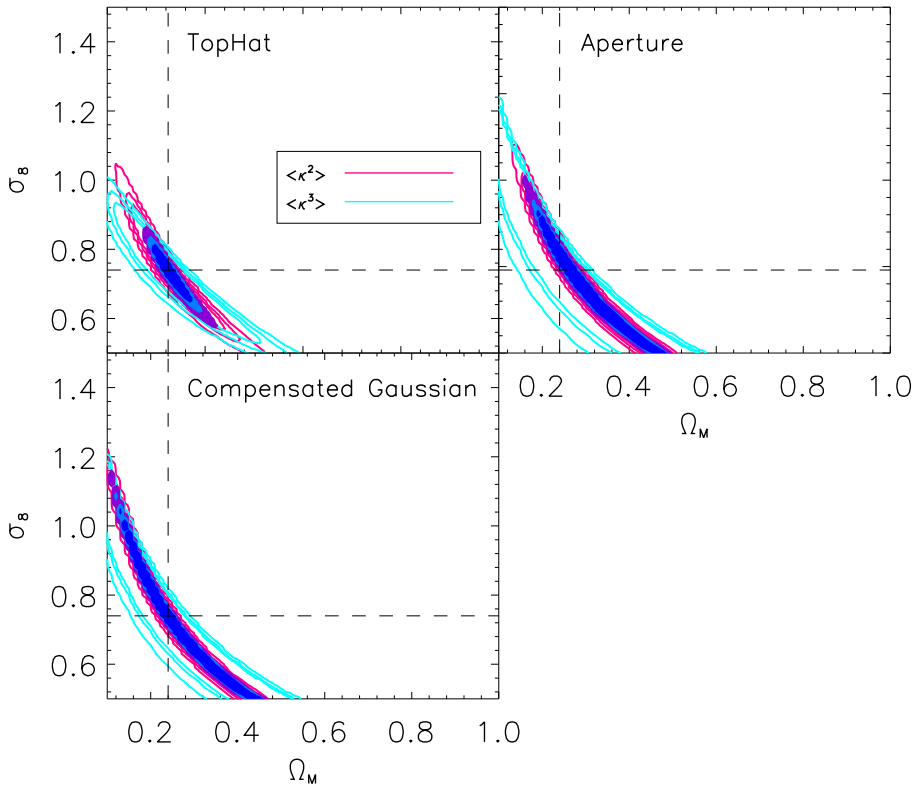

Figure 6.11: The cosmological constraints on $\Omega_{\rm m}$-σ_8 plane obtained with different smoothing filters. The contours show the $\langle\kappa^2\rangle$ and $\langle\kappa^3\rangle$ joint likelihood forecast based on CFHTLS completed area. The survey area is 170 deg^2 and the limiting magnitude is 24.5 with the full redshift distribution. Here the pink (dark grey) contours show the $\langle\kappa^2\rangle$ and the cyan (light grey) contours show the $\langle\kappa^3\rangle$ constraints. The filled contours correspond to the 1σ, 2σ and 3σ errors for the joint likelihood. The fiducial model used is a ΛCDM with $\Omega_m = 0.24$ and $\sigma_8 = 0.74$. The degeneracy direction of the $\langle\kappa^2\rangle$ and $\langle\kappa^3\rangle$ likelihood is different (especially when the maps are smoothed with compensated Gaussian filter) so their joint likelihood results in a tighter constraints on the parameters. The joint likelihood here is calculated by taking into account the cross-correlations between $\langle\kappa^2\rangle$ and $\langle\kappa^3\rangle$ at all scales.

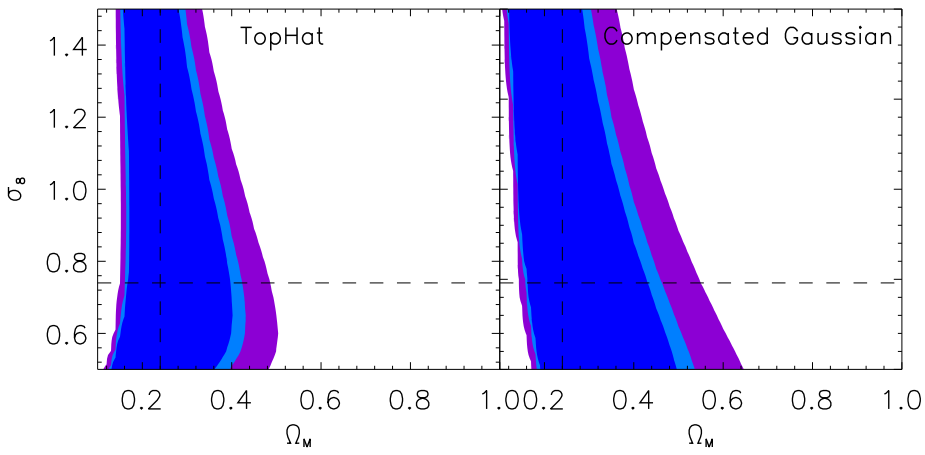

Figure 6.12: The skewness S_3 likelihood analysis for the CFHTLS-wide predictions. The smoothing filters top-hat and compensated Gaussian are used. The aperture filter does not provide any constraint on the $\Omega_{\rm m} - \sigma_8$ plane for the given survey characteristics. The covariance matrix contains both the cosmic variance and the statistical noise.

would be the most optimal to infer constraints using the joint two- and and three-point shear statistics. The expected likelihood contours for the complete KIDS survey are shown in the panel 6.13a, whereas panel 6.13b shows the same results when a deeper ($m_{\rm lim}$=24.5) and narrower (area=450 deg^2) survey given the same observing time was considered. As expected from Figure 6.8 the shallower KIDS gives better results for the joint likelihood, but the skewness would be slightly better measured from the deeper ($m_{\rm lim}$=24.5) survey.

6.6 Conclusion and Discussion

We studied how useful the measurement of the two- and three-point shear statistics can be to derive cosmological constraints under realistic observing conditions. One of the limitations of the previous work on this topic was the disconnection between the source redshift distribution and the survey depth under consideration. Here,

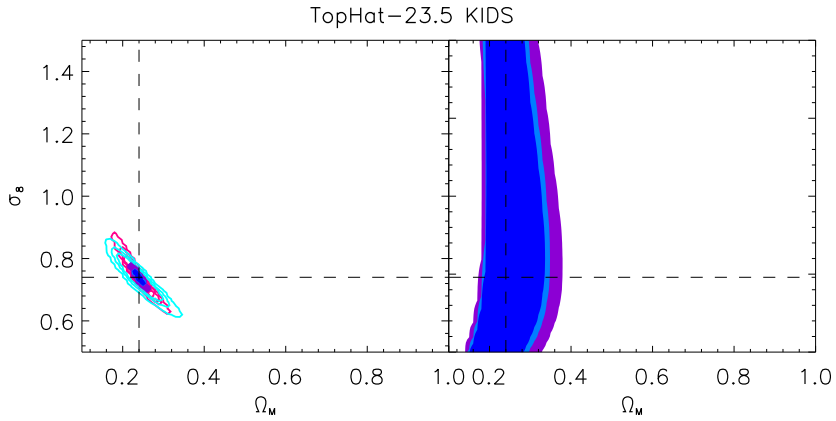

(a)

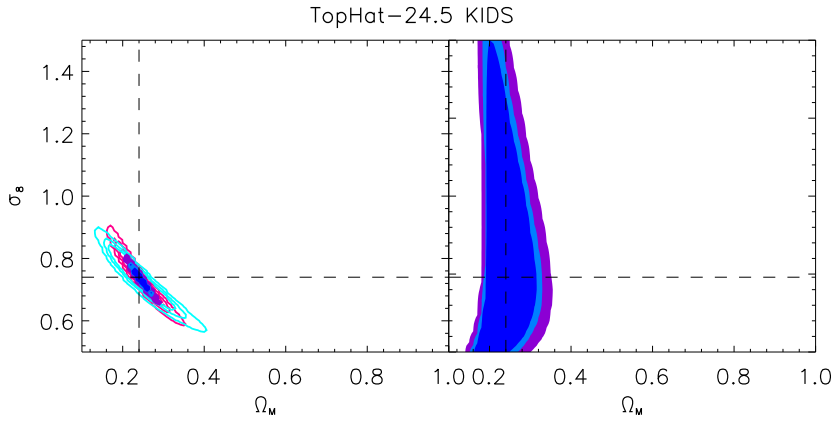

(b)

Figure 6.13: The comparison between a KiDS-like survey at two limiting magnitudes. The right panels show the likelihood contours of $\langle\kappa^2\rangle$ and $\langle\kappa^3\rangle$ smoothed with the top-hat filter. The left panels are the skewness contours. The survey area for the panel (a) is 1500 deg^2 as is planned for the KiDS survey with $m_{\rm lim}$=23.5. In panel (b) the observing time is kept the same and the survey area if adjusted to 450 deg^2 for $m_{\rm lim}$=24.5.

a set of ray-tracing simulations was populated with source galaxies that follow a redshift distribution and galaxy number density calibrated from real data.

We then investigated how well the parameters σ_8 and Ω_m can be measured with different smoothing filters for different survey depths. For a fixed observing time, the results of the study favoured the medium depth and width survey over shallower and wider or deeper and narrower surveys. There is an optimal survey depth versus size for which the source density (survey depth) and cosmic variance (survey area) are balanced, which turns out to be a large and shallow survey. CFHTLS survey proves to be promising for the measurements of two- and three-point statistics. Also our results can be applied to surveys covering a large fraction of the sky with no limitation on the observing time (e.g.PanSTARRS and LSST) by a simply rescaling the covariance matrices. They can also be extended to space data if the amplitude of ellipticity noise and galaxy number counts are adjusted according to space observations (this is particularly relevant for a wide field space imager like that of JDEM).

We find that the lensing statistics are best measured at scales between 1 to 30 arcminutes, where the contribution of statistical noise, cosmic variance and the mixed term are minimal. We also find that the different smoothing filters give similar results although the top-hat appears to include more modes and is therefore slightly better than the others. Combining $\langle\kappa^2\rangle$ and $\langle\kappa^3\rangle$ is promising to achieve cosmological constraints in the $\Omega_m - \sigma_8$ parameter space. On the contrary the skewness of the convergence does not appear capable of breaking the degeneracy between σ_8 and Ω_m as initially expected (Bernardeau et al. [1997] and van Waerbeke et al. [1999]). The reason is that the cosmic variance on S_3 is comparable to the difference in lensing signal amplitude for the different cosmological models of interest. Only very large surveys will be able to measure the skewness accurately.

We forecasted the cosmological constraints for the CFHTLS-wide completed survey finding that the combination of two- and three-point functions on the CFHTLS will greatly enhance the measurement of σ_8 and Ω_m. A similar calculation showed the potential precision achievable with the future KiDS survey.

This study has some limitations which will be investigated in future work. One of them is the fact that the source galaxies are clustered in three dimensional space which overlap with lens redshift distribution (a problem known as the source clus-

tering problem, Bernardeau [1998]). This effect leads to a change in the skewness of the convergence (by as much as 25%), and its impact on the three-point statistics has not been evaluated yet. A recent study also showed potential impact on the two-point statistics, although at a moderate level (Forero-Romero et al. [2007]). Another limitation is the potential impact of intrinsic alignment on three-point statistics. This is particularly relevant for shallow surveys such as PanSTARRS or KiDS (Semboloni et al. [2008]). This effect should be taken into the account as well. We would be able to investigate these two complications with ray-tracing simulations which include galaxies in dark matter halos; this can be realized by the use of semi analytical models such as the ones described in Forero-Romero et al. [2007].

Chapter 7

CFHTLenS results

In this chapter we first provide an overview of the CFHTLS data and the CFHTLenS collaboration. We then explain the object selection and procedure for the three-point statistics studies performed on this data set and present the results of the joint 2- and 3-point statistics cosmological parameter constraints. This is the first ever ground-based weak lensing higher order statistics constraint.

7.1 CFHTLS Data

The Canada-France-Hawaii Telescope is a 3.6 meter telescope located at the top of Mauna Kea in Hawaii. The telescope is operated by the National Research Council (NRC) of Canada, the Institut National des Science de l'Univers of the Centre National de la Recherche Scientifique (CNRS) of France, and the University of Hawaii. The legacy survey started in 2003 with weak gravitational lensing studies as one of the major science goals. The wide component of the survey consist of 160 $\deg^2$ of optical data acquired by Megacam during 450 nights (2300 hours) over the span of five years. MegaCam is the wide -ield imaging camera on Megaprime and is a 340 Megapixel camera (2048×4612 pixels) with 0.187 arcsec resolution per pixel. Thus the field of view covered by MegaCam is roughly 1 $\deg^2$. The data were collected in five bands (u^*, g', r', i' and z') down to the limiting magnitude of 24.5 in i' band. Figure 7.1 shows the Megacam filter set transmission for every band [1].

[1] http://www.cfht.hawaii.edu/Instruments/Imaging/Megacam/specsinformation.html

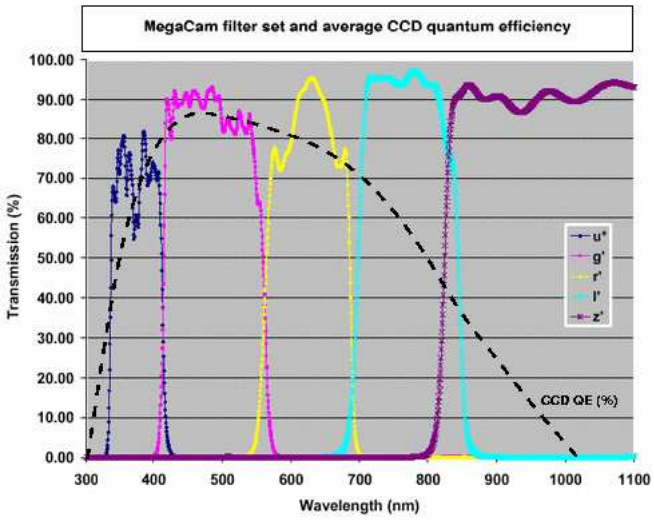

Figure 7.1: MegaCam filter set transmission and average CCD quantum efficiency. See footnote for credits.

Also table 7.1 lists the mean bandwidth of each of the five filters of this particular camera. The wide data are collected from four selected fields on the sky, W1 (72 pointing), W2 (25 pointings), W3 (49 pointings) and W4 (25 pointings). Figure 7.2 shows the location of CFHTLS wide and deep fields on the sky [2]. The width of the survey allows for a very large number of galaxies. It is crucial to have as many galaxies as possible in the sample since the shape distortions can only be studied statistically. The observations of the CFHTLS are publicly available through the Canadian Astronomy Data Centre (CADC) [3]. The CFHTLS-wide component is optimal for weak lensing studies for the following reasons. The survey covers a wide area, enabling observation of many galaxies. Since weak lensing studies are statistical in nature, a larger sample is very desirable. Also many parts of the survey overlap with pre-existing surveys, for which spectroscopic redshifts have been estimated. This allows for well-calibrated photometric redshift estimates of such a large sample of galaxies. Accurate redshift estimates are crucial to the interpretation of the weak lensing measurements. The seeing for the survey was at

[2] http://www.cfht.hawaii.edu/Science/CFHTLS/
[3] http://www1.cadc-ccda.hia-iha.nrc-cnrc.gc.ca/cadc/

$\theta \leq 0.8$ arcsec in the *i*-band filter, which allows for shape measurements of many resolved galaxies. The *i*-band seeing was the best compared to other filters. The first generation of cosmic shear results from the CFHTLS wide survey can be found in Hoekstra et al. [2006], Benjamin et al. [2007] and Fu et al. [2008] and the deep component in Semboloni et al. [2006].

7.2 CFHTLenS Collaboration

Canada France Hawaii Telescope Lensing Survey (CFHTLenS) is a worldwide collaboration of many faculty, postdocs and graduate students. The science nodes include institutions in Canada, France, The Netherlands, Germany, Italy, Scotland, England, Spain, China and Japan (see the collaboration website [4] for more details). The collaboration was formed in 2009 (PI: Dr. Ludovic van Waerbeke and Dr. Catherine Heymans), with the main goal of better understanding and reducing the systematics effects of the CFHTLS data. In the process, the CFHTLenS team re-reduced the CFHTLS data and produced scientific catalogues independent from the previous releases. The earlier releases suffered from residual systematics, such as strong B-modes at large scales, strong galaxy-star cross-correlation residuals in nearly half of the fields and large field-to-field variance.

The image stacking, masking and photometric redshift estimation, along with shape measurements have been done by the collaboration with the goal of controlling and understanding the systematics in the data. For over three years many systematics tests have been performed by the team to investigate the effects of reduction steps on the systematics and to verify the sanity of the data set. The weak lensing shear is about a 1% change in the galaxy shape and small hidden systematics can lead to very biased interpretations of the data.

The data reduction pipeline is based on the `THELI` pipeline (Erben et al. [2005] and Erben et al. [2009]) [5] which is publicly available. In summary, the photometric redshifts were measured with the publicly available `BPZ` (Bayesian Photometric Redshifts) code (Benítez [2000]), as explained in Hildebrandt et al. [2011]. This method combines the spectral redshift χ^2 minimization with magnitude/redshift

[4] http://www.cfhtlens.org/

[5] http://www.astro.uni-bonn.de/ theli/

Table 7.1: MegaCam filter characteristics.

Filter	u^*	g'	r'	i'	z'
Central wavelength (nm)	374	487	625	770	n/a
Wavelength range (nm) at 50 %	337–411	414–559	564–685	698–843	823-...
Bandwidth (nm)	74	145	121	145	n/a
Mean transmission (%)	69.7	84.6	81.4	89.4	90.2

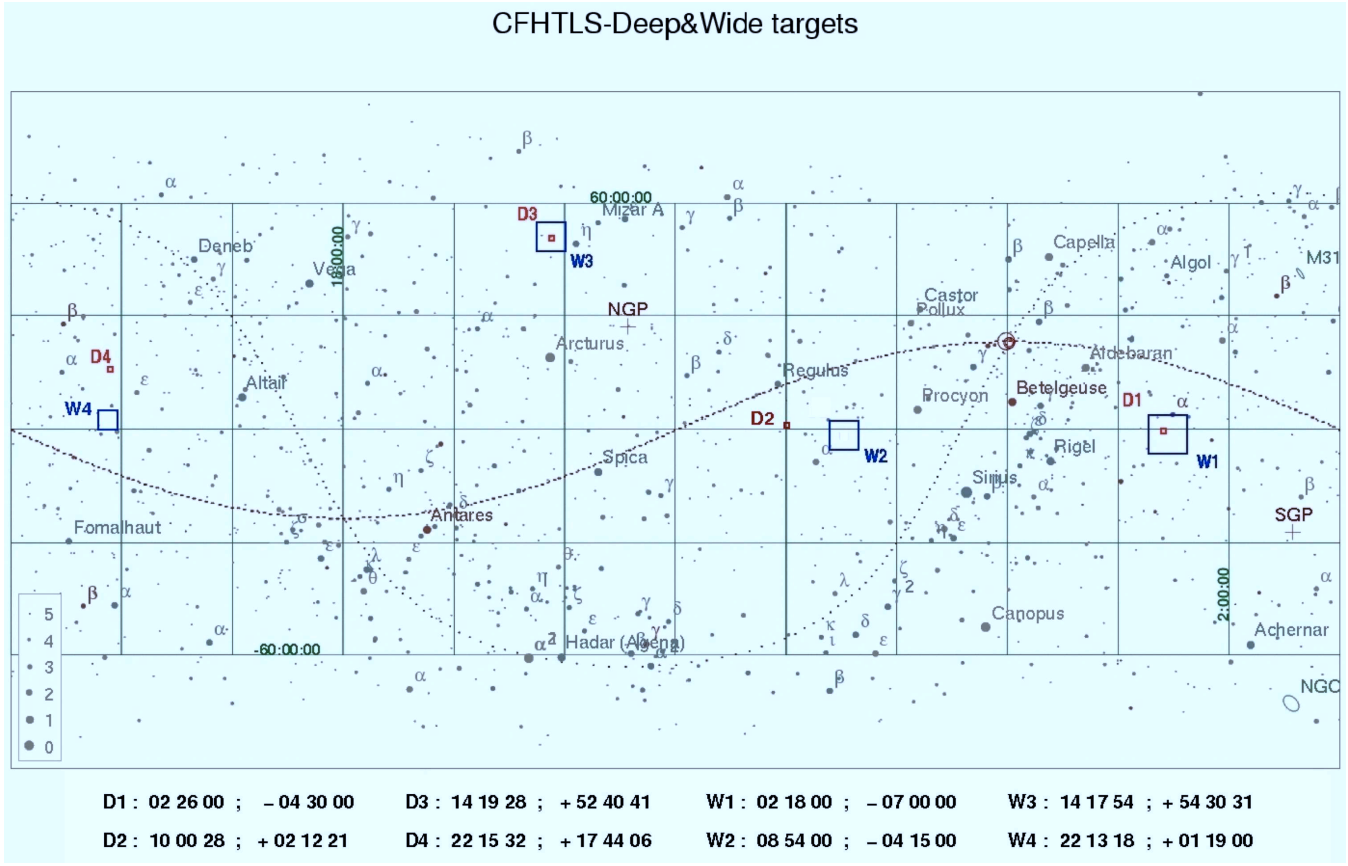

Figure 7.2: Position of CFHTLS wide (blue squares) and deep (small red squares) fields on the sky.

priors. The accuracy of the photometric redshifts was tested against the spectroscopic redshifts from the VIMOS VLT Deep Survey (VVDS) which overlaps 20 of the CFHTLenS fields. As part of the process, each galaxy is assigned a parameter `ODDS` which describes the accuracy of the photometric redshift estimation for that galaxy. We use this parameter to eliminate low accuracy redshifts from the data.

The galaxy shapes were carefully measured by the Bayesian approach called the `lensfit` method [Miller et al., 2007] which assumes a theoretical galaxy surface brightness profile, convolved with the modeled PSF (Point Spread Function) and Bayesian priors on the noise to calculate likelihood on shear estimation. Each galaxy is then assigned a `weight` value based on the accuracy of the shape measurement. The details of the systematics tests will follow in Heymans and van Waerbeke et al. in prep.

For every 1 deg^2 of data a list of measured ellipticities, best photometric redshift estimates and coordinates is provided along with many more parameters such as `weight`, `ODDS`, magnitudes and mask flags. We then apply selections to these parameters to trim the catalogue into a cleaner catalogue for our analyses, which will follow in the next section. The choice of selection cuts is important since it is desirable to have as many objects in the catalogues as possible without sacrificing the integrity of the data. In section 7.3.1 we explain the selection criteria used in our 2+3-point statistics study.

7.2.1 Masking

Every CFHTLenS field suffers from bright stars as well as other astronomical features that must be eliminated from the analysis. Some examples of such features include the extended halos around the very bright stars, the stellar diffraction spikes and tracks of asteroids and satellites. In order to remove such objects from the catalogues, various shapes of masks have to be laid on the image so that the objects within those regions can be excluded from the shear catalogues. An automated masking routine developed by Erben et al. [2009] was applied to the CFHTLenS images. Although automatic masking is very beneficial for such large surveys, it has some shortcoming as well.

As a contribution to the collaboration and the data processing section, along

with other PhD students in the team, we checked the automated masks generated for each of the fields by eye. As a result of eyeballing the images, we found some satellite/asteroid trails that were left unmasked, that if not attended to, would have been detected as very elongated galaxies by the object detection routines. These false detections will then result in extreme shear values and hence bias the average shear measurements. Also the automatic scripts are overly conservative in removing the stellar halos. There are many background faint galaxies that lie within a stellar halo which are useful for the lensing studies. As explained before we are interested in a large sample of galaxies, so a careful observation of the automatically masked stellar halos could rescue many of these faint galaxies and enlarge the sample in the catalogues.

As an example we show parts of the `W1p3p1` field. Figure 7.3 shows a faint asteroid trail that was missed in the automated masking. The white box is what was manually placed around the trail to mask it out. Figure 7.4 shows the result of the automated masking, the green lines contour the stars and their diffraction spikes, while the red lines mask out the asteroid trails. One can see the over plotted magenta ellipses that are the result of the object detection software `SExtractor` [Bertin and Arnouts, 1996][6]. This shows that if the asteroid trails were not masked out they would have been picked up as very elongated objects. In 7.5 we show the stellar halo for which the mask (the white lines) was adjusted to both minimize the masked area and also include the very long diffraction spikes.

7.2.2 The Clone

As yet another contribution to the CFHTLenS collaboration, we developed a pipeline to generate the Clone of the CFHTLenS data. The Clone is sets of catalogues that represent the real data in all aspects, except that the shear values are taken from noise-free simulations in order to assist the systematics tests and the study of various aspects in the catalogues such as masking biases. We generate seven full sets of clones that are available to all members of the collaboration for the purposes of covariance matrix calculations. Chapter 9 is dedicated to explaining the details of the clone production.

[6] http://www.astromatic.net/software/sextractor

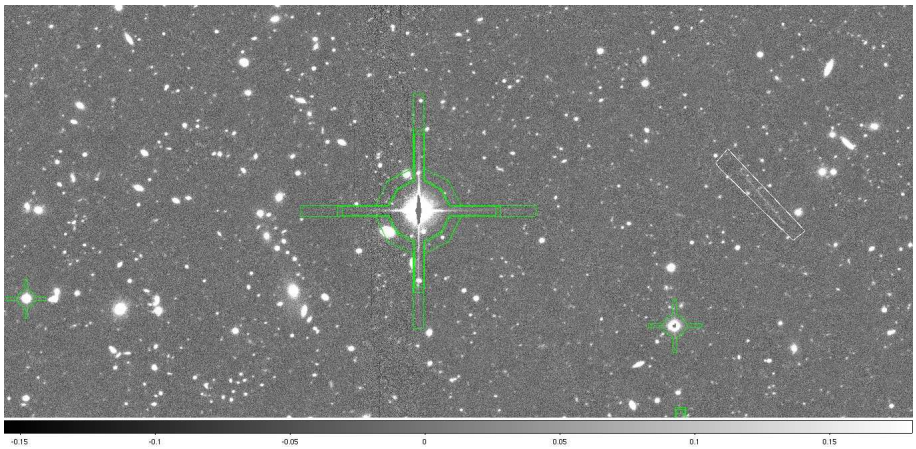

Figure 7.3: A faint asteroid/satellite trail that was missed by the automated masking (green). A manual mask (white) was added to the image.

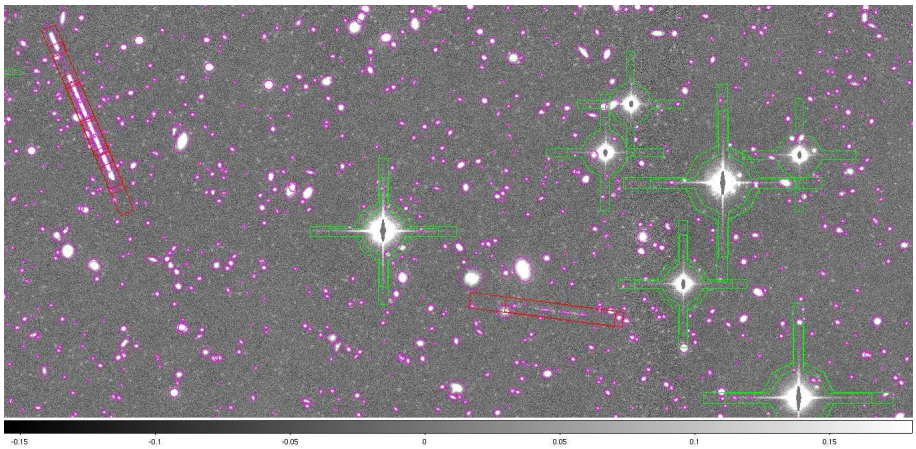

Figure 7.4: The asteroid/satellite trails (bright straight white lines) can be picked up as highly sheared objects by the object detection software `SExtrator`. The magenta ellipses show the detected objects.

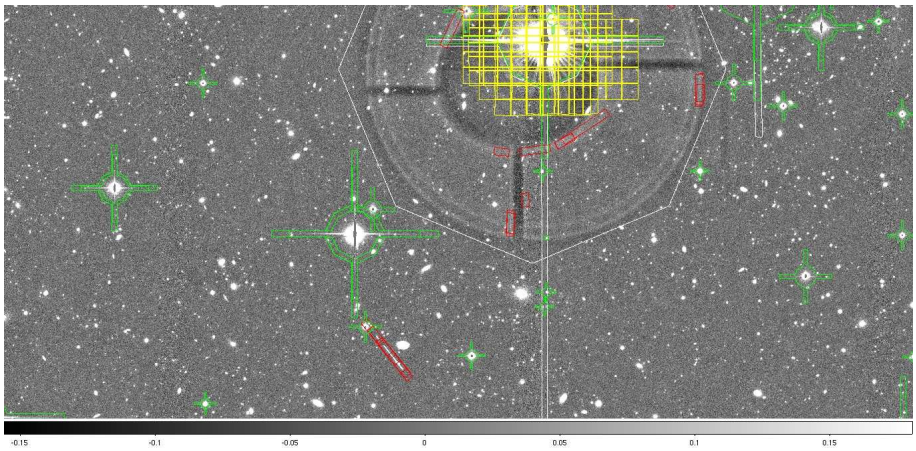

Figure 7.5: An example of stellar diffraction spikes bleeding on the CCD which have to be masked manually (white). Also the mask on the high contrast stellar halo must be adjusted. Masks shown in green, yellow and red colors are generated automatically. White masks are the additional manual masking.

7.3 CFHTLenS 2+3-point Statistics

The two-point $\langle M_{\rm ap}^2 \rangle$ statistics have proved to be a powerful tool to study the power spectrum and Gaussian fluctuations in the Universe. Since $\langle M_{\rm ap}^2 \rangle$ is the variance of the field inside the aperture it is unable to measure any non-Gaussianities of the field, for which higher order statistics such as $\langle M_{\rm ap}^3 \rangle$ are required. The density contrast shown in equation 2.14 by construction has a minimum value of -1. However when structures grow, it can increase indefinitely leading to large values. One can see that when considering non-linear structure formation, the matter density distribution is far from a Gaussian, so it is sensible to seek higher order statistics to probe the non-Gaussian features. It has also been suggested (Bernardeau et al. [1997]; van Waerbeke et al. [1999]; Van Waerbeke et al. [2001a], Kilbinger and Schneider [2005]; Takada and Jain [2004]) that the higher order statistics when combined with the standard two-point statistics can improve the cosmological constraints of the two-point statistics alone. Furthermore with the aid of numerical simulations we demonstrated in Vafaei et al. [2010] (see chapter 5) the degree of this improvement for various filter choices.

Previously several studies have been performed that detected the non-Gaussian signal in the weak lensing field (Bernardeau et al. [2002]; Bernardeau et al. [2003]; Pen et al. [2003] on the VIRMOS-DESCART survey and Jarvis et al. [2004] on the CTIO survey). None of the mentioned detections however lead to cosmological parameter estimations. This is understandable, given that the three-point signal is much weaker and nosier than the two-point one. Also there is an overall $10-20\%$ inaccuracy in the theoretical predictions of the three-point functions which affects the parameter estimations (Van Waerbeke et al. [2001a]; Semboloni et al. [2011a]). Systematic effects such as the non uniform point spread function of the telescope alter the shape of the observed galaxies (Heymans et al. [2006a]; Massey et al. [2007]; Kitching et al. [2009]; Semboloni et al. [2009]), while ignoring the intrinsic alignment of the source galaxies due to the local dark matter distribution, can arise biases to the estimations (Crittenden et al. [2001]; Hirata and Seljak [2004]).

Recently Semboloni et al. [2011b] used the Hubble Space Telescope COSMOS survey to measure the two- and three-point statistics of the cosmic shear. The results are the first space-based higher order statistic, and in addition they provided remarkable cosmological constraints. Here we follow the same procedure with the choice of compensated filter of van Waerbeke [1998] and Crittenden et al. [2002], which we previously (in chapter 4) referred to as the compensated Gaussian filter. This choice compared to the Schneider et al. [1998] filter, has the advantage of ease of calculations of the three-point correlation function. The following sections describe the galaxy selection criteria, redshift distribution, theoretical predictions, covariance matrices and the preliminary results of the likelihood analysis of the three point measurements on the CFHTLenS data set.

7.3.1 Galaxy Selection and Redshift Distribution

We choose all the *i*-band catalogues of W1-4 fields. The sub fields in each case are combined to make a large mosaic catalogue. The following cuts are made to exclude objects with `ODDS` ≤ 0.7; `bestzphot` ≤ 0.1; `weight` ≤ 0; and `Mask` ≤ 2 in the analysis. We cut out objects with redshifts less than 0.1, because it was shown by Erben et al. [2009] that these objects contain the highest levels of cross contamination between the redshift bins. We also chose galaxies with non zero

weights. The mask flag represents the level of masking. As explained in section 7.2.1, the student members of the CFHTLenS collaboration performed a manual mask check on the images. Some of the stellar halos were conservatively masked by the automated routine. By choosing objects with mask flag ≤ 2, we take a less conservative approach and consider the objects within those masks as valid members of our sample.

The number of subfields with *i*-band data for each mosaic is: W1 (63 out of 72 subfields); W2 (all 25 subfields); W3 (all 49 fields); and W4 (20 out of 25 fields). This results in a total area of 157 deg^2 rather than 171 deg^2. We included the *i*-band data only, while the investigation on preference between $i-$ and $y-$ band sub-fields was in progress by the systematics team. The total number of galaxies in each of the mosaic fields, after the basic cuts is: W1:2,363,977; W2:705,772; W3:1,730,225; and W4:626,185. This is a total of 5,426,168 galaxies in our analysis, which leads to $n_{\rm g} = 9.6$ per arcmin^2. The assumption is that the whole area of the mosaics are filled with galaxies and ignore the area lost due to masking. This assumption clearly underestimates the galaxy number density that in turn causes an over estimation of the noise, which is preferable to its under estimation. A more careful approach would be to verify the fraction of the mosaic area that is covered by masks when the masking criterion of $\texttt{mask} \leq 2$ is chosen.

The source galaxy redshift distribution plays an important role in interpreting the measured weak lensing signal. Various weak lensing statistics relate to the convergence power spectrum, as explained in chapter 4, which in turn, in combination with the source galaxy redshift distribution, are related to the matter power spectrum (See equation 3.34). For the purpose of the theoretical prediction the redshift probability distribution function needs to be calculated. We include the weight of each galaxy in the distribution, since their contribution to the correlation function is proportional to the weight. We use the function suggested by Brainerd et al. [1996] to fit the total redshift distribution:

$$n(z) = \frac{\beta}{z_0 \Gamma\left(\frac{1+\alpha}{\beta}\right)} \left(\frac{z}{z_0}\right)^{\alpha} \exp\left[-\left(\frac{z}{z_0}\right)^{\beta}\right]. \tag{7.1}$$

Here α, β and z_0 are free parameters. The best fit values for the free parame-

Field	$\alpha \pm 1\sigma$	$\beta \pm 1\sigma$	$z_0 \pm 1\sigma$
W1	0.786 ± 0.007	3.378 ± 0.0231	1.064 ± 0.002
W2	0.494 ± 0.757	3.379 ± 4.497	1.059 ± 0.411
W3	1.738 ± 0.245	1.786 ± 0.122	0.632 ± 0.036
W4	1.759 ± 0.220	2.016 ± 0.1458	0.683 ± 0.034
All	2.231 ± 0.002	1.346 ± 0.001	0.420 ± 0.0003

Table 7.2: Redshift distribution fitting parameters based on equation 7.1, along with the standard deviation for each parameter.

ters, along with 1σ standard deviation for all cases, are shown in table 7.2. Figures 7.6a−7.6d show the redshift distribution for each of the CFHTLS fields overplotted with the fitting function. For all the four fields combined, the total redshift distribution of the entire survey (after the galaxy selection mentioned in earlier) is shown in figure 7.7. Although individual fields seem to have less agreement between the redshift distribution and best fit curve, the total redshift distribution when all the four fields are combined, matches the fitting formula well. As shown in van Waerbeke et al. [2006], the Poisson noise limit on the redshift distribution is only valid for smaller surveys. So the slight disagreement on individual fields is not a concern for CFHTLenS sized survey. The fitting parameter errors are listed in table 7.2.

We also need an accurate redshift distribution to generate the covariance matrices. We treat the simulations as samples of data and compute the covariance between the measurements on the simulations. In order to best represent the actual data, the simulated slices have to be stacked according to the same redshift distribution as the data set. For this purpose, we divide the data catalogue into redshift bins such that the simulated slice with z_ℓ is the center of the bin. The width of each bin is the span of two adjacent source planes z_s that contain that z_ℓ slice. We then sum the number of galaxies in each bin and divide by the total area of the mosaic in arcmin^2 per redshift slice. As before, the area lost to masking is ignored. Figure 7.8 shows the resulting distribution for the simulated maps. We stack the redshift slices accordingly and then add the noise map generated the same way as in chapter 6. The two- and three-point statistics are calculated on the resulting map using various smoothing filters.

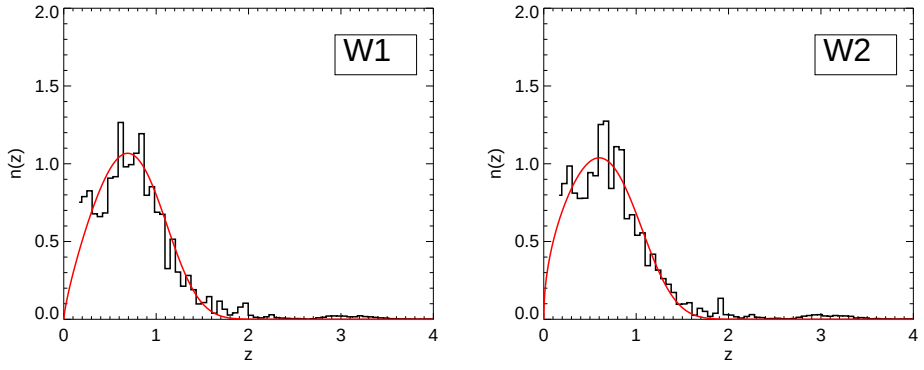

(a) W1

(b) W2

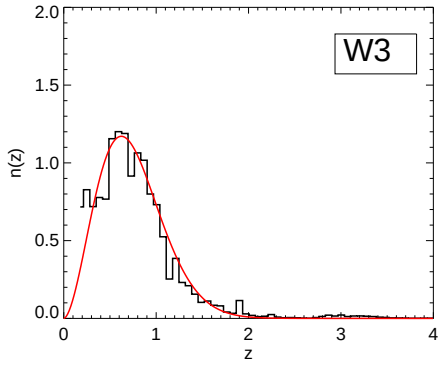

(c) W3

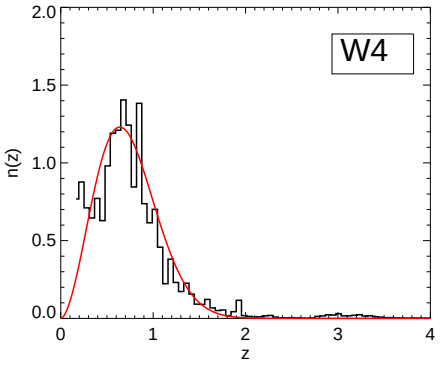

(d) W4

Figure 7.6: The weighted normalized histogram of the redshift distribution for each of the CFHTLenS fields. The galaxy selection is applied to the catalogues. The red line is the fitting formula with the values of the free parameters listed for each field in table 7.2.

7.3.2 Three-point Correlation Function and Theoretical Predictions

Combining equations 4.17 and 3.34 one can write the following:

$$\langle M_{\rm ap}^2 \rangle = 2\pi \left(\frac{3H_0^2\Omega_{\rm m}}{2c^2} \right)^2 \int_0^{\chi_{\rm H}} {\rm d}\chi \frac{g^2(\chi)}{a^2(\chi)} \int_0^{\infty} s{\rm d}s P\left(\frac{s}{f_K(\chi)}, \chi \right) [I(s\theta)]^2, \qquad (7.2)$$

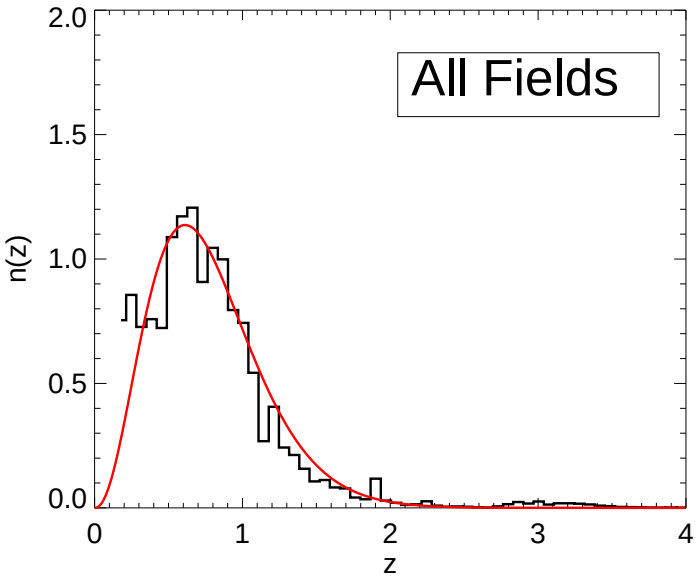

Figure 7.7: Galaxy redshift distribution for all the CFHTLenS mosaics combined after the selection criterion was applied to the catalogues. The red line is the fitting formula based on equation 7.1.

with

$$g(\chi) = \int_{\chi}^{\chi_{\rm H}} {\rm d}\chi' p_{\rm s}(\chi') \frac{f_K(\chi - \chi')}{f_K(\chi')}. \tag{7.3}$$

where $f_K(\chi)$ is the comoving angular distance, χ is the radial comoving coordinate, and $\chi_{\rm H}$ is the radial comoving coordinate of the horizon. One can see that the aperture variance $\langle M_{\rm ap}^2 \rangle$ depends both the matter power spectrum and the redshift distribution of the source galaxies $p_{\rm s}(\chi)$. Here $I(s\theta)$ is chosen to be the filter profile of the compensated Gaussian filter as explained in equation 4.18.

Schneider et al. [1998] found a similar relation for the third moment of the compensated filter statistics to be

$$\begin{aligned} \langle M_{\rm ap}^3 \rangle \quad &= \left(\frac{9 H_0^3 \Omega_{\rm m}}{2c^3} \right)^2 \frac{\Omega_{\rm m}}{2\pi} \int_{\chi}^{\chi_H} {\rm d}\chi \frac{g^3(\chi)}{a^3(\chi) f_K(\chi)} \int_0^{\infty} {\rm d}^2 s_1 P\left(\frac{s_1}{f_K(\chi)}, \chi \right) I(s_1\theta) \\ &\quad \times \int_0^{\infty} {\rm d}^2 s_2 P\left(\frac{s_2}{f_K(\chi)}, \chi \right) I(s_2\theta) I(|s_1 + s_2|) F_2(s_1, s_2). \end{aligned} \tag{7.4}$$

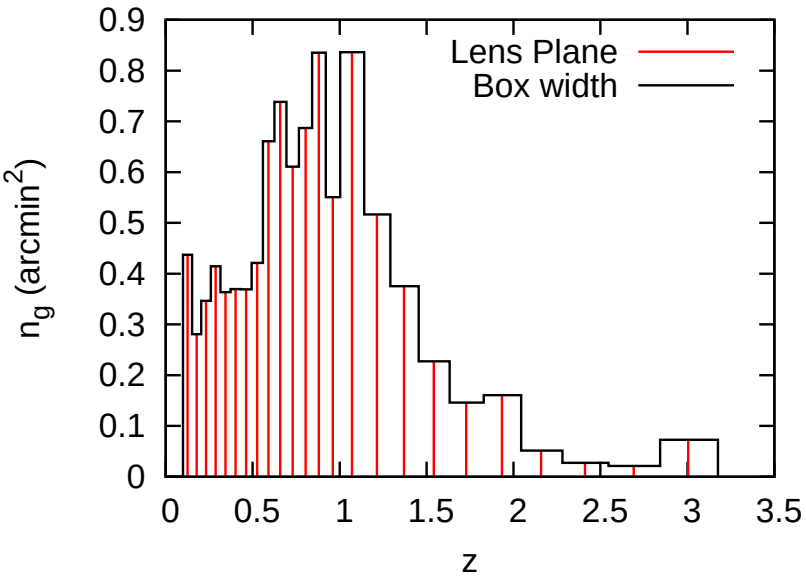

Figure 7.8: The weighted simulation map distribution per redshift slice to re-sample the redshift distribution of the data. The black lines show the simulation box width and the red impulse lines show the redshift of the lens plane that was used as the projected map.

Here $F_2(s_1, s_2)$ is the coupling between the two models of density fluctuation. This term can be calculated using the fitting formula suggested by Scoccimarro and Couchman [2001] who used N-body simulations to calibrate for the bispectrum calculations to 15% accuracy. Using the same fitting formula Van Waerbeke et al. [2001a] built the third order lensing predictions which were shown to be within $10-15$ % of the simulations. The predictions used here are based on the work of Van Waerbeke et al. [2001a], modified for the compensated Gaussian filter. The non-linear correction to the linear power spectrum is based on Peacock and Dodds [1996], and the transfer function was calculated based on the recipe of Eisenstein and Hu [1998]. We varied Ω_m between 0.1 and 1.0 and σ_8 between 0.4 and 1.4 in steps of 0.05. The rest of the cosmological parameters are fixed based on WMAP7 (Komatsu et al. [2011]) results, which are the ones used in the numerical simulations as well.

The relation in equation 7.4 shows how matter power spectrum and third mo-

ment of aperture mass are related. Similar to the two-point statistics approach, in practice we estimate the third moment of the aperture mass through calculations of the correlation function. The difference is that this time we consider correlations between the shear components of triplet galaxies rather than pairs. For this work we consider only the equilateral triangles, using the three-point correlation function (`3pcf`) code which was developed by Elisabetta Semboloni and first applied to the COSMOS data in Semboloni et al. [2011b]. This code is built based on the formalism of Zhang and Pen [2005] and Jarvis et al. [2004] for both two- and three-point correlation function measurements. Non-equilateral triangles will be included in the future steps of this project.

7.3.3 Covariance Matrix

The covariance matrix **C** can be split into three components as suggested by Schneider et al. [2002a]. We showed the components previously in chapter 6 equation 6.9. Here we compute the full **C** term by adding noise to the noise-free simulated convergence κ maps, so that all three terms will be included in the final covariance matrix. In order to add noise to the maps, we follow the recipe of van Waerbeke [2000], also applied in Vafaei et al. [2010]. The Gaussian random noise maps are generated and then scaled by a factor shown in 6.6 which depends on σ_ε (the shear variance), $n_{\rm g}$ (the galaxy number density) and Θ (the pixel size of the map).

For ellipticity variance we compute $\sqrt{\sigma^2_{\varepsilon_1}+\sigma^2_{\varepsilon_2}}$, where each of the σ_{ε_i} are the weighted variances of each of the shear components.The overall value is $\sigma^2_\varepsilon = 0.38$ for the four fields combined.

The covariance is defined as

$$\mathbf{C}(x_i,x_j) \equiv \langle (X(x_i)-\mu(x_i))(X(x_j)-\mu(x_j))\rangle, \tag{7.5}$$

where the angle brackets represent the ensemble average and $X(x_i)$ is the measured statistic at a given scale x_i with mean of $\mu(x_i)$ over all simulation realizations (185). We use 18 scales, for the single statistics case which leads to an 18×18 covariance matrix. For the joint statistics when 2- and 3-point measurements are combined, 36 scales are used: 18 for 2-point; and another 18 for 3-point statistics. The scales are the following: 0.42, 0.63, 0.84, 1.05, 1.26, 1.47, 1.89, 2.10, 3.15, 4.2, 6.3, 8.40,

10.5, 21.0, 29.4, 42.0, 50.4 and 58.8 arcmins. The correction factor (α^*) introduced by Hartlap et al. [2007] to remove the bias induced by having a limited number of samples is

$$\alpha^* = \frac{(n-1)}{(n-1)-p-1}. \tag{7.6}$$

In the case of single statistics, the number of scales p =18 and number of realization n =185, which is the total number of independent simulation realizations we have. For these values, we find $\alpha^* = 1.115$ and for the case of the joint likelihood, where p =36, we find α^*=1.25. We multiply each covariance matrix by the corresponding α^* factor for the likelihood analysis.

In order to display the level of correlation between the data points, we compute the correlation coefficient $\rho(x_i, x_j)$, defined as

$$\rho(x_i, x_j) = \frac{\mathbf{C}(x_i, x_j)}{\sqrt{\mathbf{C}(x_i, x_i)\mathbf{C}(x_j, x_j)}}. \tag{7.7}$$

Figure 7.9a shows the correlation coefficient for the noise-free 2-point statistics of the compensated Gaussian filter. In figure 7.9b we show the correlation coefficient of the 3-point statistics for the same filter. Note that each pixel is a smoothing scale: 0.42, 0.63, 0.84, 1.05, 1.26, 1.47, 1.89, 2.10, 3.15, 4.2, 6.3, 8.40, 10.5, 21.0, 29.4, 42.0, 50.4 and 58.8 arcmins. The apparent sharp transition between 13th and 14th pixel is due to the jump in the smoothing scale from 10.5 to 21.0 arcmins. This apparent sharp transition is visible in the following correlation coefficient matrices, since the choice of smoothing scales is not uniform. The reason is that as found in section 6.4, smoothing scales in the range of 1 to 10 arcmins have the lowest noise to signal ratio and hence desirable for our analysis.

When noise is added to the simulations, the level of correlation between the scales changes. In figures 7.10a−7.10c we show the noisy correlation coefficient results for the two-point statistics of top-hat, aperture and compensated Gaussian filters in order. Firstly one can compare the off diagonal correlation of these filters. It can be seen top-hat filter has the most correlated scales. Secondly, when comparing figure 7.9a to 7.10c, one can see the effects of noise added to the simulations, which decreases the correlations between the scales for the 2-point compensated Gaussian measurements.

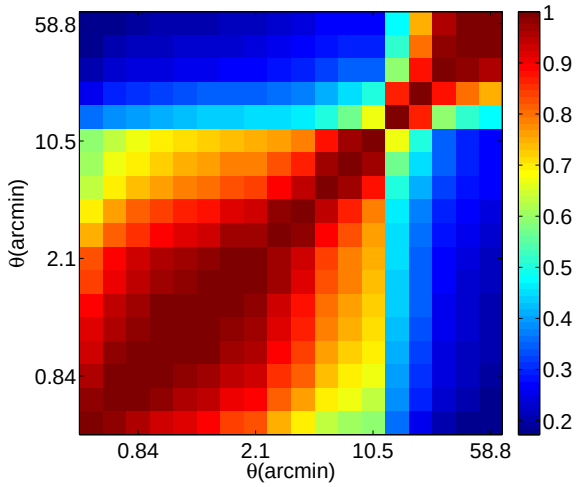

(a) Noisefree 2-points Compensated Gaussian

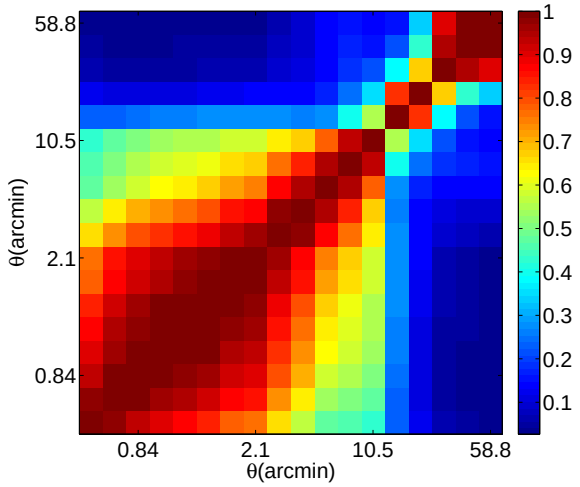

(b) Noisefree 3-points Compensated Gaussian

Figure 7.9: The correlation coefficient matrix for the noise-free 2- and 3-points statistics. The compensated Gaussian filter was used here with 18 scales. The noise-free simulated maps are stacked according to the CFHTLenS data redshift distribution.

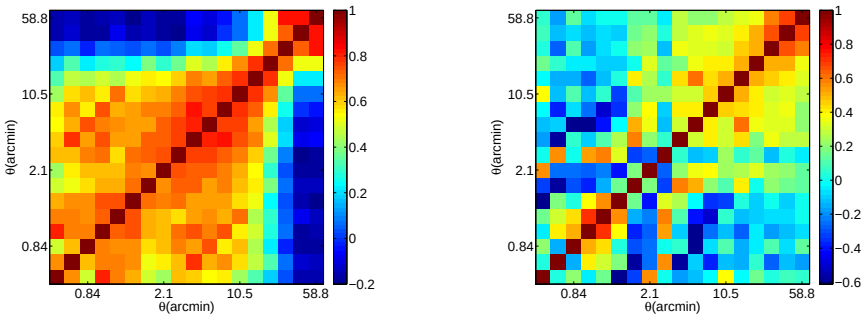

(a) 2-points top-hat

(b) 2-points Aperture

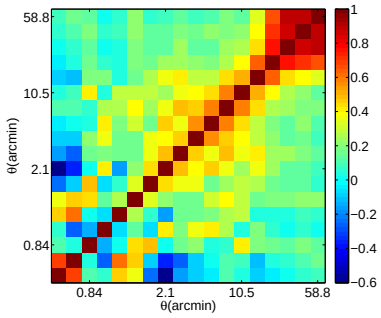

(c) 2-points Compensated Gaussian

Figure 7.10: The correlation coefficient matrix for the noisy 2- point statistics for various filter choices. The number of scales is 18. The noisy simulated maps are stacked according to the CFHTLenS data redshift distribution.

7.3.4 Likelihood Analysis

We use the standard likelihood analysis to infer cosmological parameter constraints from the measured data. The likelihood function we use here is

$$\mathscr{L} = \exp\left[-\frac{1}{2}(d-m)^T * \mathbf{C}^{-1} * (d-m)\right], \tag{7.8}$$

where d represents the data, m is the theoretical model and $\mathbf{C}^{-1}$ is the inverse covariance matrix over all simulated 185 lines of sight. We use 18 scales of measurement here. In Vafaei et al. [2010] we also showed that one can rescale the

covariance matrix for the 2- and 3-point statistics to adjust for the desired survey size, as the elements of the covariance matrix scale with the area. Here we rescale the simulated maps (each 12.84 deg^2) to 12.5 times larger, which leads to 160 deg^2. The theoretical models are generated based on the recipe explained previously in section 4.6 with variable Ω_m and σ_8, while all other cosmological parameters are kept constant to those of the WMAP7 (Komatsu et al. [2011]) values.

Figures 7.11a and 7.11b show the results of the EE and BB components of the two-point statistics for the top-hat and aperture filters, and 7.12a shows the two-point statistics measured with compensated Gaussian filter. Figure 7.12b shows the EEE, EEB, EBB and BBB components of the three-point statistics with compensated Gaussian filter. In these figures a subset of 18 smoothing scales are chosen to keep the plots less busy. This is justified due to high levels of correlation between the smoothing scales as shown previously. The likelihood contours presented later contain the full 18 smoothing scale measurements. The error-bars are 1σ deviations from 185 noisy simulations weighted according to the same redshift distribution. The theoretical predictions are shown as black lines. For pure cosmic shear signal, all combinations containing B-modes must vanish. The B-modes can be used to quantify the amplitude of the potential residual systematics in the data.
We present the results of the likelihood analysis of the two-point statistics of the CFHTLenS data in figure 7.13a$-$7.13c. The contours differ slightly from those shown in figure 6.5. The main reason lies in the fact that the galaxy number density in Vafaei et al. [2010] was assumed to be 22 per arcmin^2 for a survey of 24.5 limiting magnitude. With the selection cuts we applied to the CFHTLenS data, this number has dropped considerably to 9.6 galaxies per arcmin^2. The difference appears in the noise map generation and hence affects the size of the likelihood contours. Also the median redshifts for the two analyses are different (0.9 there and 0.7 here).

When two- and three-point statistics are combined, the joint likelihood results in much improved constraints. Figure 7.14b shows the preliminary results of the joint likelihood analysis of the CFHTLenS data. This result is in agreement with the predictions of Vafaei et al. [2010] and Semboloni et al. [2011b], stating that the joint two- and three-point statistics leads to much tighter likelihood contours than either statistic alone. Figure 7.14b shows the difference in the size of the likeli-

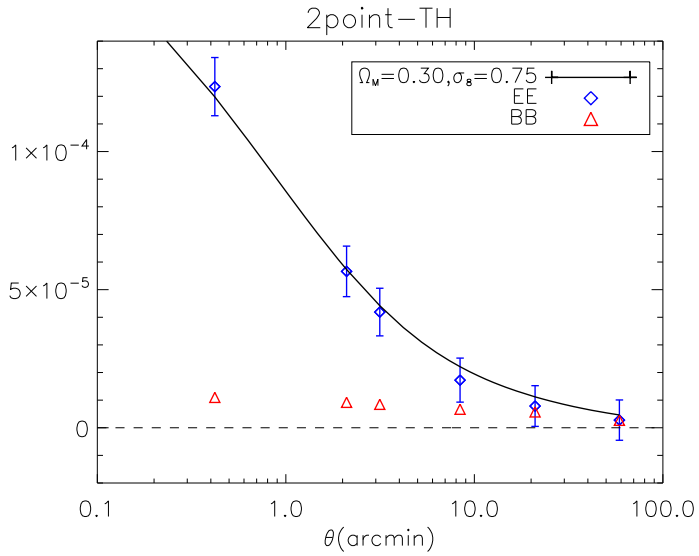

(a) 2-points top-hat

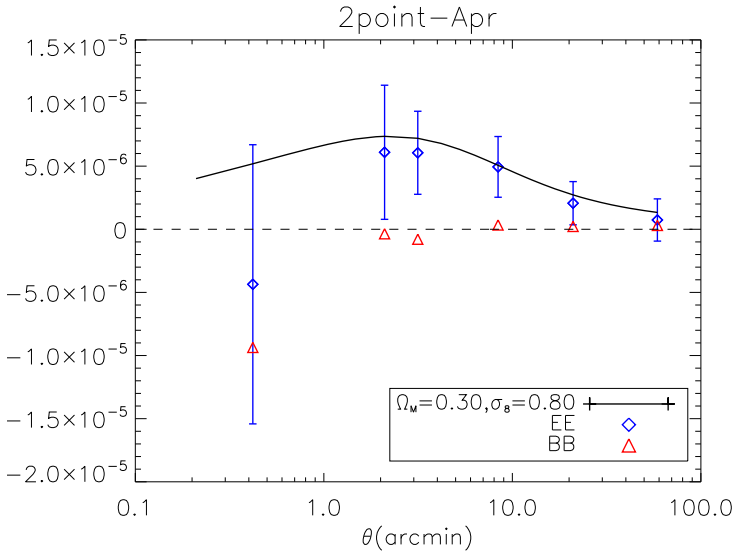

(b) 2-points Aperture

Figure 7.11: CFHTLenS 2-point measurements with top-hat (top) and aperture (bottom) filter. The errorbars are the 1σ deviations from 185 noisy simulations. Blue lines are the EE modes, red lines are the BB modes and the black lines are the theoretical predictions.

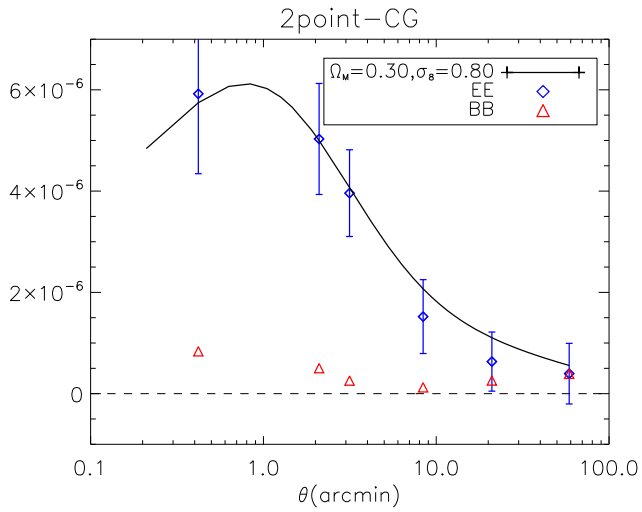

(a) 2-points Compensated Gaussian

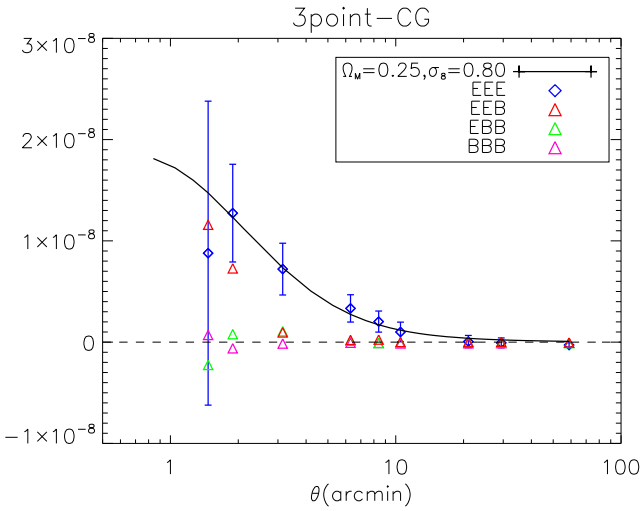

(b) 3-points Compensated Gaussian

Figure 7.12: CFHTLenS 2-point (top) and 3-point (bottom) measurements with compensated Gaussian filter. The two-point error-bars are the 1σ deviations from 185 noisy simulations. The three-point error-bars contain the shape noise only, estimated from 10,000 noise realizations. The colored lines show E-mode (blue), EBB (magenta), EBB (green), BB and BBB (red), and the theoretical model is shown in black.

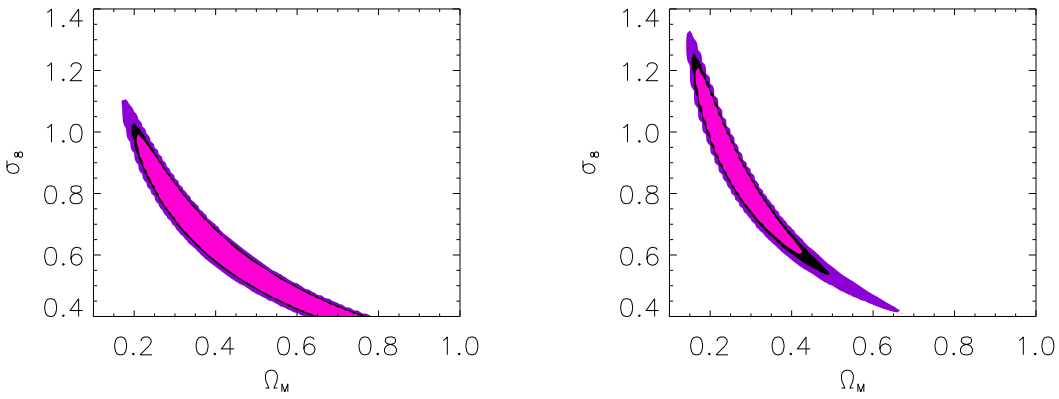

(a) CFHTLenS top-hat 2-points

(b) CFHTLenS Aperture 2-points

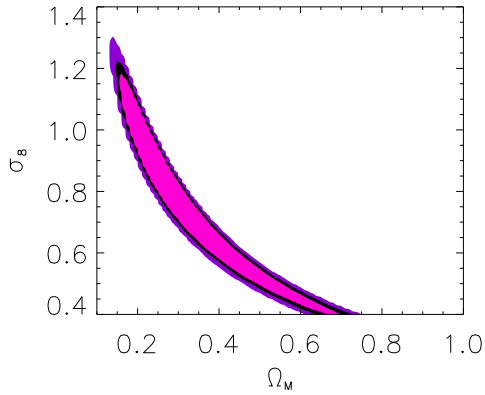

(c) CFHTLenS Compensated Gaussian 2-points

Figure 7.13: The 2-point likelihood analysis of the CFHTLenS data with three filter choices.

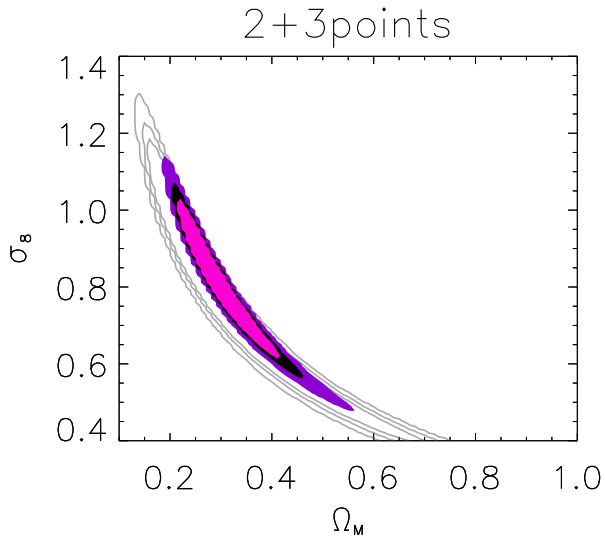

(a) CFHTLenS 2+3-points

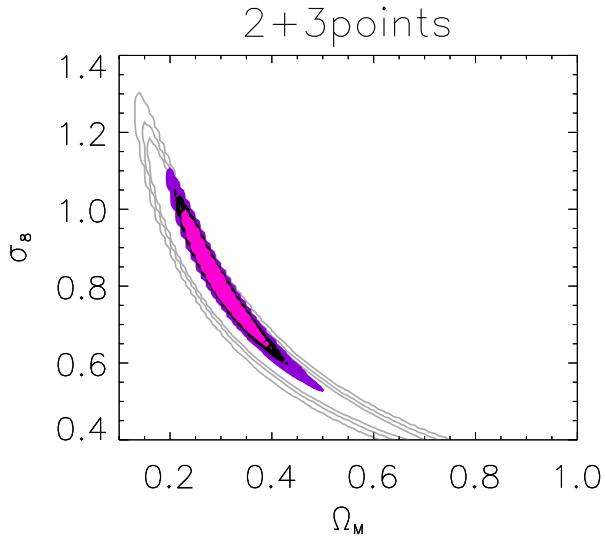

(b) CFHTLenS 2+3-points without α^* correction

Figure 7.14: The 2+3-point joint likelihood analysis of the CFHTLenS data with three filter choices. Top panel shows the likelihood constraints, when the correction coefficient is applied, while the bottom panel shows the case otherwise. The grey contour shows the case 2-point statistics only.

hood contours if the correction factor α^* is not applied to the covariance matrix. Semboloni et al. [2011b] also showed the results of three-point statistics when non-equilateral triangles are considered, which showed improvements over the equilateral combinations. As the next stage of this project we will focus on quantifying the effects of systematics, such as the residual PSF, intrinsic galaxy alignment and source clustering which have not yet been included in this work, but have been shown to have considerable effects on the three-point statistics. Also it is important to quantify the accuracy of the three-point statistics theoretical predictions further and to include baryonic matter effects on the power spectrum, since it was shown by Semboloni et al. [2011a] that these contributions affect the non-linear matter power spectrum considerably. Addition of redshift tomography is a natural step forward for the higher order statistics. This involves analysing the lensing statistics in several redshift bins. It has been shown by Joachimi et al. [2011] that inclusion of redshift tomography improves the constraints on intrinsic alignments and hence cosmological parameters estimations.

Chapter 8

PDF Statistics

In this chapter we explain another means of incorporating the information embedded in the weak lensing data. Here we use the simulations described in chapter 5 as a path finder for this method. This chapter is divided into two sections; which we call κ-PDF and κ-min. In summary we use the Probability Distribution Function (PDF) and the minimum value of the convergence κ to constrain the cosmological parameters, and show, with the aid of the simulations, that these methods prove to have promising potentials as complementary weak lensing estimators to the standard two-point statistics for future surveys. We also investigate whether there is extra information to be extracted from the PDF, which is not already contained in the combination of two- and three-point statistics.

8.1 Convergence Probability Distribution Function Method: κ-PDF

The idea of using the full PDF information, instead of other moments such as the two- and three-point statistics, has been originally introduced by van Waerbeke [2000]; Jain and Van Waerbeke [2000].The PDF is the normalized histogram generated from the convergence maps. The exact shape of the PDF depends on the cosmological parameters that affect the matter distribution and consequently the projected mass in the Universe. Hence the overall shape of the PDF can be used to constrain a subset of the cosmological parameters. As shown in figure 8.1, dif-

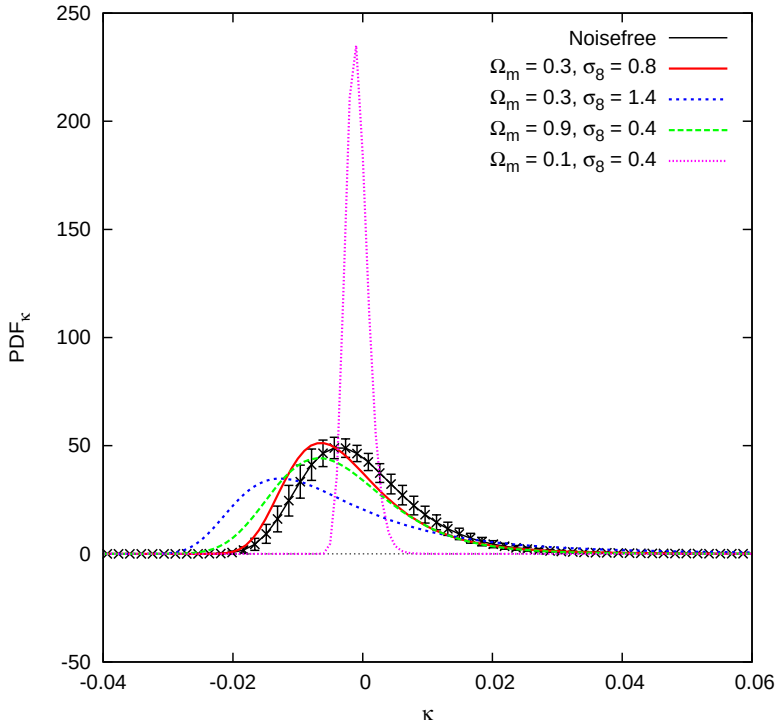

Figure 8.1: The measured noise-free PDF over 800 bins, over plotted with theoretical predictions for various cosmological parameter configurations. The errorbars represent the standard deviation between 185 lines of sight for a survey of the size 12.84 deg^2, which is the simulated map size. The top-hat smoothing scale here is 4 arcminutes and all the sources are at redshift z=1.

ferent values of cosmological parameters Ω_m and σ_8 affect the shape of the PDF. This figure shows the noise-free convergence PDF measured on the simulations in comparison to theoretical predictions formed based on various values of Ω_m and σ_8. More details on the measurements, analysis and theoretical models will follow in this chapter.

8.1.1 Binning and Sampling

We use 185 noise-free convergence maps at redshift 1.0. Each map is smoothed with the top-hat smoothing filter of a certain smoothing scale (1, 2, 4 or 8 arcmin-

utes). Previously in Vafaei et al. [2010] we found these scales to carry the highest signal-to-noise ratio for combined sampling variance and shot noise for the two- and three-point statistics. After smoothing, a rim of the size of the smoothing scale is removed from each map to eliminate the edge effects due to smoothing. This means that for larger smoothing scales, the effective area of the simulated map is smaller. We then bin the convergence maps into 800 bins and calculate the histogram. The fine binning is chosen so that the profile of the convergence distribution is collected accurately. Each histogram is then normalized to calculate the PDF. Figure 8.2 shows the PDF of κ over 185 lines of sight. We choose 800 bins between -0.7 and $+0.7$, with the bin width 0.00175 in κ. The limits are chosen sufficiently wide to accommodate the fact that the width of the PDF changes with the smoothing scale. The same figure shows the effects of varying the smoothing scale. We can see that the larger the smoothing scale, the narrower the width of the PDF becomes. The reason is that larger smoothing windows wash out a larger region of the map (that could contain extreme values of κ) to an average value.

We also know that the variance of κ decreases as function of smoothing scale. This means that a higher smoothing scale corresponds to lower κ variance, which in turn means narrower κ-PDF. It can also be seen that the PDF starts with negative values of κ. This is because convergence κ, by definition, is the dimensionless surface mass density. The density contrast δ, as previously introduced in chapter 2 equation 2.14, can have the minimum value of -1.0 when the local density is 0, which represents the emptiest regions of the line of sight. The average κ over the entire sky is zero. Since the convergence is the projected mass, a negative convergence region is emptier than elsewhere in the Universe, which yields a negative minimum of convergence value. From figure 8.2 one can see that the shape of the convergence PDF is also very distinct, starting with a negative value and then increasing to the maximum and then decreasing at higher values of κ, which correspond to the most massive parts of the (projected) sky, due to large halos and clusters of galaxies along the line of sight. These high κ regions are also relatively rare, hence the lower PDF amplitude.

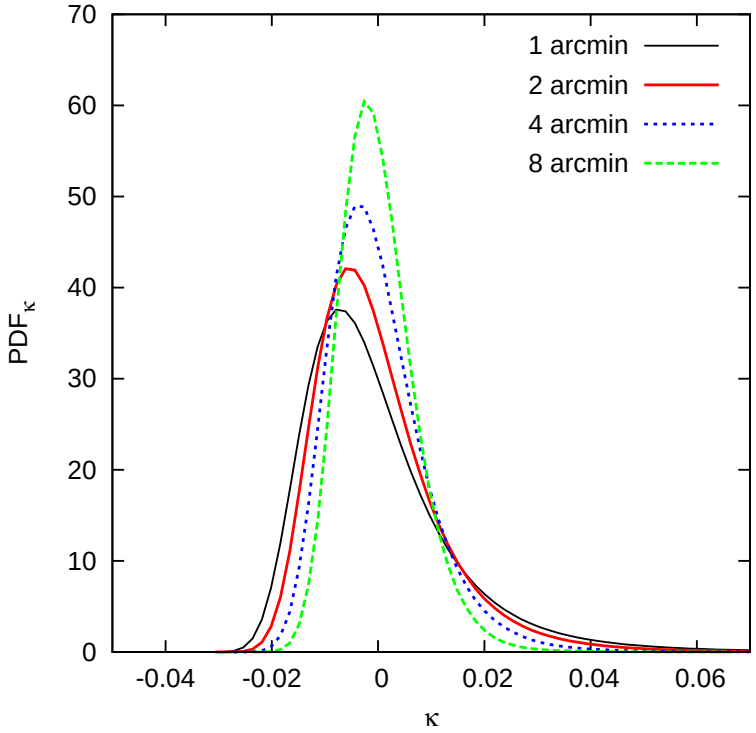

Figure 8.2: The PDF of noise-free convergence maps averaged over 185 lines of sight. Each map is smoothed with a top-hat filter and each line in the plot represents a certain smoothing scale. Each PDF is calculated by binning the data into 800 equally sized bins between $\pm$ 0.7 in κ.

8.1.2 Noise Addition

Motivated by the mass reconstruction routines (Kaiser and Squires [1993]), Schneider [1996] pointed out the importance of understanding the noise properties in the mass maps in order to study the mass distribution from lensing. Seitz and Schneider [1996] and Squires and Kaiser [1996] identified some noise properties in the mass maps through the numerical simulations. Later Lombardi and Bertin [1998] derived the first analytical estimate of the total reconstructed cluster mass variance, taking into account the noise correlations. Interestingly van Waerbeke [2000] found that the mass map can be considered as the sum of the lensing signal and a 2D Gaussian random noise map. Assuming that the ellipticities are uncorrelated

between the different sources, van Waerbeke [2000] derived the factor by which the Gaussian noise map is scaled:

$$f = \sqrt{\frac{\sigma_\varepsilon^2}{2\pi n_g \Theta^2}}. \tag{8.1}$$

Here $\sigma_\varepsilon = 0.44$ is the intrinsic ellipticity variance, $\Theta = 0.21$ is the pixel size of the map in arcmins and $n_{\rm g} = 12$ arcmin^{-2} is the galaxy number density for a typical ground-based survey of limiting magnitude 24.5. The factor 2 is due to conversion between the two component ellipticity to convergence. The assumption of uncorrelated intrinsic ellipticities of the source galaxies can be challenged, and hence further studies need to be performed to establish the noise properties in the mass maps more realistically. For the purposes of this project, we consider this assumption to be valid and find that the resulting PDF, although smeared due to noise, can still be used to constrain cosmological parameters. Figure 8.3 shows the noise-free, noisy and noise-only PDFs from 185 realizations binned in 800 bins. One can see the effects of noise, broadening the noise-free PDF. The smoothing scale here is chosen to be 2 arcmin. As can be seen in figure 8.4, the choice of the smoothing scale affects the noisy PDF as well. Every line is an average over 185 lines of sight, which is a sum of smoothed convergence and smoothed Gaussian noise maps. The resulting shape of the PDF depends on the smoothing scale and the filter function in addition to the cosmological parameters.

The first, second and third moments of the noise-free, noisy and noise-only maps, averaged over the 185 lines of sight, from all four smoothing scales are summarized in table 8.1. These values are used to generate the theoretical predictions.

8.1.3 Covariance Matrix

We compute the covariance matrix for the 800-bin measurements. The covariance matrices are calculated based on

$$\mathbf{C}(n_i, n_j) \equiv \langle (x(n_i) - \mu(n_i))(x(n_j) - \mu(n_j)) \rangle, \tag{8.2}$$

	Scale (arcmin)	$\langle x \rangle$	$\sigma_{\langle x \rangle}$	$\langle x^2 \rangle$	$\sigma_{\langle x^2 \rangle}$	$\langle x^3 \rangle$	$\sigma_{\langle x^3 \rangle}$
Noisefree κ	1	-4.43E-06	1.63E-03	2.19E-04	2.80E-05	7.10E-06	2.42E-06
Noise	1	3.17E-05	4.42E-04	2.48E-03	1.95E-05	1.75E-08	1.38E-06
Noisy κ	1	2.72E-05	1.69E-03	2.19E-04	2.93E-05	7.00E-06	2.91E-06
Noisefree κ	2	-3.5E-06	1.64E-03	1.45E-04	2.24E-05	3.02E-06	1.28E-06
Noise	2	2.59E-05	4.44E-04	6.32E-04	8.78E-06	-5.27E-09	3.78E-07
Noisy κ	2	2.24E-05	1.70E-03	1.45E-04	2.34E-05	2.99E-06	1.38E-06
Noisefree κ	4	-3.50E-06	1.67E-03	8.70E-05	1.67E-05	1.00E-06	5.45E-07
Noise	4	1.72E-05	4.49E-04	1.59E-04	4.97E-06	-2.45E-09	8.60E-08
Noisy κ	4	1.37E-05	1.73E-03	8.72E-05	1.77E-05	9.94E-07	5.71E-07
Noisefree κ	8	-2.65E-06	1.74E-03	4.89E-05	1.23E-05	2.69E-07	1.99E-07
Noise	8	1.20E-05	4.64E-04	4.02E-05	2.71E-06	8.13E-10	2.41E-08
Noisy κ	8	9.40E-06	1.80E-03	4.89E-05	1.32E-05	2.70E-07	2.11E-07

Table 8.1: The moments of the noise-free, noisy and noise-only simulated maps. The standard deviations are calculated over 185 samples.

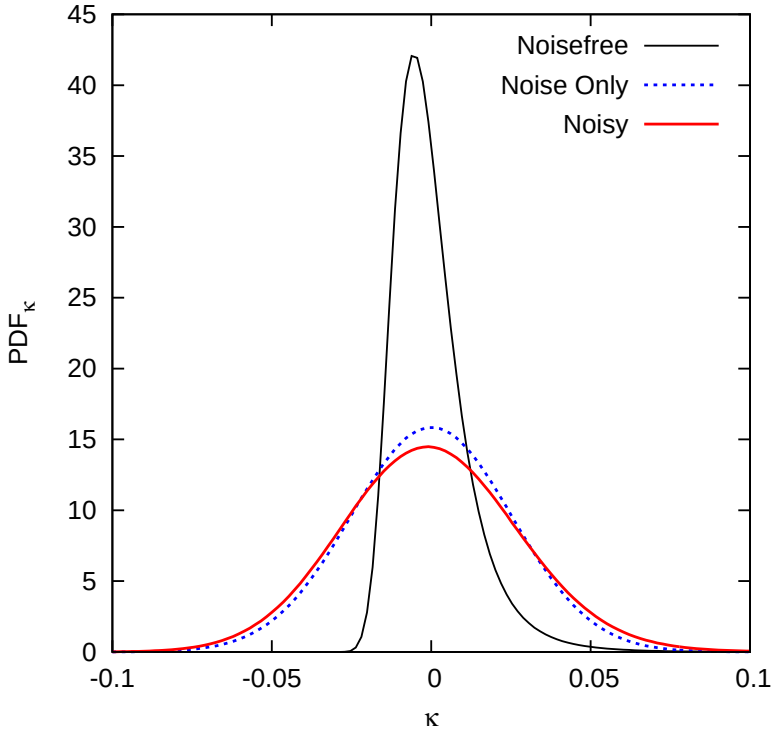

Figure 8.3: The noise-free, noisy and noise-only PDFs for top-hat smoothing scale of 2 arcmin. This plots shows how the PDF of noise-free κ is convolved with the Gaussian noise to produce the noisy κ PDF.

where x is the PDF of noisy κ data at a certain bin n_i, and $\mu(n_i)$ is the average PDF calculated from the entire simulation set for that particular bin n_i. The size of these matrices is trimmed to avoid any full zero rows and columns in the covariances. The resulting matrices are of the following dimension: 186 $\times$ 186 (noise-free), 160 $\times$ 160 (noise-only) and 248 $\times$ 248 (noisy). In order to display the level of correlation between the data points, we compute the correlation coefficient, defined as:

$$\rho(n_i, n_j) = \frac{\mathbf{C}(n_i, n_j)}{\sqrt{\mathbf{C}(n_i, n_i)\mathbf{C}(n_j, n_j)}}. \tag{8.3}$$

The correlation coefficient matrices for noise-free, noisy and noise-only cases are illustrated in figures 8.5a - 8.5c.

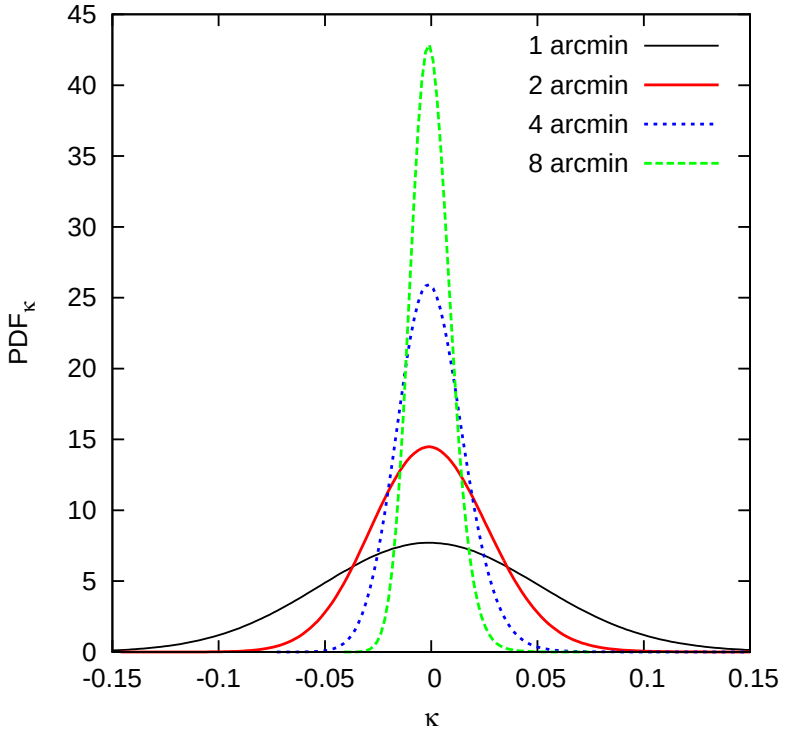

Figure 8.4: The PDF of noisy convergence maps averaged over 185 lines of sight. Each pair of convergence and noise map is smoothed with a top-hat filter and each line in the plot represents a certain smoothing scale. Each PDF is calculated by binning the data into 800 equally sized bins between $\pm$ 0.7 in κ.

For the purposes of likelihood calculations, the inverse of the covariance matrix is required. Such large matrices are unstable to invert since they are generated by 185 samples with 800 data points. As shown by Hartlap et al. [2007], a covariance matrix of size p calculated from n samples has to firstly, satisfy $n-2 > p$ and secondly be rescaled by α^* to remove the bias due to limited number of samples:

$$\alpha^* = \frac{(n-1)}{(n-1)-p-1}. \tag{8.4}$$

Throughout this chapter, for the covariance matrix calculations we used $n = 185$ as the total number of realizations. Table 8.3 shows the values of α^* for various

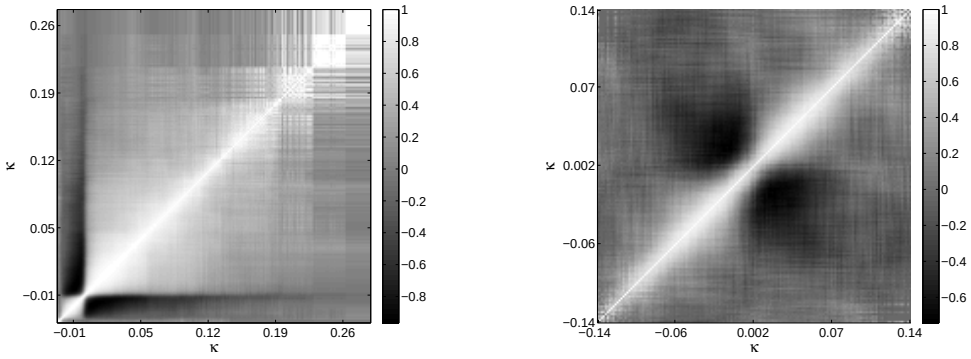

(a) NoiseFree

(b) Noise Only

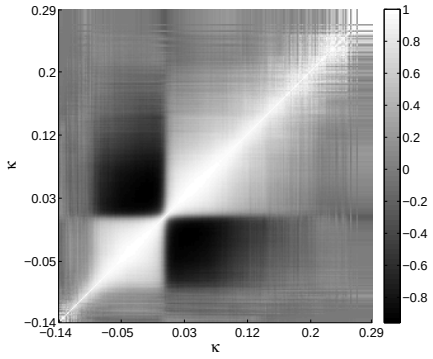

(c) Noisy

Figure 8.5: The correlation coefficient matrix for the noise-free, noisy and noise-only binned measurements. The number of bins is 800 for all these cases. Here the matrices are trimmed to void full zero rows and columns. The smoothing scale used is 2 arcmin with top-hat filter.

number of data points used in the analysis (as in table 8.2). For the likelihood analysis, we multiply the covariance matrix by α^*, so that, the bias induced by the limited number of samples is removed.

Figure 8.6 shows the data points, sampled for the case of 2 arcmin top-hat smoothing scale for both noise-free and noisy PDFs over-plotted with the fully binned measurements. It is important to note that although we choose the sampling to be 10 points evenly spaced over the limits of PDF, this number changes (decreases) depending on the smoothing scale, to accommodate the variation in the width of the data. The actual number of sampled data for all cases of our analysis is shown in table 8.2. The choice of 10 scales was made in order to keep the bias factor α^* close to unity, while sampling from the whole range of the PDF. A futrure step to this work is to fine tune the sampling such that it captures the features of the PDF, such as the location of the peak and the tails more efficiently. Also, figures 8.7a–8.7c show the sub-sample correlation coefficient matrix for each of the noise combinations. The correlation coefficient matrices are derived from covariances that are calculated for a survey of size 12.84 deg^2 (simulation map size). We use these covariance matrices later in section 8.1.5 for the likelihood analysis purposes.

8.1.4 Theoretical Predictions

We opened this chapter with figure 8.1 to show how different cosmological parameters affect the shape of the convergence PDF smoothed with 4 arcmin top-hat function. One can see that for the same values of $\Omega_{\rm m}$, larger σ_8 values lead to a broader PDF, meaning that a clumpier Universe contains the projected mass of a wider range. On the other hand, for a given value of σ_8, smaller values of $\Omega_{\rm m}$ lead to a very limited range of projected mass. Various studies have been performed to calculate the theoretical prediction for the full PDF of κ (Munshi and Coles [2000], Munshi and Jain [2001] and Valageas [2000]). Here we employ the method of Valageas [2000], who derived the theoretical predictions for the full PDF of κ from the generating functions which are cumulants of various moments of the distribution. This approach is widely used in statistics, and Valageas [2000] showed its applications for calculating the convergence PDF. Later Bernardeau and Valageas [2000] extended the method to obtain the full κ-PDF for the aperture mass

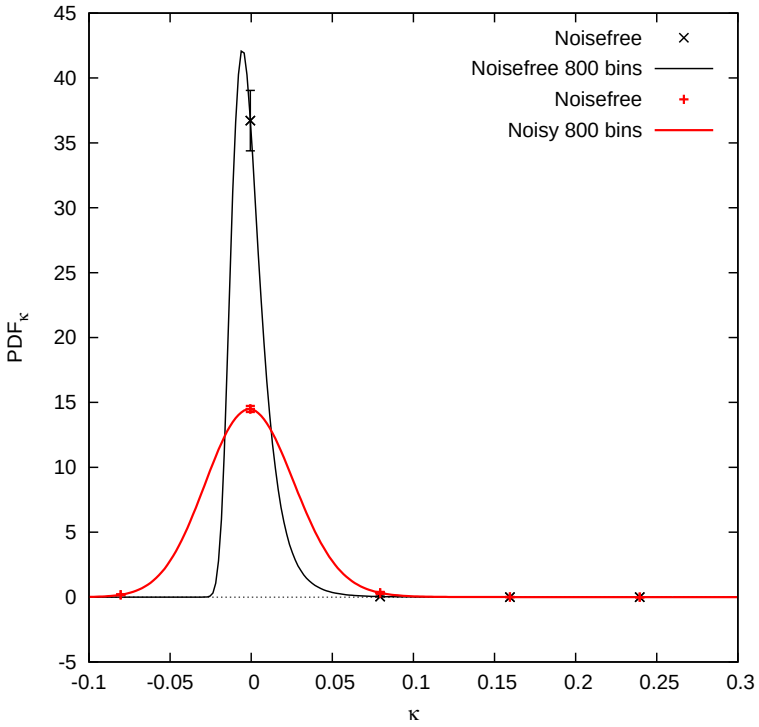

Figure 8.6: The noise-free and noisy sampled PDFs over-plotted with the fully binned measurement on the simulated maps. The noisefree case has four sampled scales and the noisy case has five scales that entered the likelihood analysis. The smoothing scale here is 2 arcmin with top-hat filter, and the error-bars are the standard deviation calculated between 185 lines of sight.

filter.

In the presence of noise, the noise-free PDF is convolved with the pure Gaussian noise, appropriately scaled to the survey conditions. The theoretical predictions for the noisy PDF are then different from those of the noise-free case and have to be computed separately. In figure 8.8, we observe the effects of various cosmological parameter values on the noisy PDF. Although the effects are much more subtle than in the noise-free case, there is still a distinction between the models and hence the noisy PDF can be used in the likelihood analysis.

For the noise-free case, we have a parameter space of Ω_m in the range of 0.1

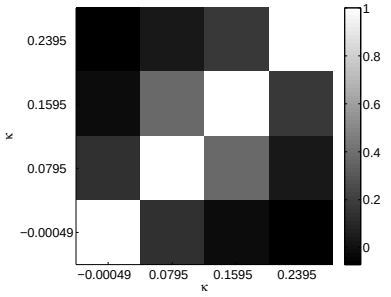

(a) NoiseFree

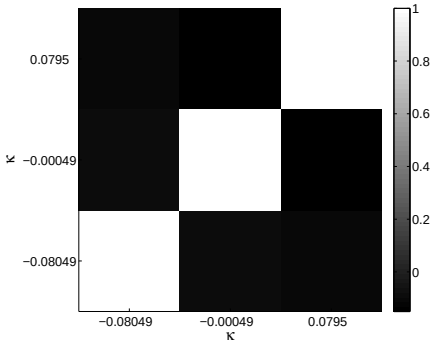

(b) Noise Only

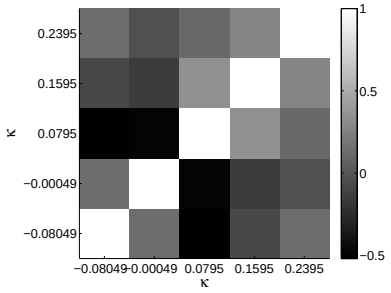

(c) Noisy

Figure 8.7: The correlation coefficient matrix for the noise-free, noisy and noise-only binned measurements. The number of bins is different in each case, since the original covariances were trimmed in addition to sampling. The trimming is done so that the covariance matrix is free of all zero rows or columns. The smoothing scale used here is 2 arcmin with top-hat filter.

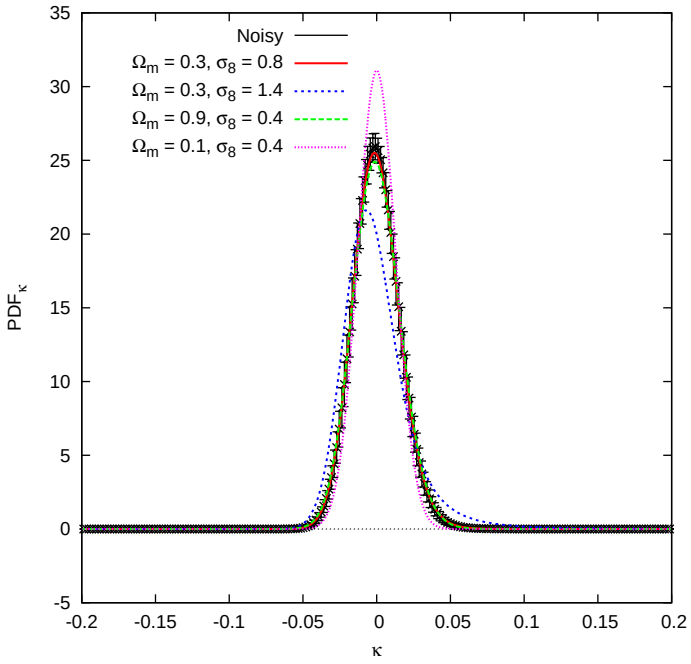

Figure 8.8: The measured noisy PDF over 800 bins, over-plotted with theoretical predictions for various cosmological parameter configurations. The error-bars represent the standard deviation between 185 lines of sight. The top-hat smoothing scale here is 4 arcmin.

to 1.0 and σ_8 in the range of 0.4 to 1.4 with 0.1 spacing in both cases. This leads to 10 nodes on $\Omega_{\rm m}$ and 11 nodes in the σ_8 side on the likelihood plane. For noisy predictions, we have a finer sampling of the likelihood plane, with $\Omega_{\rm m}$ in the range of 0.1 to 1.0 and σ_8 in the range of 0.2 to 1.4, with 0.05 spacing. This leads to 19 nodes in $\Omega_{\rm m}$ and 25 nodes in the σ_8 side. Throughout our likelihood analysis, the grid is interpolated to 1/5 finer scale for smoother likelihood contours.

8.1.5 Likelihood Analysis Results

We use the standard likelihood definition:

$$\mathscr{L} = \exp\left[-\frac{1}{2}(d-m)^{\rm T} * \mathbf{C}^{-1} * (d-m)\right], \tag{8.5}$$

Table 8.2: The number of scales for each PDF run, with originally 10 data points chosen out of 800 bins.

Scale	p(Noisefree)	p(Noisy)	$\nu_{\rm min}$,$\nu_{\rm max}$	$\Delta\,\nu$
1 arcmin	5	7	± 0.6	1.5×10^{-3}
2 arcmin	4	5	± 0.4	1.0×10^{-3}
4 arcmin	4	5	± 0.2	5.0×10^{-4}
8 arcmin	5	6	± 0.1	2.5×10^{-4}

p	4	5	6	7
α^*	1.028	1.034	1.039	1.045

Table 8.3: The covariance matrix bias factor α^* for different numbers of data p based on equation 8.4 The number of samples n in all calculations is 185.

where d represents the data and m is the theoretical model. $\mathbf{C}^{-1}$ is the inverse covariance matrix over all 185 lines of sight. The data d here is the mean of the sampled PDF on the noisy, smoothed simulations. The covariance matrix is computed over 185 simulation realizations. In this analysis we ignore the cosmological parameter dependence of the covariance matrix, since our set of simulations consist of one particular cosmology. For the future work, one could in principle generate a whole set of simulations for each point in cosmological parameter space. This approach, although ideal, is exteremly costly. Figures 8.9a–8.9d show the likelihood constraints from the noise-free measurements, whereas the noisy results are presented in figures 8.10a–8.10d. Each panel presents a certain smoothing scale. The number of scales used in each case can be found in table 8.2.

One might argue that the constraints from the realistic noisy analysis are not sufficiently limiting for the cosmological parameter estimation studies. Note that the analysis is performed for a survey of size 12.84 deg^2. For a survey 12.5 times large (i.e. 160 deg^2), we rescale the covariance matrix and find the constraints shown in figures 8.11a–8.11d. This shows great promise for κ-PDF methods, as an alternative weak lensing estimator for future surveys.

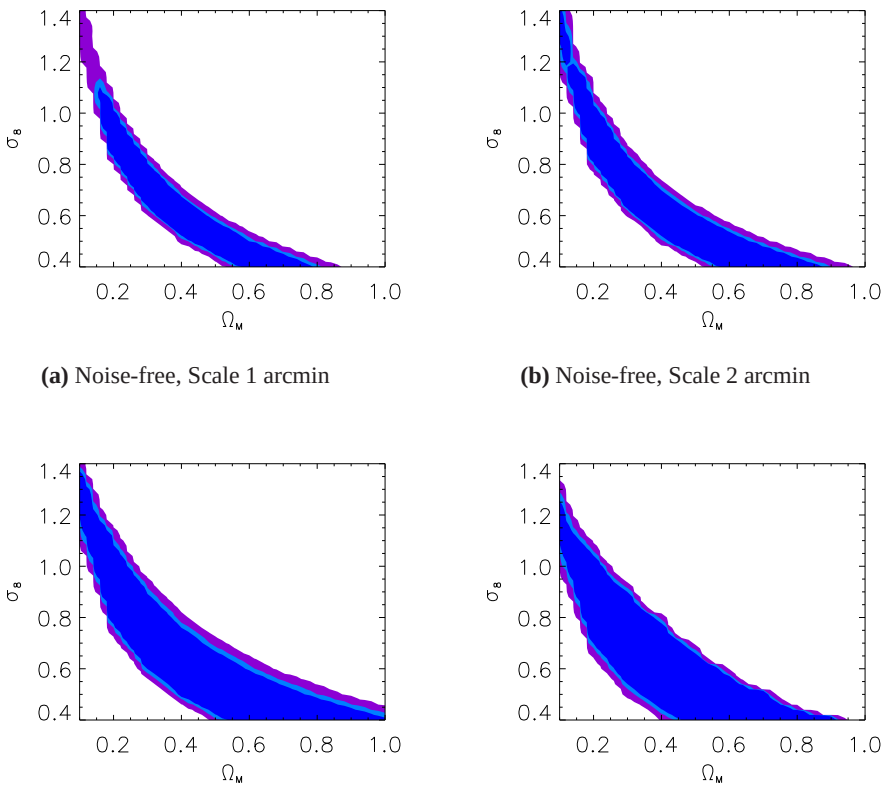

(a) Noise-free, Scale 1 arcmin

(b) Noise-free, Scale 2 arcmin

(c) Noise-free, Scale 4 arcmin

(d) Noise-free, Scale 8 arcmin

Figure 8.9: The likelihood results for the 4 smoothing scales of the full noise-free κ-PDF analysis for a survey size of 12.84 deg^2.

8.2 Convergence Minimum Value Method: κ-min

The idea here, is very similar to the previous section, in that we use the information embedded in the shape of the convergence PDF to learn more about the cosmological parameters. The only difference here, is that the focus is on a particular part of the PDF, which the minimum non-zero value. Although we focus on one point pf the PDF and seemingly discard all other information, this choice has its own advantages. One is that the cosmological dependence of the minimum convergence is purely goemtrical as can be seen from equations 6.1 and 6.2. For the empti-

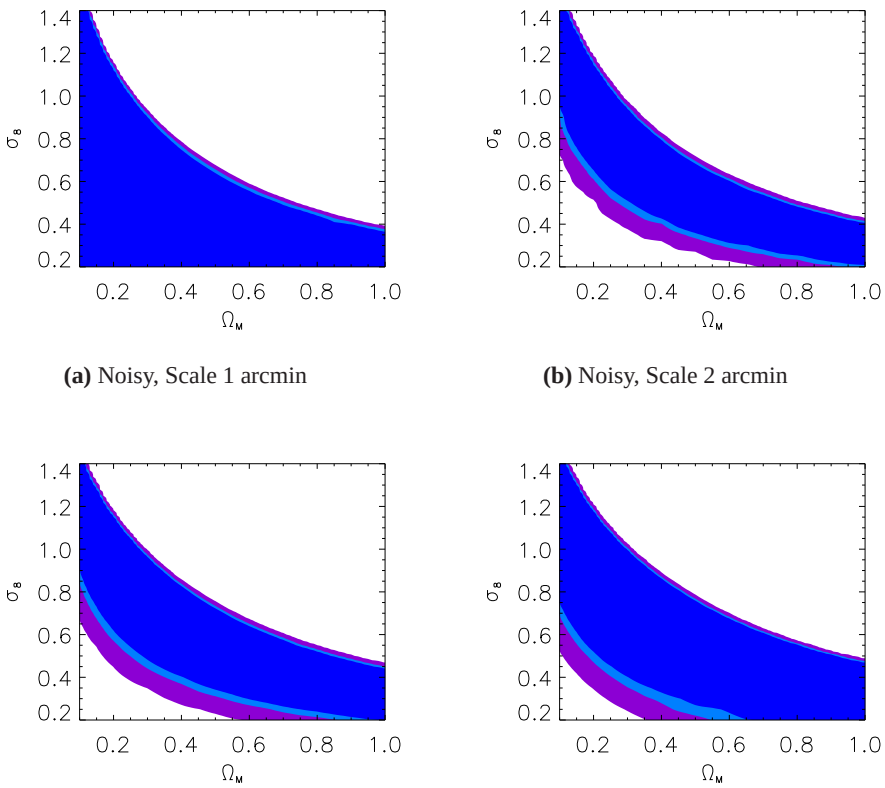

(a) Noisy, Scale 1 arcmin

(b) Noisy, Scale 2 arcmin

(c) Noisy, Scale 4 arcmin

(d) Noisy, Scale 8 arcmin

Figure 8.10: The likelihood results for the 4 smoothing scales of the full noisy κ-PDF analysis for a survey size of 12.84 deg^2.

est line of sight, $\delta = -1$, so the lensing configuration is the only contribution to the systematics. The constraints obtained from this method, although weaker than full PDF, can be used to isolate systematic effects and to serve as cross checks of the mass recosntruction methods. Also, although the value of κ-min is related to the full reconstructed PDF, when convolved with noise, the sensitivity to extended positive tail of the distribution is reduced. As explained before the PDF of κ starts off as a negative value, which is the point of our focus in this method. The minimum κ corresponds to the emptiest parts of the line of sight, where voids exist. As mentioned earlier, convergence is a projection along the redshift, so emptiness

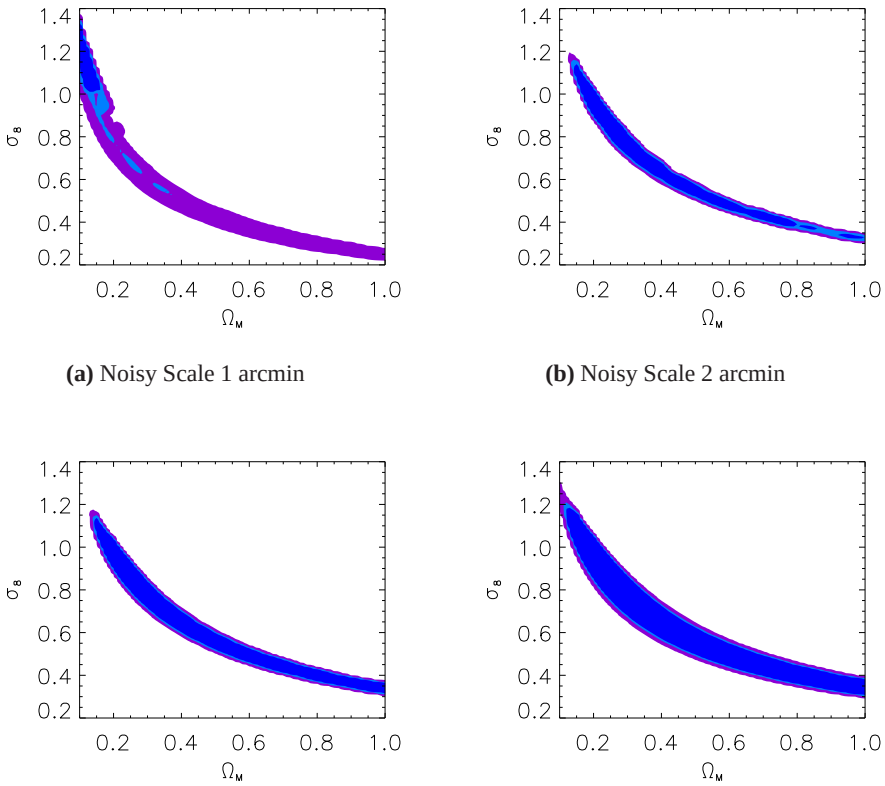

(a) Noisy Scale 1 arcmin

(b) Noisy Scale 2 arcmin

(c) Noisy Scale 4 arcmin

(d) Noisy Scale 8 arcmin

Figure 8.11: The likelihood results for the 4 smoothing scales of the full noisy κ-PDF analysis for a survey that is 12.5 times larger than the simulated maps with area of 160 deg^2 which is close to the effective area of the CFHTLenS survey.

is relative and an emptier line of sight means that no dark matter halos, cluster of galaxies or any other massive object lies in between.

8.2.1 Noise-free and Noisy

In figure 8.12 we show the κ-min value measured over all the simulated noise-free maps. Each color band represents a different smoothing scale used. As can be seen, larger smoothing scales lead to larger values of κ-min, meaning that the very

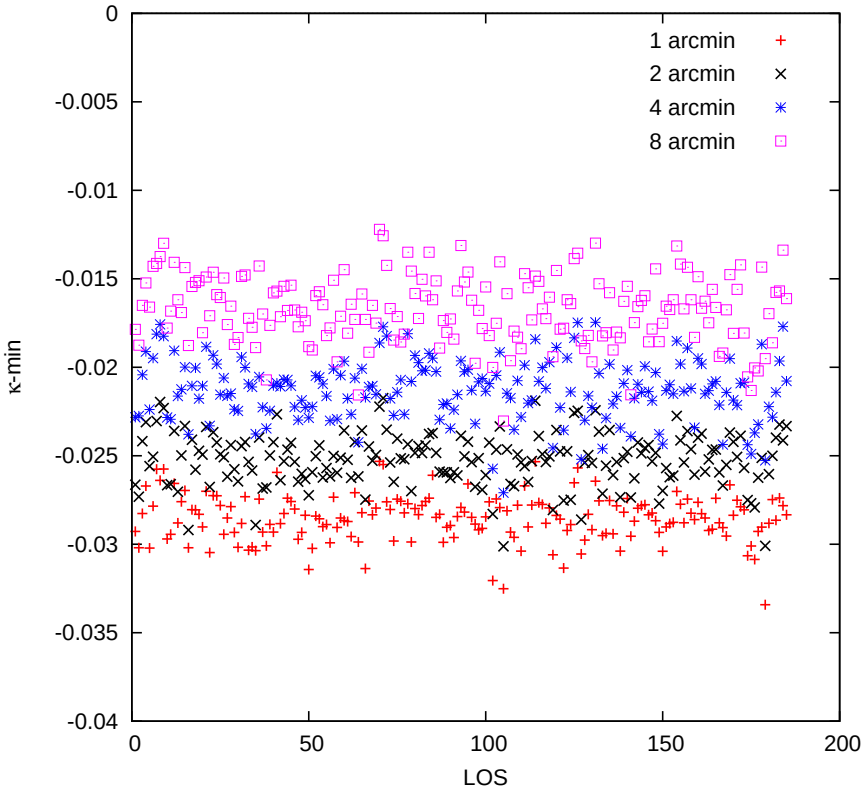

Figure 8.12: Values of κ-min over the 185 noise-free simulated maps. Each color band represents a particular smoothing scale.

empty regions get erased by smoothing.

Noise is added to the maps, exactly the same way as in the full PDF method. The difference is that, here, we take the minimum value of the resulting map. Figure 8.13 shows the κ-min values as a function of smoothing scale, and ther errorbars represent the standard deviation between 185 lines of sight. We overplot the theoretical predictions for various cosmological parameter combinations to illustrate the fact that κ-min is sensitive to the cosmology and can be used in principle to constrain cosmological parameters. The theoretical values are extracted by taking the minimum values from the full PDF predictions. In other words, full convergence PDF must be predicted and the minimum non-zero value of it has to be extracted. In figure 8.14, one can see how the noise-free and noisy κ-min values

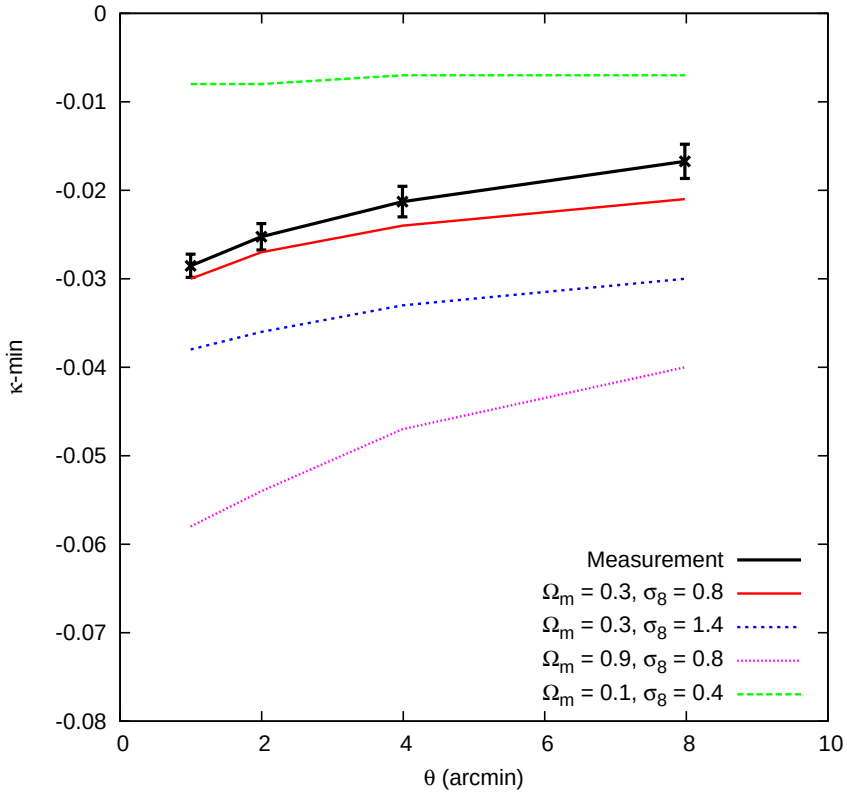

Figure 8.13: The noise-free simulated κ-min values as a function of smoothing scale. The error-bars represent the variance between the 185 lines of sight. The minimum noise-free κ values predicted by different cosmological parameters are shown for comparison.

compare to each other as a function of smoothing scale. The general trend is that, the smaller smoothing scales lead to more negative values of κ-min, which means emptier regions do not get washed out by smoothing in absence of noise. Also one can see that the convolution with Gaussian noise drives the minimum κ to more negative values, falsely implying emptier regions than reality. It is then essential to have a good understanding of the noise properties in the real data in order to be able to separate these effects.

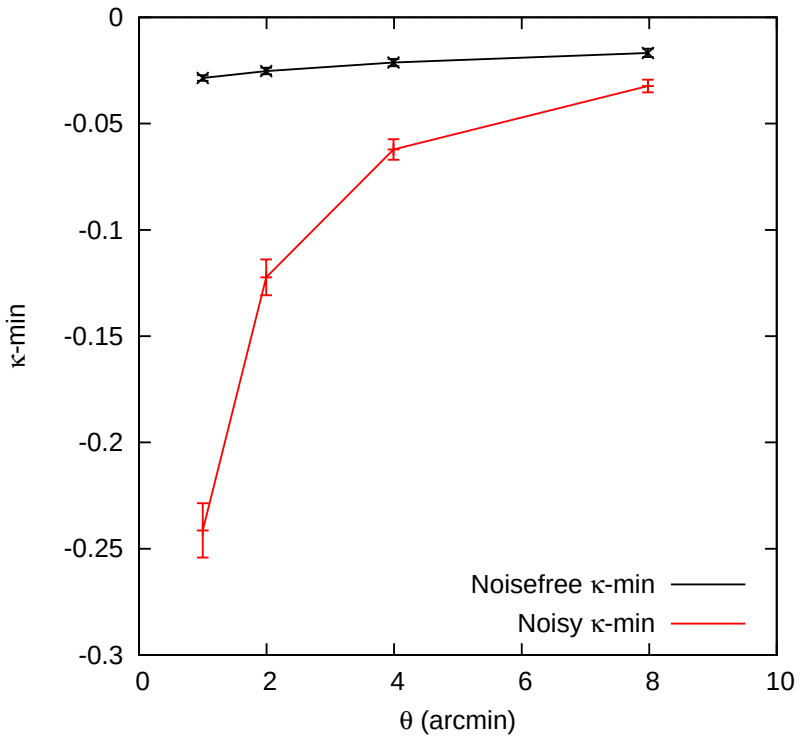

Figure 8.14: The κ-min as a function of smoothing scale for noise-free and noisy case in comparison. The error-bars represent the standard deviation between the 185 lines of sight.

8.2.2 Results: All Scales

We calculate the noise-free and noisy covariances from the 4 smoothing scales: 1; 2; 4; and 8 arcminutes, among the 185 simulated lines of sight. Here, the number of data points is $p = 4$ (corresponding to four smoothing scales) and number of samples is 185. This results in the covariance matrix bias factor $\alpha^* = 1.028$, which is applied to the covariance matrix. We also compute the correlation coefficient from equation 8.3 for each noise case. Figures 8.15a and 8.15b shows the noise-free and noisy correlation coefficient matrices for the κ-min analysis when the top-hat filter is used.

We also compare the results of the likelihood analysis, of both noise-free and noisy κ-min estimates. Figure 8.16 displays the results from the noise-free case.

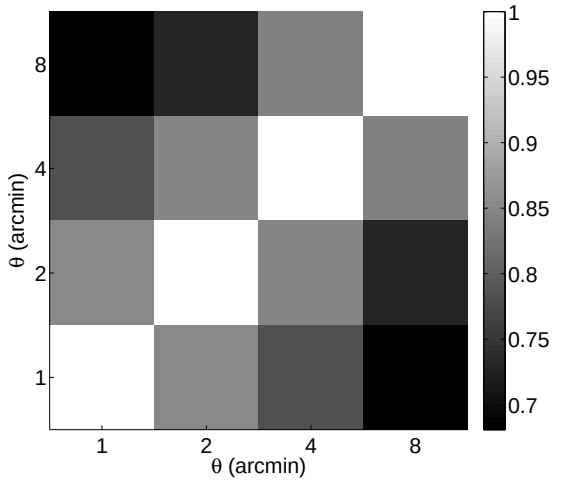

(a) κ-min Noisefree Covariance Matrix

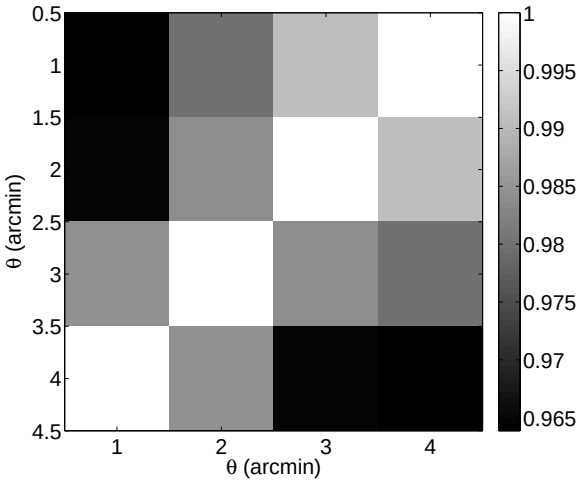

(b) κ-min Noisy Covariance Matrix

Figure 8.15: The noise-free and noisy correlation coefficient matrices of the κ-min analysis. The measurements are the minimum smoothed κ value with 4 smoothing scales and over 185 lines of sight for a single redshift slice at z=1.

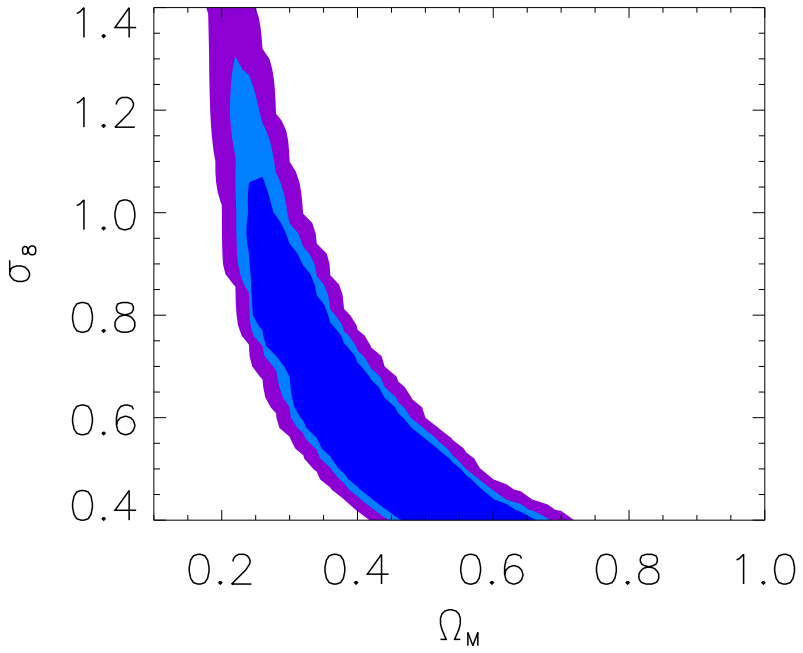

Figure 8.16: The likelihood results for the noise-free minimum convergence κ measurements over 4 smoothing scales for a survey size of 12.84 deg^2.

When the noise effects are considered, it can be seen from figure 8.17 that the constraints become weaker, to the point that, for a survey of the size of the simulation maps used here (12.84 deg^2), κ-min is not a suited estimator. However, by rescaling the covariance matrix for a survey, 12.5 times larger (area 160 deg^2), we obtain promising constraints as shown in figure 8.18. This is interesting because the systematic dependence of an estimator such as κ-min is different from those affecting the higher order statistics. The reason is that κ-min is mainly geometry dependent. This presents an advantage for combining κ-min measurements with other weak lensing estimators, to obtain tighter cosmological constraints. An immidiate future step of this work is to verify the validity of the rescaling process for the full PDF as we did previously for the two- and three-point statistics. This

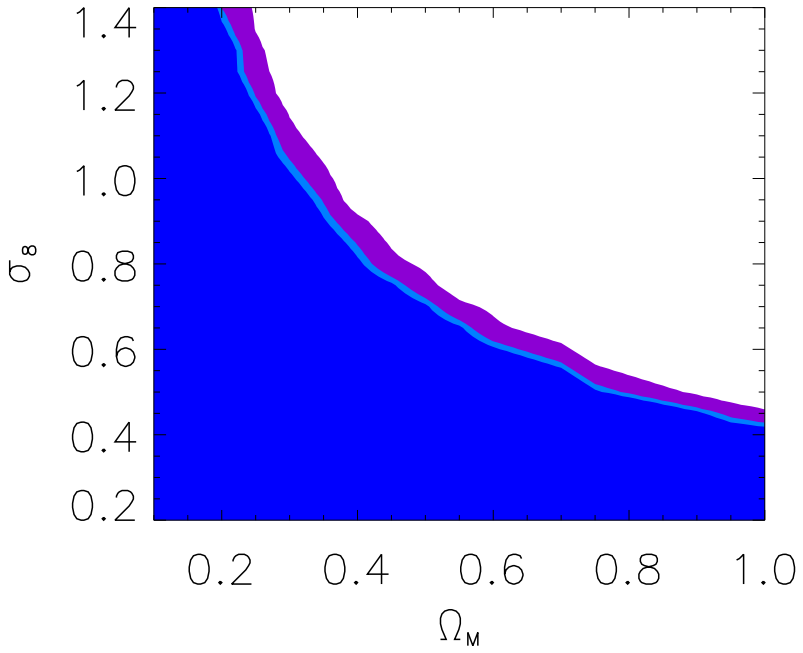

Figure 8.17: The likelihood results for the noisy minimum convergence κ measurements over 4 smoothing scales for a survey size of 12.84 deg^2. A survey this small is unable to provide any significant cosmological constraints.

is beyond the scope of this thesis as the goal here was to explore the convergence PDF method as a path finder, and further investigations are required.

8.3 Practical Approach for the Future

In order to implement the PDF statistics in real data, one needs to perform mass reconstruction on the shear catalogues. The details of such a challenging procedure are beyond the scope of this thesis. However, there are plenty of future steps one can take to improve the current work. First, we would consider other smoothing filters to find the optimal function. One could also combine the smoothing scales

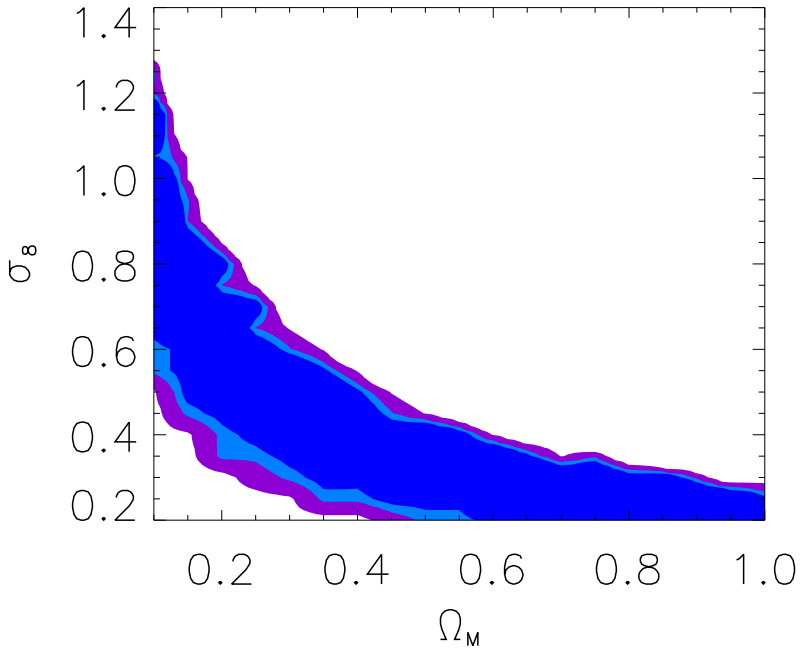

Figure 8.18: The likelihood results for the noisy minimum convergence κ measurements over 4 smoothing scales for a survey size of 160 deg^2.

for the full PDF to take advantage of the joint likelihoods between the scales. The purpose of this work was to explore the possibilities of alternative weak lensing estimators. However, to fullfil the potentials of the PDF method, we will extend the analysis to include broad redshift distribution, to mimic realistic survey conditions better. Besides, in this work, the choice of sampling here has been very limited. One can consider non-even sampling, such that the main features of the PDF, (minimum, peak position, etc) are included in the sampling process. All of these action items are set to be taken up in the near future as the next stage of this project. The technique will then be applied to the reconstructed mass maps from the CFHTLenS data.

Chapter 9

The Clone

The following sections explain the purpose, production and format of the “Clone”, which was generated as part of my contribution to the CFHTLenS collaboration. The clone files are made available to the CFHTLenS members for the purposes of covariance matrix calculations and systematics testing.

9.1 Purpose

Chapter 7 explained the CFHTLenS data in detail. The shapes and photometric redshifts of all the galaxies are included in the catalogues for various scientific applications. For most weak lensing analysis estimation of covariance matrices is an essential part of the process. In the linear and Gaussian regime, one can derive the terms of the covariance matrix analytically. This convenience however, does not exist, when considering the full non-linear and non-Gaussian terms. The best way to obtain realistic covariance estimation, is to have many samples of the data and calculate the covariance between them. In case of astronomical data, this is not possible, since we only observe one sky. The survey area can be divided up into patches to get around this issue, however measurements at larger scales will not be possible. One great solution is to use the numerical simulations to generate mock catalogues that mimic the noise amplitude, masking, redshift distribution and overall geometry of the survey. The simulated data can also be used to test the pipelines and the integrity of the systematics tests.

Ω_m	Ω_Λ	σ_8	h	n_s	Ω_b
0.279	0.721	0.817	0.701	0.96	0.04

Table 9.1: Cosmological parameters of the input simulations.

For these purposes, we generated the clone of the CFHTLenS data, that resembles the data catalogues in many aspects, such as the galaxy number density; position; and redshift distribution, with added simulated noise-free and noisy shear information for each galaxy.

9.2 Introduction

The Clone is a hybrid of data and simulations. It is partly generated from 185 different dark matter particle simulations. The cosmological parameters of the simulations are listed in table 9.1 based on WMAP7 parameter values. Each simulation is completely independent of the others with different and randomized initial conditions. It is important to use independent simulations to obtain realistic covariance matrices. Each simulation line-of-sight has 26 redshift slices with source redshift from 0.050 to 3.17. The clone serves as copies of the real data. Table 9.2 shows the particular simulations line of sight chosen for each clone run. Each CFHTLenS subfield is cloned 7 times. Figures 9.3, 9.4, 9.5 and 9.6 show the orientation of subfields in each CFHTLenS mosaic. Each color patch shows a group of fields that are cloned using the same line of sight. Each simulation map accommodates up to 9 CFHTLenS fields as the size of simulation maps is 1024×1024 with pixel size of 0.21 arcminutes and each CFHTLenS subfield covers 1 deg^2. The data for mos fields have been taken in *i*-band. The fields denoted with **Y**, have only *y*-band data available. Fields with + have both *i*- and *y*-band data. For these fields the same line-of-sight of simulations are used for both bands.

9.3 Clone Production Foundation

For every galaxy in the data files with (x,y) position and redshift z, we find the corresponding location on the line-of-sight map. For that particular position on the simulations, the values of noise-free reduced shear (defined in equation 3.25)

are quoted as the simulated clone. There are few more technical steps along the way that will be explained in the following sections. The steps include: format conversion; pixel size difference; sky deprojection; and shear assignment.

The original data is in `ldac` binary format. The first step is to extract the galaxy identification number, `wcs` (world coordinates) and best redshift estimate of each galaxy in the input catalogue and convert them to ascii format. Each input catalogue contains the pixel position of the galaxies as well, however the origin, (0,0), is chosen to be at the bottom left corner of each subfield. The pixel coordinates of the data run from 1 to 21,000 pixels with pixel resolution on 0.186 arcseconds. We need to use the global pixel coordinate to conserve the relative positions of the fields with respect to each other. This coordinate system has to be properly converted from `wcs` coordinates to match up with the simulation pixel size.

Another issue to deal with is the fact that the sky is not flat. Hence, a simple `wcs` to (x,y) coordinate transformation is not sufficient to encompass the curvature of the sky at high declinations. The effects of high declination distortion have to be taken into account, since the simulations are generated as flat maps. The non-equatorial field (W3) is more affected by these distortions due to high declination. For this purpose we convert the `wcs` coordinates to global (x,y) pixel coordinates using `sky2xy` software, which is part of `WCSTools` software package. [1] This routine takes the world coordinate information from the header of the mask fits images for each mosaic field and generates the corresponding (x,y) coordinate which runs for the whole mosaic. There is a great advantage in this step already, and that is the continuous pixel values for the whole mosaic. This enables cloning of 9 neighboring fields by using the (x,y) coordinates.

Mask images have the lower pixel resolution than the data catalogue, 0.01666 arcminutes per pixel (instead of 0.186 arcseconds), so the resulting pixel resolution of the (x,y) coordinate is the same as the mask images. Although this seems to be a significant drop in pixel resolution from the original input data, it does not cause any problems in clone generation. The reason is that the simulation pixel size is 0.21 arc minutes, which is more than 12 times larger than the projected global pixel

[1] http://tdc-www.harvard.edu/wcstools/sky2xy/

coordinate resolution. When using the clone, scales less than 0.21 arcminutes fall below the resolution of the simulations and hence, not acceptable.

9.4 Shear Assignment

With proper pixel coordinates assigned as explained above, we locate each galaxy in three dimensions on the simulated line of sight. We take the (x,y,z) coordinates of the galaxies in a group of subfields (to a maximum of 9) as shown in colored patches in figures 9.3, 9.4, 9.5 and 9.6. The first step, is to find the corresponding simulation redshift slice to the galaxy's best photometric redshift estimate from the catalogue. The simulations have 26 redshift slices, which are generated by collapsing the simulations boxes as they evolve over time. The evolved boxes are adjacent, so there is no gap between them. If the galaxy's redshift is within a given simulation box, the corresponding source redshift is assigned to the galaxy. Figure 9.1 shows the simulation boxes and lens and source planes. Galaxies falling within a simulation box are assigned the reduced shear values from the central collapsed slice inside of that box. The next step is to find the (x,y) position on that particular redshift slice map.

9.5 Rejected Galaxies

For any galaxy with best estimated photometric redshift outside the redshift range of the simulations, a shear value of 99 is assigned. These galaxies will be taken out of the catalogues before using. The simulated redshift slices are chosen so that the galaxy's redshift lies between the previous source redshift and the assigned one. So for galaxy at redshift $z_{s-1} < z_g \leq z_s$ the simulated slice at z_s is taken. To obtain a more accurate shear value than the discrete sheets, we can interpolate the shear between the two maps that encompass the galaxy. Although each simulation box is rotated and moved before the central collapse, every convergence map is the geometric weighted sum of all the denisty δ-maps from the source to redshift zero. So the interpolation is a valid approach to find a more continuous distribution of the simulated shear values. For this purpose, the clone contains the lower and upper shear values for each galaxy that correspond to the two maps that encompass the galaxy redshift at a particular location. The upper value is what is used as the

simulated value, and the lower value is added for the case of interpolation. For galaxies between the observer and the first slice at $z = 0.0494$ there is no lower shear values, so these galaxies are assigned shear values of 66 to be taken out of the catalogue as well.

9.6 Noise Addition

In order to have the most realistic shear values compared to data, reasonable levels of noise should be added to the simulated shear. The observed noisy ellipticity of a galaxy is a combination of its intrinsic reduced shear and a randomized ellipticity term caused by random intrinsic ellipticity of the galaxy.

We randomize the orientation of the input galaxy's ellipticity to destroy the lensing signal. The ellipticity dispersion is then calculated as $\sqrt{\sigma_{\varepsilon_1}^2 + \sigma_{\varepsilon_2}^2}$. We the two real and imaginary components of this randomized ellipticity to the corresponding simulated reduced shear components as shown in Seitz and Schneider [1997]:

$$e^{obs} = \frac{e^s + g}{1 + g^* e^s} \tag{9.1}$$

The resulting simulated observed ellipticity resembles the observed ellipticity from the data statistically. Here g is the reduced shear, defined as $\gamma/(1-\kappa)$ and e^s is the randomized ellipticity of the galaxy.

9.7 Redshift PDF Re-sampling

Each photometric redshift estimate of the catalogue is the best value from a probability distribution $P(z)$ as a function of redshift. For every galaxy, a 40 bin PDF is given in the catalogues. The bins start from z =0.01 to z =2.00 with bin size z =0.05. We use this PDF of redshifts to re-sample a new redshift value for any given galaxy. We re-sample the redshift of all individual galaxies from the same PDF that the best redshift came from.For a localized PDF, the re-sampled redshift is most likely very close to the best value in the catalogue. However, if the PDF is very wide, the probability of finding a different value for redshift is much higher. The goal is to have 10 re-sampled values of the redshift to study if there are any biases due to the redshift estimates in the catalogues.

We follow the recipe of Monte Carlo re-sampling as explained in chapter 6.5 of Wall and Jenkins [2003]. Figure 9.2 shows the shape of the input PDF for 6 sample galaxies and the PDF of 1000 re-sampled redshifts, from which 10 are chosen to be in the clone catalogue. The black lines are the PDF from the data catalogue. The red crosses are the result of 1000 re-samples of the PDF. It can be seen that the distribution of these 1000 values follows the original PDF closely. Also we chose a range of PDF distributions to demonstrate different levels of estimated redshift accuracy for different galaxies. For the 10 re-sampled redshift values, we generate 10 different clones by random sampling the simulation (x,y) plane. These clones of clone can be used to test redshift estimate biases in the catalogues. So far, two generations of clone have been released to the CFHTLenS collaboration and with added number of simulations, new generations will be generated.

Field	Clone 1	Clone 2	Clone 3	Clone 4	Clone 5	Clone 6	Clone 7
W1-1	10	100	101	102	103	104	105
W1-2	106	107	108	109	11	110	111
W1-3	112	113	114	115	116	117	118
W1-4	119	12	120	121	122	123	124
W1-5	125	126	127	128	129	13	130
W1-6	131	132	133	134	135	136	137
W1-7	138	139	14	140	141	142	143
W1-8	144	145	146	147	148	149	15
W1-9	150	151	152	153	154	155	156
W2-1	157	159	16	160	161	162	163
W2-2	164	165	166	167	168	169	17
W2-3	170	171	172	173	175	176	177
W2-4	178	179	18	180	181	185	186
W3-1	187	188	189	19	190	191	192
W3-2	193	194	195	196	197	198	199
W3-3	20	21	22	23	24	25	26
W3-4	27	28	29	30	31	32	33
W3-5	34	35	36	37	38	39	40
W3-6	41	42	43	44	45	46	47
W3-7	48	49	50	51	52	53	54
W3-8	55	56	57	58	59	60	61
W3-9	62	63	64	65	66	67	68
W4-1	69	70	71	72	73	74	75
W4-2	76	77	78	79	80	81	82
W4-3	83	84	85	86	87	88	89
W4-4	90	91	92	93	94	95	96

Table 9.2: Particular line of sights used for each clone run.

Missing Fields	1-9	158	174	182	183	184	200
Leftover Fields	97	98	99				

Table 9.3: Particular line of sights used for each clone run.

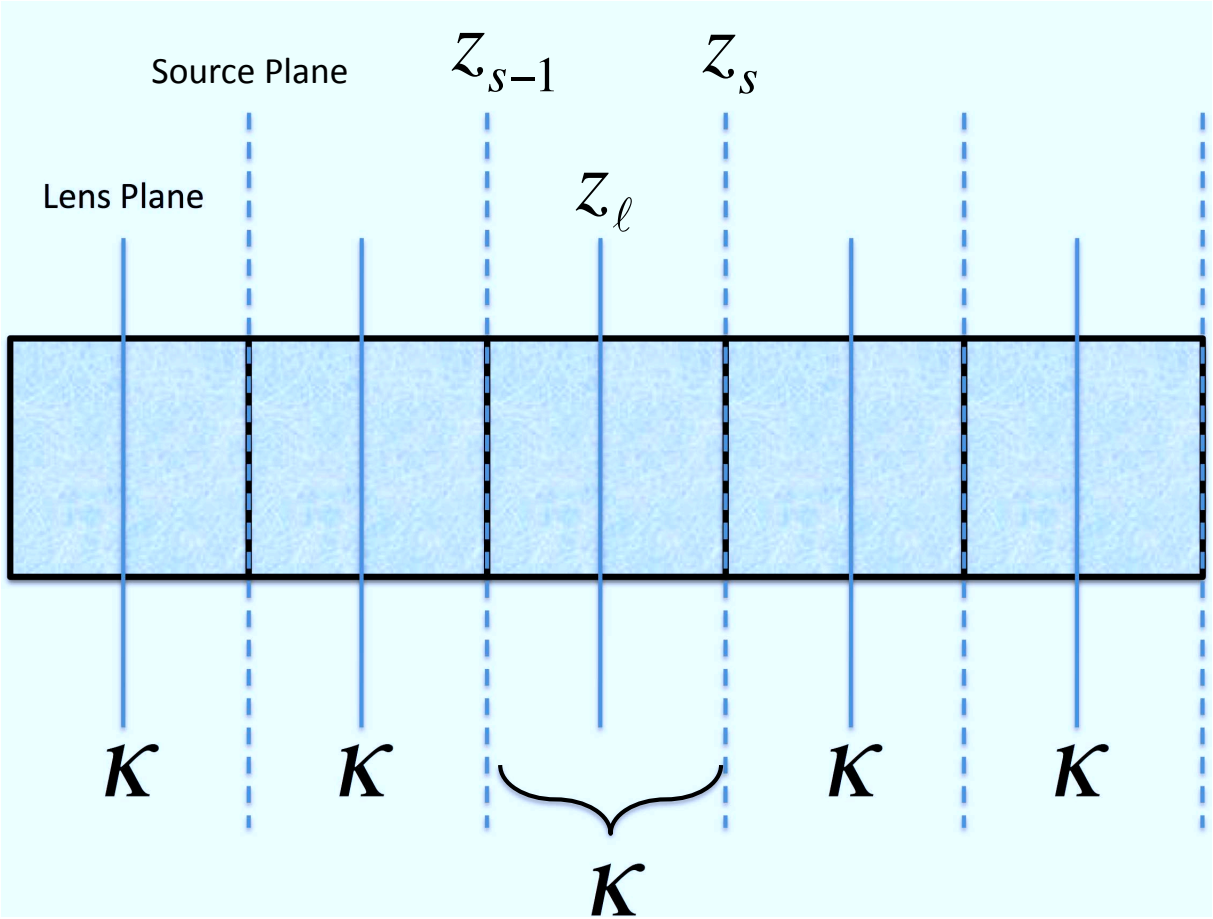

Figure 9.1: Lens and source redshift slices within simulation boxes at different redshifts. The simulation boxes are collapsed at the lens plane. Galaxies within each simulation box are assigned shear values of the central collapsed map.

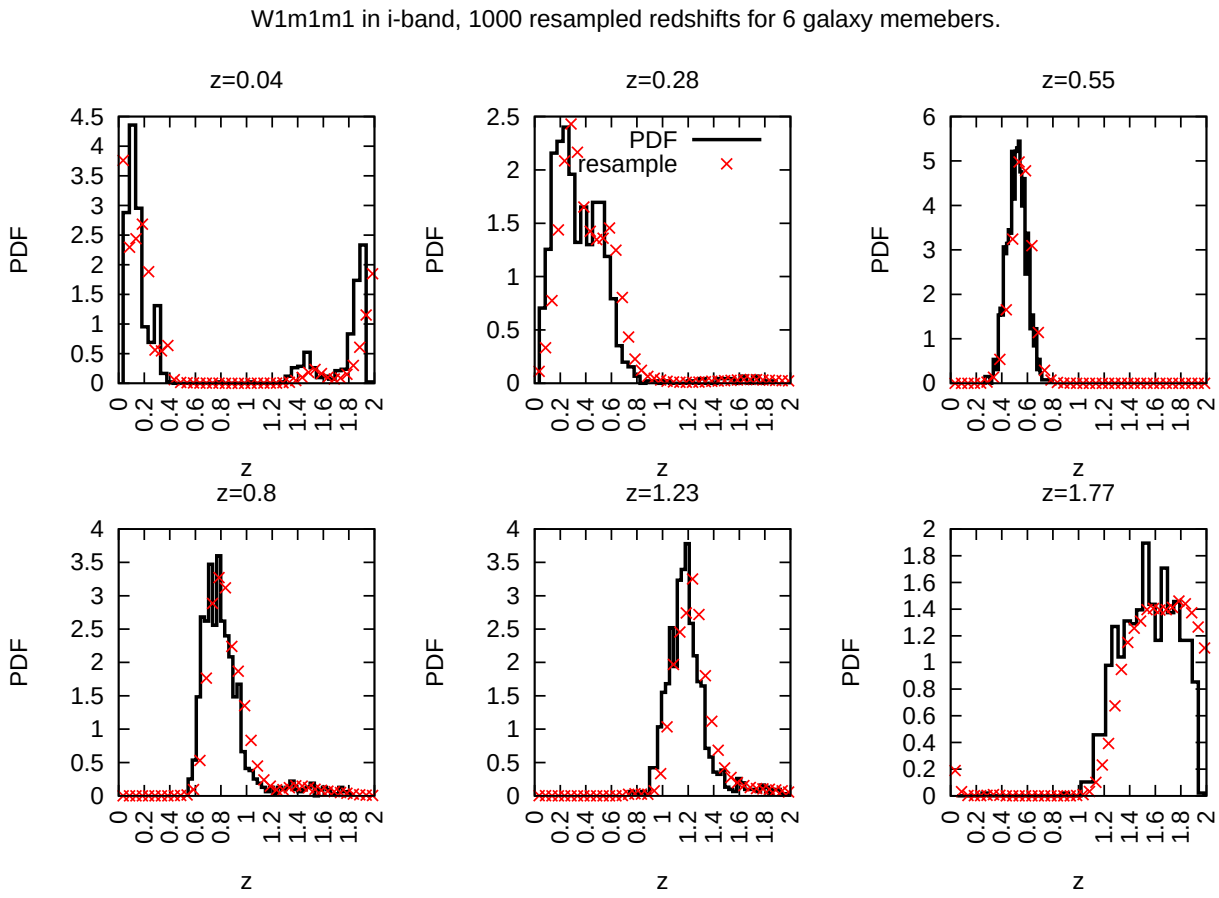

Figure 9.2: The PDF and 1000 re-sampled redshifts for 6 galaxy members of `W1m1m1` *i*-band data. For the clone catalogue 10 re-sampled redshifts are used for each galaxy.

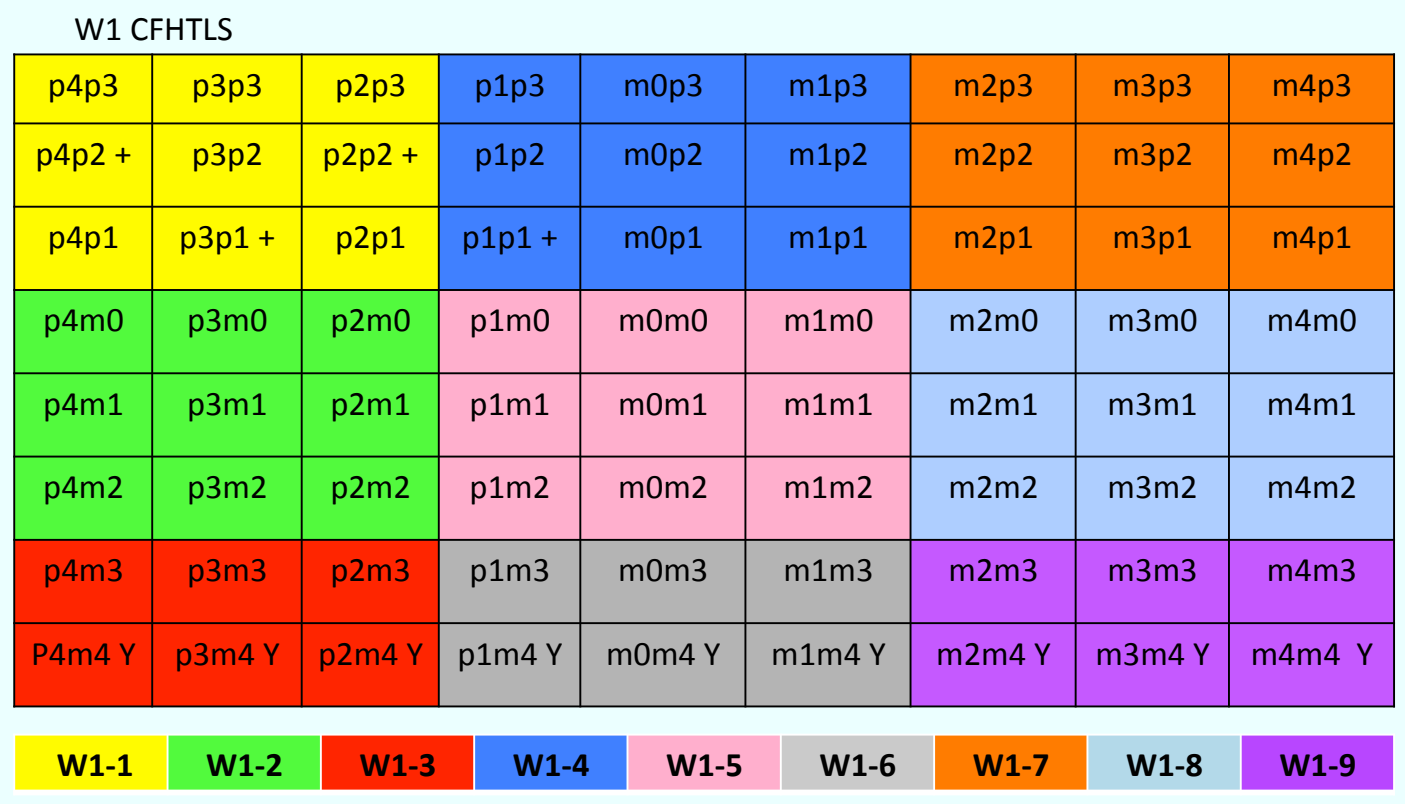

Figure 9.3: Orientation of all W1 subfields. Fields with **Y** in the naming have only the *y*-band data. Other fields have only the *i*-band data and fields with + have both *i*- and *y*-band data.

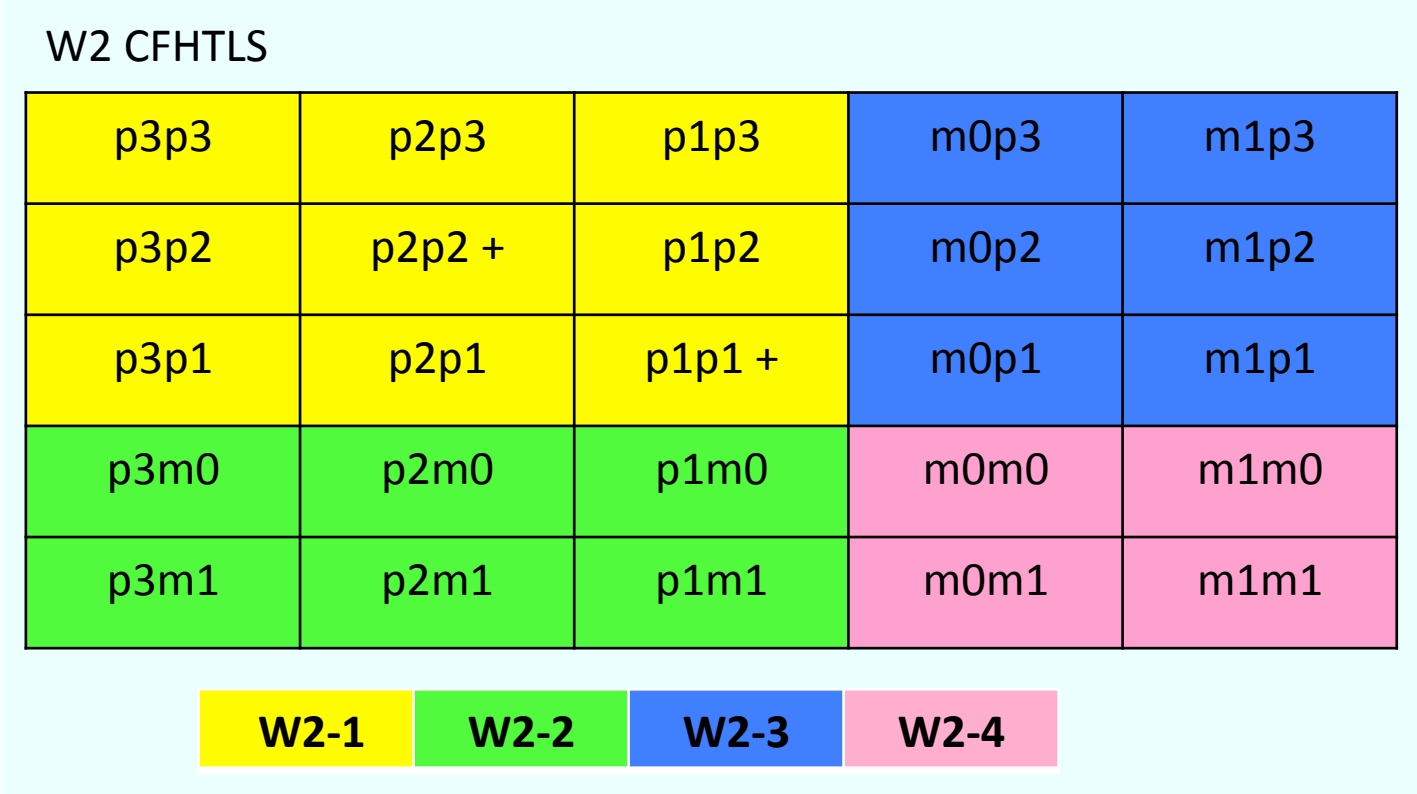

Figure 9.4: Orientation of all W2 subfields. Fields with **Y** in the naming have only the *y*-band data. Other fields have only the *i*-band data and fields with + have both *i*- and *y*-band data.

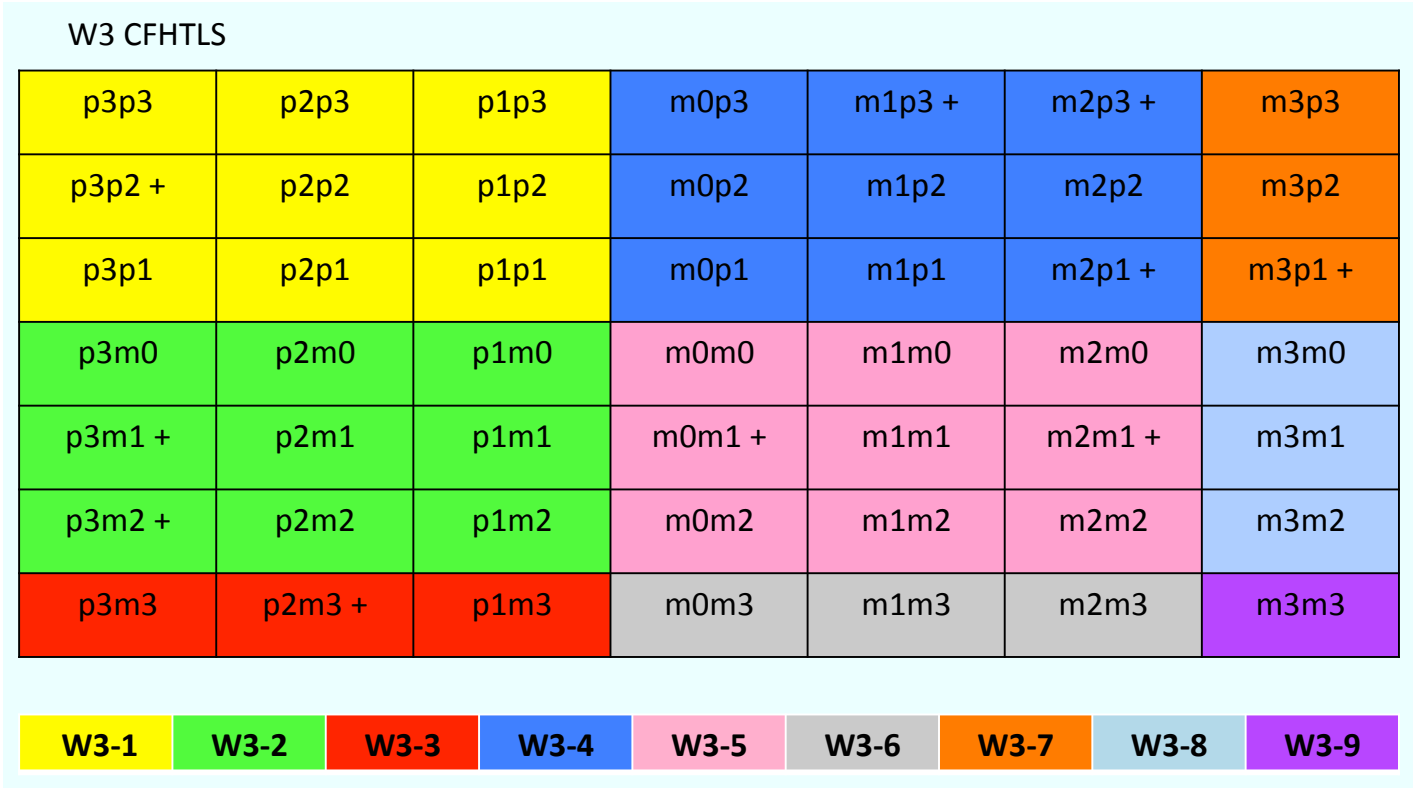

Figure 9.5: Orientation of all W3 subfields. Fields with **Y** in the naming have only the *y*-band data. Other fields have only the *i*-band data and fields with + have both *i*- and *y*-band data.

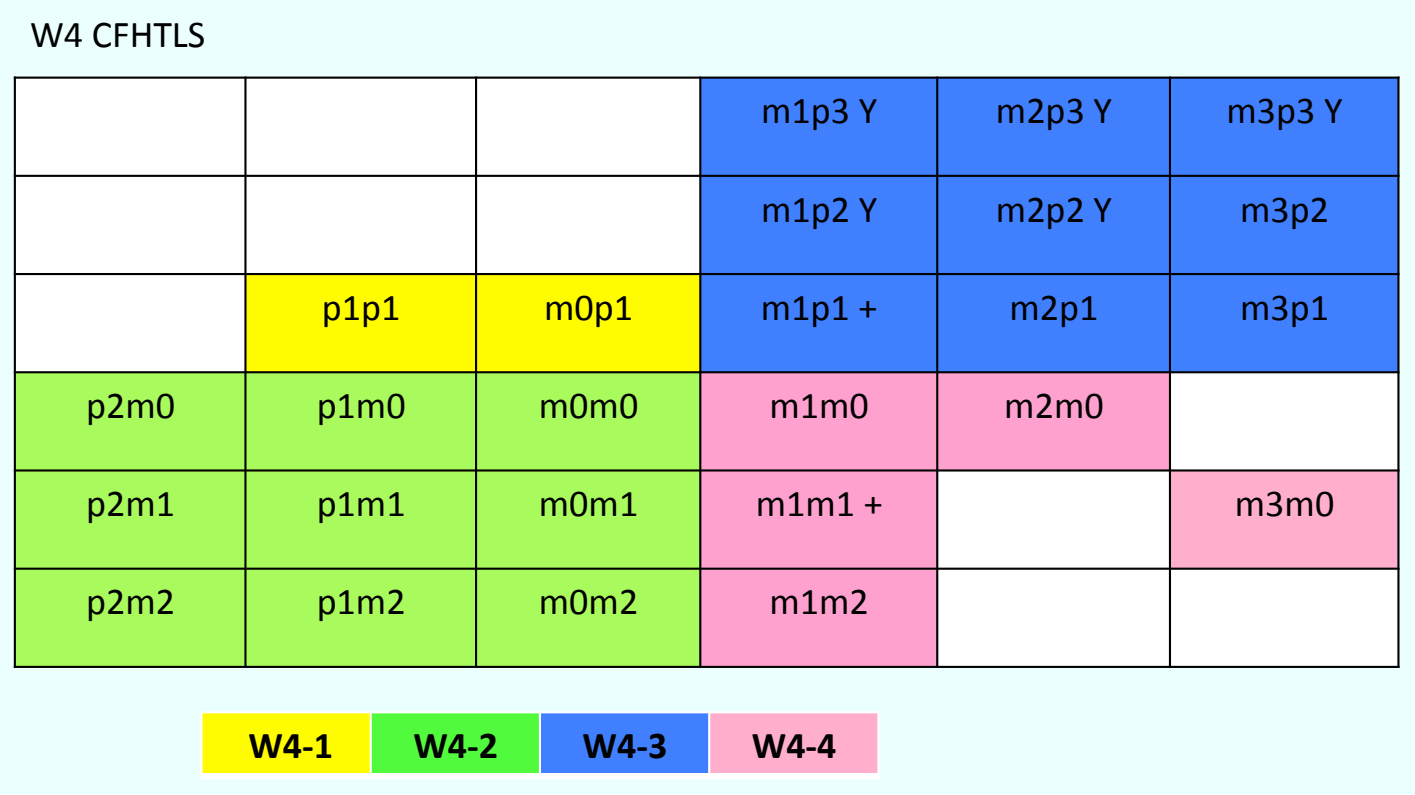

Figure 9.6: Orientation of all W4 subfields. Fields with **Y** in the naming have only the *y*-band data. Other fields have only the *i*-band data and fields with + have both *i*- and *y*-band data.

Chapter 10

Conclusion and Future Work

In this thesis we studied three alternative weak lensing estimators that are complimentary to the standard two-point statistics. Chapter 1 introduced the topic of gravitational lensing and the motivation for seeking alternative estimators. Chapter 2 briefly reviewed the standard model of cosmology and parameters describing this model. In chapter 3, we explained the gravitational lensing phenomenon with the focus on cosmic shear and the relationship between matter and lensing power spectra. In chapter 4, various second and third order cosmic shear statistics were introduced. These quantities were then used in the following chapter 5, as we tested the accuracy and integrity of the numerical simulations developed for the purposes of weak lensing studies. We examined 185 lines of sight of dark matter simulations and showed that they follow the theoretical predictions very closely.

The simulations were also implemented to make forecasts for higher-order statistics for upcoming surveys. Using the simulations, we showed that combining the two- and three-point statistics improves cosmological parameter constraints considerably. We also demonstrated an optimal survey design that will enhance the higher order weak lensing signal. We presented these results in chapter 6.

In chapter 7, we applied the higher order statistical techniques to the observed data. We used 160 $\deg^2$ of the CFHTLS data that were collected at the Canada France Hawaii Telescope. The cosmic shear catalogues have been carefully reduced and tested for various systematics effects by the CFHTLenS collaboration.

We measured both two- and three-point statistics through estimations of corre-

lation functions. We computed the joint likelihood and showed that the cosmological constraints can be indeed significantly improved when higher order statistics are included. These preliminary results are the first 2+3-point statistics based cosmological constraints from a ground-based survey.

Employing numerical simulations, we explored another avenue of complementary statistics that can be derived from weak lensing data. In chapter 8 we showed that the projected reconstructed mass maps, can also be used to constrain cosmological parameters. We added realistic noise to the simulations to mimic the data and measured the probability distribution function of the projected mass. In addition, we explored the emptiest parts of the simulated Universe that correspond to the voids. We showed that such empty regions could also be used to distinguish between cosmological parameters.

This work was performed as a proof of concept. In the future we plan to extend this work by combining the projected mass maps to represent the galaxy redshift distribution. We would then be able to quantify the strength of this approach in constraining cosmological parameters in comparison to two- and three-point statistics. We plan to implement the method developed on the mass maps generated from the CFHTLenS data.

Finally in chapter 9 we presented the clone of the CFHTLenS data, which was produced as part of this thesis, for the purpose of covariance matrix estimations and systematics testing of various scientific projects within the collaboration.

Future weak lensing surveys such as DES (Dark Energy Survey[1]), KiDS (Kilo Degree Survey[2]), JDEM (Joint Dark Energy Mission[3]) and Euclid[4] are planned to be in operation in the next decade. These surveys will cover even larger areas of the sky. The contributions of the CFHTLenS collaboration are directly applicable to future surveys and will enhance their data quality. Our work on numerical simulations can be extended to test the systematics of these surveys and provide forecasts for optimal survey strategies. Future data sets will result in larger mass maps of the dark matter distribution. So it will be much more feasible to include

[1] http://www.darkenergysurvey.org/
[2] http://www.astro-wise.org/projects/KIDS/index.shtml
[3] http://jdem.gdfc.nasa.gov
[4] http://sci.esa.int/science-e/www/area/index.cfm?fareaid=102

the PDF statistics in the upcoming weak lensing analysis. Also the studies using higher-order statistics can be applied to such large surveys to further improve the cosmological constraints.

Bibliography

A. Amara and A. Réfrégier. Optimal surveys for weak-lensing tomography. MNRAS, 381:1018–1026, Nov. 2007. doi:10.1111/j.1365-2966.2007.12271.x.

D. J. Bacon, A. R. Refregier, and R. S. Ellis. Detection of weak gravitational lensing by large-scale structure. MNRAS, 318:625–640, Oct. 2000. doi:10.1046/j.1365-8711.2000.03851.x.

A. J. Banday, K. M. Gorski, C. L. Bennett, G. Hinshaw, A. Kogut, C. Lineweaver, G. F. Smoot, and L. Tenorio. Root Mean Square Anisotropy in the COBE DMR Four-Year Sky Maps. ApJ, 475:393, Feb. 1997. doi:10.1086/303585.

J. M. Bardeen, J. R. Bond, N. Kaiser, and A. S. Szalay. The statistics of peaks of Gaussian random fields. ApJ, 304:15–61, May 1986. doi:10.1086/164143.

M. Bartelmann and P. Schneider. Weak gravitational lensing. Phys. Rep., 340: 291–472, Jan. 2001. doi:10.1016/S0370-1573(00)00082-X.

N. Benítez. Bayesian Photometric Redshift Estimation. ApJ, 536:571–583, June 2000. doi:10.1086/308947.

J. Benjamin, C. Heymans, E. Semboloni, L. van Waerbeke, H. Hoekstra, T. Erben, M. D. Gladders, M. Hetterscheidt, Y. Mellier, and H. K. C. Yee. Cosmological constraints from the 100-deg^2 weak-lensing survey. MNRAS, 381:702–712, Oct. 2007. doi:10.1111/j.1365-2966.2007.12202.x.

F. Bernardeau. The effects of source clustering on weak lensing statistics. A&A, 338:375–382, Oct. 1998.

F. Bernardeau and P. Valageas. Construction of the one-point PDF of the local aperture mass in weak lensing maps. A&A, 364:1–16, Dec. 2000.

F. Bernardeau, L. van Waerbeke, and Y. Mellier. Weak lensing statistics as a probe of {OMEGA} and power spectrum. A&A, 322:1–18, June 1997.

F. Bernardeau, Y. Mellier, and L. van Waerbeke. Detection of non-Gaussian signatures in the VIRMOS-DESCART lensing survey. A&A, 389:L28–L32, July 2002. doi:10.1051/0004-6361:20020700.

F. Bernardeau, L. van Waerbeke, and Y. Mellier. Patterns in the weak shear 3-point correlation function. A&A, 397:405–414, Jan. 2003. doi:10.1051/0004-6361:20021567.

G. Bernstein. Advanced Exposure-Time Calculations. 2001.

E. Bertin and S. Arnouts. SExtractor: Software for source extraction. A&AS, 117:393–404, June 1996.

R. D. Blandford, A. B. Saust, T. G. Brainerd, and J. V. Villumsen. The distortion of distant galaxy images by large-scale structure. MNRAS, 251:600–627, Aug. 1991.

T. G. Brainerd, R. D. Blandford, and I. Smail. Weak Gravitational Lensing by Galaxies. ApJ, 466:623, Aug. 1996. doi:10.1086/177537.

M. L. Brown, A. N. Taylor, N. C. Hambly, and S. Dye. Measurement of intrinsic alignments in galaxy ellipticities. MNRAS, 333:501–509, July 2002. doi:10.1046/j.1365-8711.2002.05354.x.

L.-Y. Chiang, P. Coles, and P. Naselsky. Return mapping of phases and the analysis of the gravitational clustering hierarchy. MNRAS, 337:488–494, Dec. 2002. doi:10.1046/j.1365-8711.2002.05931.x.

P. Coles and L.-Y. Chiang. Characterizing the nonlinear growth of large-scale structure in the Universe. Nature, 406:376–378, July 2000. doi:10.1038/35019009.

R. G. Crittenden, P. Natarajan, U.-L. Pen, and T. Theuns. Spin-induced Galaxy Alignments and Their Implications for Weak-Lensing Measurements. ApJ, 559:552–571, Oct. 2001. doi:10.1086/322370.

R. G. Crittenden, P. Natarajan, U.-L. Pen, and T. Theuns. Discriminating Weak Lensing from Intrinsic Spin Correlations Using the Curl-Gradient Decomposition. ApJ, 568:20–27, Mar. 2002. doi:10.1086/338838.

M. Davis and P. J. E. Peebles. A survey of galaxy redshifts. V - The two-point position and velocity correlations. ApJ, 267:465–482, Apr. 1983. doi:10.1086/160884.

S. Dodelson. *Modern cosmology*. 2003.

O. Doré, T. Lu, and U.-L. Pen. The Non-Linear Fisher Information content of cosmic shear surveys. *ArXiv e-prints*, May 2009.

J. Dunkley, D. N. Spergel, E. Komatsu, G. Hinshaw, D. Larson, M. R. Nolta, N. Odegard, L. Page, C. L. Bennett, B. Gold, R. S. Hill, N. Jarosik, J. L. Weiland, M. Halpern, A. Kogut, M. Limon, S. S. Meyer, G. S. Tucker, E. Wollack, and E. L. Wright. Five-Year Wilkinson Microwave Anisotropy Probe (WMAP) Observations: Bayesian Estimation of Cosmic Microwave Background Polarization Maps. ApJ, 701:1804–1813, Aug. 2009. doi:10.1088/0004-637X/701/2/1804.

G. Efstathiou, M. Davis, S. D. M. White, and C. S. Frenk. Numerical techniques for large cosmological N-body simulations. ApJS, 57:241–260, Feb. 1985. doi:10.1086/191003.

T. Eifler, M. Kilbinger, and P. Schneider. Comparing cosmic shear measures. Optimizing the information content of cosmic shear data vectors. A&A, 482: 9–19, Apr. 2008. doi:10.1051/0004-6361:20078573.

A. Einstein. Die Grundlage der allgemeinen Relativitätstheorie. *Annalen der Physik*, 354:769–822, 1916. doi:10.1002/andp.19163540702.

D. J. Eisenstein and W. Hu. Baryonic Features in the Matter Transfer Function. ApJ, 496:605–+, Mar. 1998. doi:10.1086/305424.

T. Erben, M. Schirmer, J. P. Dietrich, O. Cordes, L. Haberzettl, M. Hetterscheidt, H. Hildebrandt, O. Schmithuesen, P. Schneider, P. Simon, E. Deul, R. N. Hook, N. Kaiser, M. Radovich, C. Benoist, M. Nonino, L. F. Olsen, I. Prandoni, R. Wichmann, S. Zaggia, D. Bomans, R. J. Dettmar, and J. M. Miralles. GaBoDS: The Garching-Bonn Deep Survey. IV. Methods for the image reduction of multi-chip cameras demonstrated on data from the ESO Wide-Field Imager. *Astronomische Nachrichten*, 326:432–464, July 2005. doi:10.1002/asna.200510396.

T. Erben, H. Hildebrandt, M. Lerchster, P. Hudelot, J. Benjamin, L. van Waerbeke, T. Schrabback, F. Brimioulle, O. Cordes, J. P. Dietrich, K. Holhjem, M. Schirmer, and P. Schneider. CARS: the CFHTLS-Archive-Research Survey. I. Five-band multi-colour data from 37 sq. deg. CFHTLS-wide observations. A&A, 493:1197–1222, Jan. 2009. doi:10.1051/0004-6361:200810426.

J. E. Forero-Romero, J. Blaizot, J. Devriendt, L. van Waerbeke, and B. Guiderdoni. LEMOMAF: Lensed Mock Map Facility. MNRAS, 379: 1507–1518, Aug. 2007. doi:10.1111/j.1365-2966.2007.12060.x.

L. Fu, E. Semboloni, H. Hoekstra, M. Kilbinger, L. van Waerbeke, I. Tereno, Y. Mellier, C. Heymans, J. Coupon, K. Benabed, J. Benjamin, E. Bertin, O. Doré, M. J. Hudson, O. Ilbert, R. Maoli, C. Marmo, H. J. McCracken, and B. Ménard. Very weak lensing in the CFHTLS wide: cosmology from cosmic shear in the linear regime. A&A, 479:9–25, Feb. 2008. doi:10.1051/0004-6361:20078522.

J. E. Gunn. A Fundamental Limitation on the Accuracy of Angular Measurements in Observational Cosmology. ApJ, 147:61–+, Jan. 1967. doi:10.1086/148981.

J. Harnois-Deraps, S. Vafaei, and L. Van Waerbeke. Gravitational Lensing Simulations I : Covariance Matrices and Halo Catalogues. *ArXiv e-prints*, Feb. 2012.

J. Hartlap, P. Simon, and P. Schneider. Why your model parameter confidences might be too optimistic. Unbiased estimation of the inverse covariance matrix. A&A, 464:399–404, Mar. 2007. doi:10.1051/0004-6361:20066170.

C. Heymans, L. Van Waerbeke, D. Bacon, J. Berge, G. Bernstein, E. Bertin, S. Bridle, M. L. Brown, D. Clowe, H. Dahle, T. Erben, M. Gray, M. Hetterscheidt, H. Hoekstra, P. Hudelot, M. Jarvis, K. Kuijken, V. Margoniner, R. Massey, Y. Mellier, R. Nakajima, A. Refregier, J. Rhodes, T. Schrabback, and D. Wittman. The Shear Testing Programme - I. Weak lensing analysis of simulated ground-based observations. MNRAS, 368: 1323–1339, May 2006a. doi:10.1111/j.1365-2966.2006.10198.x.

C. Heymans, M. White, A. Heavens, C. Vale, and L. van Waerbeke. Potential sources of contamination to weak lensing measurements: constraints from N-body simulations. MNRAS, 371:750–760, Sept. 2006b. doi:10.1111/j.1365-2966.2006.10705.x.

S. Hilbert, J. Hartlap, S. D. M. White, and P. Schneider. Ray-tracing through the Millennium Simulation: Born corrections and lens-lens coupling in cosmic shear and galaxy-galaxy lensing. A&A, 499:31–43, May 2009. doi:10.1051/0004-6361/200811054.

H. Hildebrandt, T. Erben, K. Kuijken, L. van Waerbeke, C. Heymans, J. Coupon, J. Benjamin, C. Bonnett, L. Fu, H. Hoekstra, T. D. Kitching, Y. Mellier, L. Miller, M. Velander, M. J. Hudson, B. T. P. Rowe, T. Schrabback,

E. Semboloni, and N. Benitez. CFHTLenS: Improving the quality of photometric redshifts with precision photometry. *ArXiv e-prints*, Nov. 2011.

C. M. Hirata and U. Seljak. Intrinsic alignment-lensing interference as a contaminant of cosmic shear. Phys. Rev. D, 70(6):063526, Sept. 2004. doi:10.1103/PhysRevD.70.063526.

H. Hoekstra, Y. Mellier, L. van Waerbeke, E. Semboloni, L. Fu, M. J. Hudson, L. C. Parker, I. Tereno, and K. Benabed. First Cosmic Shear Results from the Canada-France-Hawaii Telescope Wide Synoptic Legacy Survey. ApJ, 647: 116–127, Aug. 2006. doi:10.1086/503249.

O. Ilbert, S. Arnouts, H. J. McCracken, M. Bolzonella, E. Bertin, O. Le Fèvre, Y. Mellier, G. Zamorani, R. Pellò, A. Iovino, L. Tresse, V. Le Brun, D. Bottini, B. Garilli, D. Maccagni, J. P. Picat, R. Scaramella, M. Scodeggio, G. Vettolani, A. Zanichelli, C. Adami, S. Bardelli, A. Cappi, S. Charlot, P. Ciliegi, T. Contini, O. Cucciati, S. Foucaud, P. Franzetti, I. Gavignaud, L. Guzzo, B. Marano, C. Marinoni, A. Mazure, B. Meneux, R. Merighi, S. Paltani, A. Pollo, L. Pozzetti, M. Radovich, E. Zucca, M. Bondi, A. Bongiorno, G. Busarello, S. de La Torre, L. Gregorini, F. Lamareille, G. Mathez, P. Merluzzi, V. Ripepi, D. Rizzo, and D. Vergani. Accurate photometric redshifts for the CFHT legacy survey calibrated using the VIMOS VLT deep survey. A&A, 457:841–856, Oct. 2006. doi:10.1051/0004-6361:20065138.

B. Jain and L. Van Waerbeke. Statistics of Dark Matter Halos from Gravitational Lensing. ApJ, 530:L1–L4, Feb. 2000. doi:10.1086/312480.

M. Jarvis, G. M. Bernstein, P. Fischer, D. Smith, B. Jain, J. A. Tyson, and D. Wittman. Weak-Lensing Results from the 75 Square Degree Cerro Tololo Inter-American Observatory Survey. AJ, 125:1014–1032, Mar. 2003. doi:10.1086/367799.

M. Jarvis, G. Bernstein, and B. Jain. The skewness of the aperture mass statistic. MNRAS, 352:338–352, July 2004. doi:10.1111/j.1365-2966.2004.07926.x.

M. Jarvis, M. Takada, B. Jain, and G. Bernstein. Weak Lensing Cosmology with LSST: Three-Point Shear Correlations. In *American Astronomical Society Meeting Abstracts*, volume 37 of *Bulletin of the American Astronomical Society*, page 1208, Dec. 2005.

B. Joachimi, P. Schneider, and T. Eifler. Analysis of two-point statistics of cosmic shear. III. Covariances of shear measures made easy. A&A, 477:43–54, Jan. 2008. doi:10.1051/0004-6361:20078400.

B. Joachimi, R. Mandelbaum, F. B. Abdalla, and S. L. Bridle. Constraints on intrinsic alignment contamination of weak lensing surveys using the MegaZ-LRG sample. A&A, 527:A26, Mar. 2011. doi:10.1051/0004-6361/201015621.

N. Kaiser. On the spatial correlations of Abell clusters. ApJ, 284:L9–L12, Sept. 1984. doi:10.1086/184341.

N. Kaiser. Weak gravitational lensing of distant galaxies. ApJ, 388:272–286, Apr. 1992. doi:10.1086/171151.

N. Kaiser. Nonlinear cluster lens reconstruction. ApJ, 439:L1–L3, Jan. 1995. doi:10.1086/187730.

N. Kaiser. Weak Lensing and Cosmology. ApJ, 498:26, May 1998. doi:10.1086/305515.

N. Kaiser and G. Squires. Mapping the dark matter with weak gravitational lensing. ApJ, 404:441–450, Feb. 1993. doi:10.1086/172297.

N. Kaiser, G. Wilson, and G. A. Luppino. Large-Scale Cosmic Shear Measurements. *ArXiv Astrophysics e-prints*, Mar. 2000.

A. Kiessling, A. F. Heavens, A. N. Taylor, and B. Joachimi. SUNGLASS: a new weak-lensing simulation pipeline. MNRAS, 414:2235–2245, July 2011. doi:10.1111/j.1365-2966.2011.18540.x.

M. Kilbinger and P. Schneider. Cosmological parameters from combined second- and third-order aperture mass statistics of cosmic shear. A&A, 442:69–83, Oct. 2005. doi:10.1051/0004-6361:20053531.

T. D. Kitching, A. Amara, F. B. Abdalla, B. Joachimi, and A. Refregier. Cosmological systematics beyond nuisance parameters: form-filling functions. MNRAS, 399:2107–2128, Nov. 2009. doi:10.1111/j.1365-2966.2009.15408.x.

E. Komatsu, J. Dunkley, M. R. Nolta, C. L. Bennett, B. Gold, G. Hinshaw, N. Jarosik, D. Larson, M. Limon, L. Page, D. N. Spergel, M. Halpern, R. S. Hill, A. Kogut, S. S. Meyer, G. S. Tucker, J. L. Weiland, E. Wollack, and E. L. Wright. Five-Year Wilkinson Microwave Anisotropy Probe Observations: Cosmological Interpretation. ApJS, 180:330–376, Feb. 2009. doi:10.1088/0067-0049/180/2/330.

E. Komatsu, K. M. Smith, J. Dunkley, C. L. Bennett, B. Gold, G. Hinshaw, N. Jarosik, D. Larson, M. R. Nolta, L. Page, D. N. Spergel, M. Halpern, R. S.

Hill, A. Kogut, M. Limon, S. S. Meyer, N. Odegard, G. S. Tucker, J. L. Weiland, E. Wollack, and E. L. Wright. Seven-year Wilkinson Microwave Anisotropy Probe (WMAP) Observations: Cosmological Interpretation. ApJS, 192:18–+, Feb. 2011. doi:10.1088/0067-0049/192/2/18.

A. Lewis, A. Challinor, and A. Lasenby. Efficient Computation of Cosmic Microwave Background Anisotropies in Closed Friedmann-Robertson-Walker Models. ApJ, 538:473–476, Aug. 2000. doi:10.1086/309179.

D. N. Limber. The Analysis of Counts of the Extragalactic Nebulae in Terms of a Fluctuating Density Field. ApJ, 117:134, Jan. 1953. doi:10.1086/145672.

M. Lombardi and G. Bertin. Improving the accuracy of mass reconstructions from weak lensing: local shear measurements. A&A, 330:791–800, Feb. 1998.

R. Massey, C. Heymans, J. Bergé, G. Bernstein, S. Bridle, D. Clowe, H. Dahle, R. Ellis, T. Erben, M. Hetterscheidt, F. W. High, C. Hirata, H. Hoekstra, P. Hudelot, M. Jarvis, D. Johnston, K. Kuijken, V. Margoniner, R. Mandelbaum, Y. Mellier, R. Nakajima, S. Paulin-Henriksson, M. Peeples, C. Roat, A. Refregier, J. Rhodes, T. Schrabback, M. Schirmer, U. Seljak, E. Semboloni, and L. van Waerbeke. The Shear Testing Programme 2: Factors affecting high-precision weak-lensing analyses. MNRAS, 376:13–38, Mar. 2007. doi:10.1111/j.1365-2966.2006.11315.x.

A. Meiksin and M. White. The growth of correlations in the matter power spectrum. MNRAS, 308:1179–1184, Oct. 1999. doi:10.1046/j.1365-8711.1999.02825.x.

H. Merz, U.-L. Pen, and H. Trac. Towards optimal parallel PM N-body codes: PMFAST. NewA, 10:393–407, Apr. 2005. doi:10.1016/j.newast.2005.02.001.

L. Miller, T. D. Kitching, C. Heymans, A. F. Heavens, and L. van Waerbeke. Bayesian galaxy shape measurement for weak lensing surveys - I. Methodology and a fast-fitting algorithm. MNRAS, 382:315–324, Nov. 2007. doi:10.1111/j.1365-2966.2007.12363.x.

J. Miralda-Escude. The correlation function of galaxy ellipticities produced by gravitational lensing. ApJ, 380:1–8, Oct. 1991. doi:10.1086/170555.

D. Munshi and P. Coles. Weak lensing from strong clustering. MNRAS, 313: 148–152, Mar. 2000. doi:10.1046/j.1365-8711.2000.03190.x.

D. Munshi and B. Jain. Statistics of weak lensing at small angular scales: analytical predictions for lower order moments. MNRAS, 322:107–120, Mar. 2001. doi:10.1046/j.1365-8711.2001.04069.x.

D. Munshi, P. Valageas, L. van Waerbeke, and A. Heavens. Cosmology with weak lensing surveys. Phys. Rep., 462:67–121, June 2008. doi:10.1016/j.physrep.2008.02.003.

L. C. Parker, H. Hoekstra, M. J. Hudson, L. van Waerbeke, and Y. Mellier. The Masses and Shapes of Dark Matter Halos from Galaxy-Galaxy Lensing in the CFHT Legacy Survey. ApJ, 669:21–31, Nov. 2007. doi:10.1086/521541.

J. A. Peacock. *Cosmological Physics*. Jan. 1999.

J. A. Peacock and S. J. Dodds. Reconstructing the Linear Power Spectrum of Cosmological Mass Fluctuations. MNRAS, 267:1020, Apr. 1994.

J. A. Peacock and S. J. Dodds. Non-linear evolution of cosmological power spectra. MNRAS, 280:L19–L26, June 1996.

P. J. E. Peebles. *The large-scale structure of the universe*. 1980.

P. J. E. Peebles. *Principles of Physical Cosmology*. 1993.

U.-L. Pen, T. Zhang, L. van Waerbeke, Y. Mellier, P. Zhang, and J. Dubinski. Detection of Dark Matter Skewness in the VIRMOS-DESCART Survey: Implications for Ω_0. ApJ, 592:664–673, Aug. 2003. doi:10.1086/375734.

J. Pielorz, J. Rödiger, I. Tereno, and P. Schneider. A fitting formula for the non-Gaussian contribution to the lensing power spectrum covariance. A&A, 514:A79+, May 2010. doi:10.1051/0004-6361/200912854.

H. P. Robertson. Kinematics and World-Structure. ApJ, 82:284, Nov. 1935. doi:10.1086/143681.

J. Salmon. Generation of Correlated and Constrained Gaussian Stochastic Processes for N-Body Simulations. ApJ, 460:59–+, Mar. 1996. doi:10.1086/176952.

P. Schneider. Detection of (dark) matter concentrations via weak gravitational lensing. MNRAS, 283:837–853, Dec. 1996.

P. Schneider, L. van Waerbeke, B. Jain, and G. Kruse. A new measure for cosmic shear. MNRAS, 296:873–892, June 1998. doi:10.1046/j.1365-8711.1998.01422.x.

P. Schneider, L. van Waerbeke, M. Kilbinger, and Y. Mellier. Analysis of two-point statistics of cosmic shear. I. Estimators and covariances. A&A, 396: 1–19, Dec. 2002a. doi:10.1051/0004-6361:20021341.

P. Schneider, L. van Waerbeke, and Y. Mellier. B-modes in cosmic shear from source redshift clustering. A&A, 389:729–741, July 2002b. doi:10.1051/0004-6361:20020626.

T. Schrabback, J. Hartlap, B. Joachimi, M. Kilbinger, P. Simon, K. Benabed, M. Bradač, T. Eifler, T. Erben, C. D. Fassnacht, F. W. High, S. Hilbert, H. Hildebrandt, H. Hoekstra, K. Kuijken, P. J. Marshall, Y. Mellier, E. Morganson, P. Schneider, E. Semboloni, L. van Waerbeke, and M. Velander. Evidence of the accelerated expansion of the Universe from weak lensing tomography with COSMOS. A&A, 516:A63, June 2010. doi:10.1051/0004-6361/200913577.

R. Scoccimarro. Transients from initial conditions: a perturbative analysis. MNRAS, 299:1097–1118, Oct. 1998. doi:10.1046/j.1365-8711.1998.01845.x.

R. Scoccimarro and H. M. P. Couchman. A fitting formula for the non-linear evolution of the bispectrum. MNRAS, 325:1312–1316, Aug. 2001. doi:10.1046/j.1365-8711.2001.04281.x.

C. Seitz and P. Schneider. Steps towards nonlinear cluster inversion through gravitational distortions. III. Including a redshift distribution of the sources. A&A, 318:687–699, Feb. 1997.

S. Seitz and P. Schneider. Cluster lens reconstruction using only observed local data: an improved finite-field inversion technique. A&A, 305:383, Jan. 1996.

U. Seljak and M. Zaldarriaga. A Line-of-Sight Integration Approach to Cosmic Microwave Background Anisotropies. ApJ, 469:437–+, Oct. 1996. doi:10.1086/177793.

E. Semboloni, Y. Mellier, L. van Waerbeke, H. Hoekstra, I. Tereno, K. Benabed, S. D. J. Gwyn, L. Fu, M. J. Hudson, R. Maoli, and L. C. Parker. Cosmic shear analysis with CFHTLS deep data. A&A, 452:51–61, June 2006. doi:10.1051/0004-6361:20054479.

E. Semboloni, L. van Waerbeke, C. Heymans, T. Hamana, S. Colombi, M. White, and Y. Mellier. Cosmic variance of weak lensing surveys in the non-Gaussian regime. MNRAS, 375:L6–L10, Feb. 2007. doi:10.1111/j.1745-3933.2006.00266.x.

E. Semboloni, C. Heymans, L. van Waerbeke, and P. Schneider. Sources of contamination to weak lensing three-point statistics: constraints from N-body simulations. MNRAS, 388:991–1000, Aug. 2008. doi:10.1111/j.1365-2966.2008.13478.x.

E. Semboloni, I. Tereno, L. van Waerbeke, and C. Heymans. Sources of contamination to weak lensing tomography: redshift-dependent shear measurement bias. MNRAS, 397:608–622, Aug. 2009. doi:10.1111/j.1365-2966.2009.14926.x.

E. Semboloni, H. Hoekstra, J. Schaye, M. P. van Daalen, and I. G. McCarthy. Quantifying the effect of baryon physics on weak lensing tomography. MNRAS, 417:2020–2035, Nov. 2011a. doi:10.1111/j.1365-2966.2011.19385.x.

E. Semboloni, T. Schrabback, L. van Waerbeke, S. Vafaei, J. Hartlap, and S. Hilbert. Weak lensing from space: first cosmological constraints from three-point shear statistics. MNRAS, 410:143–160, Jan. 2011b. doi:10.1111/j.1365-2966.2010.17430.x.

S. F. Shandarin and Y. B. Zel'dovich. The large-scale structure of the universe: Turbulence, intermittency, structures in a self-gravitating medium. *Reviews of Modern Physics*, 61:185–220, Apr. 1989. doi:10.1103/RevModPhys.61.185.

R. E. Smith, J. A. Peacock, A. Jenkins, S. D. M. White, C. S. Frenk, F. R. Pearce, P. A. Thomas, G. Efstathiou, and H. M. P. Couchman. Stable clustering, the halo model and non-linear cosmological power spectra. MNRAS, 341: 1311–1332, June 2003. doi:10.1046/j.1365-8711.2003.06503.x.

D. N. Spergel, R. Bean, O. Doré, M. R. Nolta, C. L. Bennett, J. Dunkley, G. Hinshaw, N. Jarosik, E. Komatsu, L. Page, H. V. Peiris, L. Verde, M. Halpern, R. S. Hill, A. Kogut, M. Limon, S. S. Meyer, N. Odegard, G. S. Tucker, J. L. Weiland, E. Wollack, and E. L. Wright. Three-Year Wilkinson Microwave Anisotropy Probe (WMAP) Observations: Implications for Cosmology. ApJS, 170:377–408, June 2007. doi:10.1086/513700.

G. Squires and N. Kaiser. Unbiased Cluster Lens Reconstruction. ApJ, 473:65, Dec. 1996. doi:10.1086/178127.

M. Takada and B. Jain. Cosmological parameters from lensing power spectrum and bispectrum tomography. MNRAS, 348:897–915, Mar. 2004. doi:10.1111/j.1365-2966.2004.07410.x.

I. Tereno, C. Schimd, J.-P. Uzan, M. Kilbinger, F. H. Vincent, and L. Fu. CFHTLS weak-lensing constraints on the neutrino masses. A&A, 500: 657–665, June 2009. doi:10.1051/0004-6361/200811077.

S. Vafaei, T. Lu, L. van Waerbeke, E. Semboloni, C. Heymans, and U.-L. Pen. Breaking the degeneracy: Optimal use of three-point weak lensing statistics. *Astroparticle Physics*, 32:340–351, Jan. 2010. doi:10.1016/j.astropartphys.2009.10.003.

P. Valageas. Statistical properties of the convergence due to weak gravitational lensing by non-linear structures. A&A, 356:771–787, Apr. 2000.

C. Vale and M. White. Simulating Weak Lensing by Large-Scale Structure. ApJ, 592:699–709, Aug. 2003. doi:10.1086/375867.

L. van Waerbeke. Scale dependence of the bias investigated by weak lensing. A&A, 334:1–10, June 1998.

L. van Waerbeke. Noise properties of gravitational lens mass reconstruction. MNRAS, 313:524–532, Apr. 2000.

L. Van Waerbeke and Y. Mellier. Gravitational Lensing by Large Scale Structures: A Review. *ArXiv Astrophysics e-prints*, May 2003.

L. van Waerbeke, F. Bernardeau, and Y. Mellier. Efficiency of weak lensing surveys to probe cosmological models. A&A, 342:15–33, Feb. 1999.

L. Van Waerbeke, Y. Mellier, T. Erben, J. C. Cuillandre, F. Bernardeau, R. Maoli, E. Bertin, H. J. McCracken, O. Le Fèvre, B. Fort, M. Dantel-Fort, B. Jain, and P. Schneider. Detection of correlated galaxy ellipticities from CFHT data: first evidence for gravitational lensing by large-scale structures. A&A, 358:30–44, June 2000.

L. Van Waerbeke, T. Hamana, R. Scoccimarro, S. Colombi, and F. Bernardeau. Weak lensing predictions at intermediate scales. MNRAS, 322:918–926, Apr. 2001a. doi:10.1046/j.1365-8711.2001.04241.x.

L. Van Waerbeke, Y. Mellier, M. Radovich, E. Bertin, M. Dantel-Fort, H. J. McCracken, O. Le Fèvre, S. Foucaud, J.-C. Cuillandre, T. Erben, B. Jain, P. Schneider, F. Bernardeau, and B. Fort. Cosmic shear statistics and cosmology. A&A, 374:757–769, Aug. 2001b. doi:10.1051/0004-6361:20010766.

L. Van Waerbeke, Y. Mellier, R. Pelló, U.-L. Pen, H. J. McCracken, and B. Jain. Likelihood analysis of cosmic shear on simulated and VIRMOS-DESCART data. A&A, 393:369–379, Oct. 2002. doi:10.1051/0004-6361:20020932.

L. van Waerbeke, M. White, H. Hoekstra, and C. Heymans. Redshift and shear calibration: Impact on cosmic shear studies and survey design. *Astroparticle Physics*, 26:91–101, Sept. 2006. doi:10.1016/j.astropartphys.2006.05.008.

A. Walker. On Milne's theory of world-structure. *Proc. Lond. Math. Soc., II. Ser.*, 42:90–127, 1936. doi:10.1112/plms/s2-42.1.90.

J. V. Wall and C. R. Jenkins. *Practical Statistics for Astronomers*. Nov. 2003.

M. White and W. Hu. A New Algorithm for Computing Statistics of Weak Lensing by Large-Scale Structure. ApJ, 537:1–11, July 2000. doi:10.1086/309009.

S. D. M. White, M. Davis, G. Efstathiou, and C. S. Frenk. Galaxy distribution in a cold dark matter universe. Nature, 330:451–453, Dec. 1987. doi:10.1038/330451a0.

S. D. M. White, G. Efstathiou, and C. S. Frenk. The amplitude of mass fluctuations in the universe. MNRAS, 262:1023–1028, June 1993.

D. M. Wittman, J. A. Tyson, D. Kirkman, I. Dell'Antonio, and G. Bernstein. Detection of weak gravitational lensing distortions of distant galaxies by cosmic dark matter at large scales. Nature, 405:143–148, May 2000.

Y. B. Zel'Dovich. Gravitational instability: An approximate theory for large density perturbations. A&A, 5:84–89, Mar. 1970.

L. L. Zhang and U.-L. Pen. Fast n-point correlation functions and three-point lensing application. NewA, 10:569–590, July 2005. doi:10.1016/j.newast.2005.04.002.

T.-J. Zhang, U.-L. Pen, P. Zhang, and J. Dubinski. Optimal Weak-Lensing Skewness Measurements. ApJ, 598:818–826, Dec. 2003. doi:10.1086/379119.